Synthesis, Non-Linear Optical and Electrochemical Properties of Novel Organo-Imido Polyoxometalate Derivatives

A thesis submitted to the University of East Anglia

For the degree of Doctor of Philosophy

2016

Ahmed Hadi Abdulameer Al-Yasari

Energy Materials Laboratory

School of Chemistry

Norwich

This thesis is dedicated to my Father
Alhaj
Hadi Al-Yasari

Abstract

This thesis concerns the design and synthesis of a new class of earth abundant redox-active, hybrid inorganic-organic chromophores for use in second-order non-linear optics (NLO): organoimido polyoxometalates (POMs). It presents the first experimental measurements of 2nd order NLO (frequency doubling) coefficients (β) (by hyper-Rayleigh scattering, HRS) and the first spectroelectrochemical measurements on such species. Towards the aim of producing practical miniaturized devices, the species characterised include systems functionalised with pyrrole and carbazole donors that can be electropolymerized to form potentially redox switchable, photoactive films. These are the first reported POM-containing electropolymers with a covalently attached POM, and indicate the potential of these materials for straightforward electrodeposition onto optically transparent, conductive surfaces.

To investigate the structure-activity relationships of the β response, the series of organoimido-Lindqvist chromophores included organic groups with different electron donors (such as amino, dimethylamino, and diphenylamino functionalities), or acceptors (such as iodo, and nitro), and different π-conjugated bridges. Significant β-values were obtained for derivatives with resonance electron donors, and result from strong ligand-to-polyoxometalate charge transfer transitions. No activity was observed for derivatives with resonance electron acceptors, indicating that the POM can only behave as an acceptor. β values increase steadily as the donor strength increases, and/or the π-conjugation extends, in similar fashion to organic systems. Interestingly, the highest β_0-values obtained these derivatives exceed those of any dipolar organic system with comparable donor, π-system and absorption profile, and thus they have much more favourable transparency/non-linearity trade-offs. Resonance Raman and Stark spectroscopy results have confirmed involvement of the POM in the charge transfer transition, which results in unusual dipole moment changes leading to high NLO activity based on the two state model.

Acknowledgements

Contents

Abbreviations

NLO	Non-linear optical
POMs	Polyoxometalates
SHG	Second harmonic generation
SFG	Sum frequency generation
DFM	Difference frequency mixing
EFISHG	Electric field induced second harmonic generation
MPF	Multi-photon fluorescence
τ	Fluorescence life-time
M_F	Fluorescence wave
M_R	Excitation wave
pTSNa	Sodium p-toluenesulfonate
DAST	Dimethyl-Amino-Stilbazolium Tosylate
MLCT	Metal to ligand charge-transfer
LMCT	Ligand to metal charge-transfer
CT	Charge-transfer
ICTL	Intermolecular charge transfer layers
LB	Langmiur- Blodgett
PMMA	Polymethyl methacrylate
OPA	Optical parametric amplification
HRS	Hyper-Raleigh scattering
BLA	Bond length alternation
ICT	Intramolecular charge-transfer
EO	Electro-optical
DR1	Disperse red one
SCE	Saturated calomel electrode
DCP	*N,N'*-diisopropylcarbodiimide
DCC	*N,N'*-dicyclohexylcarbodiimide
EC	Electrochromic devices
HPA	Heteropolyanions

EQCM	Electrochemical quartz crystal microbalance
PV	Photovoltaic
1D	One-dimensional
LPCT	Ligand-to-Polyoxometalate charge transfer
PLCT	Polyoxometalate-to-ligand charge transfer
2D	Two-dimensional
THF	Tetrahydrofuran
TEA	Triethylamine
MeCN	Acetonitrile
DMSO	Dimethyl sulfoxide
FTO	Fluorine-doped tin oxide
GC	Glassy carbon
CV	Cyclic voltammetry
I_p^c	Cathodic peak current
I_p^a	Anodic peak current
E_p^c	Cathodic peak potential
E_p^a	Anodic peak potential
$\nu^{1/2}$	Square root of scan rate
ΔE	The peak potential separation
$E_{1/2}$	Mid-potential between the two peak potentials of a reversible CV
HOMO	High energy occupied molecular orbitals
LUMO	Low energy unoccupied molecular orbitals
PMT	photomultiplier PMT
QC	The quadratic coefficient
MPF	Multi-photon fluorescence
τ	Life-time
MF	Fluorescence wave
MR	Excitation wave
ET	Electronic transition
$\Delta\mu_{12}$	Dipole moment change
RFT-IR	Reflectance fourier transform infrared spectroscopy

XPS	X-ray photoelectron spectroscopy
SEM	Scanning electron microscopy
FIB	Focused Ion Beam
TEM	Transmission electron microscopy
PL	Photoluminescence
EL	Electroluminescence
LED	Light-emitting diodes

Chapter 1

Introduction and Overview

Hybrid materials based on photo- and electro-active molecules or clusters have a wealth of potential applications in solar energy conversion, catalysis, optics and photonics, electronics, sensors, biomaterials and as molecular device components.[1-8] For eventual practical applications, the deposition of interesting materials on surfaces is essential and challenging. This can be achieved in the form of monolayers, multilayers, and polymeric thin films. Molecular non-linear optical (NLO) materials with the ability to respond to external stimulus are one such material, and attract attention for miniaturized devices with switching and memory functions. NLO effects arise from the interaction of intense, coherent laser light with matter in a non-linear function of the applied electromagnetic field. Examples of these effects are frequency doubling, frequency tripling, and two-photon absorption. Second Harmonic generation (SHG) arises from the modification of the incident beam by the induced dipoles in a medium irradiated with laser light resulting in doubling of the laser light frequency, Figure 1.1.
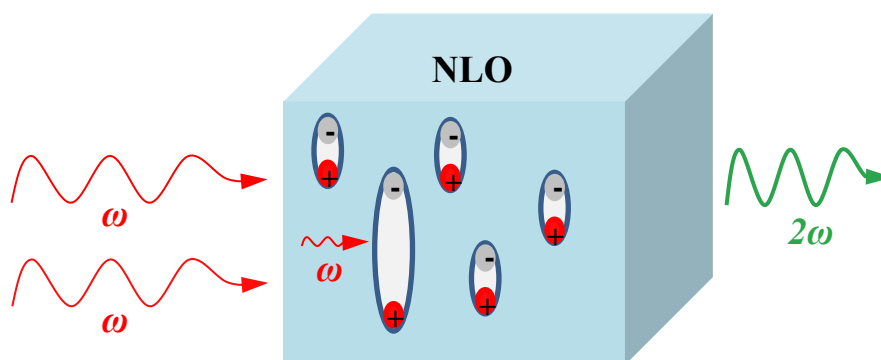
Figure 1.1 Schematic representation of the formation of induced polarisation resulting in doubling the frequency of the incident light**.**

NLO materials are technologically useful – they allow manipulation and exploitation of laser beams for diverse applications such as laser shows, scanning and imaging, telecommunications, photodynamic therapy, electro-optical/all optical data processing, and telecommunications.[9-12]

In this thesis, we will be discussing the synthesis of derivatised polyoxometalates (POMs), their NLO properties, and deposition into polymeric thin films. Specifically, we will be developing organoimido polyoxometalates (POMs), based on earth abundant elements, as redox-active NLO chromophores that can be electropolymerized to form redox switchable, photoactive films. The properties of these materials are little investigated and in addition to non-linear optics and molecular electronics, may find applications in photovoltaics, photocatalysis, or electrocatalysis.

In the following introduction, several areas relevant to this project will be discussed: including NLO, optical switching, conducting polymers, and polyoxometalate chemistry.

1.1. Second-order NLO materials

The study of NLO effects started with the discovery of SHG shortly after demonstration of the first laser, from a quartz crystal pumped by a ruby laser in 1961.[13] The generation of SHG – in other words doubling the frequency of laser light - is the most widely used application for non-linear materials. Figure 1.2 illustrates the frequency doubling or SHG that occurs by simultaneously combining two photons at ω through virtual transitions while a single photon at 2ω is generated in a single quantum mechanical process.
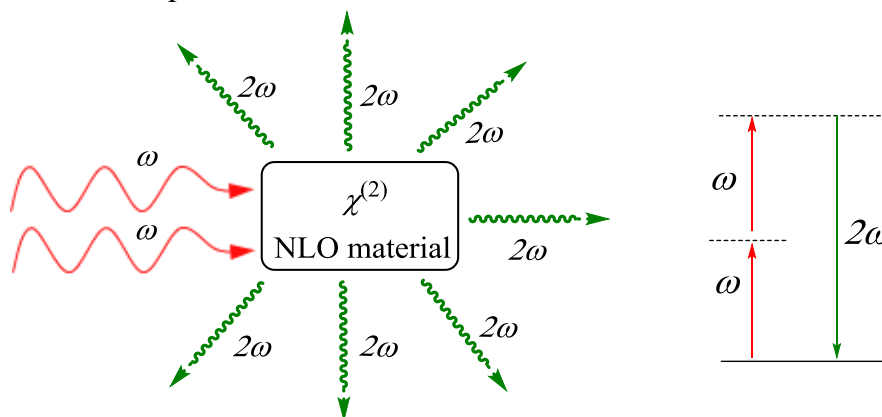
Figure 1.2 Representation of second-harmonic generation (right) and Jablonski diagram of second harmonic generation (left).[14]

1.1.1 Physical Background

It is important first to understand the concepts 'light' and 'matter' before explaining the interaction between them. According to Maxwell's theory, light consists of two oscillating fields, electric (E) and magnetic (B), oriented orthogonally to each other and perpendicular to the direction of propagation. Matter consists of atoms, with negatively charged electrons bound to a positively charged nucleus. When light interacts with matter, its electric field (E) displaces (polarizes) the electron density of the atom. An induced dipole moment is formed because of this interaction that oscillates with the same frequency as the applied optical field. A linear relationship (α) between the induced electric-dipole moment and the electric field is obtained when the intensity of the incident light is relatively low (equation 1.1).

$$\text{Polarization} = \mu = \alpha E \tag{1.1}$$

For bulk or macroscopic materials, the linear susceptibility (χ) of a collection of molecules is used (equation 1.2).

$$P = \chi E \tag{1.2}$$

The polarization acts as a source of radiation at the frequency that describes all the optical properties of a material and the corresponding phenomena such as absorption, reflection, refraction, and diffusion. When the electric field of the light is intense, the relationship between the induced dipole moments and the electric field is no longer linear and the optical susceptibility (χ) becomes dependent on the applied electric field. The polarization thus can be expressed in a power series of the applied electric field.[14-16]

$$P = P^L + P^{NL} \tag{1.3}$$

$$P = \chi^{(1)}E + \chi^{(2)}EE + \chi^{(3)}EEE + \dots \tag{1.4}$$

or

$$\mu = \alpha E + \beta EE + \gamma EEE + \dots \tag{1.5}$$

Where α is the linear polarizability, β is the second-order polarizability or the first hyperpolarizability, and γ is the third-order polarizability or the second hyperpolarizability. The non-linear polarisation of a material with a second-order non-

linear susceptibility irradiated with an optical field at two frequencies (ω_1, ω_2) will act as a source of radiation at new frequencies; $2\omega_1$, $2\omega_2$, $\omega_1+\omega_2$, $|\omega_1-\omega_2|$, which describe the origin of non-linear phenomena such as second harmonic generation (SHG), sum frequency generation (SFG), difference frequency mixing (DFM), and optical rectification (OR). The focus of this work is frequency doubling, SHG.

The first hyperpolarizability, β is a third rank tensor containing 27 elements which are not independent and in which symmetry plays a crucial role. For example, some of these 27 elements disappear depending on the symmetry of the molecule; the first hyperpolarizability, β becomes zero for centrosymmetric materials. These 27 elements correspond to the possible combinations of the three Cartesian components of the polarisation and of the two interacting electric fields. Molecular symmetry can be used to reduce these 27 elements so typically, only a few components are non-zero. In this work, for all the molecules studied there is usually only one component much larger than the others, which allow us to neglect them and reduce the 27 tensors to only one component.

1.1.2 The two state model

The two state model of Oudar and Chemla[13,17] relates the first hyperpolarizability β and molecular parameters which can be used to help design molecules as NLO chromophores. The first hyperpolarizability β can be resonantly enhanced due to enhancement of higher excited states when the studied molecule has an absorption band close to the fundamental or second-harmonic (SH) wavelength. Thus the static (off-resonance) first hyperpolarizability β_0, is useful for comparison of the quadratic NLO properties at different wavelengths, and can be calculated by the two state model assuming only one transition contributes to the NLO properties.

$$\beta_{\text{o}} = \frac{3\Delta\mu_{12}\,(\mu_{12})^2}{2(E_{\text{max}})^2}$$

(1.6)

Where μ_{12} is the electronic transition dipole moment, E_{max} of the optical transition between ground and excited state, and $\Delta\mu_{12}$ is the change in dipole moment between ground and excited state. β_0 is β extrapolated to zero frequency, by definition does not vary with frequency (β does vary with frequency), and is measured under non-resonant conditions where there is no reabsorption of SH which can lead to dramatic over or underestimates of β due to involvement of higher excited states. It can be clearly seen from equation (1.6) that β_0 will generally increase with the decrease of the energy E_{max} (the intramolecular charge-transfer (ICT)).

Equation 1.7 can be used to calculate the static first hyperpolarizability β_0 from the experimental first hyperpolarizability β under non-resonant conditions:

$$\beta_{\text{o}} = \beta \left[1 - \left(\frac{\lambda_{\text{max}}}{\lambda}\right)^2\right]\left[1 - \left(\frac{2\lambda_{\text{max}}}{\lambda}\right)^2\right]$$

(1.7)

Where λ_{max} is the wavelength at maximum absorption and λ is the wavelength of the incident light (laser) that was used during the measurement. This model is only valid in the off-resonant regime, i.e. when the second-harmonic wavelength is much longer than λ_{max} (the wavelength at maximum absorption).

1.1.2 Measuring NLO effects

There are four techniques that can be used to measure the first hyperpolarizability β: (i) second harmonic generation (SHG), (ii) electric field-induced second harmonic generation (EFISH), (iii) hyper-Raleigh scattering (HRS), (iv) stark spectroscopy. The last three methods are molecular level techniques and the former is a macroscopic

level technique. Franken *et al.* first demonstrated SHG in 1961 after the invention of the first laser.[13] In recent years, SHG has been used in high-resolution optical microscopy in biological and medical science. SHG is a coherent, fast, and electronic in origin re-emission process of one photon by non-centrosymmetric solids (crystals) after excitation process with two photons with the same frequency. It can be used for single crystals as well as for oriented thin films. However, this limits its use for solids only. EFISH is the original method used for determination of β in solution which requires alignment of molecules in a solvent by applying a static electric field giving rise to a strong NLO response.[18,19] Since an external electric field is required, this method cannot be used for charged compounds.

An additional technique, Stark spectroscopy can be used to indirectly determine the first hyperpolarizability β, which has recently been used by many groups.[20-22] It also provides information about the change in dipole moment and polarization associated with a transition, which reflects the degree of charge separation. This technique is used to measure the change in the charge transfer spectral profile while a strong DC external electric field is applied. In order to obtained high β values, large transition dipole moment and dipole moment change are needed based on the two state model. Stark has the advantage of avoiding complications from resonance enhancement and reabsorption, however, Stark calculated values often appear to be overestimated compared to real measurements of SH light obtained from EFISH or HRS.[23] Furthermore, care must be taken to avoid mistakenly adding together contributions from geometrically opposed dipoles.

Hyper-Rayleigh scattering (HRS) is a newer technique that enables direct and accurate measurement of the first hyperpolarizability β at the molecular level. In addition, it can be used without applying an electric field to determine the molecular and supramolecular symmetry.[24] HRS has some advantages over the older technique of EFISH. HRS is spontaneous, weak, non-coherent, isotropic, and dephased re-emission process of one photon by the randomly oriented molecules in a liquid

solution after excitation process with two photons.[25] HRS is far more straightforward to interpret than EFISH and can be used for all structure types, including octupoles[26-28] and V-shapes as well as dipoles.

The intensity of the scattered light of a single molecule can be calculated by taking an orientational average over all possible orientations for β (equation 1.8):

$$I_{2\omega} = \frac{16\pi^5}{c\lambda^4 r^2} \left\langle \beta_{HRS}^2 \right\rangle I_\omega^2$$

(1.8)

HRS measurement is usually performed using an intense laser beam at a single wavelength in the near infrared resulting in an incoherently scattered frequency-doubled light at an angle of 90° from the incident light beam from an isotropic solution (Figure 1.3).[29-31] In other words, the fundamental incident light is passing through the sample in the x-direction, and polarizes it in the z-direction while the scattered light is collected in the y-direction. Thus, the sample will have a polarization state with x and z components and β_{HRS} will be the sum of both polarizations in the x and z-directions:

$$\left\langle \beta_{HRS}^2 \right\rangle = \left\langle \beta_{ZZZ}^2 \right\rangle + \left\langle \beta_{XZZ}^2 \right\rangle$$

(1.9)
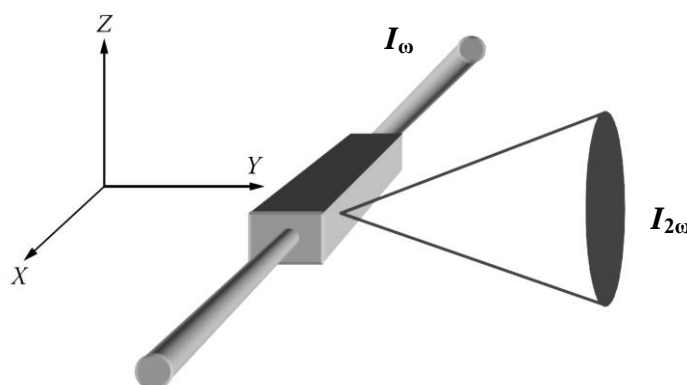
Scheme 1.3 90° angle HRS geometry with I_ω the incident laser beam and $I_{2\omega}$ the second-harmonic signal.[32] Reproduced with permission from reference 32.

For a polar molecule with C_2 symmetry (linear) and only 2 independent and non-zero tensor components, and also assuming that β_{zzz} is much larger than β_{xzz} which is true for most molecules with a Z molecular dipole axis, β_{HRS} can be calculated by equation 1.10:

$$\left\langle \beta_{HRS}^2 \right\rangle = \frac{6}{35} \left\langle \beta_{ZZZ}^2 \right\rangle$$

(1.10)

Moreover, β_{zzz} is directly comparable with β_{EFISH} (β obtained using EFISH method, where dipoles are aligned). It is important to understand the factors that may contribute to the magnitude of the first hyperpolarizability β, as it is a critical parameter for use of NLO materials in various applications and devices. These are chemical structure-NLO property relationships, molecular orientation, and resonance enhancement. The latter, resonance enhancement, is predicted by the same theory that predicts resonance-enhanced Raman scattering. This can occur when the SH frequency is close in energy to the electronic transitions of the chromophore leading to greatly enhanced NLO response. In other words, the origin of this effect lies in matching the SH frequency with an allowed dipole transition from the ground state.

In order to study the involvement of higher excited states (resonance effects) on the first hyperpolarizability, both Wang and co-workers and Shoute and co-workers reported the performance of HRS measurements at a number of different wavelengths.[33-40] They outlined that the first hyperpolarizability increases in magnitude when the SH frequency approaches resonance. On the other hand, first hyperpolarizability β decreases to reach a particular frequency independent value when the SH frequency moves far away from the resonance, called off-resonant (non-resonant conditions) first hyperpolarizability β. In this thesis, two different wavelengths were used 800 and 1064 nm to explore such effects on the first hyperpolarizability β.

1.1.3 Organic /Metallo-organic molecular chromophores

1.1.3.1 Neutral Organic Chromophores

Initial studies of NLO materials were focused purely on inorganic and organic systems. Inorganic crystals of $LiNbO_3$ and KH_2PO_4 were the first solids to demonstrate second-order NLO properties.[13,41,42] There followed studies on inorganic semiconductors such as GaAs, which are used in commercial applications such as optical switches and modulators.[43] However, crystals of these inorganic materials faced a "trade-off" problem between response time and the magnitude of optical non-linearity. The response time, which sets the applications of these materials, is determined by the mechanism of the charge transport process - the way of charge displaced in the material in response to light. The nature of charge transport varies strongly, for instance, in inorganic crystals; ionic displacements are the dominant process. This is normally slow, compared to other mechanisms such as electronic displacements within the molecular structure as in organic/organometallic molecular materials. Semiconducting inorganic crystals are also costly and difficult to produce, and finally they absorb strongly in the visible region. All these drawbacks discounted many possible applications of these materials. As an alternative, organic materials were investigated due to their fast and large NLO response over a broad frequency range, versatility, ease of fabrication and integration into composites.[44,45] Since second-order NLO activity requires a non-centrosymmetric system, most NLO chromophores have been designed as one-dimensional charge transfer molecules. It was demonstrated that any system composed from a benzene backbone with the presence of an electron-donor group on one end and electron-accepting groups on the other end would produce an SHG signal. These groups form a non-centrosymmetric molecule resulting in a permanent dipole moment. Typically, NLO molecules consist of an electron donating group (such as $N(CH_3)_2$, NH_2, OCH_3, OH) and an accepting group (such as NO, NO_2, CHO, CN) connected by π-electron conjugated segments which serves as a charge transmitter, shown schematically in Figure 1.4.
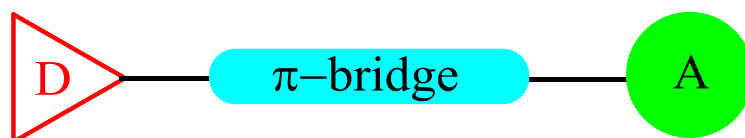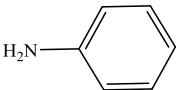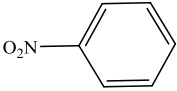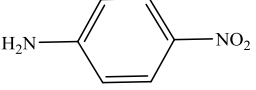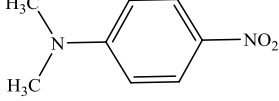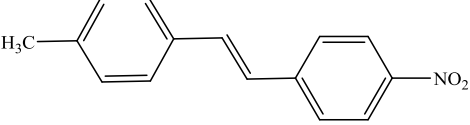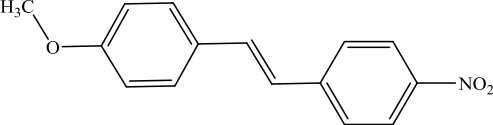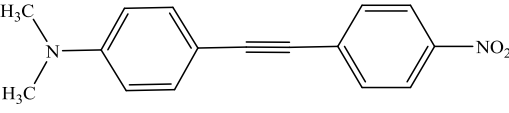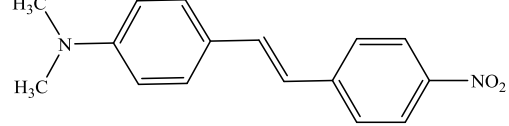
Figure 1.4 Schematic presentation of NLO molecule, where D is donor group and A is acceptor group.

Table 1.1 gives examples of selected organic chromophores with different donor and acceptor strength, and conjugation length, with their β_0 values.[41]

Table 1.1 The effect of the donor and the acceptor groups on β_0.[41]

Compound	β_0 (10^{-30} esu)
	1.1
	2.2
	9.2
	12.0
	15.0
	28.0
	46.0
	53.0

Several studies have been carried out to find the optimum combinations of acceptor, donor, and the length of the conjugation bridge.[46] It has been argued that for a given conjugation bridge length there is an optimal combination of donor and acceptor strengths and beyond this point, changing donor or acceptor strengths will lower the NLO response.[47,48] Bourhill and co-workers demonstrated that bond length alternation (BLA) is a relevant parameter in the optimization of the first hyperpolarizability which can be understood within the context of the two state model.[49] BLA, the average length difference between single and double bonds in π-conjugation of the molecule, are affected by the energetics of resonance structures in the ground state of a dipolar chromophore. Aromaticity is one of the contributing terms affecting these energetic of resonance structures, which can be destabilized by charge separation within molecules. Moreover, charge separation can be enhanced or interrupted by aromaticity. Increasing aromaticity of the acceptor or introducing heteroaromatic rings such as thiophene in place of phenyl group in the conjugated bridges would enhance the degree of ground-state polarization (namely the degree of charge separation) and hence enhance the NLO activity.

1.1.3.2 Charged Organic Chromophores

Neutral Organic Chromophores show lower thermal and photochemical stability. Until the mid-nineties, there had not been much research investigating charged organic compounds as NLO chromophores. As stated before, HRS is the only technique that can be used to measure the NLO properties of such kind of materials. Duan *et al.* reported the first study on the second-order hyperpolarizabilities (β) of ionic species of sodium p-toluenesulfonate (pTSNa) compared to neutral species of similar structure.[50] They found that the ionic species have higher β values than the neutral ones. Stilbazolium compounds showed extremely high non-linearities. Because of this and the possibilities of incorporating them into different macroscopic structures through anion variation or inclusion complexes (zeolites), they have attracted considerable interest. Dimethyl-amino-stilbazolium tosylate (DAST), the

only commercially exploited organic NLO chromophore as a THz-wave generation source, is an example of these compounds with a significant static β value.[51]
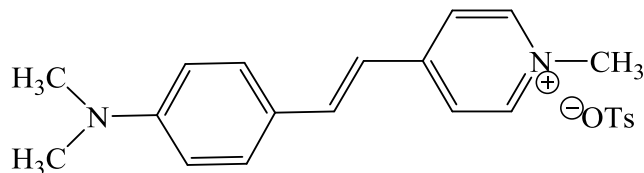
Figure 1.5 Structure and static first hyperpolarizability of DAST, $\beta_0 = 25 \times 10^{-30}$ esu (non-resonant conditions).

1.1.3.3 Transparency-Efficiency Trade-Off

Intramolecular charge-transfer (ICT) is a process of excitation of a chromophore by absorption of a photon, causing electron transfer from the donor (through the conjugated chain in case of organic chromophores) to the acceptor. This process is the origin of the intense visible colours of such chromophores. Organic NLO chromophores show large first hyperpolarizabilities, but absorb in the visible region (intense CT bands in the visible region). A red shift in the CT bands usually occurs in simple one-dimensional dipoles as β increases, causing re-absorption of the SH visible photons by the chromophore and hence causing a decrease in the optical transparency.

In order to completely avoid such problems, chromophores with CT band below 400 nm are preferable; however, this would lower the β responses, leading to a transparency-efficiency trade-off problem. This can be avoided by designing molecules with high β responses, and with absorption bands lay far from the visible region (λ_{max} below 400 nm). The aim therefore, is to design molecules where an increase in β is not accompanied by, or at least a small shift of λ_{max}. This has been achieved through octupolar and multi-dimensional chromophores,[52-55] which are often synthetically complex, or through dipolar organic materials with unusual electronic structures such as unconventional twisted ("tictoid") π-bridges (see Figure 1.6),[56] or

unusual donor sets.[57] In the case of tictoid, the increase in β is ascribed to the high

charge separation, which relates to the two state model.
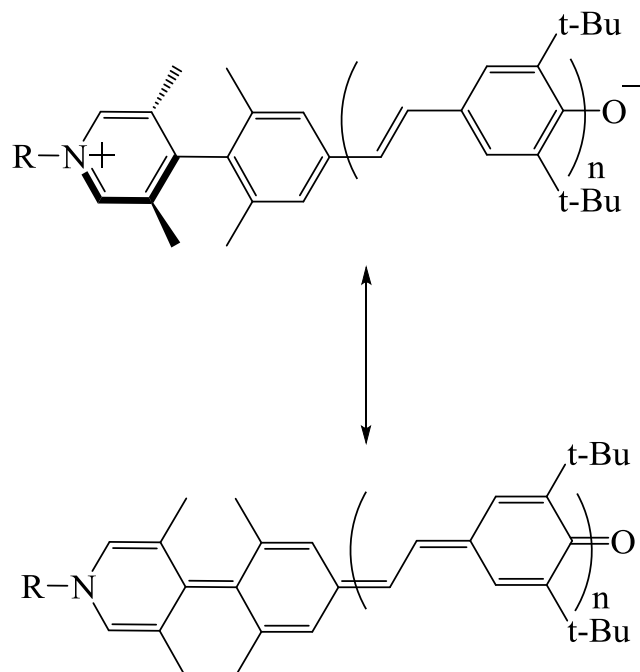
Figure 1.6 Structures of unconventional twisted π-electron system/tictoid chromophore.[58]

1.1.3.4 Metallo-organic chromophores
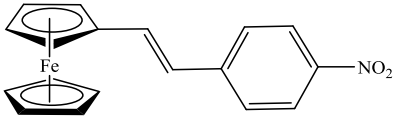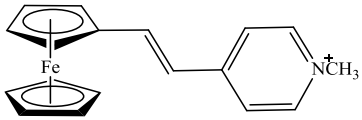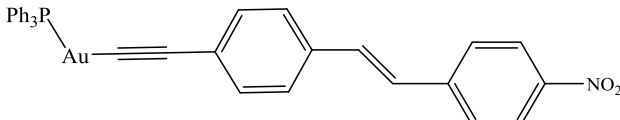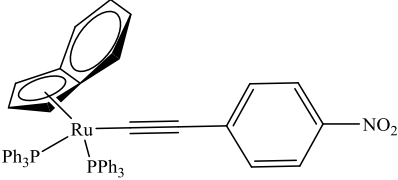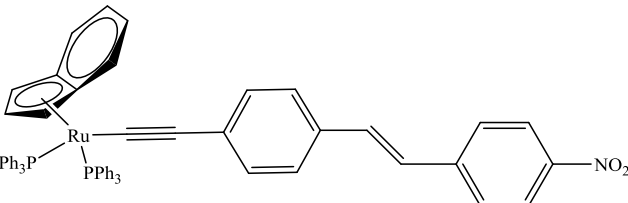
While many studies were carried out on inorganic and organic NLO materials,

organometallic compounds were not investigated until the early nineties. Metals can

introduce new features into organometallic systems such as metal to ligand (MLCT)

or ligand to metal (LMCT) charge transfer bands in the visible region, with large

transition dipole moments and low transition energies, which should result in higher

hyperpolarizabilities by the two-state model.[59,60] They can also introduce redox

activity that leads to switching properties (*vide infra*). Since metals can be electron-

poor or electron-rich depending on oxidation state and ligand environment they can be

used in donors or acceptors. In comparison to some organic systems, they can be

stronger donors or acceptors leading to large hyperpolarizabilities. However, these

materials usually show two optical transitions; an intra-ligand charge-transfer (ILCT)

which is an analogous to the CT-band in benzene-based compounds and an MLCT.

These transitions make the validity of the two-state model questionable in determining the overall β_0 values of a compound. However, it is possible to extract β_0 via assuming only the MLCT transition contributes to the NLO properties.

The most investigated class of organometallics are metallocene-based compounds, where the metallocene acts as the donor group. Green and co-workers first demonstrated the second-order NLO properties of organometallic compounds, they reported that a ferrocene derivative had a good SHG activity.[61] Other groups have also reported several studies on similar ferrocenyl compounds.[62,63] Other organometallic systems such as organoruthenium complexes have been investigated where ruthenium have been utilized as a donor (Ru^{II}), an acceptor (Ru^{III}), and even as a bridge (linker).[64,65] Examples of selected organometallic chromophores with their first hyperpolarizability β_0 are presented in Table 1.2.[66]

The push-pull {5-[4-(dimethylamino)phenylethynyl]-15-(4-nitrophenylethynyl)-10,20 diphenylporphinato}Zn^{II} complex showed extremely high β value measured by HRS at 830 and 1064 nm and exceptional thermal stability, shown in Figure 1.7.[67] Other studies have been investigated similar D–porphyrin–A systems such as phenyl-bridged metalloporphyrins, exhibit rather lower β compared to acetylenyl-bridged systems.[68] In conclusion, introducing metals, compared to that of the free ligand, increases the first hyperpolarizability β. This enhancement is attributed to the change in dipole moments upon excitation within the context of the two-state model (due to the presence of the metal d-electrons that enhances the charge transfer of the excited state) as well as two-photon resonance enhancement.

Table 1.2 Examples of selected organometallics chromophores with their β_0 values.[66]

Compound	β_0 (10^{-30} esu)
	31
	40
	49
	119
	232
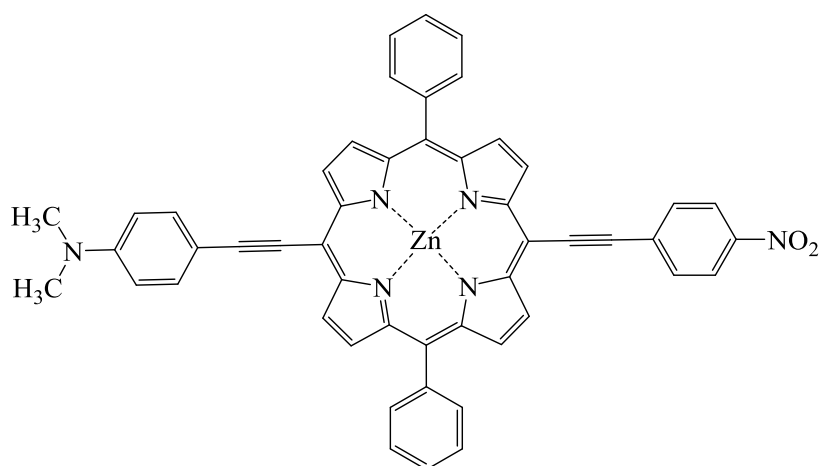
Figure 1.7 Structure of the push-pull {5-[4-(dimethylamino)phenylethynyl]-15-(4-nitrophenylethynyl)-10,20 diphenylporphinato}Zn^{II} complex (λ_{max} = 475 nm), β_0 = 800 × 10^{-30} esu (resonant conditions).

Metal-based compounds have been also used as acceptors to build NLO chromophores such as metal complexes of nitrogen heterocyclic ligands, pyridines and oligopyridines. Over the last twenty years, these classes of NLO chromophores have been received significant attention, studied by several groups specifically the substituted pyridine and stilbazole metal complexes.[66] Figure 1.8 shows an example of a substituted stilbazole Iridium complex reported by Bruce and co-workers.[69] They outlined that upon coordination of the ligand to the [IrCl(CO)$_2$] fragment, which behaves as an electron acceptor, a bathochromic shift of the ILCT was observed resulting in a significant enhancement of β values (using EFISH) from 35×10^{-30} esu for ligand to 67×10^{-30} esu for the complex.
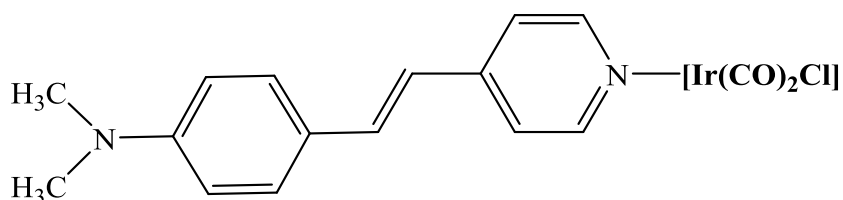
Figure 1.8 4-Donor stilbazole Iridium complex.

Ratner *et al.* investigated the NLO properties of complexes of [4-(dimethylamino)stilbazole]M(CO)$_5$ complexes (M is Cr or W).[70] Similar trend to the Iridium complex was seen, an increase in the EFISH β value (61×10^{-30} esu) of two times of the organic stilbazole ligand, which was in excellent agreement with the calculated β value (67×10^{-30} esu). Vinylpyridine[71,72], bipyridine[73], and terpyridine[74] metal complexes have been also studied, which showed an enhancement in β values upon coordination of the ligand to the metal fragments. However, most of these complexes showed red shift of the ILCT, they absorb in the visible region and this decreases their optical transparency.

1.1.4 Switching properties

Light is faster than anything else, needs much less power to be transmitted through optical fibre lines compared to electrical current through wires, and is also much less distorted during transmission. Therefore, optoelectronic and all-optical computing and telecommunications promise revolutionary increases in performance: through greater speed, higher parallelism and lower energy consumption. The potential is well illustrated by fibre optic telecommunications, which greatly expand signal bandwidth and increase speed compared to copper wire. Presently, fibre optics are used in data transmission in computing and communications, but switching is done electronically. Therefore, processing times are still relatively slow and the conversion process still consumes a great amount of energy.

The electro-optical (EO) effect is an important effect of SHG, which utilizes a DC electric field to change the refractive index of the medium, or the intensity of the SHG light. However, the latter can only modulate intensity, there is no complete "on" and "off" switching phenomena. Other methods must be investigated to provide an "on" and "off" switch, such as redox switching. Materials with switching capabilities have been used in the construction of many types of light modulators and switches,[75,76] To realise light-based devices, new materials are still required for construction of miniaturized optical and optoelectronic components.

Molecular switches can be defined as molecules that have at least two stable forms with different properties (e.g. optical, electrical, etc.) which can be reversibly switched by using stimuli such as light, electrical field, pH, reduction or oxidation (redox), and magnetism. Since NLO materials enable manipulation of laser light, so it can be used to form the basis of optical switches. However, materials with the required combination of a rapid and strong NLO response, rapid, high contrast photo- or redox switching, near infinite stability to on-off cycling, and low cost are elusive. Optical or electro-optical switches allow the possibility of easily switching and modifying light signals in response to an external electrical or optical stimulus with

lower energy consumption and greater speed. NLO-active polymers promise potential use in many photonic systems such as high-speed optical modulators, ultra-fast optical switches, and optical data storage.

1.1.4.1 Redox- Switched NOL materials

For device applications, designing new materials with large NLO responses is not the only factor that must be taken into consideration; there are other factors that also must be considered such as thermal stability, the orientation of molecular dipoles in a bulk material, and properties such as redox chemistry (redox-switching abilities). Currently, redox-switchable molecular NLO materials rely upon either oxidation or reduction of organic groups, or coordinated precious metals (eg. Ru).[77,78] Hence, they suffer from instability, high cost, and difficulty in fabrication.

In 1999, Coe defined three ways of realizing a NLO switching in D-π-A molecules, which are schematically represented in Figure 1.9.[79,80] In type I, the donor capacity of the donor moiety is reduced by proton transfer or oxidation of the donor resulting in a competing acceptor moiety A'. While in type II, the alteration of the hyperpolarizability is caused by the changes in the acceptor. A competing donor moiety D' is formed after either removing a proton or reducing the acceptor moiety. In type III, the alterations to the conjugated π-bridge such as isomerization, or cyclization can diminish the hyperpolarizability.

Type I
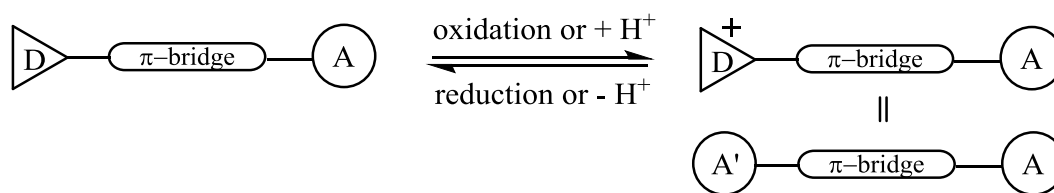
Type II
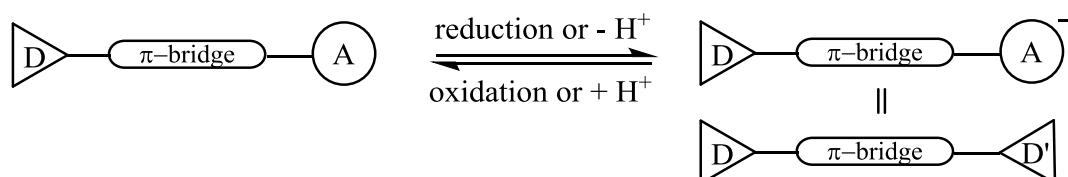
Type III
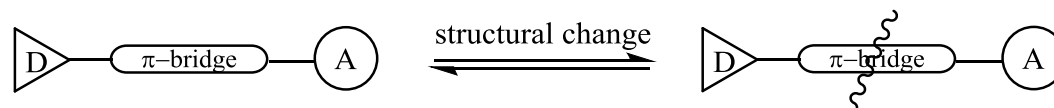
Figure 1.9 Schematic representation of three types of NLO switching possibilities.

As mentioned before, different stimuli can be applied to perform switching. Chemical switching has attracted considerable attention in the research of molecular switches. For instance, it has been shown that ruthenium acetylide complexes can be reversibly switched to the vinylidene form by modifying solvent polarity, with significant changes in their NLO responses.[81] Optically switchable compounds such as photochromic molecules are another important group that also attracted much interest in the field of molecular electronics and optical communications. Lehn *et al.* demonstrated the switching of NLO response of bis(3-thienyl)ethane derivative after 30 second of irradiation at 365 nm where the molecule undergoes photocyclisation with colour change from yellow to deep blue.[82] This process is reversed upon exposure to visible light of wavelength > 600 nm for about 5 minutes (Figure 1.10). However, the switching process takes relatively long time, and hence limits the use of these materials in actual devices. Delaire *et al.* investigated the SHG switching in poled films derived from a PMMA polymer that contains the typical azobenzene-

derived NLO chromophore disperse red one (DR1), as shown in Figure 1.11. They reported that irradiation at 488 nm of the prepared film causes an irreversible decrease (ca. 30%), followed by a reversible decrease (ca. 30%) in the intensity of 532 nm SHG.[83] These decreases are attributed to the partial trans to cis photoisomerisation of the DR1 molecules.
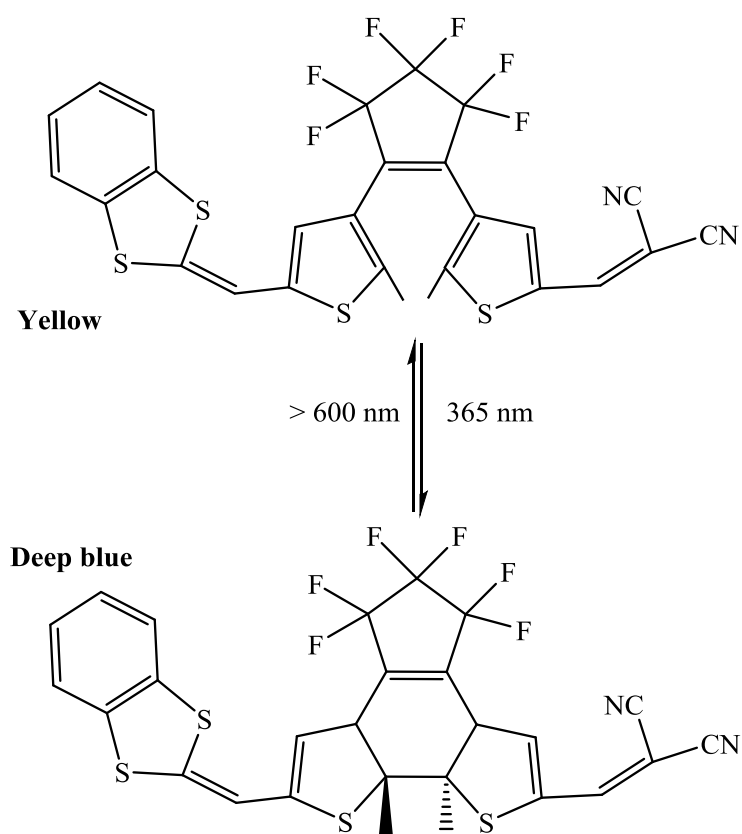
Figure 1.10 Photocyclisation of the bis(3-thienyl)ethane.
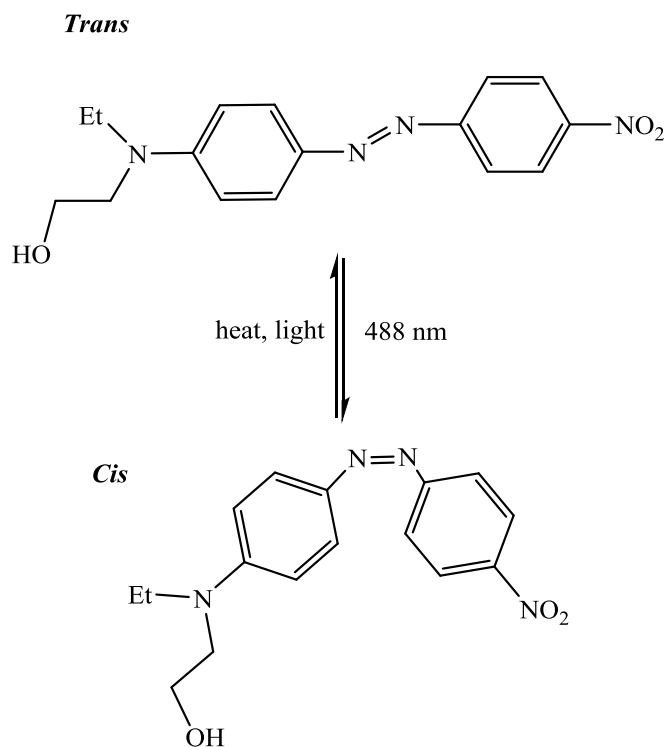
Figure 1.11 Photoisomerisation of DR1.

In 1999, Coe showed the possibility of electrochemical switching of the NLO properties using ruthenium ammine complexes of 4,4'-bipyridinium ligands (Figure 1.12) using the HRS technique, which was the first documented study of a type I switch.[84] The NLO properties were switched "on" and "off" using their well-defined reversible redox chemistry at accessible potentials of 0.46 and -0.48 V versus saturated calomel electrode (SCE). Upon oxidation, the molecule was changed from a D-π-A to A-π-A system due to the oxidation of Ru^{II} to Ru^{III}. The latter (oxidised form) was shown to have no second-order NLO response whereas the reduced (Ru^{II}) form showed a good response.
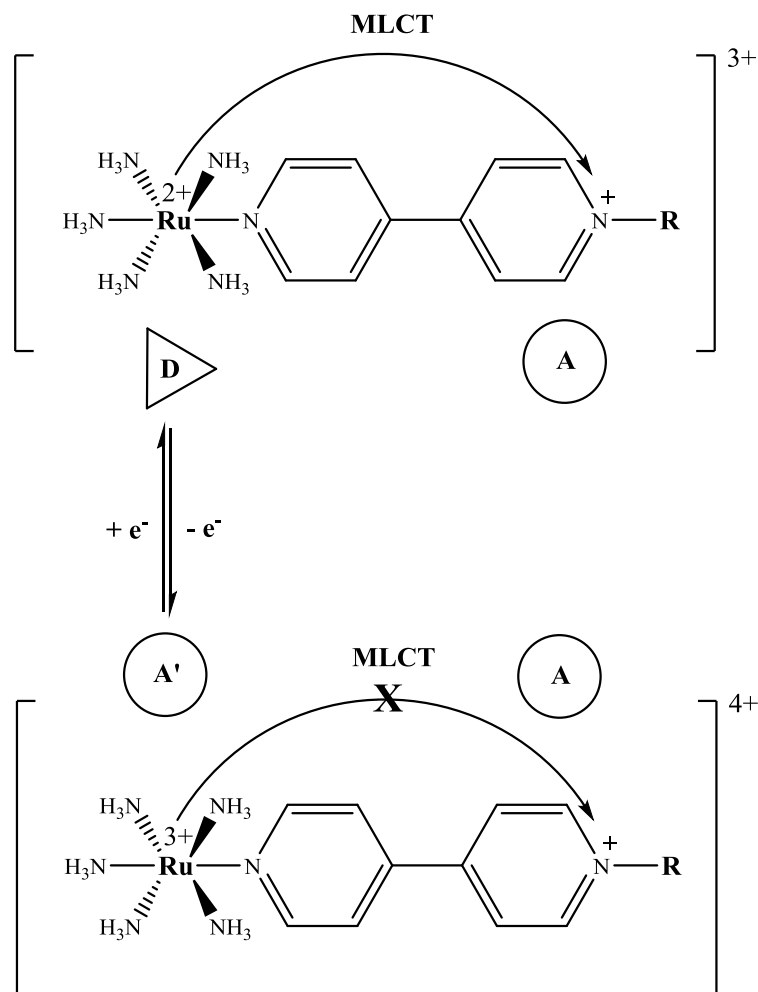
Figure 1.12 Redox switching of ruthenium ammine based complexes, R = Me, Ph, Ac.

A few years later, Coe *et al* in another paper demonstrated the redox switching of SHG responses of LB thin films containing a ruthenium(II) ammine complex.[85] They showed that the first hyperpolarizability *β* response of a deposited film of these complexes on ITO-coated glass decreases 50 % upon oxidation and the signal can be reversed and restored on reduction.

In a study built upon the work of Coe *et al.*, Malaun *et al.* reported the synthesis of another molecule that can undergo NLO switching via its redox chemistry.[86] In their study, they reported the synthesis of molecule containing an octamethylferrocene donor linked to a nitrothiophene acceptor via an ethenyl linker, which showed a static

first hyperpolarizability β_0 of 95 ($\pm$10) $\times$ 10^{-30} esu using HRS technique. Upon oxidation of the octamethylferrocene unit, the static first hyperpolarizability β_0 was reduced to 10 ($\pm$2) $\times$ 10^{-30} esu. Further studies by Coe and Malaun,[87] Powell,[88,89] Weyland and Sporer,[90] and Cifuentes[91] have all continued investigating new systems with electrochemical switching abilities. One aim of this work lies in electrochemical redox switching which will be discussed in the next section.

1.1.5 NLO active polymers

Organic molecules and polymers show large optical non-linearities that make them a suitable alternative to inorganic crystals as the crystalline state imposes limitations on applications. Therefore, many attempts have been made to produce thin film systems and explore their NLO activities. At present, there is a great demand for new materials with enhanced second-order NLO properties; which can be achieved by synthesizing highly efficient, noncentrosymmetric molecules and finding methods for assembling and integrating these materials into noncentrosymmetric bulk materials such as polymeric films or single crystals depending on the target application. Many approaches can be utilized to make noncentrosymmetric thin films such as epitaxy, Langmuir-Blodgett (LB) layers, intermolecular charge transfer layers (ICTL), and functionalized polymers.[92-95] Among all these approaches, functionalized polymers are the most successful approach as all others show problems such as light scattering by crystallites (epitaxy and LB), and temporal stability (ICTL).[96-99]

Polymeric materials for second-order NLO can be classified into five types depending on the distribution and bonding types: - (i) host-guest; (ii) linear (side-chain and main-chain); (iii) cross-linked; (iv) hyperbranched and dendric; (v) organic-inorganic hybrids. The host-guest protocol, illustrated in Figure 1.13, is the easiest to prepare, NLO chromophores are entrapped inside the polymer matrix, and aligned using different poling methods (such as static field, photo-assisted, and all optical poling)[98] to obtain noncentrosymmetric films and hence non-zero second-order

hyperpolarizability. However, poor temporal stability of the molecule after alignment and low percentage load of the NLO chromophores are the main problems with such systems.
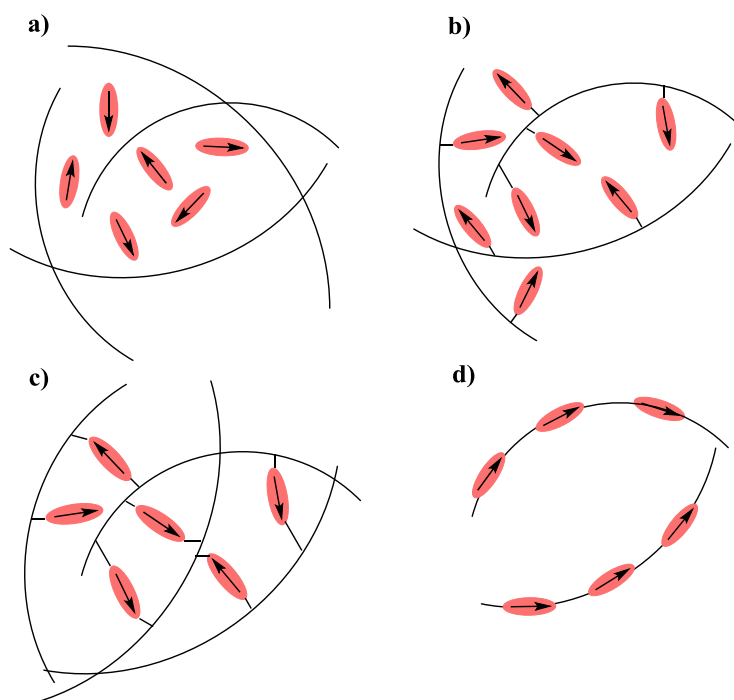
Figure 1.13 Schematic representations of different kinds of functionalization of polymeric materials: (a) host- guest system, (b) side-chain polymer (c), cross-linked polymer, and (d) main-chain polymer.

Havenga and co-workers first introduced the host-guest approach making thin electroluminescencent films, taking advantage of the very good optical properties of amorphous polymers.[100] The matrix polymer provides a good optical propagation while the NLO active chromophores would provide the second-order NLO response. In 2000, Khalil *et al.* reported the use of para-nitro aniline chromophore, grafted polymethyl methacrylate (PMMA) thin film in optical parametric amplification (OPA).[101] Recently, cross-linkable polymers of polyene-based push-pull chromophores with enhanced thermal orientation stability were reported for second-order NLO applications.[99]

It was shown that incorporating heterocyclic conjugating units such as thiophene with electron-acceptors in guest-host polymers would lead to increased non-linearities compared to polyene-based chromophores, they behave as very efficient electron relays.[102-107] Jen *et al.* reported the synthesis of heteroaromatic chromophores with large non-linearities using donor-acceptor substituted thiophene-containing conjugated units hosted in a polyimide matrix with enhanced stability, Figure 1.14.[108]
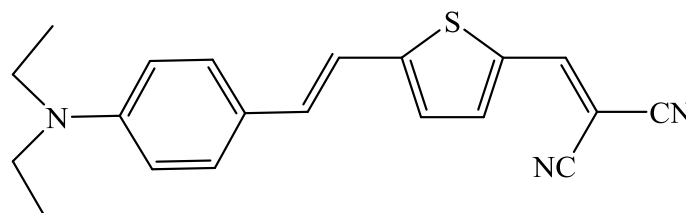
Figure 1.14 Example of a thiophene-containing NLO chromophore.

On the other hand, covalently-based NLO polymers were shown to be the best choice as these chromophores are covalently linked to the polymer backbone and hence allow a high percentage load and better stability. The cross-linked method has been utilized as an effective method to prevent the relaxation of aligned NLO chromophores in the polymer matrix; the main problem with the guest-host system; and to increase the long-term stability of the NLO activity.[109,110] However, the optical loss in such systems is significant and hence limits their practical use in many applications.

In the main chain, the chromophores are chemically incorporated in the polymer backbone itself, Figure 1.13. Despite their stability (temporal and alignment), main-chain polymers show relatively poor processability and low NLO responses compared to the side-chain systems. Therefore, the side-chain is the main focus of current research in the NLO polymer field. In the side-chain system, the NLO chromophores are covalently attached to the polymer backbone, as illustrated in Figure 1.13. Several

studies investigating this system have been carried out using many different polymers such as polyquinolines, polyester, polyethers, polyacrylamides, polyurethates, polymethacrylates, and polystyrenes.[111,112] Polyurethanes and polyimides have shown better properties, such as excellent thermal stability among all others, and therefore, attracted more attention in the fabrication of practical electro-optical (EO) polymers.

1.2. Polyoxometalates

Polyoxometalates are a well-known class of discrete early transition metal-oxide clusters having a huge variety of shapes, sizes, compositions and chemical and physical properties: from Mo_6 and smaller anions to truly nanosized molecules.[113-115] POMs are mainly formed from the transition metals vanadium (V), tungsten (W), and molybdenum (Mo) in high (V/VI) oxidation states which form polyoxoanions primarily by edge, and occasionally, corner sharing of MO_6 octahedra resulting in approximately spherical cages.[113] These structures are stable and have wide-spread applications, mainly in catalysis, electro-catalysis, analytical chemistry, medicine, materials science, and molecular devices.[113,116,117] Generally, POMs are divided into three types, heteropolyanions, isopolyanions, and giant nanosized polymolybdate clusters, which are shown in Figure 1.15.[113] Heteropolyanions are typically formed from a high proportion of one type of transition metal, which is called the "addenda atom" such as W, Mo, V, and from a smaller proportion of the other type of atoms which are called "heteroatoms" such as transition metals or nonmetals.[113] Among heteropolyanions, Keggin and Dawson structures are the most common species.[113] In 1826, Berzelius isolated the phosphomolybdate of formula $[PMo_{12}O_{40}]^{3-}$,[118] and in 1933, Keggin reported the X-ray crystallographic structure of the related anion $[PW_{12}O_{40}]^{3-}$.[119] These POMs, especially the Keggin heteropolyanions with W and Mo, have been extensively studied during the last two decades.[120] They have the general formula $[XM_{12}O_{40}]^{3-/4-}$, where X is heteroatom, M is addenda atom. Modified POMs with different electrochemical and catalytic behaviour can be obtained by replacing W(VI) or Mo(VI) ions by a transition metal (addenda) ion.[120] In 1945, the

Wells-Dawson structure $[X_2M_{18}O_{62}]^{n-}$ was first suggested by Wells, afterwards in 1953 Dawson confirmed the positions of the W atoms in $[P_2W_{18}O_{62}]^{6-}$ using single-crystal X-ray diffraction.[120]

Isopolyanions contain only one type of high-valent group 5 or group 6 transition metal ions. So far, more than 30 isopolyanions are reported, and the Lindqvist and octamolybdate are the most studied among them. The Lindqvist structure, hexamolybdate ion $[Mo_6O_{19}]^{2-}$, has a good thermal and chemical stability and can be easily prepared following the synthetic method reported by Klemperer and co-workers.[121] Its structure consists of a compact arrangement of six edge-shared MoO_6 octahedra. The overall structure has octahedral symmetry. These are attractive units for use as building blocks due to their interesting properties such as redox properties and the ability to accept one electron (electron-relay).[113,122,123]
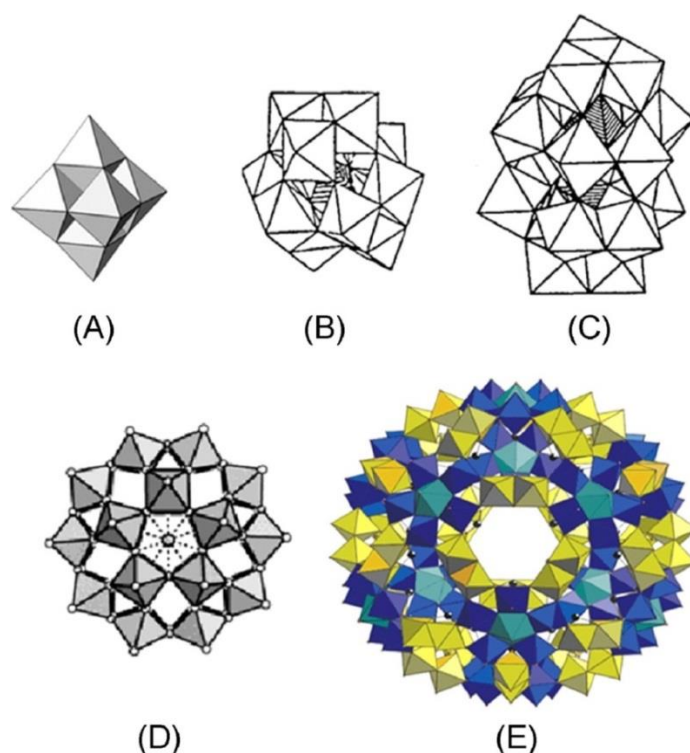
Figure 1.15 Structures of : (A) $[Mo_6O_{19}]^{n-}$; (B) Keggin-type $[XM_{12}O_{40}]^{3-/4}$; (C) Wells-Dawson type $[X_2M_{18}O_{62}]^{n-}$; (D) Preyssler-type $[MP_5W_{30}O_{110}]^{14/12-}$; (E) Keplerate $[Mo_{132}O_{372}$ $(CH_3COO)_{30}(H_2O)_{72}]^{42-}$.[113] Figure was reproduced with permission from reference 113.

1.2.1 Covalent Polyoxometalate-organic hybrid materials

The modification of POMs with organic species has received increasing interest in recent years, producing organic-inorganic hybrid materials with enhanced properties and possible synergistic effects.[124] Organic-inorganic POM-based materials may provide easier integration of POMs into functional architectures and devices. The immobilisation of POMs can be achieved by either non-covalent interactions with the support or by covalent interactions. Most immobilisation of POMs onto supports is based on non-covalent interactions between POMs and their supports. However, electrostatically immobilised POM-based materials often display POM leaching.[125] Covalently-linked organic-inorganic POM-based hybrid materials show enhanced stability towards leaching and improved performance compared to non-covalently-linked materials.[125] In addition, hybrid organic-inorganic POM-based materials would be expected to display novel combinations of properties having application in diverse areas such as non-linear optics, catalysis, electrochemistry, sensors, and photochemistry. Recently, charge-transfer hybrids based on organic donors and inorganic acceptors such as POMs have received great attention as they have potential applications in solar energy conversion and storage, and NLO materials.[116,126,127]

1.2.1.1 Lindqvist derivatives

The terminal metal-oxo groups in the Lindqvist structure are moderately active and can be replaced by various nitrogen-containing groups such as imido, diazoalkyl, and diazenido.[126] The best developed class of POM derivatives are the organoimido Lindqvist derivatives, which were first described by Kang and Zubieta.[128] The chemistry of organoimido derivatization of polyoxometalates has received increasing interest in the last decade owing to the interesting properties of the resulting derivatives. The covalent linking approach provides a fine control of the interaction between different components, improvement of the long-term stability of the assembly, and better dispersion of POMs in materials.[125] The hexamolybdate cluster can be partially or completely substituted with one or more of these organo-imido

ligands resulting organoimido derivatives.[126] Recently, many of these derivatives have been synthesised and structurally characterised.

Maatta reported the synthesis of monosubstituted organoimido derivatives of hexamolybdate using phosphinimines as imido-releasing reagents.[126] Two years later, Proust and co-workers developed this reaction using anhydrous acetonitrile instead of pyridine under nitrogen gas and argued that the molybdyl in the hexamolybdate ion behaves like the carbonyl of aldehydes, ketones or esters to some extent. It can undergo Schiff base reactions similar to those between primary amines and aldehydes or ketones, which involves nucleophilic addition of an amine to the carbonyl followed by the elimination of water molecules.[126] Therefore, in some cases, organic synthetic techniques can be extended into the chemistry of POMs derivatives.

In the meantime, Errington reported other organoimido derivatives of hexamolybdate, by reaction of alkyl and aryl isocyanates with hexamolybdate ions at elevated temperatures in acetonitrile.[129] Removing the resulting water from the reaction mixture is the critical step to complete the reaction successfully. Afterwards, Peng and Wei used the most widely-used dehydrating reagents in organic chemistry such as DCP (*N,N'*-diisopropylcarbodiimide) and DCC (*N,N'*-dicyclohexylcarbodiimide) in the reaction of hexamolybdate with amines and developed a novel DCC-dehydrating synthetic protocol to afford arylimido derivatives of POMs (Figure 1.16).[130] Other dehydrating reagents have been explored by these groups including magnesium sulphate, calcium chloride, 4 Å zeolite, phosphorus pentoxide, and calcium hydride which all showed less activating effect than DCC. That suggests DCC does not only serve as dehydrating reagent only but also activates the terminal $Mo\equiv O$ bond increasing the electrophilicity of the molybdenum atom. However, side reactions with the molybdate ions and the initial products to give by-products may occur if an excess of DCC is added. Though, the synthesis of organoimido derivatives of hexamolybdate from aromatic amines with electron-withdrawing substituents such as nitro, fluoro,

and chloro groups using DCC-dehydrating protocol is very difficult due to the weak nucleophilicity or basicity.[131]
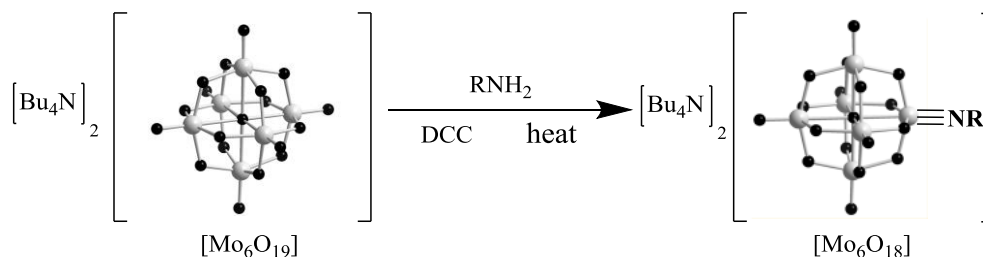
Figure 1.16 Schematic synthesis of organoimido Lindqvist derivatives.

In recent years, many synthetic protocols have been reported adapting classical reactions from organic synthesis for the synthesis of POM derivatives such as palladium-catalysed C-C bond coupling; particularly Sonogashira coupling.[132] The latter allows the grafting of organic moieties with a controlled directionality under mild conditions, has been already used successfully.[133,134]

Disubstituted derivatives have also been explored as potential building blocks for constructing POM-based hybrids. These derivatives were first synthesised by Maatta using $(n\text{-}Bu_4N)_2[Mo_6O_{19}]$ with two equivalents of 2,6-diisopropylphenyl isocyanate in refluxing pyridine for 8 days.[135,136] However, this method is an inefficient and time-consuming process and the crude products contained a mixture of higher- and lower-substituted hexamolybdates. Peng and Wei group reported the synthesis of difunctionalized arylimido derivatives of hexamolybdate with good yield and high purity using $(n\text{-}Bu_4N)_2[\alpha\text{-}Mo_8O_{26}]$ with DCC and 4-iodo-2,6-diisopropylaniline or 4-ethynyl-2,6-dimethylaniline at the ratio of 1 : 2 : 2 in refluxing dry acetonitrile for 6 to 12 hours.[137-139]

In general, d–p π electronic interactions may occur in the organoimido derivatives of POMs via the extension of the organic π electrons in the arylimido unit to the inorganic framework, which dramatically modifies the electronic structure and redox

properties of the corresponding parent POMs. These derivatives show strong electronic coupling through strong charge transfer bands (absent in the isolated clusters and organic groups) and shifted electrode potentials, as shown in Figure 1.17.[140] The incorporated organic ligands provide great potential in the controllable synthesis of organic-inorganic hybrids by using well-developed common organic methods such as coordination, addition polymerisation, carbon-carbon couplings, and esterification.[126] Various organic synthesis methods have been utilised, such as Pd-catalysed carbon-carbon coupling and esterification, to construct novel nanostructured organic-inorganic hybrids materials using organoimido substituted POMs as building blocks (Figure 1.18).[126,133] Both post-functionalization and direct functionalization can be applied to the synthesis of POMs-based materials, however, post-functionalization is more attractive for such functionalization as the complexity of the target increases.[125]
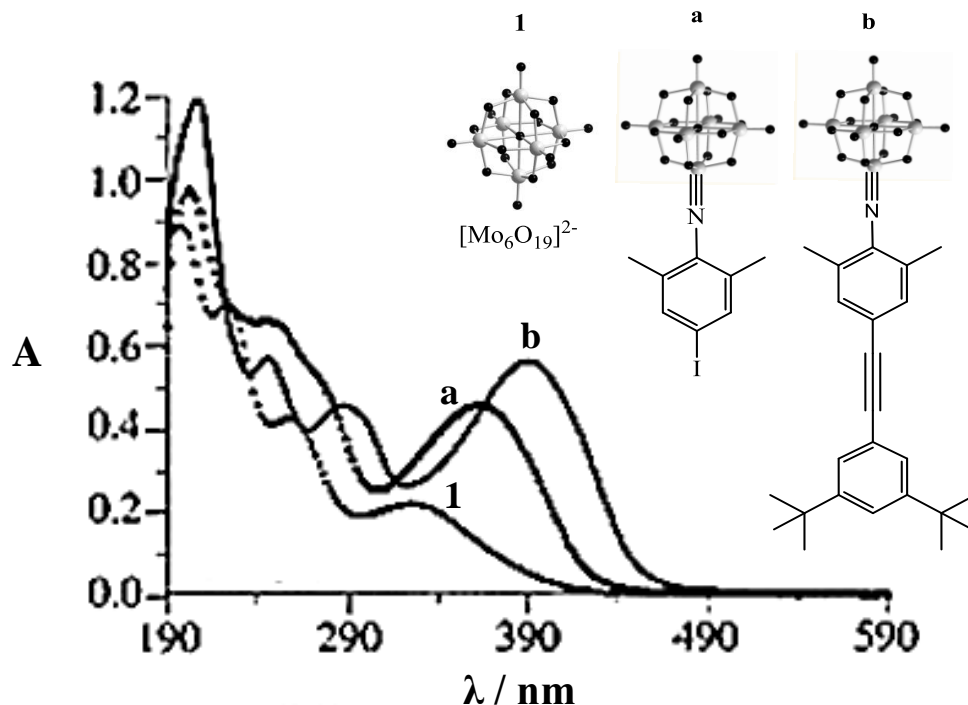
Figure 1.17 UV/Vis absorption spectra of **1**, [Bu$_4$N] [**a**], and [Bu$_4$N] [**b**].[140] Figure was reproduced with permission from reference 140.
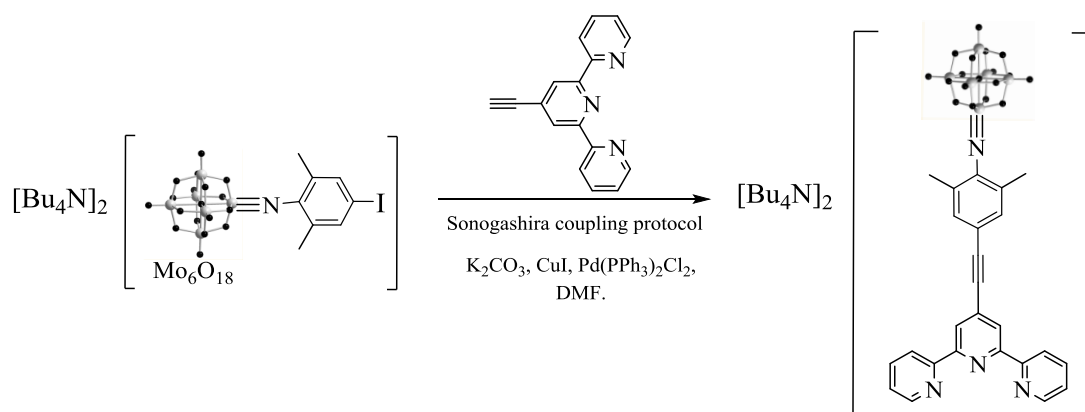
Figure 1.18 Synthesis of a molecular hybrid containing POM clusters.[133]

1.2.1.2 Keggin derivatives

By altering the stoichiometric and pH conditions, various lacunar POM species can be synthesized; however, some of these lacunaries are not stable thermodynamically and can often revert to their parent anion. Keggin "lacunary" derivatives can be prepared by removing one, two, or three oxo-metal vertices from the $[XM_{12}O_{40}]^{n-}$ parent. A cavity is formed after this removal leaving five oxygen-donors, which can be utilized for incorporating an added $[ML]^{n+}$ unit in a pseudo-octahedral geometry. An enormous range of complexes have been synthesized utilizing such vacant sites.[141,142]. In 1976, Klemperer is credited for reporting the first example of a polyoxometalate covalently bound to an organometallic group $([(CpTi)PW_{11}O_{39}]^{4-})$.[143] Since then a relatively large number of organometallic-substituted polyoxometalates have been prepared such as organosilanes, organotin, etc.[144] These are obtained by reaction of organometallic fragments with lacunary anions filling the gap left by the removal of oxo-metal octahedra from the parent anion. Knoth first reported the organosilyl Keggin cluster α-$[SiW_{11}O_{40}\{O(SiR)_2\}]^{4-}$ (Figure 1.19) by reacting $RSiCl_3$ (R = C_2H_5, CH=CH$_2$, $C_{10}H_{21}$, Ph, NC(CH$_2$)$_3$, C_3H_5) with $[\alpha\text{-}SiW_{11}O_{39}]^{8-}$ in unbuffered solutions.[145]
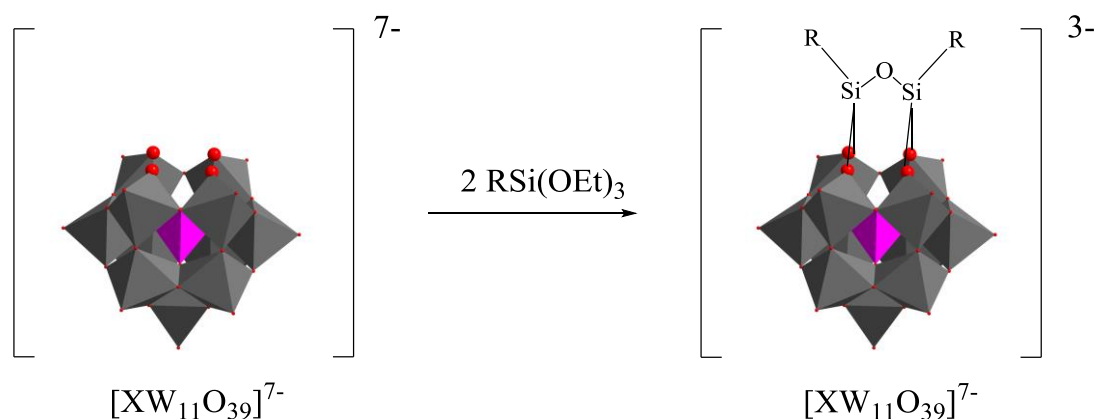
Figure 1.19 Schematic synthesis of organosilyl-$[XW_{11}O_{39}]^{7-}$.

Judenstein *et al.* extended these reactions to prepare analogues from the $[\alpha\text{-}PW_{11}O_{39}]^{7-}$ parent.[146] Moreover, Proust *et al.* outlined that hydrosilylation can be used to extend the organic part of these derivatives.[147] Subsequently, Proust and co-workers focused their attention on the synthesis of organo-silyl derivatives of the redox active Keggin and Dawson POMs.[148-150] They reported the synthesis of two Keggin clusters of amino and alkyne aryl-silyl derivatives with potential possibility for postfunctionalization to address a large range of building blocks.[149] Subsequently , a terminal alkyne functionalized organosilyl Keggin derivative was successfully grafted to heteroleptic cyclometalated iridium complexes.[151] Electrochemical measurements of these derivatives revealed a poor electronic interaction between the POMs and the organic chromophores. Weak electronic communication (coupling) between the organic part and the POMs was indicated as well by UV-Vis spectrum, which is essentially a sum of the spectrum of the two components (there is no new charge transfer transition). Such weak coupling was also noted in their parent derivatives, the Keggin clusters of amino and alkyne aryl-silyl derivatives, as well as in other analogous compounds. While electron transfer can occur between the organic or metal-organic groups and the POM, the weak electronic coupling means that the observed behaviour is simply an enhancement of phenomena that occur with no

covalent linkage. This means such systems are not of interest for NLO, where strong donor-acceptor communication is essential.

1.2.2 POMs in films and at surfaces

POMs have been utilised for modifying surfaces with potential application in heterogeneous or homogenous catalysis and have been extensively explored as photocatalysts or electrocatalysts.[152-154] Due to their interesting electronic and optical properties, POM could be used to build new materials with magnetic, electronic and optical properties. For such practical applications, strategies on the fabrication of POM-based organic-inorganic films are required.[155-157] Many strategies have been developed to prepare such films by either non-covalent interactions with surface; such as layer-by-layer (LBL),[158] Langmuir-Blodgett (LB),[159,160] or by covalent interactions through organic derivatization strategies (including polymeric films), for example- Proust and co-workers have synthesized and electrografted new organosilyl/-germyl Keggin-type polyoxotungstates onto Si surfaces resulting in an electro-active films .[161] To date, non-covalent POM-based hybrid materials have been developed much more than covalent hybrids.

Kurth *et al.* reported the fabrication of electrochromic devices (EC) utilizing LBL of europium-containing POM clusters, poly(allylamine hydrochloride), and poly(styrenesulfonate) with high electrochemical contrast, adequate response time, low operation voltage, and low power consumption.[158] These films showed excellent stability; like transition metal oxides and the function of the POMs could be turned via molecular design. Several groups have focused their attention on the fabrication of POM-based thin EC films.[162-166] Recently, Han *et al.* reported the vanadium-containing POM-based pure inorganic multi-colour EC thin film fabricated by a facile solution-based electrodeposition method. They found that colour modulation from transparent to blue and purple can be achieved by using an electrodeposited film of α-$P_2W_{15}V_3$ as EC material and nano-TiO_2 as a substrate.[155]

Generally, a carrier matrix such as polymer or organic species is usually required to prepare POM thin films as POMs themselves are poor film formers.[113,167] Conducting polymers can feature reversible redox chemistry and ionic transport and also can provide ideal network where polyoxoanions are incorporated.[113,167] In recent years, modified electrodes with conducting polymers doped with electroactive species have been of growing interest in the field of analytical chemistry. [168-170] Several studies have been made on the application of nanostructured hybrids of conducting polymers ranging from electrocatalytic activity, electrochemical supercapacitors, materials, photoelectrochemical and energy conversion and storage.[171-176] These studies have been focused on the synthesis of nanostructured hybrids of conducting polymers (polypyrrole, polythiophene, polyaniline and their derivatives) with POMs and their applications.

POMs can be trapped in a polymer matrix via either electropolymerisation of a polymerizable monomer to form a polymer film in the presence of POM anions; taking the advantage of the POM as an electrolyte (one-step method), or an electropolymerisation of a polymerizable monomer to form a polymer film first then soaking in the solution containing POMs to allow its passive diffusion into the polymer matrix (two-step method), illustrated in Figure 1.20. However, the main drawback of the two-step method is POMs leach from the film more than films prepared by one-step method.[113]
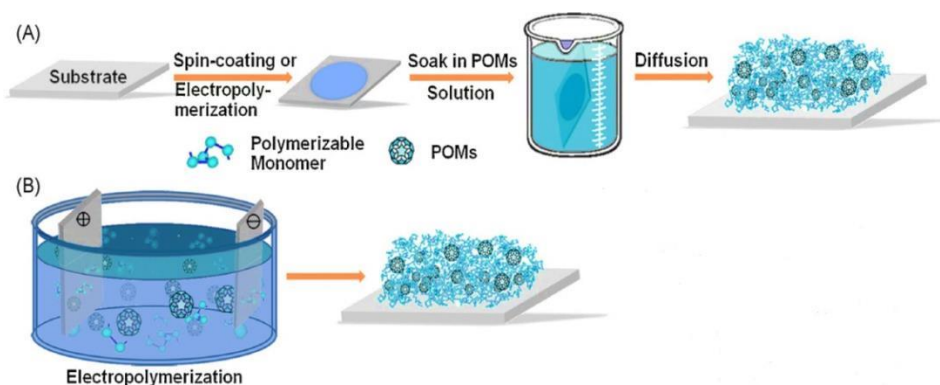
Figure 1.20 Scheme representation of preparation of POM–polymer matrix via two-step (A) and one-step (B) methods.[113] Figure is adapted with permission from reference 113.

The modification of electrode surfaces with POMs, mainly of Keggin and Dawson parent structures, has been quite well studied.[177,178] For example, hybrid nanocomposites comprising polyaniline and $H_3[PMo_{12}O_{40}]$ as electrodes for solid-state electrochemical capacitors have been studied by Gómez-Romero and co-workers.[179] Iron-substituted heteropolytungstates $[PW_{11}O_{39}Fe^{II}(OH_2)]^{4-}$ entrapped in (N-methylpyrrole) films have been synthesised and their electro-chemical properties in presence of NO^{2-} have been also explored by Bidun and co-workers.[180] In addition, Lapkowski *et al.* have reported the synthesis of polyaniline films doped with $H_4PMo_{11}Fe^{II}O_{39}$ and $H_4PMo_{11}Mn^{II}O_{39}$.[168] The electrogeneration and the electrochemical behaviour of polypyrroles doped with $[PW_{12-x}Mo_xO_{40}]^{3-}$ (x)=(0,3,6,12) has been reported by Cheng and co-workers.[120]

Polypyrrole and its derivatives are among the most studied conducting polymers. Anodic oxidation can be applied to synthesize polypyrrole from the monomer in solution, both in aqueous and non-aqueous media.[181] Polypyrrole doped with anions can be obtained by the incorporation of anions via electrochemistry simultaneously with the polymer synthesis. Abrantes *et al.* reported the synthesis of Keggin-type heteropolyanions (HPA), the phosphotungstate ($[PW_{12}O_{40}]^{3-}$) incorporated in polypyrrole during electropolymerisation in aqueous solution with its electrochemical quartz crystal microbalance (EQCM) studies.[182] Incorporating iron-substituted heteropolytungstates $[(H_2O) Fe^{III}SiW_{11}O_{39}]^{5-}$ in a polypyrrole film has been explored by Anson and co-workers. However, the resulting modified electrode showed poor electrocatalytic reduction activity to a substrate (electrocatalytic reduction of nitrite.).[177] This suggests that the pyrrole matrix could impair the specific properties of these anions. Among different electronic conducting polymers, Faber and co-workers showed that $[(H_2O) Fe^{III}PW_{11}O_{39}]^{4-}$ anion could be efficiently retained in a poly (N-methylpyrrole) film and found to be electrochemically stable and the most suitable to achieve the electrocatalytic reduction of nitrite ions.[177]

By controlling the polymerisation conditions, different spatial repetitions and structures of the POM-polymer composites can be obtained.[183] In some cases, the polymer environment affects the electrochemical properties of the trapped POMs. Moreover, desired inherent morphological properties of the polymer can be obtained by a correct selection of the incorporated POMs. However, very few studies have been reported so far on conductive polymers containing POMs through covalent bonds. In 2005, Peng *et al.* first reported the synthesis of covalently attached Lindqvist clusters to the side chains of conjugated polymers with potential applications in photovoltaic (PV) cells.[184] In this example, the {Mo$_6$} cluster is linked to the conjugated backbone through either rigid conjugated bridge (Figure 1.21, a), or flexible alkyl chains (Figure 1.21, b). In a follow up study, they reported the use of these Lindqvist-based polymers in the fabrication of photovoltaic cells, which were sandwiched between a transparent anode and a cathode producing single-layer photovoltaic cells.
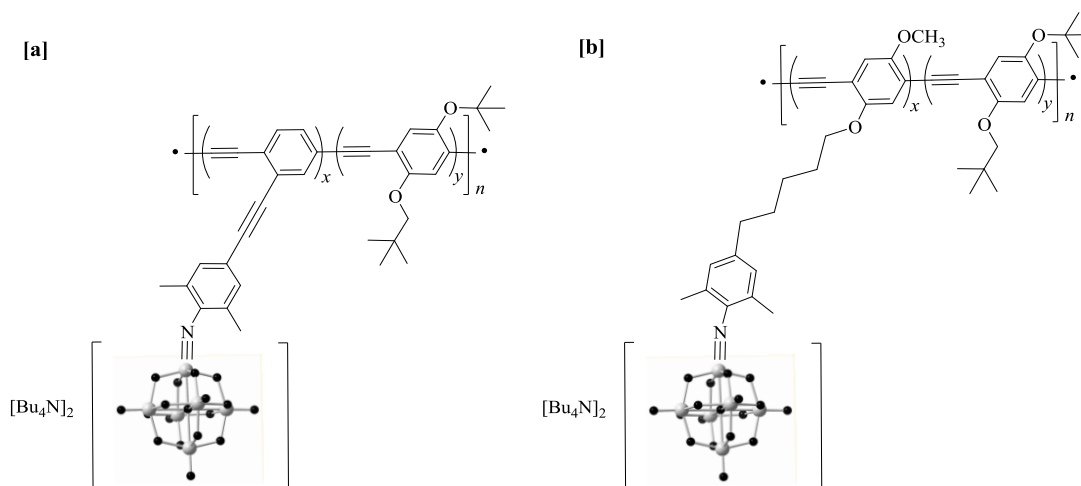
Figure 1.21 Structures of Lindqvist-based polymers; (a) the {Mo$_6$} cluster is linked to the conjugated backbone through the rigid conjugated bridge, (b) the {Mo$_6$} cluster is linked to the conjugated backbone through the flexible alkyl chains.[184]

1.2.3 POMs-based hybrids as NLO chromophores

POM-based organic and inorganic hybrid materials, especially organoimido-Lindqvist derivatives are excellent candidates as NLO materials due to their strong d-π interactions between the organic delocalised π electrons and the cluster empty d orbitals, intense electronic transitions, versatility via wide range of metals, and ease of modification to produce building blocks for targeted applications (non-centrosymmetric molecules).[133,140,184-188] However, their photonic properties have been very little addressed, so far only predicated by calculations that indicate significant second-order NLO coefficients.[189-195] This prediction, combined with the well-defined, and fast electrochemistry of the Lindqvist anion, makes such materials attractive target for use as redox switchable NLO chromophores (type II), as illustrated in Figure 1.20. There is a possibility that the delocalisation of the added electron to POM cluster would result in a strongly enough interaction with the organic part leading to effective switching activity. The molecular non-linearities of such systems are primarily one-dimensional (1D) NLO chromophore. Therefore, the structure-property relationships (two-state model) could be helpful in designing these new organoimido POM-based NLO chromophores.
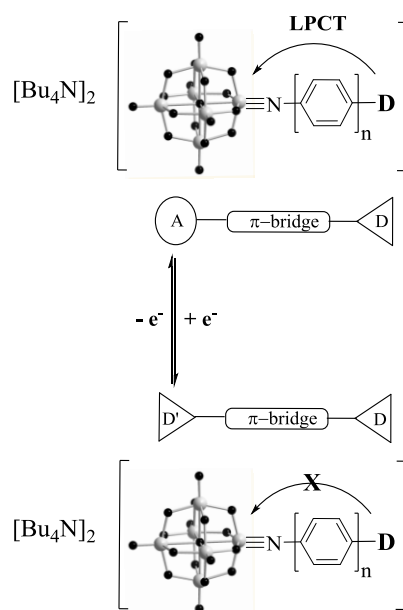
Figure 1.20 Schematic representation of the proposed redox switching in organoimido Lindqvist hexamolybdate derivatives.

Janjua *et al.*, in their computational studies, outlined that the organoimido ligand-to-POM charge transfer (LPCT) is responsible for the NLO properties. They also found that lengthening of organoimido π-conjugation or increasing the donor strength of the organoimido would enhance the NLO properties, and the strong interaction generates a strong electronic communication between organoimido moiety and Lindqvist cluster.[196] Surprisingly, though, in more recent work they have suggested that for systems where organoimido-substituted Lindqvist derivatives conjugated between the d-electron system of the POM and the p-π electron system of the aromatic rings, a polyoxometalate-to-ligand charge transfer (PLCT) was responsible for the NLO properties in such systems.[197,198] Other organo-substituted POMs derivatives have also been investigated theoretically as NLO chromophores such as organo-substituted Keggin ($XW_{11}O_{39}{}^{n-}$) and Dawson ($X_2W_{17}O_{61}{}^{n-}$) anions. However, as stated in section **1.2.1.2**, experimental observations in these materials indicate that the POM and the covalently attached organic subunit behave as separate electronic entities, making them unlikely NLO chromophores.[199,200]

Lindqvist derivatives could potentially serve as excellent switchable NLO materials as they contain redox-active metal centres, i.e. the hexamolybdate cluster. The reversible redox properties of POMs provide an ideal route for redox-based switching of second-order NLO activity; therefore, switching POM-based NLO materials may be constituted by combining their attractive redox properties and their potential NLO properties. Song and co-workers have predicted the switching NLO properties of POM-based materials.[201] In their study, the switched NLO properties of the two-dimensional (2D) Λ-shape Phenanthroline-Lindqvist hybrids derivatives with C_{2v} symmetry were investigated. They showed that the NLO responses could be switched "on" and "off" reversibly via the redox-couple of $Mo^{VI/V}$ in the hexamolybdate cluster. The reversibility of active redox couple at readily accessible potentials has a great potential for the switching of bulk NLO properties in electrode-deposited films. Incorporating electron-accepting POMs with redox properties into a conjugated

polymer may result in photo and electro-active materials with new photochromic effects.

1.3 Outline and aims of thesis

For optical applications, a NLO chromophore should have the following properties:

1- Fast optical response time

2- Good temporal and thermal stability

3- Easy of fabrication and production

4- Ability to process into crystals, thin films, etc.

5- Wide optical transparency area

This project aims to explore both the photonic properties of POMs as NLO chromophores, and the production of photo and electro-active electropolymers of these materials with switchable NLO properties for various optoelectronic applications. We will present the first experimental study of POM derivatives as NLO chromophores, focusing on the synthesis, structure and 2nd order NLO properties of new organoimido Lindqvist clusters with different organic donor/acceptor groups.

Chapter 2 presents the synthesis of chromophores, monomers, and ligands including a description of experimental procedure and characterisation methodology.

Chapter 3 describes the results and discussion of the design and synthesis of chromophores, monomers, and precursors. X-ray crystal structures, ^{1}H, and ^{13}C-NMR, MS spectra, and EA analysis results will be presented and discussed.

Chapter 4 presents the electrochemical and optical properties of the synthesized chromophores. It also describes the first spectroelectrochemical studies of POM-based chromophores.

Chapter 5 describes for the first time the experimental non-linear optical properties of organoimido Lindqvist derivatives measured by HRS and Stark spectroscopy. It also presents the study of the electronic transitions of these materials using Raman spectroscopy.

Chapter 6 describes the electropolymerisation and polymer characterisation of the polymerizable derivatives using different techniques such as SEM, TEM and reflectance FTIR. SEM and TEM images and reflectance IR of the surfaces will be presented to show specific features of the polymeric films.

Chapter 2

Experimental

2.1. Materials

Tetrahydrofuran (THF) was distilled over sodium wire under nitrogen; triethylamine (TEA) was distilled at reduced pressure over NaOH and stored over NaOH under nitrogen; acetonitrile (MeCN) was distilled over CaH_2 under nitrogen, diethyl ether was distilled over sodium wire under nitrogen, and dichloromethane was distilled over P_2O_5 and K_2CO_3 under nitrogen.[202] Dry (sure seal) dimethyl sulfoxide (DMSO) was purchased from Sigma Aldrich. All other reagents and solvents were obtained as ACS grade from Sigma Aldrich, Alfa Aesar or Fisher Scientific and used as supplied. Deuterated solvents were obtained from Goss Scientific. 3-(pyrrole-1-yl)propylamine[203] were synthesized according to previously published methods and its identity was checked by IR and ^{1}H-NMR.

2.2. Methods

Unless stated otherwise, all organic syntheses were carried out under an atmosphere of nitrogen or argon using standard Schlenk techniques. Organoimido hexamolybdate derivatives were synthesised using an adapted literature procedure,[204] under an atmosphere of dry nitrogen or argon using standard Schlenk techniques. TLC plates were developed using an ultraviolet lamp, or iodine chamber.

2.3. Instrumentation

Elemental analysis	Carlo Erba Flash 2000 Elemental Analyser.
Mass spectrometry	UK National Mass Spectrometry Service, Swansea University, Thermo Scientific LTQ Orbitrap XL
FT-IR spectroscopy	Perkin Elmer FT-IR spectrum BX and Bruker FT-IR XSA spectrometers
UV-vis spectroscopy	Agilent Cary 60 UV-vis spectrophotometer
NMR spectroscopy	Bruker AC 300 (300 MHz) and Bruker Ascend 500

	(500 MHz) spectrometers. All shifts are quoted with respect to TMS using the solvent signals as secondary standard
X-ray crystallography	Oxford Diffraction XCalibur 3 diffractometer (UEA), or Rigaku AFC 12 goniometer (National Crystallography service) equipped with an enhanced sensitivity (HG) Saturn724+ detector and FR-E+ SuperBright molybdenum rotating anode generator with HF Varimax optics (100μm focus).
Electrochemistry	Autolab (PGStat 302N, and PGStat 30) potentiostat/galvanostat, and μ-autolab III for spectroelectrochemistry (SE).[205]
Spectroelectrochemistry	Honeycomb Spectroelectrochemical cell (AKSTCKIT3), Pine Research Instrumentation
HRS	800 nm -high repetition rate femtosecond Ti:sapphire laser (Spectra Physics, Model Tsunami), 1064 nm -Spectra-Physics InSight® DS+ laser (1W average power, sub-100 fs pulses, 80 MHz).
FIB	FEI Nova200 dual beam SEM/FIB fitted with a Kleindiek micromanipulator.
TEM	Philips CM200 FEGTEM fitted with a Gatan SC200 Orius CCD camera and an Oxford Instruments 80 mm2 EDX SDD running AZtec software.
XPS	VG ESCAlab 250 with a monochromated Al Kα source.
SEM-EDS	Jeol JSM 5900LV SEM-EDS.

2.4. Compound numbering

Organic compounds are numbered as precursors (**P**) in the order in which their synthesis are described in the ligand synthesis part of chapter, 2. POM compounds are given numbers in the order in which their syntheses are described in the polyoxometalates derivatives synthesis part of chapter 2.

2.5. Notation for NMR, MS and IR spectra

NMR: s – singlet; d - doublet; t – triplet; q – quartet; quin – quintet; sex – sextet; dd, dt, td, tt – doublet of doublets etc; *p* before any other letter signifies the prefix pseudo.

ES-MS: [M]+ - molecular ion; [M-Na]+ - molecule plus a sodium ion.

EI-MS: [M]+ - molecular ion; [M – X]+ - molecular ion minus fragment X.

Fragments are identified wherever possible.

IR: sh – shoulder; vw – very weak; w – weak; m – medium; s – strong; vs – very strong.

Quaternary carbon signals were not observed for (**2-5**, **9-12**) compounds even after 1064 scans of saturated d_6-DMSO and d_3-MeCN solutions, which gave strong signal for all other ^{13}C resonances.

2.6. Electrochemical methods

All electrochemical procedures were carried out using an Autolab PGStat 30 potentiostat/galvanostat, using GPES software. Cyclic voltammetry (CV) experiments were performed in a single-compartment or a conventional three-electrode cell with a Ag/AgCl reference electrode (3M NaCl, saturated AgCl), glassy carbon (GC), Fluorine-doped tin oxide (FTO) or platinum working electrode and Pt wire auxiliary electrode. Acetonitrile was freshly distilled (from CaH_2), [N(C$_4$H$_9$-n)$_4$]PF$_6$, used as supplied from Fluka, and [N(C$_4$H$_9$-n)$_4$]BF$_4$, were used as the supporting electrolyte. Solutions containing ca. 10^{-3} M analyte (0.1 M electrolyte) were degassed by purging

with nitrogen, and during the measurements a nitrogen atmosphere was maintained. All $E_{1/2}$ values were calculated from $(E_{pa} + E_{pc})/2$ at a scan rate of 100 mV s^{-1} and referenced to internal standard Fc/Fc$^+$= +460 mV vs Ag/AgCl. Bulk electrolysis was performed using Chronoamperometry in a three-compartment cell where both reference and counter electrode were separated by a glass frit. A gold gauze was used as a high surface area working electrode, the counter electrode was a Pt gauze and as a pseudo-reference electrode an Ag wire was used.

2.6.1. Electrolyte preparation

[NBu$_4$][BF$_4$] was prepared by adding a solution of tetrabutylammonium hydrogen sulfate (169.0 g, 0.498 mol in 200 mL distilled water) into a solution of sodium tertafluoroborate (54.6 g, 0.498 mol in 200 mL distilled water) with vigorous stirring for 30 minutes forming a white precipitate. The precipitate was filtered off, washed three times with water, and dried. The air dried solid was dissolved in in freshly distilled dichloromethane and dried over magnesium sulphate overnight before being filtered off and washed with dried dichloromethane. The resulting filtrate was slowly added to 1.5 L dry diethyl ether with vigorous stirring. A white precipitate of [NBu$_4$][BF$_4$] was obtained which was collected by filtration and dried *in vacuo* for 24 hours.

2.6.2. Electrodeposition of polymer films

Prior to use, platinum and glassy carbon working electrode was cleaned by polishing the electrode with alumina powder on a cotton pad and rinsing with water and freshly distilled acetonitrile. FTO electrodes were only rinsed with freshly distilled acetonitrile. An electrodeposition solution of 2 mM of monomers was freshly prepared before each electrochemical experiment. The electrolyte was 0.1 M NBu$_4$BF$_4$ in degassed MeCN. Monomers were added to the resulting solution and then loaded into a three compartment cell. In the case of co-electropolymerisation, 2mM of pyrrole was prepared by adding the required amount of pyrrole into freshly

distilled acetonitrile. Films were formed by immersing the working electrode in the electrodeposition solution and cycling the potential (CV) between 0V and 0.8V at a scan rate 100 mV/s. If no response was noted, the experiment was repeated, increasing the voltage by 0.1 V increments to a maximum of 1.8 V. The film coated electrodes were washed with freshly distilled acetonitrile and dried for further characterization. Polymer films appeared well adhered to the electrode, with no cracking or lifting of the polymer film. Cyclic voltammetry studies of films were carried out in a fresh solution of 0.1 M [NBu$_4$][BF$_4$] in acetonitrile cycling between (-1) V to 1.5 V using a single compartment cell.

2.7. Ligands Synthesis

2.7.1. Synthesis of 9H-fluoren-9-ylmethyl (4-iodophenyl)carbamate (P1)
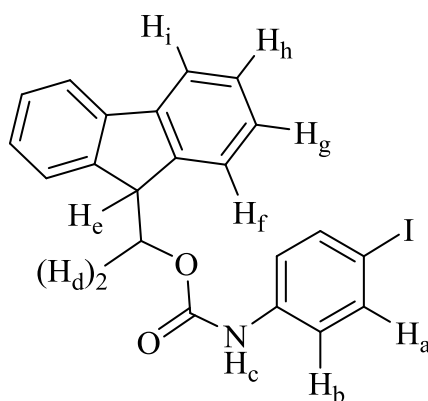
The procedure to prepare compound **P1** was based on the method of Gawande and Branco.[206] 9H-fluoren-9-ylmethyl carbonochloridate (FmocCl) (0.310 g, 1.2 mmol), 4-iodoaniline (0.219 g, 1 mmol) and H$_2$O (3 mL) were heated at 60 ºC for 2 hours. The reaction was monitored by thin layer chromatography using ethyl acetate:hexane (3:7) as eluent. The crude product was filtered and washed with water and then recrystallized from hot ethanol to yield the pure product (0.4 g, 0.906 mmol, 91 %). δ_H (500 MHz, (CD$_3$)$_2$SO) 9.82 (s, 1H, H$_c$), 7.91 (d, J =7.5 Hz, 2H, H$_a$), 7.74 (d, J = 7.5 Hz, 2H, H$_b$), 7.59-7.25 (m, 8H, H$_{f-i}$), 4.50 (d, J = 6.2 Hz, 2H, H$_d$), 4.31 (t, J = 6.2 Hz, 1H, H$_e$). δ_C (125 MHz, (CD$_3$)$_2$SO) 153.3, 143.7, 140.8, 138.9, 137.3, 127.7,

127.1, 125.1, 120.5, 120.2, 85.7, 65.7, 46.6. Anal. Calcd (found) % for $C_{21}H_{16}INO_2$:

C, 57.15 (57.21); H, 3.65 (3.54); N, 3.17 (3.29). $m/z = 442$ $[C_{21}H_{16}INO_2H]^+$. FTIR:

3342 (w); 1739 (s); 1586 (m); 1526 (s); 1446 (w); 1396 (m); 1309 (m); 1287 (w);

1237 (m); 1221 (s); 1104 (m); 1089 (m); 1063 (w); 1048 (m); 1003 (m); 986 (w); 935

(vw); 817 (s); 763 (m); 736 (vs); 621 (m); 547 (m).

2.7.2. Synthesis of N-(9-Fluorenylmethoxycarbonyl)-4-[(4-iodophenyl)ethynyl]aniline (P2)
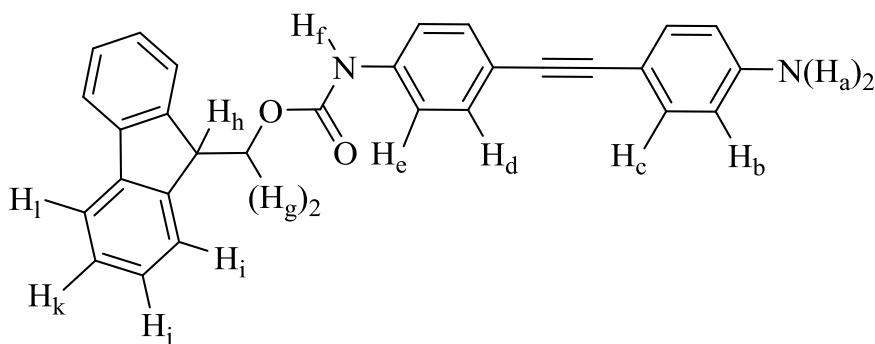
Compound **P1** (2.206 g, 5 mmol), 4-ethynylaniline (0.62 g, 5.3 mmol), $Pd(PPh_3)_2Cl_2$

(3 mol %, 0.111 g, 0.158 mmol), and CuI (5 mol %, 0.05 g, 0.265mmol) were added

to an oven-dried 50 mL two neck flask. Anhydrous THF (25 mL) and dry

triethylamine (2 mL) were then added to the flask and the reaction mixture was stirred

at 40 ºC under nitrogen. The reaction was monitored by thin layer chromatography

using ethyl acetate 8:2 toluene. After consumption of the amine (4 hours), the solution

was filtered, 50 mL H_2O added, and extracted twice with DCM (2 × 30mL). The

combined organic layers were washed with H_2O (2 × 60 mL) before being dried over

anhydrous $MgSO_4$. The solution was then diluted with DCM and layered with hexane.

The red precipitate was filtered off and the filtrate was concentrated on the rotary

evaporator to afford the crude product. This was re-dissolved in the minimum DCM

and layered with hexane to give a brown solid (1.1 g, 2.55 mmol, 51 %). δ_H (500

MHz, $(CD_3)_2CO$) 9.01 (s, 1H, H_f), 7.88 (d, $J = 7.5$ Hz, 2H, H_e), 7.73 (d, $J = 7.5$ Hz,

2H, H_d), 7.56-7.32 (m, 8H, H_{i-l}), 7.23 (d, $J = 8.8$ Hz, 2H, H_b), 6.67 (d, $J = 8.8$ Hz, 2H,

H_c), 5.02 (s, 2H, H_a), 4.52 (d, J = 6.6 Hz, 2H, H_g), 4.31 (t, J = 6.6 Hz, 1H, H_h). δ_C

(125 MHz, $(CD_3)_2CO$) 154.3, 149.9, 145.0, 142.2, 139.7, 138.6, 133.5, 132.6, 128.7,

128.0, 126.0, 120.1, 119.1, 114.1, 111.4, 90.7, 87.3, 67.2, 48.0. Anal. Calcd (found) %

for $C_{29}H_{22}N_2O_2$: C, 80.90 (80.78); H, 5.15 (5.22); N, 6.50 (6.49). m/z = 431.17

$[C_{29}H_{22}N_2O_2H]^+$. FTIR: 3343 (w); 1706 (s); 1607 (m); 1581 (m); 1521 (vs); 1449 (w);

1407 (m); 1309 (m); 1219 (vs); 1137 (w); 1104 (m); 1087 (m); 1050 (s); 982 (vw);

830 (vs); 736 (vs); 644 (m); 620 (m).

2.7.3. Synthesis of 4-{[4-(1H-pyrrol-1-yl)phenyl]ethynyl}aniline (P4)

Compound **P3** was synthesized according to the Paal-Knoor method.[207]
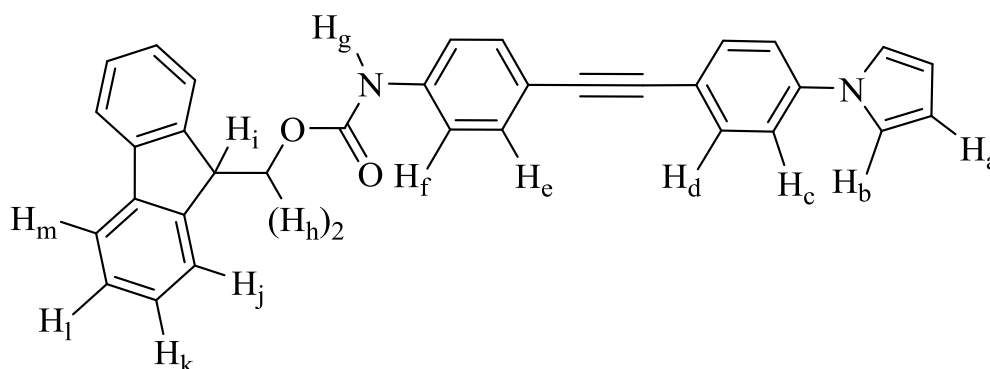
A mixture of **P2** (0.43 g, 1 mmol), 2,5-dimethoxytetrahydrofuran (0.145 g, 1.1 mmol),

and acetic acid (10 mL) were added to an oven-dried 50 mL round bottom flask

containing a magnetic stirrer bar. The reaction mixture was refluxed for 1 hour under

nitrogen and monitored by thin layer chromatography using ethyl acetate 9:1 toluene.

After cooling to room temperature H_2O (20 mL) was added and the resulting solution

was extracted with DCM (3 × 15 mL). The DCM phase was washed with H_2O (2 ×

100 mL) before being dried over anhydrous $MgSO_4$. The solution was then reduced to

dryness under vacuum to give a red solid (0.43 g, 0.89 mmol, 89 %). δ_H (500 MHz,

$CDCl_3$) 7.80 (d, J = 7.5 Hz, 2H, H_f), 7.64 (d, J = 7.5 Hz, 2H, H_e), 7.58 (d, J = 8.8 Hz,

2H, H_d), 7.51-7.32 (m, 10H, H_c, H_{j-m}), 7.38 (d, J = 8.8 Hz, 2H, H_c), 7.12 (t, J = 2.2 Hz,

2H, H_a), 6.71 (s, 1H, H_g), 6.38 (t, J = 2.2 Hz, 2H, H_b), 4.59 (d, J = 6.4 Hz, 2H, H_h),

4.30 (t, J = 6.4 Hz, 1H, H_i). δ_C (125 MHz, (CDCl$_3$) 143.6, 141.4, 140.1, 132.8, 132.4, 127.8, 127.2, 124.8, 120.5, 120.1, 120.0, 119.0, 118.3, 118.1, 110.9, 101.4, 89.5, 88.2, 67.0, 47.0, 38.8. m/z = 481 [C$_{33}$H$_{24}$N$_2$O$_2$H]$^+$. FTIR: 3297 (sh); 2944 (vw); 1701 (s); 1590 (m); 1525 (vs); 1477 (m); 1447 (m); 1407 (m); 1329 (s); 1311 (m); 1218 (s); 1137 (w); 1104 (m); 1088 (m); 1051 (s); 1018 (m); 919 (w); 828 (s); 755 (vs); 724 (vs).

Due to rapid oxidation in air, **P3** was directly used to synthesise compound **P4** via removal (deprotection of NH$_2$ group) of the Fmoc group.
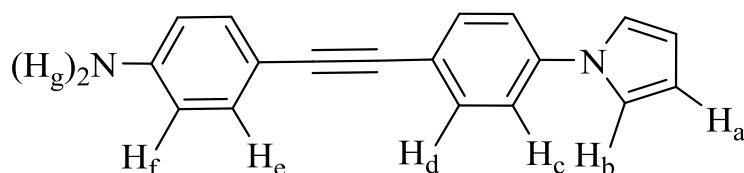
To a solution of compound **P3** (0427 g, 0.89 mmol) in anhydrous DMF (10 mL), 5 mL piperidine was added before stirring for 30 minutes under nitrogen. The mixture was then layered with H$_2$O (20 mL) to give a creamy brown precipitate before being filtered and dried. The brown solid was dissolved in acetone (50 mL), layered with H$_2$O and filtered to remove the cleaved Fmoc byproduct. The filtrate was layered with H$_2$O to give a yellow solid which was then washed with H$_2$O and dried in air before being dissolved in diethyl ether. The diethyl ether phase was dried over anhydrous MgSO$_4$, filtered and evaporated to dryness under vacuum. The resulting residue was purified by silica gel column chromatography using hexane/dichloromethane in a 95:5 % to afford a yellow solid (0.14 g, 0.54 mmol, 61 %). δ_H (500 MHz, CDCl$_3$) 7.55 (d, J = 8.8 Hz, 2H, H_d), 7.37 (d, J = 8.8 Hz, 2H, H_c), 7.35 (d, J = 8.6 Hz, 2H, H_e), 7.12 (t, J = 2.2 Hz, 2H, H_b), 6.66 (d, J = 8.6 Hz, 2H, H_f), 6.37 (t, J = 2.2 Hz, 2H, H_a), 3.84 (s, 2H, H_g). δ_C (125 MHz, (CDCl$_3$) 146.7, 139.8, 132.9, 132.6, 121.1, 120.0, 119.0, 114.8, 112.5, 110.8, 90.6, 86.6. Anal. Calcd (found) % for C$_{18}$H$_{14}$N$_2$: C, 83.68 (83.61); H, 5.46 (5.38); N, 10.85 (11.00). m/z = 259 [C$_{18}$H$_{14}$N$_2$H]$^+$. FTIR: 3425 (w); 3332 (sh); 3215(w); 2213 (vw); 1605 (s); 1523 (m); 1476 (m); 1323 (s); 1279 (m);

1120 (m); 1070 (m); 1016 (m); 918 (m); 827 (vs); 725 (vs); 613 (s). UV-vis (MeCN) λ, nm (ε, M^{-1} cm^{-1}): 320 (44.7 $\times$ 10^3).

2.7.5. Synthesis of 4-(1H-pyrrol-1-yl)aniline[208] (P5)
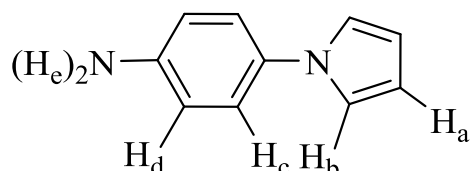
A mixture of 2,5-dimethoxytetrahydrofuran **1** (1.451 g, 11mmol), p-phenylenediamine (1.081 g, 10 mmol) and $CuCl_2$ (10 mol %, 0.15 g, 1.1 mol) was refluxed with stirring in H_2O (3 mL), for 2 hrs. The completion of the reaction was monitored by TLC using a mixture of ethyl acetate and hexane (5:95%). The reaction mixture was cooled to room temperature, before being diluted with ethyl acetate (20 mL). The aqueous phase was re-extracted (2 $\times$ 20 mL) with ethyl acetate and the combined organic extracts were dried over magnesium sulphate, before being concentrated and dried in a vacuum. The resulting residue was purified by silica gel column chromatography using hexane/ethyl acetate in a 95:5 % to afford yellowish solid (0.7 g, 4.42 mmol, 47 %). δ_H (500 MHz, CD_3CN) 7.17 (d, J = 8.8 Hz, 2H, H_c), 7.00 (t, J = 2.2 Hz, 2H, H_b), 6.70 (d, J = 8.8 Hz, 2H, H_d), 6.22 (t, J = 2.2 Hz, 2H, H_a), 4.18 (s, 2H, H_e). δ_C (125 MHz, (CD_3CN) 147.4, 132.6, 122.8, 120.3, 116.0, 110.3. Anal. Calcd (found) % for $C_{10}H_{10}N_2$: C, 75.92 (75.98); H, 6.37 (6.32); N, 17.70 (17.60). m/z = 159 $[C_{10}H_{10}N_2H]^+$. FTIR: 3417 (vw); 3326 (sh); 3217 (w); 1625 (m); 1517 (s); 1443 (s); 1400 (m); 1320 (m); 1256(m); 1127 (w); 1076 (m); 1018 (m); 921 (w); 821 (s); 721 (vs); 612 (vs). UV-vis (MeCN) λ, nm (ε, M^{-1} cm^{-1}): 264 (18.4 $\times$ 10^3).

2.7.6. Synthesis of 9-(4-iodophenyl)-9H-carbazole (P6)
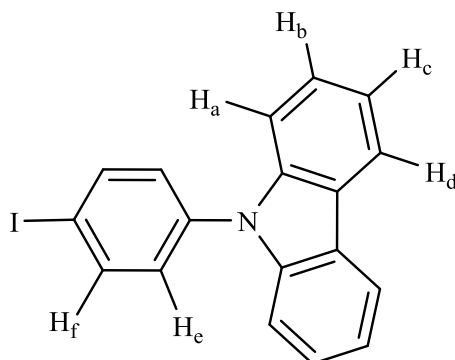
A mixture of carbazole (2 g, 12mmol), 1,4-diiodobenzene (6 g, 19.6 mmol), copper powder (1.2 g, 18.88 mmol) and potassium carbonate (2.4 mg, 17.36 mmol) was dissolved in 1,2-dichlorobenzene (32 mL) and refluxed at 180 ºC for 48 hrs. The solution was taken and concentrated on the rotary evaporator before isolating the product by Kugelrohr distilling out unreacted carbazole at 280 ºC. The remaining product was then recrystallized in hot acetone to give a creamy coloured solid (1.81 g, 4.92 mmol, 41 %). δ_H (500 MHz, $(CD_3)_2SO$) 8.25 (d, $J = 7.7$ Hz, 2H, H_a), 8.02 (d, $J = 8.5$ Hz, 2H, H_f), 7.46 (d, $J = 8.5$ Hz, 2H, H_e), 7.44 - 7.26 (m, 6H, H_{b-d}). δ_C (125 MHz, $(CD_3)_2SO$) 134.2, 139.5, 137.1, 129.4, 126.8, 123.3, 121.8, 120.8, 110.0, 93.5. $m/z = 370$ $[C_{18}H_{12}INH]^+$. FTIR: 3044 (sh); 1622 (vw); 1595 (m); 1580 (m); 1151 (m); 1494 (s); 1479 (s); 1449 (vs); 1361 (m); 1335 (s); 1316 (s); 1293 (w); 1229 (vs); 1183 (m); 1121 (m); 1101 (w); 1005 (w); 934 (m); 913 (w); 855 (w); 823 (s); 747 (vs); 723 (vs); 707 (m); 634 (m); 617 (m).

2.7.7. Synthesis of 4-{[4-(9H-carbazol-9-yl)phenyl]ethynyl}aniline (P7)
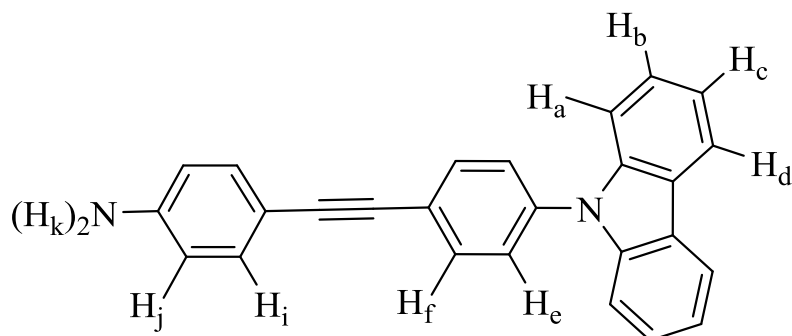
P6 (300 mg, 0.8 mmol), 4-ethynylaniline (112 mg, 0.96 mmol), copper iodide powder (3.8 mg, 0.02 mmol) and $Pd(PPh_3)_2Cl_2$ (56 mg, 0.08 mmol) were dissolved in acetonitrile (10 mL) and triethylamine (0.1 mL, 0.072 mmol) was added. The solution was stirred for 24 hrs at 60 °C. The reaction mixture was filtered and washed with water (2 × 10 ml), and then DCM (2 × 10 mL). The combined organic layers were dried over $MgSO_4$ and concentrated on the rotary evaporator to give the crude product as red solid which was purified by silica gel column chromatography (Hexane:DCM, 1:2 ratio) to afford the desired product as yellow solid (0.246 g, 0.686 mmol, 86 %).

δ_H (300 MHz, $(CD_3)_2SO$) 8.26 (d, J =7.7 Hz, 2H, H_a), 7.74 (d, J =8.3 Hz, 2H, H_e), 7.64 (d, J = 8.3 Hz, 2H, H_f), 7.50-7.23 (m, , 6H, H_{b-d}), 7.26 (d, J = 8.5 Hz, 2H, H_i), 6.59 (d, J = 8.5 Hz, 2H, H_j), 5.64 (s, 2H, H_k). δ_C (125 MHz, $(CD_3)_2SO$) 149.7, 139.9, 136.1, 132.7, 132.6, 126.8, 126.4, 122.9, 122.5, 120.6, 120.3, 113.6, 109.7, 107.8, 92.3, 86.0. Anal. Calcd (found) % for $(C_{26}H_{18}N_2)_{0.87}(CH_2Cl_2)_{0.13}$: C, 84.62 (84.51); H, 4.96 (4.51); N, 7.54 (7.80). m/z = 359 $[C_{26}H_{18}N_2H]^+$. FTIR: 3458 (m); 3366 (m); 3206 (vw); 3040 (w); 2207 (m); 1620 (s); 1602 (s); 1518 (s); 1476 (m); 1446 (s); 1334 (m); 1312 (m); 1286 (m); 1222 (s); 1169 (s); 1136 (m); 1014 (vw); 912 (m); 826 (vs); 751 (vs); 724 (s); 645 (s); 623 (m). UV-vis (MeCN) λ, nm (ε, M^{-1} cm^{-1}): 234 (39.5 × 10^3), 292.5 (31.3 × 10^3), 339.5 (46.2 × 10^3).

2.7.8. Synthesis of 4-[(4-aminophenyl)ethynyl]-N,N-diphenylaniline (P8)
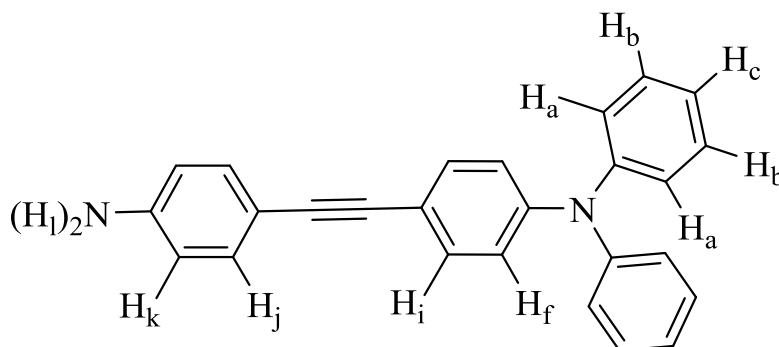
A dried 50 ml two neck round flask was charged with 4-bromotriphenylamine (324 mg, 1 mmol), 4-ethynylaniline (140 mg, 1.2 mmol), copper iodide powder (4.8 mg, 0.025 mmol), $Pd(PPh_3)_2Cl_2$ (70 mg, 0.1 mmol) and triphenylphosphine (131 mg, 0.5 mmol) and then evacuated and filled with Ar ($\times$ 3). THF (10 mL) was added to the mixture and the solution was refluxed for 96 hrs. The solution was filtered, then washed with water (10 mL) and (3 $\times$ 15 mL) DCM. The organic layer was taken and dried with magnesium sulphate before being concentrated *in vacuo*. The product was then purified by silica column chromatography using eluents hexane:DCM; 1:2 to afford a light-red solid (0.25 g, 0.69 mmol, 69 %). δ_H (500 MHz, $(CD_3)_2SO$) 7.35 (d, 2H, J = 8.8 Hz, H_f), 7.33 (m, 4H, H_a), 7.15 (d, J = 8.6 Hz, 2H, H_j), 7.08 (m, 6H, H_{b+c}), 6.89 (d, J = 8.8 Hz, 2H, H_i), 6.54 (d, J = 8.6 Hz, 2H, H_k), 5.51 (s, 2H, H_l). δ_C (125 MHz, $(CD_3)_2SO$) 149.2, 146.8, 146.6, 132.4, 132.0, 129.70, 124.7, 123.8, 121.9, 116.4, 113.6, 108.5, 90.3, 86.5. Anal. Calcd (found) % for $C_{26}H_{20}N_2$: C, 86.62 (86.73); H, 5.59 (5.67); N, 7.77 (7.63). m/z = 361 $[C_{26}H_{20}N_2H]^+$. FTIR: 3481 (vw); 3390 (w); 2198 (vw); 1613 (m); 1586 (m); 1517 (m); 1486 (s); 1319 (m); 1275 (s); 1176 (m); 1153 (w); 1075 (w); 1012(w); 824 (s); 757 (s); 721 (s); 693 (s); 616 (s); 517 (vs). UV-vis (MeCN) λ, nm (ε, M^{-1} cm^{-1}): 205.0 (57.5 $\times$ 10^3), 233.5 (12.7 $\times$ 10^3), 348.0 (41.1 $\times$ 10^3).

2.7.9. Synthesis of [4-(1H-pyrrol-1-yl)phenyl]acetaldehyde (P9)
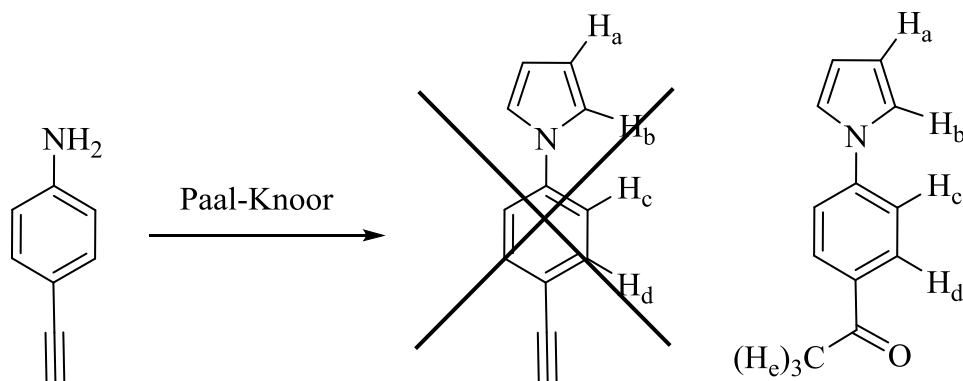
The synthesis of **P9** was carried out according to the Clauson-Kaas method.[209] 4-ethynylaniline (0.117 g, 1 mmol), 2,5-dimethoxytetrahydrofuran (0.145 g, 1.1 mmol), and acetic acid (30 mL) were charged in an oven-dried 100 mL round bottom flask containing a magnetic stirrer bar. The reaction mixture was refluxed for 2 hours under nitrogen and monitored by thin layer chromatography using ethyl acetate 3:7 hexane. The solution was concentrated on the rotary evaporator to give the crude product as black solid which was purified by silica gel column chromatography (Hexane:ethylacetate, 7:3 ratio) to afford the desired product as yellow solid. (0.15 g, 0.81 mmol, 81 %). δ_H (500 MHz, CDCl$_3$) 8.04 (d, J = 8.9 Hz, 2H, H$_d$), 7.48 (d, J = 8.9 Hz, 2H, H$_c$), 7.19 (t, J = 2.3 Hz, 2H, H$_b$), 6.41 (t, J = 2.3 Hz, 2H, H$_a$), 2.62 (s, 3H, He). δ_C (125 MHz, ((CD$_3$)$_2$SO) 196.6, 143.2, 133.3, 130.0, 119.1, 118.4, 114.4, 26.6. Anal. Calcd (found) % for C$_{12}$H$_{11}$NO: C, 78.11 (78.05); H, 5.96 (6.08); N, 7.59 (7.57). m/z = 186.09 [C$_{12}$H$_{11}$NOH]$^+$. FTIR: 3143 (vw); 33104 (vw); 1625 (vs); 1600 (s); 1519 (s); 1473 (m); 1455 (w); 1427 (m); 1358 (m); 1329 (s); 1308 (m); 1276 (m); 1260 (s); 1192 (m); 1124 (w); 1079 (w); 1064 (m); 1016 (m); 960 (m); 920 (m); 832 (vs); 720 (vs); 730 (vs); 609 (s).

2.8. Synthesis of Polyoxometalate Derivatives

2.8.1. Synthesis of [(C₄H₉)₄N]₂[Mo₆O₁₉] (1)
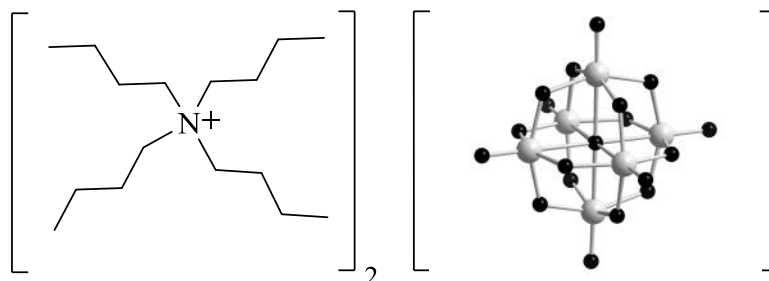
Compound **1** was synthesized according to previously published methods.[210] $Na_2MoO_4.2H_2O$ (5g, 20.01 mmol) was dissolved in water (20 mL) and acidified with 6M HCl (5.8 mL, 34.8 mmol) with vigorous stirring, followed by the addition of tetrabutylammonium bromide (2.42, 7.5 mmol) in water (4 mL) solution. The resulting slurry was heated at 75 ℃ with stirring for 45 min resulting in a yellow product, which was collected by filtration and washed with water (3 × 40 mL). This was first dried in air and recrystallized from hot acetone and washed with diethyl ether (2 × 20 mL) to afford yellow crystals (3.68g, 2.7 mmol, 78 % based on Mo). The final product was dried *in vacuo* for 24 hours. Anal. Calcd (found) % for $C_{32}H_{72}N_2O_{19}Mo_6$: C, 28.16 (28.09); H, 5.31 (5.41); N, 2.05 (2.09). FTIR: 2962 (m); 2872 (m); 1467 (m); 1380 (m); 1172 (vw); 1109 (vw); 1062 (vw); 1035 (vw); 949 (vs); 877 (m); 782 (vs); 738 (vs). UV-vis (MeCN) λ, nm (ε, M^{-1} cm^{-1}): 223.0 (24.9 × 10^3); 261.0 (13.4 × 10^3); 323.0 (7.1 × 10^3).

2.8.2. Synthesis of $[(C_4H_9)_4N]_2[Mo_6O_{18}NC_6H_4I]$ (2)
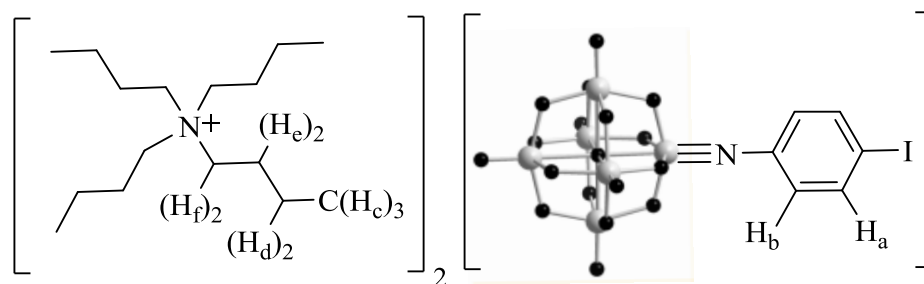
A mixture of 4-iodoaniline (0.219 g, 1 mmol), $(n\text{-}Bu_4N)_2[Mo_6O_{19}]$, **1** (1.773 g, 1.3 mmol), and DCC (1,3-dicyclohexylcarbodiimide) (0.3094 g, 1.5 mmol) was heated in dry DMSO (15 mL) for 10 h at 70 °C. A colour change to red-orange was observed. After cooling to room temperature, the solution was filtered into a flask containing diethyl ether (200 mL) and ethanol (50 mL). An orange precipitate was formed and collected by filtration and washed with 10 mL ethanol and then ether (10 mL) several times. The resulting solid was recrystallized twice from hot acetonitrile and washed with ethanol and diethyl ether to afford an orange solid (0.86g, 0.549 mmol, 55 %). The final product was dried *in vacuo* for 24 hours. δ_H (500 MHz, CD_3CN) 7.75 (d, J = 8.5 Hz, 2H, H_b), 6.99 (d, J = 8.5 Hz, 2H, H_a), 3.09 (*p*t, J = 8.6 Hz, 16H, H_f), 1.60 (quin, J = 8.1 Hz, 16H, H_e), 1.36 (sex, J = 7.4 Hz, 16H, H_d), 0.97 (t, J = 7.4 Hz, 24 H, H_c). δ_C (125 MHz, CD_3CN). 138.7, 128.4, 59.4, 24.4, 20.4, 13.9. Anal. Calcd (found) % for $C_{38}H_{76}N_3O_{18}IMo_6$: C, 29.15 (29.09); H, 4.89 (5.01); N, 2.68 (2.70). m/z = 540 $[C_6H_4NIMo_6O_{18}]^{2-}$, 440.1 $[Mo_6O_{19}]^{2-}$, 1123.6 $[(NBu_4)\{Mo_6O_{19}\}]^-$, 1323.5 $[(NBu_4)[C_6H_4NIMo_6O_{18}]]^{1-}$. FTIR: 2961 (m); 2872 (m); 1560 (vw); 1477 (s); 1376 (m); 1315 (m); 1151 (w); 1106 (vw); 1052 (vw); 1025 (w); 1000 (w); 973 (s); 947 (vs); 878 (m); 829 (m); 770 (vs). UV-vis (MeCN) λ, nm (ε, M^{-1} cm^{-1}): 242.0 (48.2 × 10^3); 270.0 (32 × 10^3); 355.0 (27 × 10^3).

2.8.3. Synthesis of [(C$_4$H$_9$)$_4$N]$_2$[Mo$_6$O$_{18}$N$_2$C$_{10}$H$_8$] (3)
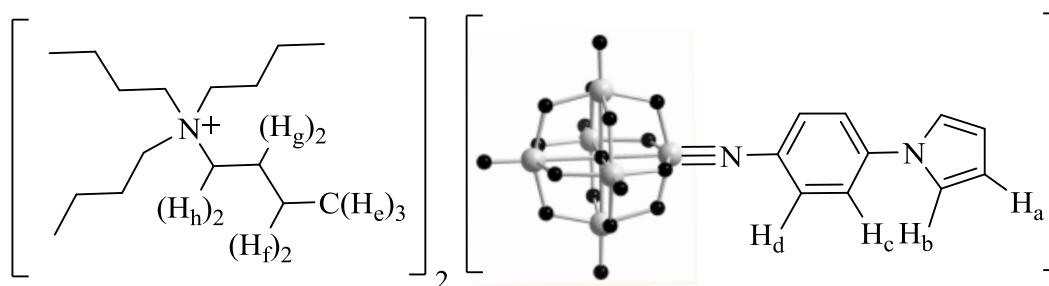
Compound **3** was synthesized in similar fashion to **2**. **P5**, 4-(1H-pyrrol-1-yl) aniline (0.158 g, 1 mmol), (n-Bu$_4$N)$_2$[Mo$_6$O$_1$], **1** (1.773 g, 1.3 mmol), and DCC (1,3-dicyclohexylcarbodiimide) (0.2886 g, 1.4 mmol) were combined in a dry Schlenk flask under nitrogen and dry DMSO (15 mL) was added. While the solution heated for 10 hours at 65 °C, its colour turned to red. After cooling to room temperature the red solution was filtered into a flask containing dry ether (200 mL) and ethanol (50 mL). The solid was washed with ethanol (10 mL) and then ether (10 mL) several times, and the resulting solid recrystallized twice from acetonitrile to yield an orange solid (1.2 g, 0.7975 mmol, 80 %). δ_H (500 MHz, CD$_3$CN) 7.49 (d, J = 8.8 Hz, 2H, H$_d$), 7.32 (d, J = 8.8 Hz, 2H, H$_c$), 7.20 (t, J = 2.0 Hz, 2H, H$_b$), 6.31 (t, J = 2.0 Hz, 2H, H$_a$), 3.10 (pt, J = 8.6 Hz, 16H, H$_h$), 1.61 (quin, J = 7.8 Hz 16H, H$_g$), 1.36 (sex, J = 7.4 Hz, 16H, H$_f$), 0.97 (t, J = 7.4, 24 H, H$_e$). δ_C (125 MHz, CD$_3$CN) 128.5, 120.4, 120.1, 112.2, 59.4, 24.4, 20.4, 13.9. Anal. Calcd (found) % for C$_{42}$H$_{80}$N$_4$O$_{18}$Mo$_6$: C, 33.5 (33.59); H, 5.35 (5.29); N, 3.72 (3.65). m/z = 509.7 [C$_{10}$H$_8$N$_2$Mo$_6$O$_{18}$]$^{2-}$, 439.7 [Mo$_6$O$_{19}$]$^{2-}$, 1020 [H[C$_{10}$H$_8$N$_2$Mo$_6$O$_{18}$]]$^{1-}$, 1123.6 [(NBu$_4$)[Mo$_6$O$_{19}$]]$^{1-}$. FTIR: 3131 (vw); 2962 (m); 2873 (m); 1590 (s); 1505 (s); 1481 (s); 1381 (w); 1324 (s); 1250 (vw); 1178 (m); 1153 (w); 1108 (w); 1062 (s); 1015 (w); 972 (s); 949 (vs); 940 (vs); 914 (s); 880 (m); 843 (s); 771 (vs); 738 (vs). UV-vis (MeCN) λ, nm (ε, M^{-1} cm^{-1}): 223.0 (39.6 × 10^3); 281.0 (28.2 × 10^3); 371.0 (32.3 × 10^3).

2.8.4. Synthesis of [(C$_4$H$_9$)$_4$N]$_2$[Mo$_6$O$_{18}$N$_2$C$_{18}$H$_{12}$] (4)
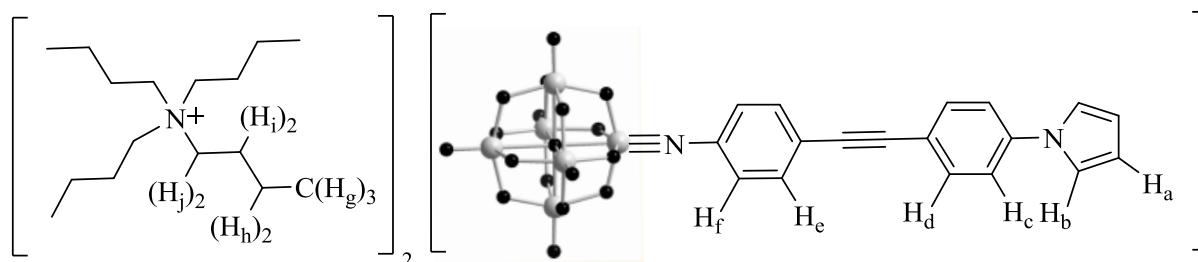
A mixture containing **P4**, 4-{[4-(1H-pyrrol-1 yl)phenyl]ethynyl}aniline (0.258 g, 1 mmol), (n-Bu$_4$N)$_2$[Mo$_6$O$_{19}$], **1** (1.773 g, 1.3 mmol), DCC (1,3-dicyclohexylcarbodiimide) (0.2886 g, 1.4 mmol) and dry DMSO (15 mL) was heated at 70 ºC for 10 hours under nitrogen. During the course of the reaction, the solution changed colour to dark-red. After cooling to room temperature the solution was filtered into a flask containing ether (200 mL) and ethanol (50 mL). The solid was washed with ethanol and ether several times, then the resulting solid recrystallized three times from an 50:50; acetonitrile:ethanol mixture to yield orange-red solid (0.8 g, 0.5 mmol, 50 %). δ_H (500 MHz, CD$_3$CN) 7.62 (d, J = 8.8 Hz, 2H, H$_f$), 7.55 (d, J = 8.5 Hz, 2H, H$_d$), 7.52 (d, J = 8.8 Hz, 2H, H$_e$), 7.25 (d, J = 8.4 Hz, 2H, H$_c$), 7.23 (t, J = 2.2 Hz, 2H, H$_b$), 6.33 (t, J = 2.2 Hz, 2H, H$_a$), 3.09 (pt, J = 8.6 Hz, 16H, H$_j$), 1.61 (quin, J = 8.0 Hz, 16H, H$_i$), 1.36 (sex, J = 7.3 Hz, H$_h$), 0.97 (t, J = 7.4 Hz, 24 H, H$_g$). δ_C (125 MHz, CD$_3$CN) 134.1, 132.7, 127.2, 120.8, 120.1, 112.0, 59.4, 24.4, 20.4, 13.9. Anal. Calcd (found) % for C$_{50}$H$_{84}$N$_4$O$_{18}$Mo$_6$: C, 37.41 (37.35); H, 5.27 (5.14); N, 3.49 (3.57). m/z = 560 [C$_{18}$H$_{12}$N$_2$Mo$_6$O$_{18}$]$^{2-}$. FTIR: 2960 (m); 2872 (m); 2210 (vw); 1605 (w); 1584 (w); 1519 (s); 1470 (s); 1378 (m); 1332 (s); 1151 (vw); 1118 (w); 1065 (m); 1017 (vw); 974 (s); 945 (vs); 880 (m); 841 (m); 769 (vs). UV-vis (MeCN) λ, nm (ε, M^{-1} cm^{-1}): 290.0 (40.1 $\times$ 10^3); 386.0 (43.8 $\times$ 10^3).

2.8.5. Synthesis of $[(C_4H_9)_4N]_2$ $[C_{14}H_{10}N_2Mo_6O_{18}]$ (5)
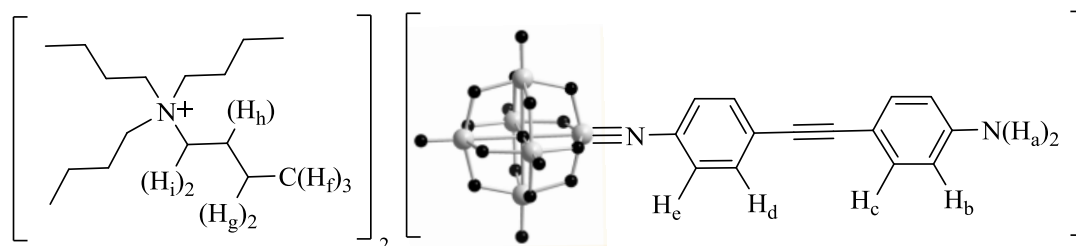
Compound **2** (790 mg, 0.50 mmol), 4-ethynylaniline (70 mg, 0.6 mmol), Pd(PPh$_3$)$_2$Cl$_2$ (7 mg, 0.01 mmol), CuI (3 mg, 0.015 mmol) and K$_2$CO$_3$ (500 mg, 3.6 mmol) were added to an oven-dried (50 mL) round bottom flask containing a magnetic stirrer bar. Anhydrous acetonitrile (10 mL) and dry triethylamine (0.5 mL) were then added to the flask with a syringe. After being stirred at room temperature for 0.5 h under nitrogen, the reaction mixture was filtered and the filtrate was concentrated to about 2 mL before pouring into diethyl ether to afford a red solid. The resulting solid was washed successively with ethanol (10 mL) and ether (10 mL) and then recrystallized twice from (acetonitrile: ethanol) mixture to yield a red solid (0.4 g, 0.257 mmol, 51 %). δ_H (300 MHz, CD$_3$CN) 7.46 (d, J = 8.7 Hz, 2H, H$_e$), 7.26 (d, J = 8.9 Hz, 2H, H$_c$), 7.20 (d, J = 8.7 Hz, 2H, H$_d$), 6.63 (d, J = 8.9 Hz, 2H, H$_b$), 4.5 (s, 2H, H$_a$), 3.10 (pt, J = 8.6 Hz, 16H, H$_i$), 1.61 (quin, J = 7.9 Hz, 16H, H$_h$), 1.37 (sex, J = 7.4 Hz, 16H, H$_g$), 0.97 (t, J = 7.4 Hz, 24 H, H$_f$). δ_C (125 MHz, CD$_3$CN) 134.0, 132.1, 127.2, 115.1, 59.4, 24.4, 20.4, 13.9**.** Anal. Calcd (found) % for C$_{46}$H$_{82}$N$_4$O$_{18}$Mo$_6$: C, 35.53 (35.41); H, 5.31 (5.26); N, 3.60 (3.49)**.** m/z = 535 [C$_{14}$H$_{10}$N$_2$Mo$_6$O$_{18}$]$^{2-}$, 439.6 [Mo$_6$O$_{19}$]$^{2-}$, 1123.6 [(NBu$_4$){Mo$_6$O$_{19}$}]$^{1-}$, 1311.69 [(NBu$_4$)[C$_{14}$H$_{10}$N$_2$Mo$_6$O$_{18}$]]$^{1-}$. FTIR: 3362 (w); 2960 (m); 2872 (m); 2201 (m); 1619 (m); 1605 (m); 1582 (m); 1515 (m); 1481 (m); 1331 (m); 1300 (w); 1179 (w); 1135 (w); 1064 (vw); 1029 (vw); 974 (m); 946 (vs); 840 (m); 773 (vs). UV-vis (MeCN) λ, nm (ε, M^{-1} cm^{-1}): 281.0 (39.2 × 10^3); 406.0 (35.8 × 10^3).

2.8.6. Synthesis of [(C₄H₉)₄N]₂[Mo₆O₁₈NC₈H₅] (6)

$$\left[\begin{array}{c} \text{(structure of } (C_4H_9)_4N^+ \text{ cation with labeled protons } (H_f)_2, (H_g), (H_e)_2, C(H_d)_3) \end{array}\right] \left[\begin{array}{c} \text{(structure of } Mo_6O_{18}\equiv N-\text{aryl}-\equiv CH_a \text{ with labeled protons } H_c, H_b) \end{array}\right]_2$$
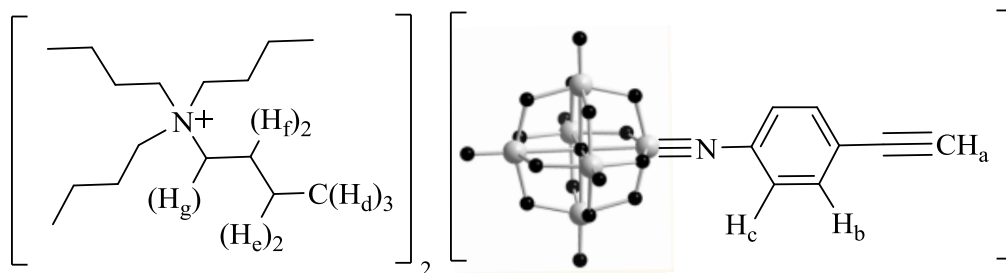
4-ethynylaniline (0.117 g, 1 mmol), (n-Bu₄N)₂[Mo₆O₁₉], **1** (1.773 g, 1.3 mmol), and DCC (1,3-dicyclohexylcarbodiimide) (0.288 g, 1.4 mmol) were heated in dry DMSO (15 mL) for 10 h at 70 °C. The colour of the solution changed to orange while it was heated. The solution was filtered into a flask containing diethyl ether (200 mL) and ethanol (50 mL) resulting in an orange precipitate. The orange precipitate was washed with ethanol and ether several times, then recrystallized twice from hot acetonitrile and washed with ethanol and diethyl ether to afford orange crystals (1.1g, 0.549 mmol, 75 %). δ_H (500 MHz, CD₃CN) 7.49 (d , J = 8.8 Hz, 2H, H_c), 7.19 (d, J = 8.8 Hz, 2H, H_b), 3.49 (s, 1H, H_a), 3.10 (pt, J = 8.6 Hz, 16H, H_g), 1.61 (quin, J = 8.1 Hz, 16H, H_f), 1.36 (sex, J = 7.4 Hz, 16H, H_e), 0.97 (t, J = 7.4 Hz, 24 H, H_d). δ_C (125 MHz, CD₃CN) 133.4, 127.0, 122.3, 97.5, 83.4, 81.7, 59.4, 24.4, 20.4, 13.9. Anal. Calcd (found) % for C₄₀H₇₇N₃O₁₈Mo₆: C, 32.82 (32.91); H, 5.30 (5.29); N, 2.87 (2.93). m/z = 389 [C₈H₅NMo₆O₁₈]²⁻. FTIR: 3258 (sh); 2961 (m); 2871 (m); 1477 (s); 1378 (m); 1334 (m); 1167 (w); 1099 (vw); 976 (m); 948 (vs); 882 (w); 844 (m); 766 (vs); 650. UV-vis (MeCN) λ, nm (ε, M⁻¹ cm⁻¹): 264.0 (36.2 × 10³); 358.0 (27 × 10³).

2.8.7. Synthesis of [(C₄H₉)₄N]₂[Mo₆O₂₀N₂C₆H₄] (7)
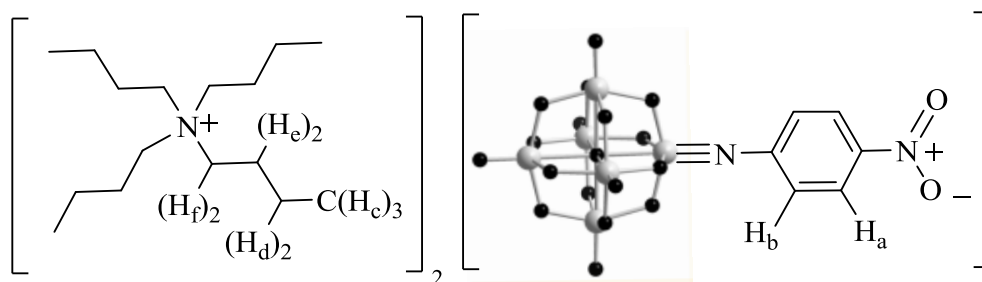
A mixture of 4-nitrolaniline (0.138 g, 1 mmol), (n-Bu₄N)₂[Mo₆O₁₉], **1** (1.773 g, 1.3 mmol), and DCC (1,3-dicyclohexylcarbodiimide) (0.288 g, 1.4 mmol) were heated in dry DMSO (15 mL) for 10 h at 70 ℃. The colour of the solution changed to orange while it was heated. The solution was filtered into a flask containing diethyl ether (200 mL) and ethanol (50 mL) resulting in a yellow precipitate. This was washed with ethanol (10 mL) and ether (10 mL) several times, before being recrystallized twice from hot acetonitrile and finally washed with ethanol (10 mL) and diethyl ether (10 mL) to afford a yellow crystals (0.878g, 0.6 mmol, 60 %). δ_H (500 MHz, CD₃CN) 8.22 (d, J = 9.1 Hz, 2H, H$_a$), 7.34 (d, J = 9.1 Hz, 2H, H$_b$), 3.10 (pt, J = 8.5 Hz, 16H, H$_f$), 1.61 (quin, J = 8.0 Hz, 16H, H$_e$), 1.36 (sex, J = 7.4 Hz, 16H, H$_d$), 0.97 (t, J = 7.4 Hz, 24 H, H$_c$). δ_C (125 MHz, CD₃CN) 146.4, 126.9, 125.2, 118.4, 59.1, 24.1, 20.1, 13.6. Anal. Calcd (found) % for C₃₈H₇₆N₄O₂₀Mo₆: C, 30.74 (30.69); H, 5.15 (5.25); N, 3.77 (3.82). m/z = 499.68 [C₆H₄N₂Mo₆O₂₀]²⁻. FTIR: 2961 (m); 2873 (m); 1578 (m); 1514 (m); 1480 (m); 1379 (w); 1320 (s); 1105 (w); 975 (m); 949 (vs); 857 (m); 768 (vs). UV-vis (MeCN) λ, nm (ε, M⁻¹ cm⁻¹): 216.0 (38.3 × 10³), 254.0 (26.3 × 10³); 287.0 (20.3 × 10³), 370.5 (30.2 × 10³).

2.8.8. Synthesis of [(C$_4$H$_9$)$_4$N]$_2$[Mo$_6$O$_{20}$N$_2$C$_{14}$H$_8$] (8)
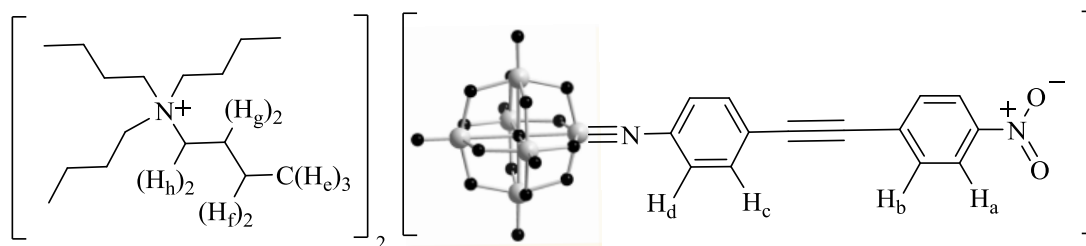
Compound **2** (735 mg, 0.50 mmol), ethynyl-4-nitrobenzene (88 mg, 0.6 mmol), Pd(PPh$_3$)$_2$Cl$_2$ (7 mg, 0.01 mmol), CuI (3 mg, 0.016 mmol) and K$_2$CO$_3$ (500 mg, 3.6 mmol) were added to a schlenk flask which was then evacuated and backfilled with nitrogen three times. Anhydrous acetonitrile (10 mL) and dry triethylamine (0.5 mL) were then added to the flask. After stirring at room temperature for 0.5 h under nitrogen, the reaction mixture was filtered and the filtrate was concentrated to about 2 mL before pouring into diethyl ether (200 mL) to afford a dark-red solid. This was washed successively with ethanol (10 mL) and ether (10 mL) and then recrystallized twice from (MeCN:EtOH) mixture to yield dark-red solid (0.475 g, 0.3 mmol, 60 %). δ_H (300 MHz, CD$_3$CN) 8.24 (d, J = 8.9 Hz, 2H, H$_a$), 7.75 (d, J = 8.9 Hz, 2H, H$_b$), 7.61 (d, J = 8.8 Hz, 2H, H$_d$), 7.26 (d, J = 8.8 Hz, 2H, H$_c$), 3.10 (*p*t, J = 8.6 Hz, 16H, H$_h$), 1.61 (quin, J = 8.0 Hz, 16H, H$_g$), 1.36 (sex, J = 7.4 Hz, 16H, H$_f$), 0.97 (t, J = 7.3 Hz, 24 H, H$_e$). δ_C (125 MHz, CD$_3$CN) 148.2, 133.3, 132.8, 130.2, 126.9, 124.5, 121.9, 109.6, 93.9, 90.8, 59.1, 24.1, 20.1, 13.6**.** Anal. Calcd (found) % for C$_{46}$H$_{82}$N$_4$O$_{18}$Mo$_6$: C, 34.86 (34.76); H, 5.08 (5.01); N, 3.53 (3.59)**.** m/z = 549.9 [C$_{14}$H$_8$N$_2$Mo$_6$O$_{20}$]$^{2-}$, 1341.5 [(NBu$_4$)[C$_{14}$H$_8$N$_2$Mo$_6$O$_{20}$]]$^{1-}$. FTIR: 2961 (m); 2873 (m); 2212 (m); 1592 (m); 1515 (m); 1479 (m); 1379 (w); 1338 (s); 1105 (w); 974 (m); 947 (vs); 775 (vs). UV-vis (MeCN) λ, nm (ε, M^{-1} cm^{-1}): 241.0 (36.0 × 10^3); 269.0 (29.9 × 10^3); 389.0 (49.6 × 10^3).

2.7.9. Synthesis of $[(C_4H_9)_4N]_2[Mo_6O_{18}N_2C_{20}H_{14}]$ (9)
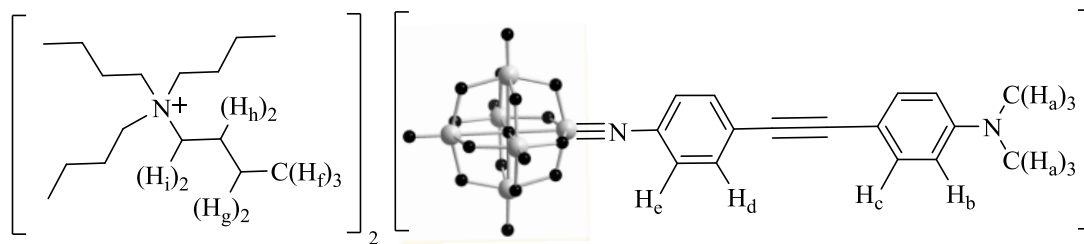
Compound **2** (395 mg, 0.25 mmol), 4-ethynyl-*N,N*-dimethylanilinenylaniline (43.5 mg, 0.3 mmol), $Pd(PPh_3)_2Cl_2$ (3.5 mg, 0.005 mmol), CuI (1.5 mg, 0.0079 mmol) and K_2CO_3 (250 mg, 1.8 mmol) were added to a schlenk flask which was evacuated and backfilled with nitrogen three times and then charged with anhydrous acetonitrile (10 mL) and dry triethylamine (0.5 mL). The reaction mixture was stirred at room temperature for 0.5 h under nitrogen, and then filtered and the filtrate concentrated to about 2 mL before pouring into diethyl ether to afford a dark-red solid. This was washed successively with ethanol and ether to yield dark-red solid (0.3 g, 0.189 mmol, 74 %). δ_H (500 MHz, CD_3CN) 7.46 (d, J = 8.6 Hz, 2H, H_e), 7.37 (d, J = 8.9 Hz, 2H, H_c), 7.20 (d, J = 8.6 Hz, 2H, H_d), 6.72 (d, J = 8.9 Hz, 2H, H_b), 3.10 (*p*t, J = 8.6 Hz, 16H, H_i), 2.98 (s, 6H, H_a), 1.61 (quin, J = 8.0 Hz, 16H, H_h), 1.36 (sex, J = 7.4 Hz, 16H, H_g), 0.97 (t, J = 7.4 Hz, 24 H, H_f). δ_C (125 MHz, CD_3CN) 151.8, 133.8, 132.1, 127.2, 124.7, 112.9, 109.8, 95.3, 87.8, 59.4, 40.4, 24.4, 20.4, 13.9. Anal. Calcd (found) % for $C_{48}H_{86}N_4O_{18}Mo_6$: C, 36.42 (36.54); H, 5.47 (5.40); N, 3.53 (3.57). *m/z* = 549 $[C_{16}H_{14}N_2Mo_6O_{18}]^{2-}$, 1098 $[H[C_{16}H_{14}N_2Mo_6O_{18}]]^{1-}$, $[(NBu_4)[C_{16}H_{14}N_2Mo_6O_{18}]]^{1-}$. FTIR: 2960 (m); 2872 (m); 2198 (m); 1606 (m); 1581 (m); 1522 (m); 1480 (m); 1362 (m); 1200 (w); 1196 (vw); 1167 (vw); 1132 (w); 1063 (vw); 1029 (vw); 974 (m); 944 (vs); 769 (vs). UV-vis (MeCN) λ, nm (ε, M^{-1} cm^{-1}): 247.5 (36.2 × 10^3); 292.0 (44.5 × 10^3); 421.0 (41.2 × 10^3).

2.8.10. Synthesis of [(C$_4$H$_9$)$_4$N]$_2$[Mo$_6$O$_{18}$N$_2$C$_8$H$_{10}$] (10)
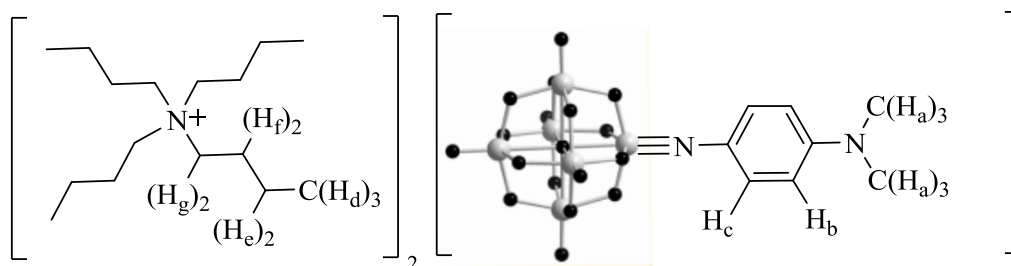
(n-Bu$_4$N)$_2$[Mo$_6$O$_{19}$], **1** (0.88 g, 0.65 mmol), 4-amino-*N,N*-dimethylaniline (0.068 g, 0.5 mmol), and DCC (1,3-dicyclohexylcarbodiimide) (0.11 g, 0.57 mmol) were added to a 50 mL flask under N$_2$ and then heated in dry DMSO (15 mL) for 10 h at 65 ºC. The colour of the solution changed to black while it was heated. The solution was filtered into a flask containing diethyl ether (200 mL) and ethanol (50 mL) resulting in a black precipitate which was washed with ethanol (10 mL) and ether (10 mL) several times, then recrystallized twice from hot acetonitrile and washed with ethanol (10 mL) and diethyl ether (10 mL) to afford black crystals (0.65g, 0.43 mmol, 86 %). δ_H (300 MHz, CD$_3$CN) 7.15 (d, *J* = 9.1 Hz, 2H, H$_c$), 6.63 (d, *J* = 9.1 Hz, 2H, H$_b$), 3.09 (*p*t, *J* = 8.4 Hz, 16H, H$_g$), 3.07 (s, 6H, H$_a$), 1.61 (quin, *J* = 8.0 Hz, 16H, H$_f$), 1.36 (sex, *J* = 7.3 Hz, 16H, H$_e$), 0.97 (t, *J* = 7.3 Hz, 24 H, H$_d$). δ_C (125 MHz, CD$_3$CN) 129.1, 111.9, 59.4, 40.4, 24.4, 20.4, 13.9. Anal. Calcd (found) % for C$_{40}$H$_{82}$N$_4$O$_{18}$Mo$_6$: C, 32.40 (32.31); H, 5.57 (5.48); N, 3.77 (3.82). *m/z* = 498 [C$_8$H$_{10}$N$_2$Mo$_6$O$_{18}$]$^{2-}$. FTIR: 2960 (m); 2872 (m); 1590 (s); 1511 (w); 1477 (m); 1365 (m); 1223 (w); 1176 (m); 971 (s); 944 (vs); 882 (m); 768 (vs). UV-vis (MeCN) λ, nm (ε, M^{-1} cm^{-1}): 221.0 (37.5 × 10^3); 258.0 (30.6 × 10^3); 424.0 (32.0 × 10^3).

2.8.11. Synthesis of [(C₄H₉)₄N]₂[Mo₆O₁₈N₂C₂₆H₁₈] (11)

$$2.8.11.\ \text{Synthesis of } [(C_4H_9)_4N]_2[Mo_6O_{18}N_2C_{26}H_{18}]\ (11)$$
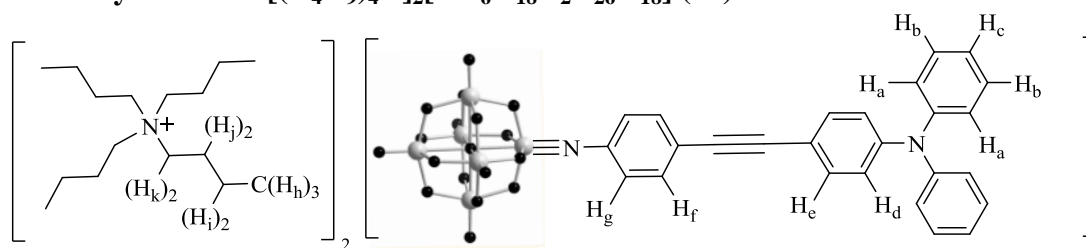
A mixture of 4-[(4-aminophenyl)ethynyl]-N,N-diphenylaniline (**P8**) (0.36 g, 1 mmol),
(n-Bu₄N)₂[Mo₆O₁₉], **1** (1.773 g, 1.3 mmol), and DCC (1,3-dicyclohexylcarbodiimide)
(0.237 g, 1.15 mmol) was heated in dry DMSO (15 mL) for 10 h at 68 °C. After
cooling to room temperature, the solution was filtered into a flask containing diethyl
ether (200 mL) and ethanol (50 mL) and left to stand for 4 hours resulting in a red
sticky precipitate. This was washed with ethanol (10 mL) and ether (10 mL) several
times before being recrystallized twice from hot acetonitrile and washed with ethanol
(10 mL) and diethyl ether (10 mL) to give red crystals (0.68g, 0.5 mmol, 40 %). δ_H
(500 MHz, CD₃CN) 7.50 (d , J = 8.3 Hz, 2H, H_g), 7.38 (d, J = 8.5 Hz, 2H, H_e), 7.33
(t, J = 7.8 Hz, 4H, H_b), 7.22 (d, J = 8.3 Hz, 2H, H_f), 7.12 (m, 6H, H_{a+c}), 6.94 (d, J =
8.5 Hz, 2H, H_d), 3.09 (*p*t, J = 8.6 Hz, 16H, H_k), 1.60 (quin, J = 8.0 Hz, 16H, H_j), 1.36
(sex, J = 7.4 Hz, 16H, H_i), 0.97 (t, J = 7.3 Hz, 24 H, H_h). δ_C (125 MHz, CD₃CN)
148.2, 133.9, 132.6, 130.9, 127.4, 126.5, 125.3, 124.1, 122.7, 116.1, 94.0, 89.0, 59.6,
24.6, 20.6, 14.0. Anal. Calcd (found) % for C₅₈H₉₀N₄Mo₆O₁₈: C, 40.80 (40.71); H,
5.31 (5.43); N, 3.28 (3.28). *m/z* = 611 [C₂₆H₁₈N₂Mo₆O₁₈]²⁻. FTIR: 2960 (m); 2872
(m); 2201 (vw); 1581 (m); 1507 (m); 1482 (s); 1379 (w); 1331 (m); 1168 (vw); 1136
(vw); 1100(vw); 1057 (vw); 1028 (vw); 974 (s); 945 (vs); 881 (w); 843 (w); 770 (vs);
696 (s). UV-vis (MeCN) λ, nm (ε, M⁻¹ cm⁻¹): 292.0 (41.2 × 10³); 326.5 (36.2 × 10³);
414.0 (45.3 × 10³).

2.8.12. Synthesis of [(C₄H₉)₄N]₂[Mo₆O₁₈N₂C₂₆H₁₆] (12)

$$\textbf{2.8.12. Synthesis of } [(C_4H_9)_4N]_2[Mo_6O_{18}N_2C_{26}H_{16}] \textbf{ (12)}$$
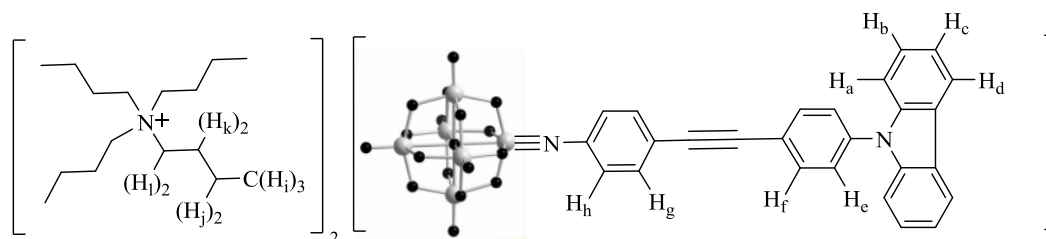
4-{[4-(9H-carbazol-9-yl)phenyl]ethynyl}aniline (**P7**) (0.359 g, 1 mmol), (n-Bu₄N)₂[Mo₆O₁₉], **1** (1.773 g, 1.3 mmol), and DCC (1,3-dicyclohexylcarbodiimide) (0.237 g, 1.15 mmol) were heated in dry DMSO (15 mL) for 12 h at 65 ºC. The colour of the solution changed to red while it was heated. After cooling to room temperature, the solution was filtered into a flask containing diethyl ether (200 mL) and ethanol (50 mL) resulting in an orange precipitate. The latter was washed with ethanol (10 mL) and ether (10 mL) several times, then recrystallized twice from hot acetonitrile and washed with ethanol (10 mL) and diethyl ether (10 mL) to afford orange crystals (1.19g, 0.549 mmol, 70 %). δ_H (500 MHz, CD₃CN) 8.20 (d, J = 7.7 Hz, 2H, H$_d$), 7.81 (d, J = 8.6 Hz, 2H, H$_h$), 7.66 (d, J = 8.6 Hz, 2H, H$_g$), 7.61 (d, J = 8.6 Hz, 2H, H$_f$), 7.46 (m, 4H, H$_{b+c}$), 7.32 (m, 2H, H$_a$), 7.26 (d, J = 8.6 Hz, 2H, H$_e$), 3.10 (pt, J = 8.6 Hz, 16H, H$_l$), 1.61 (quin, J = 8.0 Hz, 16H, H$_k$), 1.36 (sex, J = 7.4 Hz, 16H, H$_j$), 0.97 (t, J = 7.4 Hz, 24 H, H$_i$). δ_C (125 MHz, CD₃CN) 141.5, 134.3, 132.8, 128.1, 127.3, 127.2, 126.6, 124.4, 123.2, 122.6, 121.4, 110.9, 59.4, 24.4, 20.4, 13.9. Anal. Calcd (found) % for C₅₈H₈₈N₄Mo₆O₁₈: C, 40.85 (40.93); H, 5.20 (5.13); N, 3.28 (3.30). m/z = 610.2 [C₂₆H₁₆N₂Mo₆O₁₈]²⁻. FTIR: 2960 (m); 2873 (m); 2162 (vw); 1625 (vw); 1597 (w); 1513 (m); 1479 (m); 1449 (s); 1378 (w); 1334 (m); 1229 (m); 1169 (w); 1150 (w); 1103 (w); 1062 (w); 1014 (w); 975 (s); 947 (vs); 880 (w); 845 (m); 775 (vs); 749 (vs); 723 (s). UV-vis (MeCN) λ, nm (ε, M⁻¹ cm⁻¹): 226.5 (70.4 × 10³); 291.5 (48.4 × 10³); 326.5 (31.3 × 10³); 341 (33.7 × 10³); 384.5 (43.4 × 10³).

2.8.13. Synthesis of [(C₄H₉)₄N]₂[Mo₆O₁₇N₂C₁₂H₈I₂] (13)

2.8.13. Synthesis of $[(C_4H_9)_4N]_2[Mo_6O_{17}N_2C_{12}H_8I_2]$ (13)

or
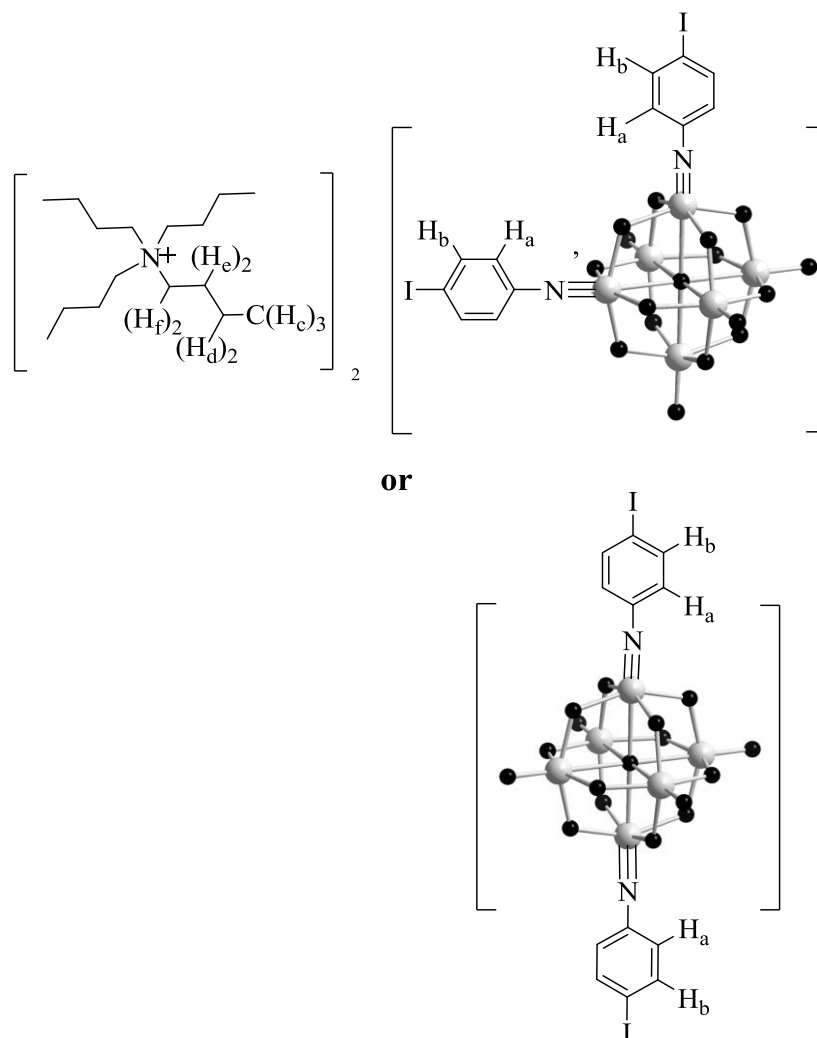
A mixture of 4-iodoaniline (0.438 g, 2 mmol), (n-Bu₄N)₂Mo₆O₁₉ (**1**) (1.364 g, 1 mmol) and DCC (1,3-dicyclohexylcarbodiimide) (0.495 g, 2.4 mmol) was heated in dry DMSO (15 mL) and a colour change to red was observed over 12 hours at 95 ºC. After cooling to room temperature, the red solution was filtered into a flask containing 200 mL dry ether and 50 mL ethanol. The precipitated solid was washed with ethanol (10 mL) and ether (10 mL) several times. This was recrystallized twice from acetonitrile to yield an orange solid (0.7 g, 0.3962 mmol, 40 %). δ_H (500 MHz, CD₃CN) 7.72 (d, J = 8.8 Hz, 4H, H$_a$), 6.95 (d, J = 8.8 Hz, 4H, H$_b$), 3.09 (pt, J = 8.5 Hz, 16H, H$_f$), 1.61 (quin, J = 8.1 Hz, 16H, H$_e$), 1.36 (sex, J = 7.3 Hz, 16H, H$_d$), 0.97 (t, J = 7.4 Hz, 24H, H$_c$). δ_C (125 MHz, CD₃CN). 138.7, 128.0, 59.4, 24.4, 20.5, 13.9. Anal. Calcd (found) % for C₄₄H₈₀N₄O₁₇I₂Mo₆: C, 29.91 (29.83); H, 4.56 (4.64); N,

3.17 (3.06). m/z = 640.6 $[C_{12}H_8N_2I_2Mo_6O_{17}]^{2-}$, 439.6 $[Mo_6O_{19}]^{2-}$. UV-vis (MeCN) λ, nm (ε, M^{-1} cm^{-1}): 228.0 (39.1 × 10^3); 260.5 (38.0 × 10^3); 354.0 (26.6 × 10^3).

2.8.14. Synthesis of $[(C_4H_9)_4N]_2[Mo_6O_{18}N_2C_7H_{10}]$ (14)
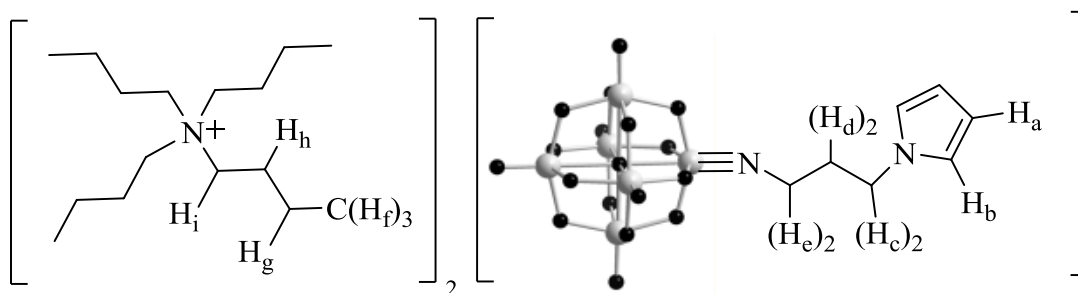
(n-Bu$_4$N)$_2$[Mo$_6$O$_{19}$], **1** (0.818 g, 0.6 mmol), 3-(pyrrole-1-yl)propylamine (0.062 g, 0.5 mmol), and DCC (1,3-dicyclohexylcarbodiimide) (0.139 g, 0.675 mmol) were heated in dry DMSO (10 mL) for 11 h at 70 °C. The solution was filtered into a flask containing diethyl ether (200 mL) and ethanol (50 mL) under N$_2$ and then stood for 5 hours resulting in a brown sticky precipitate. This was washed with ethanol (10 mL) and ether (10 mL) several times, before being recrystallized twice from acetonitrile:ethanol and finally washed with ethanol (10 mL) and diethyl ether (10 mL) to afford a brown solid (0.25g, 0.17 mmol, 34 %). δ_H (500 MHz, CD$_3$CN) 6.81 (t, J = 2.08 Hz, 2H, H$_b$), 6.06 (d, J = 2.08 Hz, 2H, H$_a$), 4.26 (m, 4H, H$_{c+e}$), 3.10 (pt, J = 8.5 Hz, 16H, H$_i$), 2.10 (m, 2H, H$_d$), 1.61 (quin, J = 8.0 Hz, 16H, H$_h$), 1.37 (sex, J = 7.3 Hz, 16H, H$_g$), 0.97 (t, J = 7.4 Hz, 24 H, H$_f$). δ_C (125 MHz, CD$_3$CN) 121.8, 108.7, 64.6, 59.3, 47.0, 34.3 24.3, 20.3, 13.8. Anal. Calcd (found) % for C$_{39}$H$_{82}$N$_4$O$_{18}$Mo$_6$: C, 31.84 (31.81); H, 5.61 (5.51); N, 3.80 (3.92). m/z = 492.71 $[C_7H_{10}N_2Mo_6O_{18}]^{2-}$. FTIR: 2959 (m); 2872 (m); 1480 (m); 1378 (w); 1270 (w); 1247 (w); 1105 (vw); 1089 (vw); 1061 (vw); 1031 (vw); 975 (m); 945 (vs); 884 (m); 771 (vs); 728 (vs); 585 (s). UV-vis (MeCN) λ, nm (ε, M^{-1} cm^{-1}): 214.5 (40.0 × 10^3); 337.0 (7.0 × 10^3).

2.8.15. Synthesis of [(C₄H₉)₄N]₃[PW₁₁O₃₉{O(Si-PhNH₂)₂}] (15)

2.8.15. Synthesis of $[(C_4H_9)_4N]_3[PW_{11}O_{39}\{O(Si\text{-}PhNH_2)_2\}]$ (15)
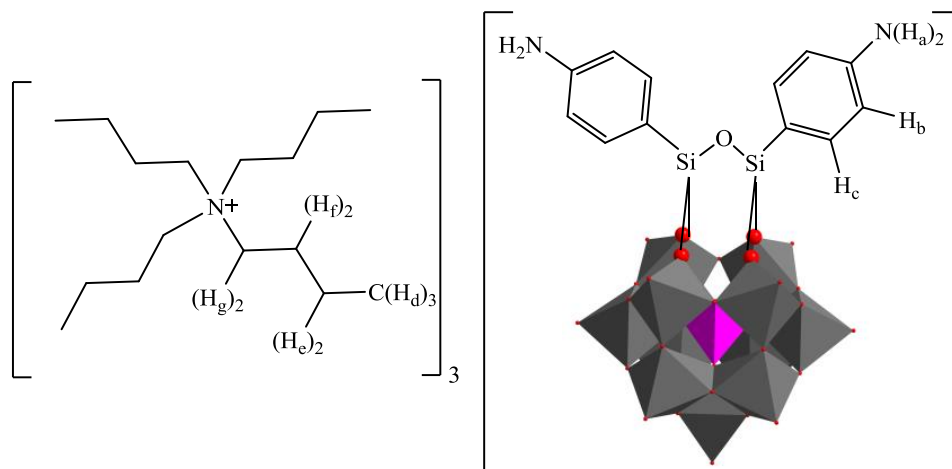
$(Bu_4N)_4[H_3PW_{11}O_{39}]$ (1.50 g, 0.411 mmol) was dissolved in acetonitrile:water mixture (52.5:22.5 mL) at 0 °C in an ice bath. A solution of p-aminophenyl trimethoxysilane (0.20 g, 0.937 mmol) in acetonitrile (15 mL) was added dropwise to the former solution, with vigorous stirring. The pH of the solution was set and held at 2.3 for 15 minutes by the drop-wise addition of 1 M HCl, and which was then left to stir overnight at room temperature, affording a light-red solution and precipitate. This was filtered and dissolved in MeCN before being filtered to remove unreacted $(Bu_4N)_4[H_3PW_{11}O_{39}]$ solid. A solution of tetrabutylammonium bromide (0.85 g, 2.646 mmol) was added and the solution then layered with ethanol and stirred at room temperature for 30 minutes resulting in the formation of a dark brown precipitate. The precipitate was then collected on a fine frit and washed with ethanol (3 × 10 mL), then dissolved in the minimum of acetonitrile, followed by the addition of triethylamine (52.5 µL) with stirring to fully deprotonate the amines. An excess of tetrabutylammonium bromide (*c.a.* 2.0 g) was added, and the solution layered with ethanol resulting in a brown precipitate. This was filtered, washed with ethanol (3 × 10 mL) and ether (3 × 10 mL) to give the product as a brown solid (1 g, 0.274 mmol, 66%). δ_H (300 MHz, CD₃CN) 7.52 (d , J = 8.5 Hz, 4H, H_c), 6.72 (d, J = 8.5 Hz, 4H, H_b), 4.41 (s, 4H, H_a), 3.09 (*p*t, J = 8.5 Hz, 24H, H_g), 1.61 (quin, J = 7.9 Hz, 24H, H_f), 1.37 (sex, J = 7.4 Hz, 24H, H_e), 0.98 (t, J = 7.3 Hz, 36 H, H_d). δ_P (202 MHz, CD₃CN) -13.49 (s, 1P). Anal. Calcd (found) % for $PW_{11}O_{40}Si_2C_{60}H_{120}N_5$: C, 19.68 (19.72); H,

3.25 (3.31); N, 1.91 (1.94). $m/z = 1588.28$ $[(Bu_4N)[C_{12}H_{12}N_2PW_{11}O_{40}Si_2]]^{2-}$. FTIR: 2960 (m); 2935 (m); 2874 (m); 1620 (m); 1600 (m); 1508 (w); 1480 (m); 1460 (m); 1379 (w); 1274 (vw); 1188 (m); 1130 (s); 1108 (m); 1064 (s); 1033 (w); 958 (vs); 900 (w); 864 (vs); 814 (vs); 706 (w); 656 (m). UV-vis (MeCN) λ, nm (ε, M^{-1} cm^{-1}): 262.5 (64.0×10^3).

2.9. X-Ray Crystallography

Crystals of X-ray quality were obtained by room temperature diffusion of diethyl ether vapor into acetonitrile. Data were collected on Oxford Diffraction XCalibur 3 diffractometer, or a Rigaku AFC 12 goniometer equipped with an enhanced sensitivity (HG) Saturn724+ detector and FR-E+ SuperBright molybdenum rotating anode generator with HF Varimax optics (100μm focus). Data reduction, cell refinement and absorption correction was carried out using Agilent Technologies CrysAlisPro[211] or Rigaku CrystalClear-SM Expert software,[212] and solved using SHELXS-97[213] *via* WinGX.[214] Refinement was achieved by full-matrix least-squares on all F_0^2 data using SHELXL-97[213], and molecular graphics were prepared using ORTEP-3.[214] In all structures, the asymmetric unit contains the complete molecular anion and both cations.

Table 2.1 Crystallographic Data Summary.

No. and structure	Crystal System	Space Group	a, b, c /Å	α, β, γ /°	V /Å³
2, [(C$_4$H$_9$)$_4$N]$_2$[Mo$_6$O$_{18}$NC$_6$H$_4$I]	triclinic	*P*-1	12.1154, 12.1829, 19.6204	93.78, 97.68, 93.37	2857.03
3, [(C$_4$H$_9$)$_4$N]$_2$[Mo$_6$O$_{18}$N$_2$C$_{10}$H$_8$]	monoclinic	*P*21/n	11.6395, 33.6792, 14.0382	90.00, 91.57, 90.00	5501.02
4, [(C$_4$H$_9$)$_4$N]$_2$[Mo$_6$O$_{18}$N$_2$C$_{18}$H$_{12}$]	orthorhombic	*P*212121	17.5590, 17.7832, 19.6079	90.00, 90.00, 90.00	6122.7
5, [(C$_4$H$_9$)$_4$N]$_2$[C$_{14}$H$_{10}$N$_2$Mo$_6$O$_{18}$]	orthorhombic	*P*212121	15.9271, 24.5421, 29.984	90.00, 90.00, 90.00	11720.3
6, [(C$_4$H$_9$)$_4$N]$_2$[Mo$_6$O$_{18}$NC$_8$H$_5$]	triclinic	*P*-1	12.3617, 19.1579, 25.2441	107.13, 94.44, 100.81	5555.14
8, [(C$_4$H$_9$)$_4$N]$_2$[Mo$_6$O$_{20}$N$_2$C$_{14}$H$_8$]	monoclinic	*P* 21/n	11.4858, 38.1339, 14.2817	90, 91.649, 90	6252.8
9, [(C$_4$H$_9$)$_4$N]$_2$[Mo$_6$O$_{18}$N$_2$C$_{20}$H$_{14}$]	monoclinic	*P*21/c	12.4494, 23.7848, 21.9894	90.00, 103.57, 90.00	6329.36
10, [(C$_4$H$_9$)$_4$N]$_2$[Mo$_6$O$_{18}$N$_2$C$_8$H$_{10}$]	monoclinic	*P*21/n	17.3560, 15.6450, 20.4840	90.00, 104.25, 90.00	5390.9
13, [(C$_4$H$_9$)$_4$N]$_2$[Mo$_6$O$_{18}$N$_2$C$_7$H$_{10}$]	monoclinic	*P*21/c	18.8960, 16.5079, 18.4858	90.00, 90.22, 90.00	5766.3

2.10. Hyper-Rayleigh Scattering (HRS)

HRS measurements were performed by the author with help from Mr. Nick Van Steerteghem, a PhD student at KU Leuven (Belgium) under the supervision of Koen Clays, during a summer secondment at KULeuven (Belgium).

General details of the hyper-Rayleigh scattering (HRS) experiment have been discussed in chapter 1. Measurements were carried out using dilute (*ca.* 10^{-5} M) acetonitrile solutions for both 800 nm and 1064 nm fundamental wavelength, to ensure a linear dependence of signal on concentration and therefore such that self-absorption of the SHG signal was negligible. All 800 nm measurements were performed by using the 800 nm fundamental of a regenerative mode-locked Ti^{3+}: sapphire laser (Spectra Physics, model Tsunami®, 100 fs pulses, 1 W, 80 MHz). Crystal violet was used as an external reference ($\beta_{xxx,800} = 327 \times 10^{-30}$ esu in

acetonitrile; from the value of 338×10^{-30} esu in methanol,[215] corrected for local field factors at optical frequencies). The reported β values are the averages taken from measurements at different amplitude modulation frequencies. Measurements at 1064 nm were performed in acetonitrile, using a Spectra-Physics InSight® DS+ laser (1W average power, sub-100 fs pulses, 80 MHz). All samples were passed through 0.45 μm filters prior to being used, to ensure any dust was removed. In this setup, the collection optics are coupled to a spectrograph (model Bruker 500is/sm), together with an EMCCD camera (Andor Solis model iXon Ultra 897). Correction for multiphoton induced fluorescence was done by subtracting the broad MPF background signal from the narrow HRS peak (FWHM ± 9 nm), as described in chapter **1**. The higher accuracy of this setup enables us to use the solvent as an internal reference (acetonitrile, $\beta_{HRS},1064 = 0.258 \times 10^{-30}$ esu.[216]).

2.11. Stark Spectroscopy

The Stark spectra were measured by Dr. John Fielden during a summer secondment at CalTech (USA). The measurements were performed using the previously reported experimental methods, data collection methods, and Stark apparatus.[22,217] The experiments were performed in butyronitrile glasses at 77 K, the local field correction limit is estimated as 1.33, and the Stark spectra were recorded a minimum of two times. The data was analysed as previously reported,[22,217] and the resulting spectra were analysed using the first and second and zeroth derivatives of the absorption spectrum. The dipole moment change $\Delta\mu_{12}$ associated with each of the optical transitions was calculated from the coefficient of the second derivative component and all equations used can be seen in Chapter 5.

Chapter 3

Molecular Design and Synthesis

3.1 Introduction

Lindqvist POMs can be derivatised by replacing or derivatising the terminal oxygens of hexamolybdate by various nitrogen-containing ligands such as organoimido $[NR]^{2-}$, hydrazido $[NNR_2]^{2-}$, nitrosonium $[NO]^+$ and diazenido $[NNR]^+$ species resulting in hybrid materials with promising and synergistic properties.[116,218] The focus of this project is the development of new organoimido hexamolybdate derivatives as NLO chromophores. This chapter describes the synthesis, and structures of new series of organoimido Lindqvist derivatives with various organic donor or acceptor groups (scheme 3.1). In addition, the synthesis of the organic ligands that have been used as precursors will be described.

3.2 Synthesis of Polyoxometalate Derivatives

A new series of organoimido hexamolybdate derivatives **2-14** (shown in Scheme 3.2) were prepared using adapted procedures for the DCC-mediated coupling of [n-Bu$_4$N]$_2$[Mo$_6$O$_{19}$] (**1**) with amines (Scheme 3.1).[219] Compound **15** has been reported previously,[149] but has not been studied for its NLO properties. The identity and purity of all these compounds were confirmed by ^{1}H and ^{13}C-NMR spectra, mass spectra (MS), elemental analyses (EA), infrared spectra (IR), UV-vis spectra (UV-vis), and X-ray crystal structures for a number of them.
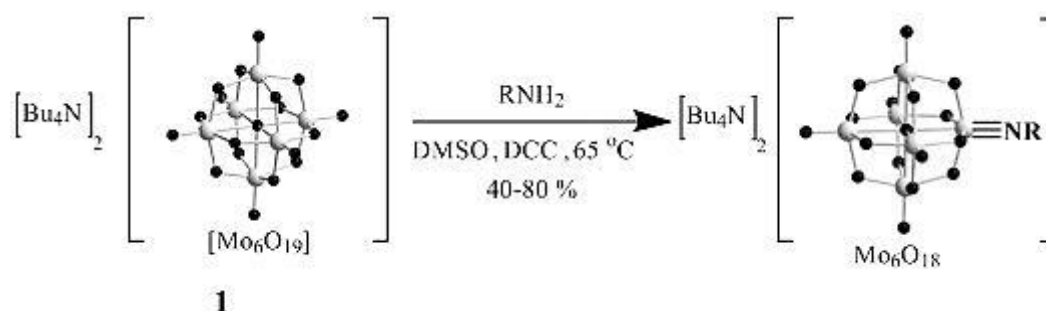
Scheme 3.1 Synthesis of new organo-imido Lindqvist POMs.

2

3

4

5

6

7

8

9

10

11

12

13

14

15
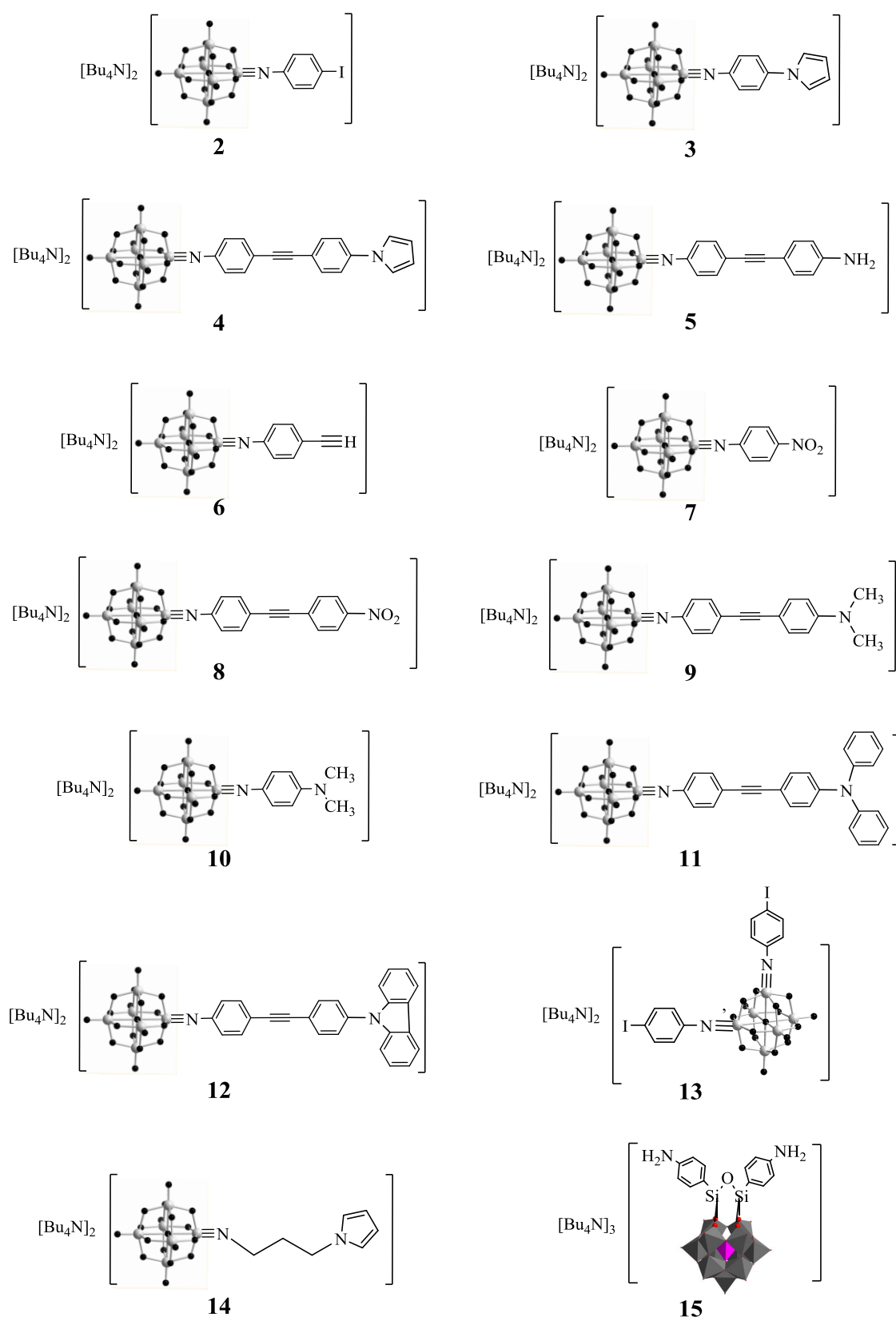
Scheme 3.2 Structures of POM-based derivatives **2** to **15**.

3.2.1 [Bu$_4$N]$_2$[Mo$_6$O$_{18}$(*p*-NPhI)], 2

Initially, we attempted synthesis of **2, 4-iodophenylimido hexamolybdate** as a precursor for a variety of coupling reactions such as Sonogashira coupling to extended aromatic systems. We followed the methods developed by Peng and Wei:[130] [NBu$_4$]$_2$[Mo$_6$O$_{19}$] (**1**), DCC and 4-iodoaniline in refluxing acetonitrile. Surprisingly, however, we found that in our hands, this widely reported approach was unsuccessful. A colour change from yellow to orange was observed, but yields were low and the product contained lots of unreacted hexamolybdate (**1**) and also more highly substituted imido derivatives. Characterisation by ^{1}H-NMR, as shown in figure (3.3), showed both protons (a and b) exhibit a pair of doublets with higher chemical shifts after imido bond formation compared to the ^{1}H-NMR of the corresponding free amine. These two protons likely correspond to compound **2**. However, another pair of doublets (marked *) for both protons (a, and b) having 13 % mole ratio of the whole product is also seen in Figure (3.3), presumably the difunctionalised derivative (compound **13**). Moreover, the integrals for the tetrabutylammonium cation peaks are higher than would be expected for **2** alone, indicating the presence of 51 % mole ratio of unreacted {Mo$_6$} or other underivatized molybdate species. These results indicate that the target molecule (compound **2**) was present, but at low yield and impure, with a large quantity of unreacted hexamolybdate.
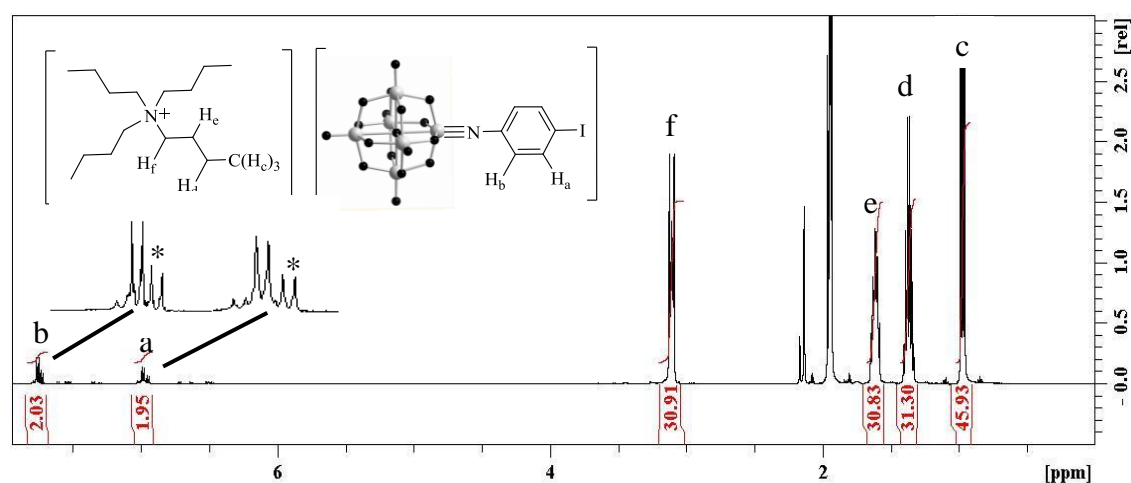

Figure 3.3 ^{1}H-NMR spectrum of compound **2** in acetonitrile-*d$_3$*.

Therefore, we tried a similar method replacing acetonitrile with dimethyl sulfoxide (DMSO),[219] and increasing the temperature from the 82 ˚C achieved in refluxing acetonitrile, to 100 ˚C. This produced mixtures of *mono-* and *bis*-imido substituted {Mo$_6$} derivatives; with higher loadings of DCC and amine increasing the proportion of *bis-* compound (entries 4-6 in Table 3.1). Entries 1-5 were aimed at optimizing synthesis of the *mono*-compound. The more upfield doublets decreased in intensity at lower loadings of DCC and amine, and at lower temperatures, lending weight to the hypothesis that they result from the *bis*-compound

Synthesis of our target, **2**, was optimized by varying the temperature, reaction time, and ratio of **1**: DCC : 4-iodoaniline, revealing that **2** could be synthesized in *ca*. 85% yield, with no *bis*-products, by working with an excess of **1** and DCC at 70 ˚C. The product was purified by hot recrystallization from acetonitrile to afford orange crystals. More importantly, however, the results summarized in Table 3.1 indicate that the reaction is highly temperature dependent – with only 0.56 equivalents of amine, 0.1% of the *bis*-derivative is produced at 80 ˚C but 5% at 100 ˚C. With 2 eq of amine and 2.1 eq of DCC, increasing the temperature from 70 ˚C to 95 ˚C changed the *mono: bis*: **1** ratio from 53:30:17, to 52:42:6. Increasing reaction times beyond 12 hours produced increasing amounts of unidentified side products, but only a slight increase in conversion, as has been previously reported for similar chemistry in acetonitrile.[185] Compound **2** has been unambiguously characterized by ^{1}H and ^{13}C-NMR, electrospray MS, EA, and IR, and X-ray crystallography. By comparison with the parent 4-iodoaniline, it can be clearly seen from the ^{1}H-NMR spectra (Figure 3.4) that the protons ortho- to the aniline group (H$_b$) shift downfield by around 1.5 ppm upon formation of the Mo-imido bond, consistent with the strongly electron withdrawing nature of the {Mo$_6$} cluster. While, for the protons meta- to the aniline group (H$_a$), these are shifted upfield.

Table 3.1 Reactions of hexamolybdate with 4-iodoaniline at different ratios, time and temperature to synthesize compound **2**.

	Compound **1** eq.	DCC eq.	Amine eq.	Time H	Temperature °C	Product distribution in initial precipitate[a] *mono* : *bis* : *unreacted **1***
1	1	0.83	0.56	10	80	40.9 : 0.1 : 59
2	1	0.83	0.56	10	100	43 : 5 : 52
3	1	1	0.67	10	70	85 : 0 : 15
4	1	1	0.67	10	100	46.5 : 6.5 : 47[b]
5	1	1.5	1.3	10	95	28 : 21 : 51
6	1	1.8	2	12	95	58 : 32 : 10

[a] Determined by ^{1}H-NMR of initial crude material precipitated from DMSO by diethyl ether/ethanol, washed with ether and ethanol several times, and dried under vacuum. [b] Hydrolysis of *bis-imido* may have occurred to produce such a large quantity of {Mo_6}.
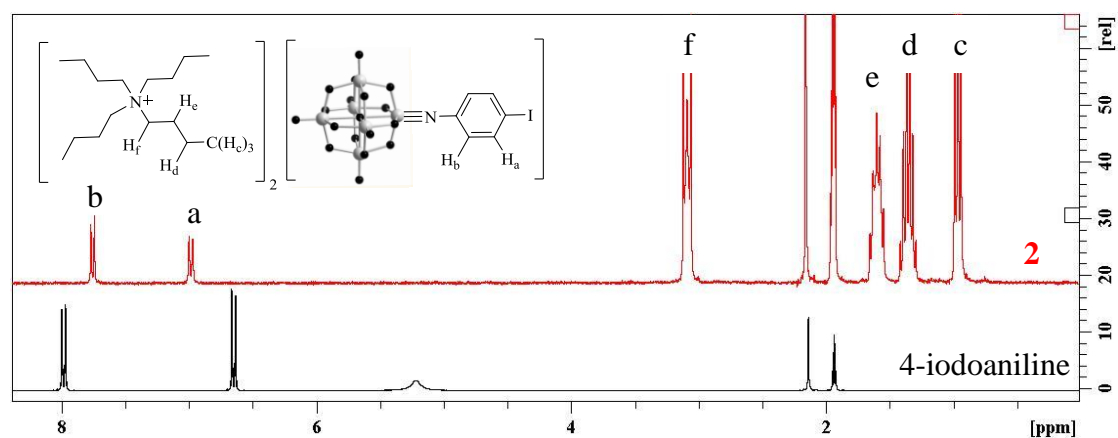

Figure 3.4 Stacked ^{1}H-NMR spectra of **2** (top, red) and its parent 4-iodoaniline (bottom, black), in acetonitrile-d_3.

Single crystals of **2** were grown for X-ray analysis by vapour diffusion of ether into acetonitrile solution, and yielded a high quality crystal structure in the space group *P*-1. This structure (Figure 3.5) reveals the substituted hexamolybdate cluster, one tetrabutylammonium (TBA), and another disordered TBA in the asymmetric unit), and show characteristic bond lengths and angles for organoimido-Lindqvist species (see Table 3.3, and also Appendix A). The Mo-N-C bond angle is closer to 180º than 120º, at 164.8º (3) indicating significant Mo^{im}-N triple bond character and a formal positive charge on N. The Mo-N bond distance, at 1.743 (4) Å, is shorter than the bridging Mo-O (*ca.* 1.92 (3) Å) which implies again a multiple bond character. However, there is no consistent pattern in the terminal Mo-O distances which are typically in the range of 1.65 to 1.70 Å.
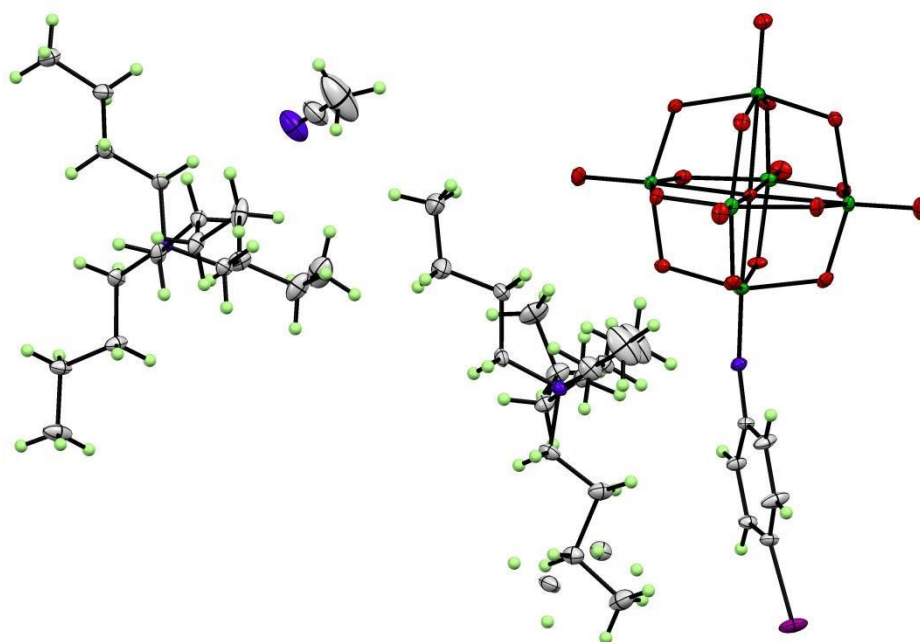

Figure 3.5 ORTEP representation of compound **2***MeCN**.** Thermal ellipsoids are at the 30% probability level. Colour scheme: Mo is green; O, red; C, gray; N, blue; I, purple; H atoms are represented by light-green balls.

3.2.2 Synthesis of bis-organoimido (13), and investigation of the reactivity of 2

The initial observations in the synthesis of **2**, which led us to synthesize pure *mono*-compound using an excess **1**, fewer equivalents of amine and DCC, and lower reaction temperatures, suggested that the second compound in the mixtures of reactions 1-6 in table (3.1) is the *bis*-compound (**13**) based on the literature.[185,220] The *bis*-compound (**13**) can be isolated in moderate yield (40%) by recrystallization of such mixtures (using entry 3 in Table 3.2), but we have been unable to find conditions which produce it exclusively. Compound **13** has been characterized by ^{1}H and ^{13}C-NMR spectra, MS, EA, and IR. There are two possible geometries for a *bis*-imido hexamolybdate – *cis* or *trans* (shown in Figure 3.6), and as *cis* is by far the more common in the literature,[220,221] we assume **13** is the *cis*-compound. However, it is not possible to unambiguously distinguish this by NMR, MS or IR spectroscopy and we have been unable to produce X-ray diffraction quality single crystals of this material. Thus, we cannot absolutely distinguish whether **13** is the *cis* or *trans bis*-imido derivative.
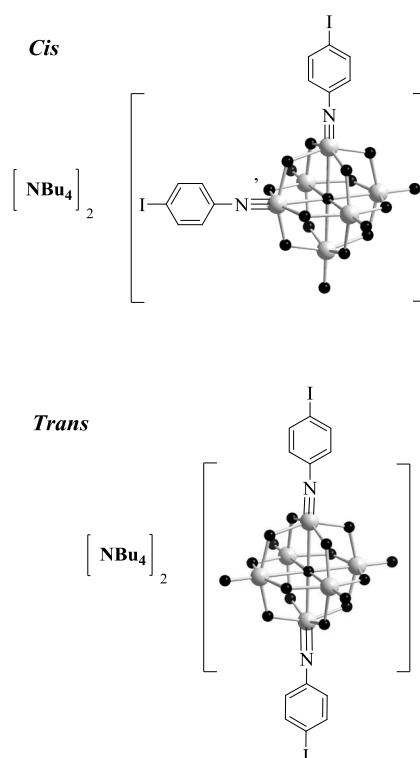

Figure 3.6 Structures of *cis* and *trans-bis*-derivative **13**.

Table 3.2 Reactions of hexamolybdate with 4-Iodoaniline at different ratios, times and temperature.

	Compound **1** eq.	DCC eq.	Amine eq.	Time H	Temperature °C	Product distribution in initial precipitate[a] *2* : *13* : *unreacted 1*
1	1	2.1	2	12	70	53 : 30 : 17
2	1	2.1	2	12	95	52 : 42 : 6
3	1	2.5	2	24	95	20 : 80 : 0
4	1	2.4	2.1	12	80	42 : 43 : 15
5	1	2.4	2.1	12	95	33 : 55 : 12
6	1	2.3	2.2	12	95	32 : 50 : 17
7	1	2.4	2.5	0.5	95	89 : 11 : 0
8	1	2.4	2.5	1	95	80 : 20 : 0
9	1	2.4	2.5	2	95	57 : 43 : 0
10	1	2.4	2.5	4	95	38 : 53 : 9
11	1	2.4	2.5	6	95	37 : 50 : 13
12	1	2.4	2.5	8	95	31 : 54 : 15
13	1	2.4	2.5	10	95	36 : 54 : 10
14	1	2.4	2.5	12	95	36 : 54 : 10
15	1	2.4	2.5	0.5	110	90 : 10 : 0
16	1	2.4	2.5	1	110	80 : 20 : 0
17	1	2.4	2.5	2	110	56 : 44 : 0
18	1	2.4	2.5	4	110	38 : 53 : 9
19	1	2.4	2.5	6	110	38 : 50 : 12
20	1	2.4	2.5	8	110	31 : 54 : 15[b]
21	1	2.4	2.5	10	110	36 : 54 : 10
22	1	2.4	2.5	12	110	36 : 54 : 10

[a] Determined by ^{1}H-NMR of initial crude material precipitated from DMSO by diethyl ether/ethanol, washed with ether and ethanol several times, and dried under vacuum. [b] Hydrolysis of *bis-imido* may be occurring to produce such a large quantity of $[Mo_6O_{19}]^{2-}$.

It was also noted that the *bis*-compound **13** was more vulnerable to hydrolysis (less

stable) than **2**. The amount of underivatized **1** was increased upon recrystallization, as

clearly seen in the ^{1}H-NMR spectrum of the final product (Figure 3.7), the integrals of

the TBA show *ca.* 45% hexamolybdate (**1**). However, elemental analysis results were

consistent with the target. The two possible explanations are that this may be related

to the inhomogeneous solid product or rapid partial hydrolysis in NMR solvent. These

results are consistent with the CV results, showing two peaks at different potentials

(chapter 4). It appears that **13** is more vulnerable to hydrolysis than *mono*-derivative

(**2**), and therefore impossible to separate **13** from unreacted **1** without very rigorous

conditions (*i.e.* a glove box). The ESI-MS spectrum of **13** (Figure 3.9) shows the

presence of both molecular ions of **13** (m/z = 640.6), and unreacted **1** (m/z = 439.6).

Compared to compound **2**, the ^{1}H-NMR of **13** showed that the protons ortho- and

meta- to the imido bond (H_{a+b}) slightly shift upfield upon formation of the second Mo-

imido bond (*bis*-compound), as shown in Figure 3.8.

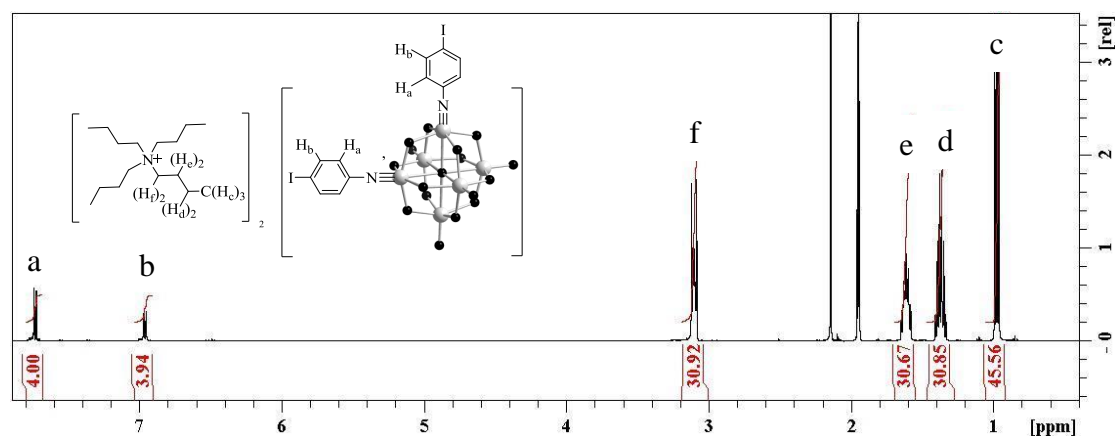**Figure 3.7** ^{1}H-NMR spectrum of compound **13** in acetonitrile-*d₃*. The geometry of **13** is

assumed to be *cis* based on the far higher frequency of *cis*-bifunctionalized hexamolybdates in
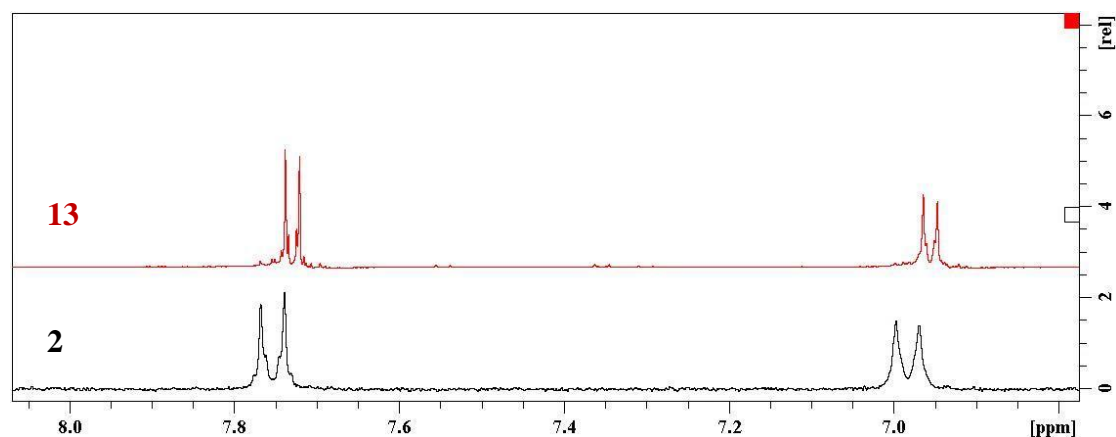
the literature.

Figure 3.8 Stacked ^{1}H-NMR spectra of **2** (bottom, black), and **13** (top, red) in acetonitrile-d_3.
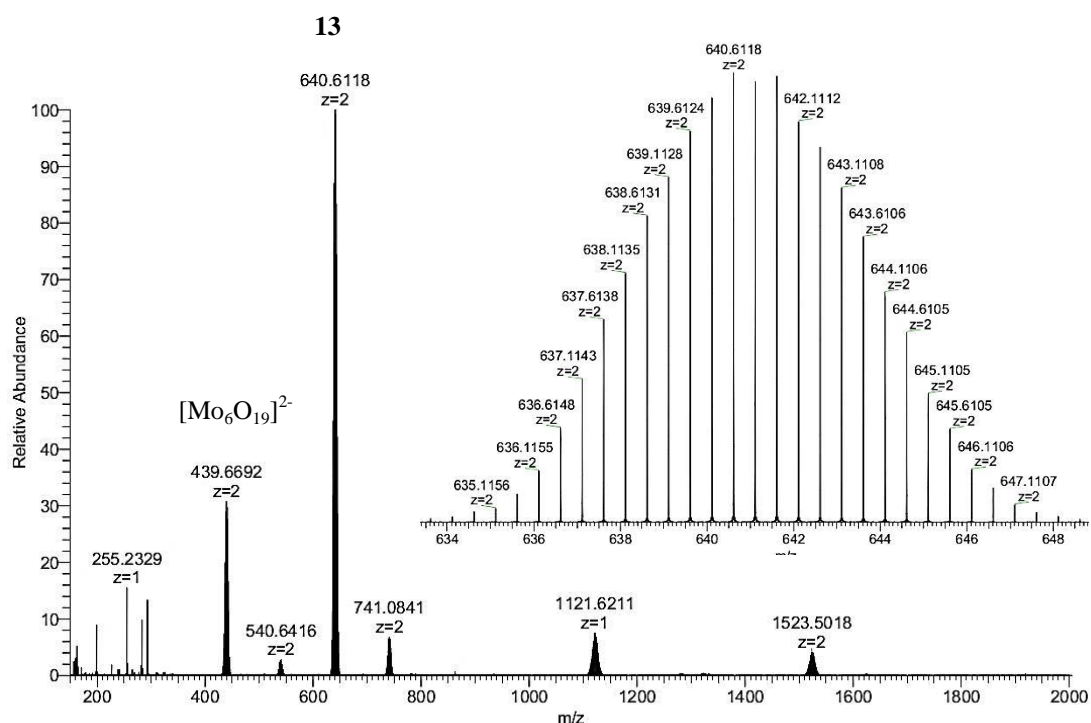

Figure 3.9 ESI-MS spectrum of **13**.

To further probe the relationship between the *mono-* and *bis*-imido hexamolybdates, the reaction was monitored over 12 hours, at 95 °C in the presence of excess DCC (2.4 eq) and 4-iodoaniline (2.5 eq) (Table 3.2 entries from 5-14). ^{1}H-NMR indicates that appreciable quantities of both **2** and **13** formed within 30 minutes, with an initial ratio of 9(**2**) : 1(**13**). Over time the proportion of **13** increases, reaching 4(**2**) : 6(**13**) after 6 hours, but thereafter changing no further (Figure 3.10), and producing

increasing amounts of unidentified side products. Moreover, increasing the temperature from 95 ℃ to 110 ℃ did not show any change in the conversion ratio. This suggests that **13** is formed via **2**, and suggested also that a step-wise approach might be a route to synthesize heterobifunctionalized hexamolybdate derivatives.
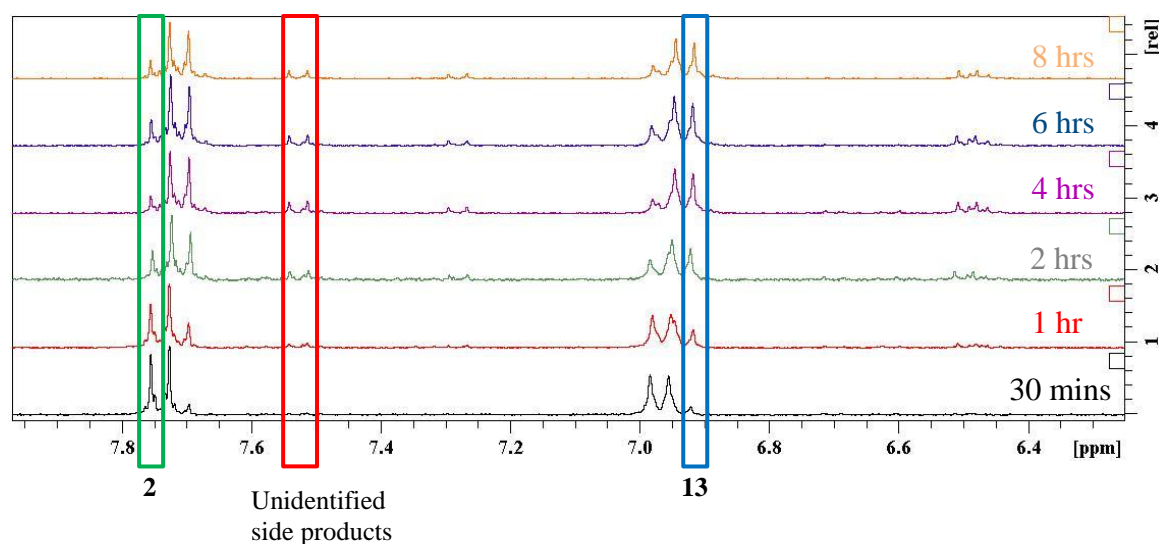

Figure 3.10 Stacked ^{1}H-NMR spectra of the crude products for entries 7-12 in table (3.2), in acetonitrile-d_3.

Aiming to achieve stepwise synthesis of heterobifunctionalized derivatives, compound **2** was reacted with 1 eq. of 4-ethynylaniline and DCC at 65 ℃ for 12 hours. The purpose of using the lower temperature was to avoid any multi-substitution side reactions. However, the ^{1}H-NMR clearly shows the presence of **2**, **6** (4-ethynyl-phenylimido Lindqvist derivative, *vide infra*), and smaller, slightly upfield peaks that can be ascribed to the more electron rich *bis*-derivatives (marked *), as shown in Figure 3.11. ESI-MS showed strong peaks for [**2**]$^{2-}$, [**6**]$^{2-}$, [**13**]$^{2-}$ and also the heterobifunctionalized compound, in an approximate ratio of 55(**2**) : 32(**6**) : 8(**13**) : 5 (heterobifunctionalized compound), shown in Figure 3.12. These ratios are also consistent with the ^{1}H-NMR integrals that can be calculated unambiguously for **2** and **6**.
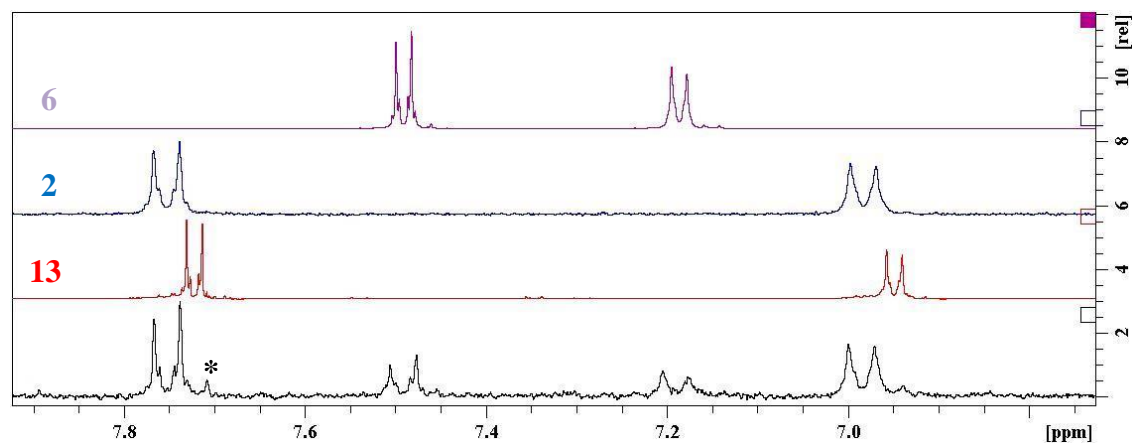
Figure 3.11 Stacked ^{1}H-NMR spectra of the crude products (bottom, black), **2** (blue), **6** (purple), and **13** (red) in acetonitrile-d_3.
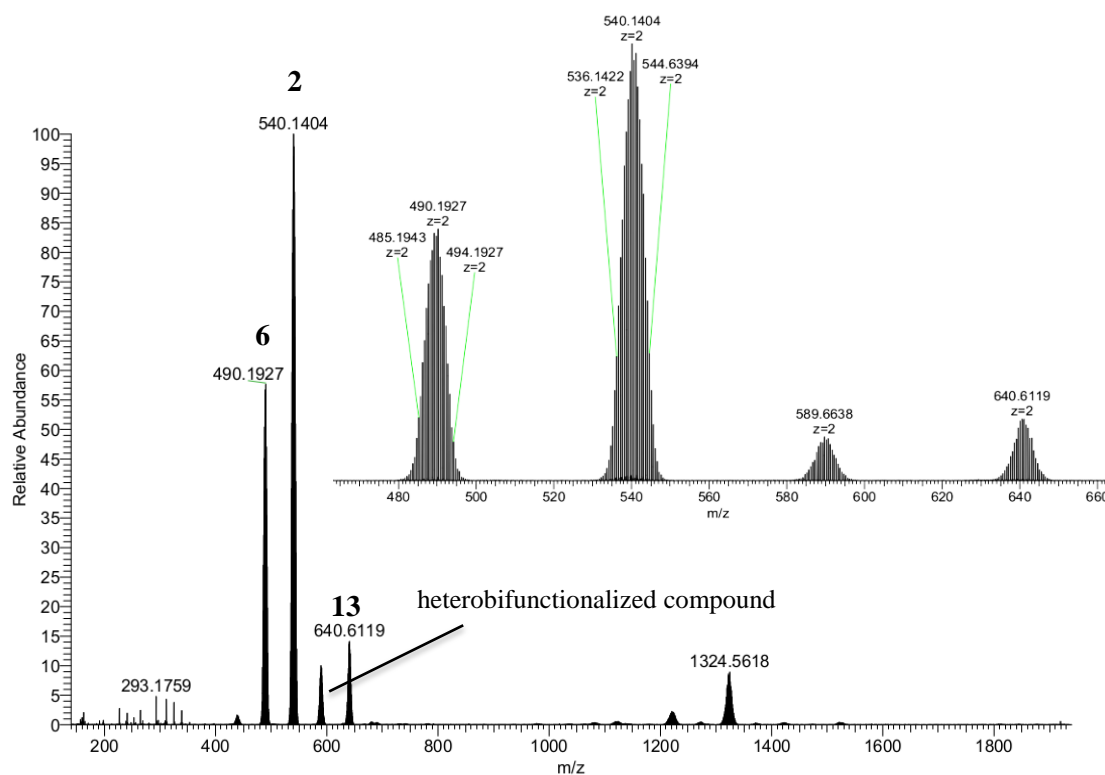

Figure 3.12 ESI-MS spectrum of the crude product of the reaction time of 12 hours, 1 eq. of 4-ethynylaniline and DCC at 65 ˚C.

Increasing the reaction time to 24 hours produced a far higher proportion of *bis*-derivatives, with a mixture of 28(**2**) : 33(**6**) : 19 (homobifunctionalized compounds) : 20 (heterobifunctionalized compounds) assigned from the ^{1}H-NMR spectrum of the crude product (Figure 3.13). It was noted from the ^{1}H-NMR spectra of both reaction times that the integration of the tetrabutylammonium peaks show no significant change suggesting no decomposition to {Mo_6}, and only small peaks corresponding to this cluster are observed in the ESI-MS. These observations – namely production of a mixture including **6** and **13** from **2** and ethynylaniline indicates ligand displacement and exchange reactions occur complicate the step-wise approach. This is consistent with the acetonitrile-based chemistry of Wei, where stepwise heterobifunctionalization proved unsuccessful.[220] Whether there is a ligand exchange between the clusters or another mechanism is unclear; however, it is an interesting question that could be explored in the future. Going deeper to fully decipher the formation mechanism of *bis* and heterobifunctionalized-imido derivatives is very challenging, however, and would require experiments beyond the scope of this thesis, which is primarily focused on materials and materials properties.
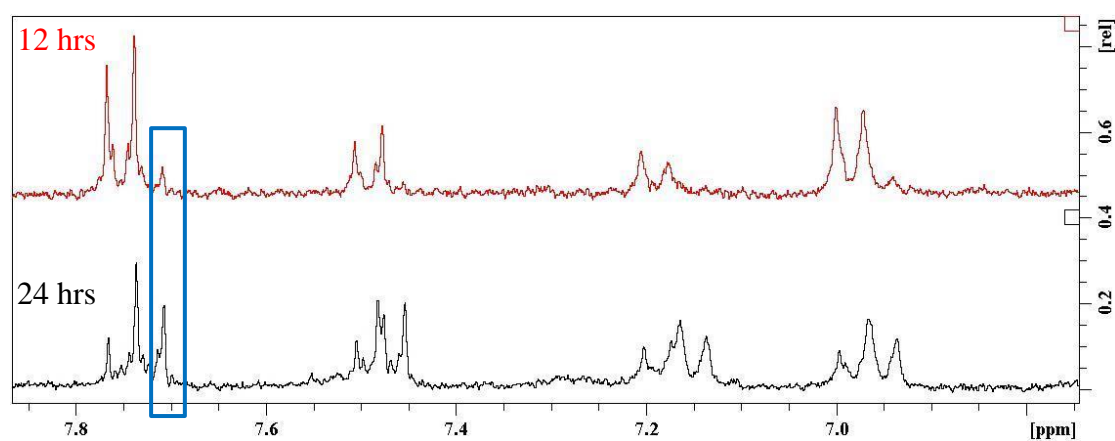

Figure 3.13 ^{1}H-NMR spectra of the crude products of the reaction times of 12 (top, red), and 24 (bottom, black) hours, showing the increase in the *bis*-derivative peak (blue box).

3.2.3. Synthesis of 3-4, 6-7, 10-14

Compounds **3** and **4**, **6** and **7**, and **10** to **14** (scheme 3.1) were synthesized following the same method used to produce **2**, shown in scheme (3.2). All derivatives have been unambiguously characterised by ^{1}H and ^{13}C-NMR, electrospray mass spectroscopy (MS), elemental analysis (EA), infrared spectroscopy (IR), and for **3**, **4**, **6**, **10,** and **14** X-ray crystal structures.

It was noted that less DCC (1.4 eq), and lower temperature (65 ºC) were required to access the 4-(1H-pyrrol-1-yl) derivative **3** from 4-(1H-pyrrol-1-yl) aniline (**P5**) in 80% yield, consistent with the increased nucleophilicity of **P5** attributed to the electron donor group (pyrrole). Similar trends were seen in the formation of derivatives **10**, **11**, **12**, and **14**. However, two or three recrystallizations were required to remove small amounts of excess hexamolybdate, accounting for losses of yield. An analogous approach was used to access the extended pyrrole derivative **4** from 4-{[4-(1H-pyrrol-1-yl)phenyl]ethynyl}aniline (**P4**) in a yield of 50%.

Assignment of the aromatic regions (supported by 2D COSY NMR) enables us to comment on the effect on chemical shift of introducing these donor groups to the organoimido system. By comparison with their parent anilines, the ^{1}H-NMR of compounds **3** and **4** also show the downfield shift of the aromatic protons, clearly demonstrating the donor-acceptor nature of these systems (Figure 3.16). However, the pyrrole protons show relatively little change in δ upon attachment of the POM. This indicates a certain degree of electronic isolation between donor and acceptor. By comparison with derivative **2**, **3** and **4** show a significant upfield shift in δ (from 7.75 to 7.49 ppm) for H_d, the proton ortho to the imido group, upon moving from an 4-iodo- to a 4-pyrrolyl phenyl, consistent with replacement of a weak electron withdrawing group (I), with a weak electron donor (pyrrole), illustrated in Figure (3.17). However, the resonance of H_c, the proton meta to the imido group, shifts

interestingly in the opposite direction (downfield). A similar trend is seen in **4**, where

an alkynyl phenyl spacer is introduced.
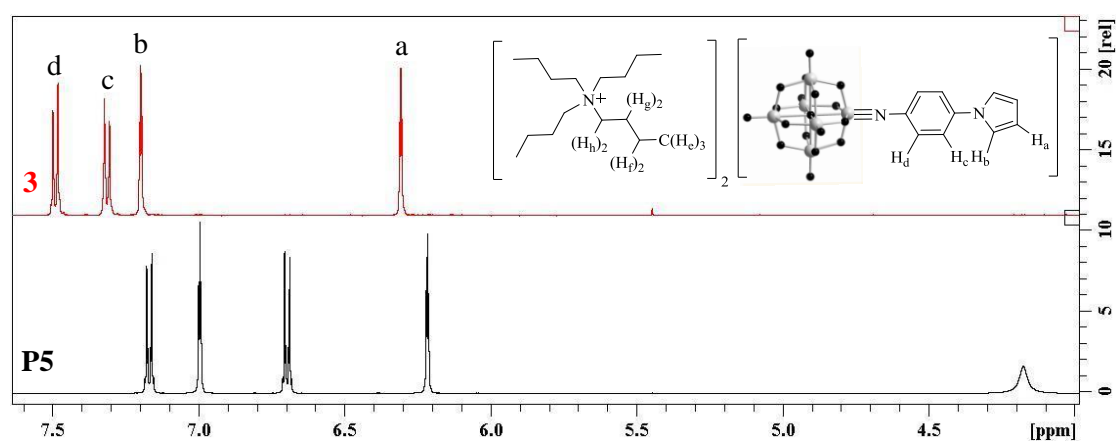
Figure 3.16 Stacked ^{1}H-NMR spectra of **3** (top, red) and its parent **P5** (bottom, black), in acetonitrile-d_3.
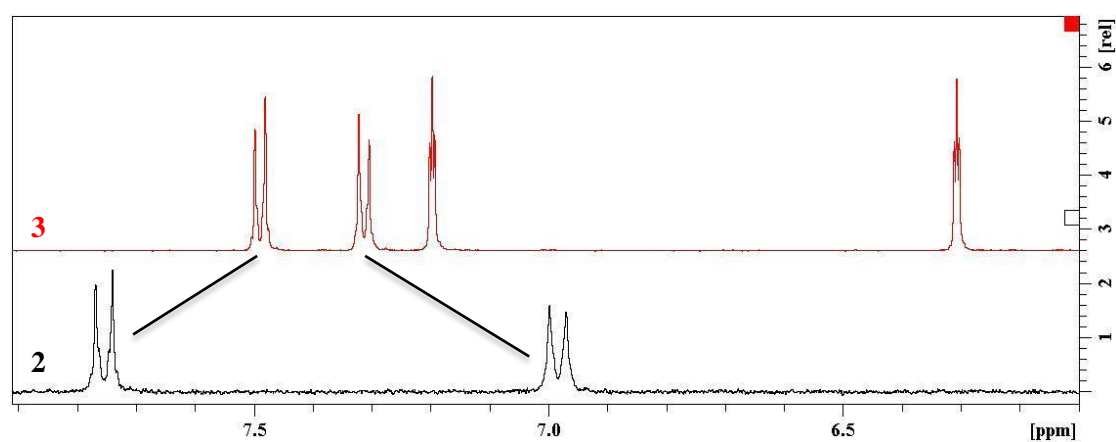
Figure 3.17 Stacked ^{1}H-NMR spectra of **2** (bottom, black) and **3** (top, red), in acetonitrile-d_3.

Single crystals of X-ray quality were obtained by vapour diffusion of diethyl ether into acetonitrile, and yielded high quality crystal structures of **3** and **4** in the space groups *P*21/n, *P*212121, respectively. In all cases, the asymmetric unit contains a complete derivative anion, and both TBA cations. An ORTEP representation of **3** is displayed in Figure (3.18), note that significant disorder is present in the TBA cations of **3** but the anion is well-resolved.
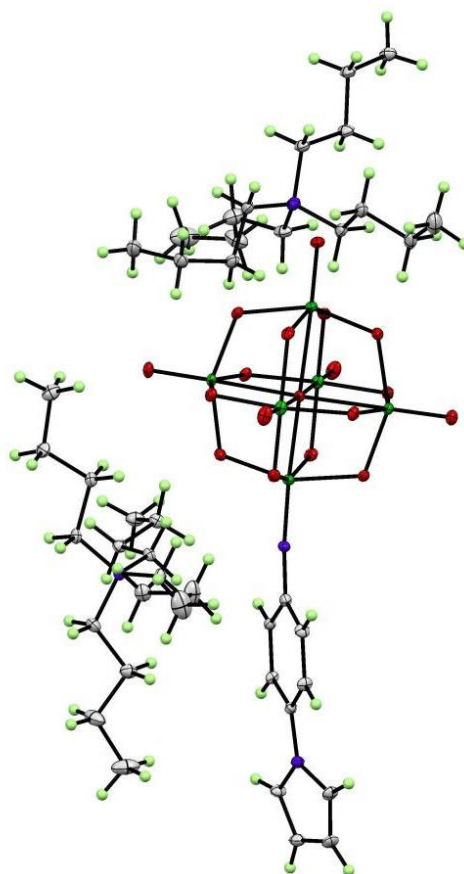
Figure 3.18 ORTEP representation of compound **3.** Thermal ellipsoids are at the 30% probability level. Colour scheme: Mo is green; O, red; C, gray; N, blue; I, purple; H atoms are represented by light-green balls.

The triple bond character of Mo^{im}-N is also seen in this derivative, the Mo-N-C bond angle is 173.3º (3) and the Mo^{im}-N distance is 1.738 (3) Å, selected characteristic bond lengths and angles are presented in table 3.3. These derivatives also show the typical imido-Lindqvist pattern of a shortened bond length from the imido-Mo (Mo^{im}) to the central oxygen (O^c), lengthened equatorial bond lengths from Mo^{im} to the oxygens bridging to the belt Mo positions (Mo^b), and a lengthened axial bond length from the trans-Mo (M^{ot}) to O^c. There is no clear pattern in Mo-N bond lengths or Mo-N-C angles with the electron donating, or accepting nature of the organic group.

Table 3.3 Selected bond lengths and angles for all structures.

	C-N-Mo^{im}	N-Mo^{im}	Mo^{im}-O^c	Mo^t-O^c	Mo^{im}-O^b (average)	Mo^t-O^b (average)
2	164.8 (3)	1.743 (4)	2.199 (3)	2.375 (3)	1.949 (3)	1.922 (3)
3	173.3 (3)	1.738 (3)	2.206 (2)	2.361 (2)	1.952 (3)	1.920 (3)
4	172.7 (11)	1.734 (11)	2.234 (8)	2.341 (8)	1.946 (8)	1.941 (9)
5	176.0 (7)	1.738 (8)	2.196 (5)	2.352 (5)	1.947 (6)	1.917 (7)
6	170.80 (4)	1.737 (4)	2.219 (3)	2.336 (3)	1.948 (3)	1.918 (3)
8	163.46 (6)	1.748 (6)	2.190 (5)	2.350 (5)	1.966 (5)	1.934 (5)
9	168.32 (3)	1.737 (3)	2.219 (2)	2.355 (2)	1.946 (2)	1.920 (3)
10	162.55 (3)	1.738 (3)	2.210 (2)	2.350 (2)	1.955 (3)	1.945 (3)
14	167.82 (5)	1.726 (7)	2.214 (6)	2.365 (6)	1.965 (5)	1.929 (5)

An analogous approach to that used to produce **2** was used to access compound **6** from 4-ethynyl aniline in 75% yield, and **7** from 4-nitroaniline in a yield of 60%. In both cases, the amine/hexamolybdate coupling proceeded cleanly, with the target compounds being the only aryl products observed by ^{1}H-NMR in crude materials (selected ^{1}H NMR data for compounds **3-4**, **6-7** and **10-12**, is presented in table 3.4). However, two or three recrystallizations were required to remove small amounts of excess hexamolybdate, accounting for losses of yield. Compounds **10-12** were synthesized using **1** (1.3 eq.), DCC (1.15 eq.), and aryl amine (1 eq.) heating at 65 ºC in dry DMSO. The decrease in the required DCC amount is due to the more strongly nucleophilic nature of these organic donors. **10** was accessed from 4-amino-*N,N*-dimethylaniline in a yield of 86%, **11** from 4-[(4-aminophenyl)ethynyl]-N,N-diphenylaniline (**P8**) in a yield of 40 %, and **12** from 4-{[4-(9H-carbazol-9-yl)phenyl]ethynyl}aniline (**P7**) in a yield of 70%. Attempts to grow crystals of **11** and **12** did not produce material suitable for single crystal X-ray diffraction, but other characterization data make their identity clear.
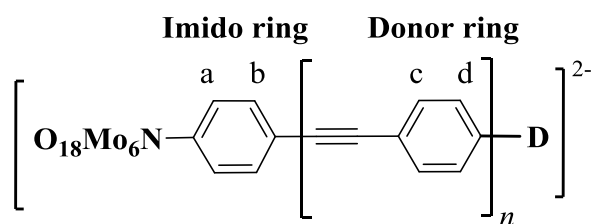
Imido ring   **Donor ring**

$$\left[O_{18}Mo_6N - \overset{a\quad b}{\bigcirc} - \equiv - \left[\overset{c\quad d}{\bigcirc} - D \right]_n \right]^{2-}$$

Table 3.4 Selected ^{1}H-NMR Data for compounds **2-4, 6-7**, and **10-12** [a].

| dication	Imido ring		Donor ring		Pyrrole, carbazole, or NPh$_2$		
	a	**b**	**c**	**d**			
2[b]	7.75	6.99	-	-	-	-	-
3[b]	7.49	7.32	-	-	7.20	6.31	-
4	7.62	7.52	7.55	7.25[c]	7.23	6.33	
5	7.46	7.20	7.26	6.63	-	-	-
6[b]	7.49	7.19	-	-	-	-	-
7[b]	7.34	8.22	-	-	-	-	-
8	7.61	7.26	7.75	8.24	-	-	-
9	7.46	7.20	7.37	6.72	-	-	-
10[b]	7.15	6.63	-	-	-	-	-
11	7.50	7.22	7.38	6.94	7.33	7.12	-
12	7.81	7.66	7.61	7.26	8.20	7.46	7.32

[a] Recorded at 300 or 500 MHz in CD$_3$CN; all values are given in ppm with respect to TMS. [b] $n = 0$. [c] Overlapped with PyH$_2$ signals.

3.2.4. Synthesis of 5, 8-9

Compound **2** was synthesized with the aim of using it to access new derivatives with further extended organic fragments (with extended donors). The goal was to form new carbon-carbon bonds via Sonogashira couplings with the iodo functionality (scheme 3.19). The Sonogashira methodology, which has been shown to be an efficient route to post-synthetic modification of organo-Lindqvist derivatives[222], was successful for

amine derivative **5** from 4-ethynylaniline in a yield of 51%, nitro derivative **8** from ethynyl-4-nitrobenzene in a yield of 60%, and dimethylamino derivative **9** from 4-ethynyl-*N,N*-dimethylanilinenylaniline in a yield of 74%. These reactions proceed quickly (0.5 hours) and cleanly due to activation of the iodo-phenyl rings by the electron withdrawing {Mo$_6$} cluster.
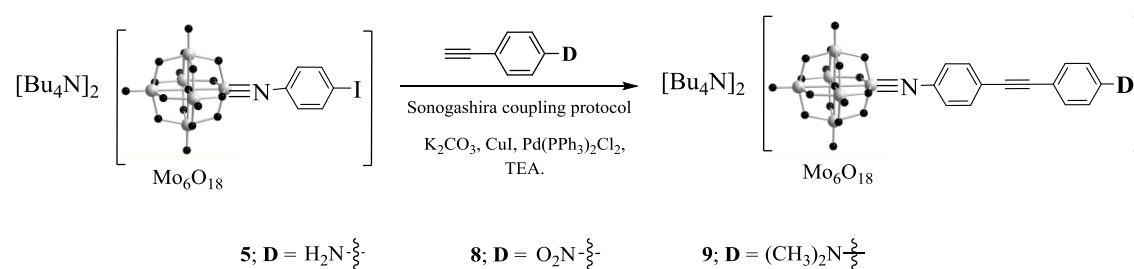
Scheme 3.19 Synthesis of extended organo-imido Lindqvist POMs using the Sonogashira protocol with **2**.

By comparison with compound **2**, the ^{1}H-NMR spectra of derivatives **5** and **9** , where an alkynyl phenyl spacer is introduced, reveal a similar trend (upfield shifts) for the proton ortho to the imido group, upon replacing of a weak electron withdrawing group (I), with the powerful amino and dimethylamino donor groups (Figure 3.20).
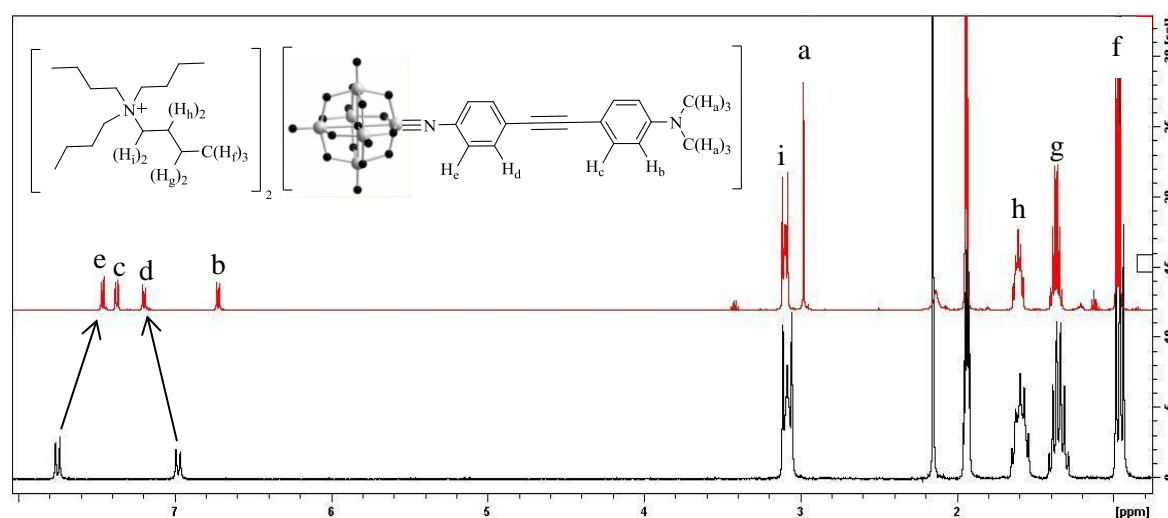

Figure 3.20 Stacked ^{1}H-NMR spectra of **9** (top) and its parent **2** (bottom), in acetonitrile-*d$_3$*.

Crystals of compounds **5**, **8** and **9** were obtained by vapour diffusion of diethyl ether into acetonitrile. The structures of these molecules were unambiguously established by X-ray crystallography: that of **5** is shown below (Figure 3.21) the others can be found in Appendix A. It is noted that significant disorder is present in the TBA cations; however, the anions are well-resolved. For instance, from the X-ray analysis of **5**, two molecules are found in the unit cell and typical features of organoimido Lindqvist compounds are observed such as a near-linear Mo^{im}-N-C bond angle and a short Mo^{im}-N distance. The two phenyl rings are significantly twisted away from the planar configuration, with a large torsion angle of 52.6°, suggesting reduced π-conjugation and a degree of electronic isolation between donor and acceptor. The π-systems of **5** and **8** both show curvature with an angle of *ca.* 168° (±8°) between the planes of the two phenyl rings. This apparent curve results from alkyne bond angles of around 175° (±1°). Similar features were seen in compound **9**; where the strong -$N(Me)_2$ electron donor group is introduced: the overall π-system is more linear (177.33° angle between the planes of the phenyl rings), but the torsion angle of 84.23° is higher. All other bond angles and lengths can be found in Appendix A.
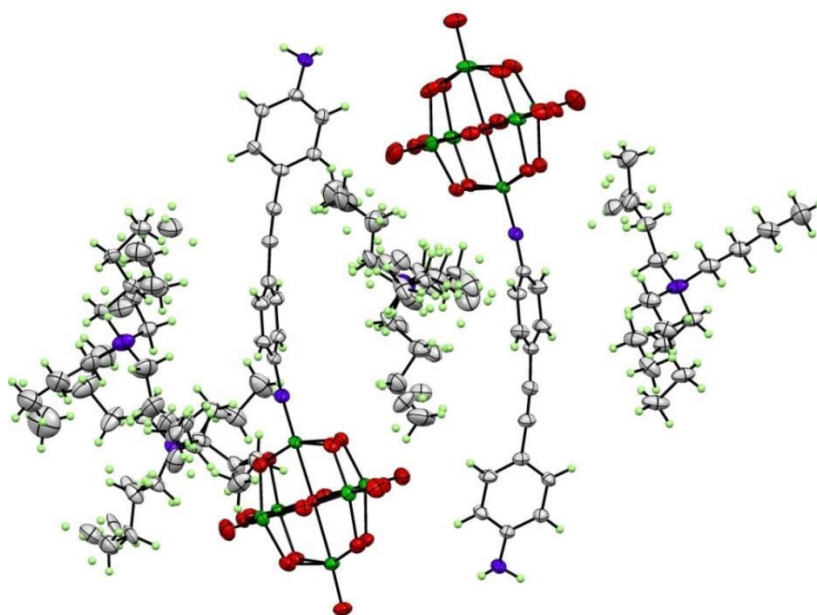

Figure 3.21 ORTEP representation of compound **5.** Thermal ellipsoids are at the 30% probability level. Colour scheme: Mo is green; O, red; C, gray; N, blue; I, purple; H atoms are represented by light-green balls.
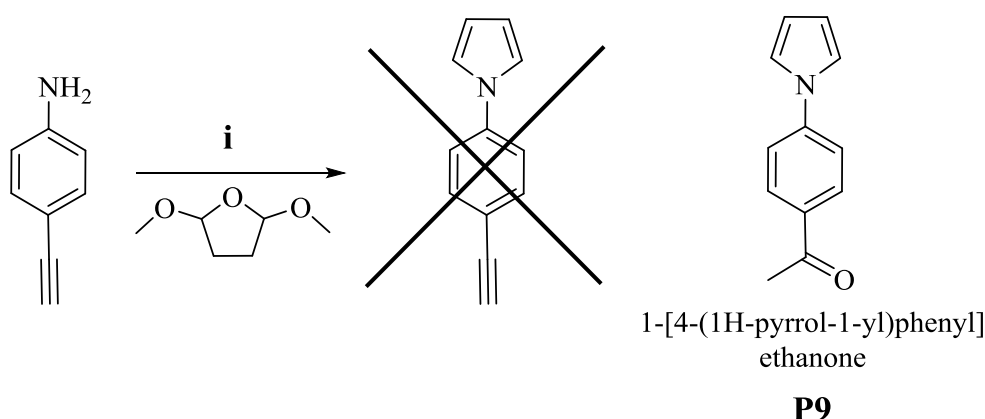
3.3. Ligand Synthesis

3.3.1. Synthesis of P1 to P4

In order to synthesize the extended pyrrole-functionalized derivative (**4**), we first tried to perform the Sonogashira coupling of derivative **6** with 1-(4-iodophenyl)-1H-pyrrole (scheme 3.22).
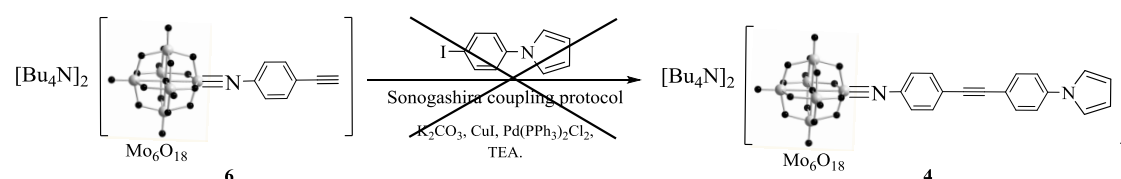
Scheme 3.22 Attempted synthesis of **4** via Sonogashira coupling protocol.

Unfortunately, our efforts to access derivative **4** proved to be unsuccessful, the ^{1}H-NMR showed only the starting material, **6**. Subsequently, we decided to approach synthesis of **4** through Sonogashira coupling of the iodophenyl imido hexamolybdate (**2**) and 1-(4-ethynylphenyl)-1H-pyrrole. To synthesize 1-(4-ethynylphenyl)-1H-pyrrole, we tried the Paal-Knorr pyrrole synthesis[207] starting from 4-ethynylaniline (Scheme 3.23). Surprisingly, ^{1}H-NMR revealed the production of 1-[4-(1H-pyrrol-1-yl)phenyl]ethanone **P9**, due to the hydration of terminal alkyne to give a methyl ketone. Support for the ^{1}H-NMR spectrum is provided by ^{13}C and DEPT experiments, which reveal the presence of ketone carbonyl signal ($\delta_C = 196.6$) and also the methyl environment ($\delta_C = 26.6$). Further purification was achieved by column chromatography to produce **P9** cleanly in a yield of 81 %. Identification and characterization of **P9** was confirmed by MS, EA, and IR.
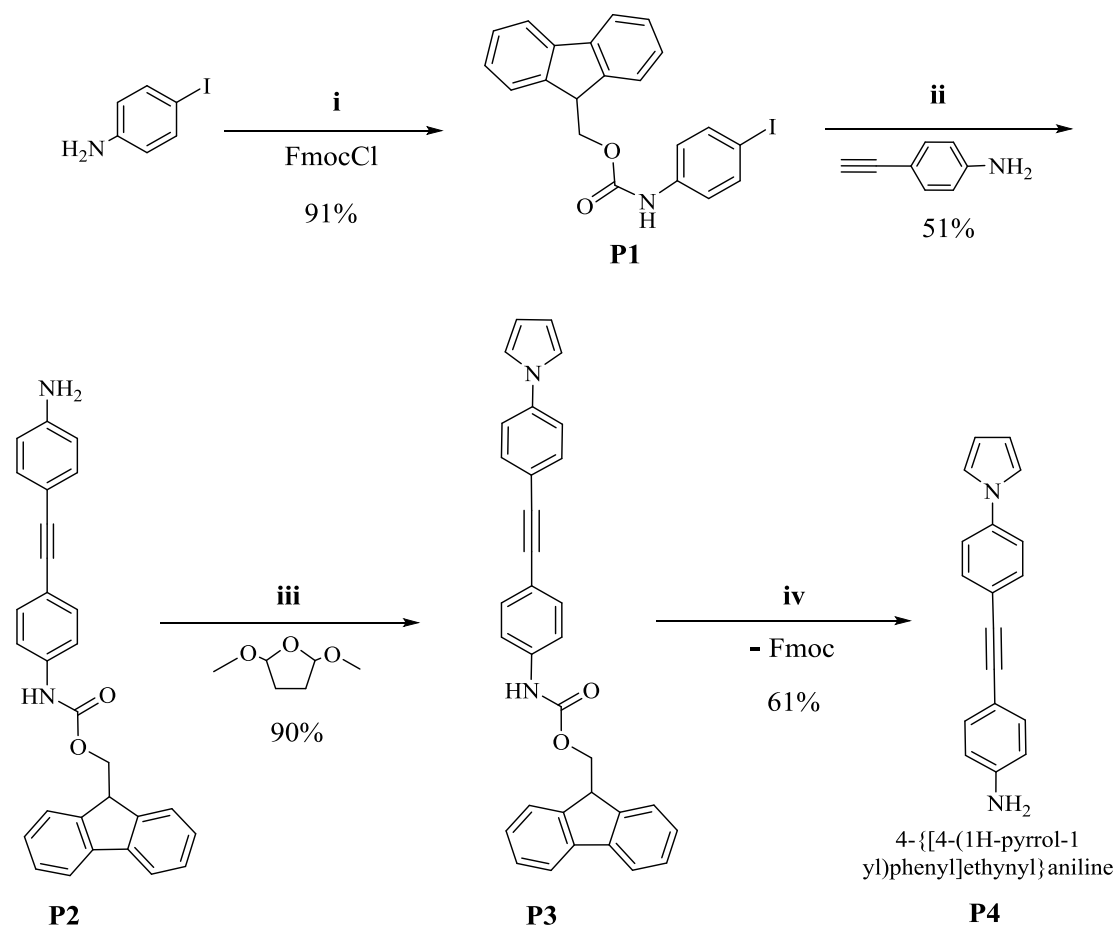
1-[4-(1H-pyrrol-1-yl)phenyl]
ethanone

P9

Scheme 3.23 Synthesis of 1-[4-(1H-pyrrol-1-yl)phenyl]ethanone **P9.** *Reagents and conditions* (**i**) AcOH, reflux at 105 °C, 2h.

Therefore, we decided to use an Fmoc protection strategy to synthesize the organic amino ligand (**P4**) first, and then use the DCC coupling to access **4**, following the synthetic routes shown in scheme 3.24. The synthesis begins with the production of **P1** which was achieved via the Fmoc protection of amines in aqueous media, following a method by Gawande and Branco.[206] This subsequently allowed us to achieve the Sonogashira coupling between **P1** and 4-ethynyl aniline successfully and cleanly to produce **P2**. The introduction of the pyrrole functionality to access **P3** was achieved by an adapted Paal-Knorr method for N-functionalised pyrroles as proposed by D'Silva and Walker.[207] The reaction proceeds as a condensation reaction with a characteristic change in colour of the reaction solution from brown to dark-red and was monitored by thin layer chromatography until the starting material had disappeared. The **P3** monomer was relatively unstable in air due to the rapid oxidation of pyrrole group; therefore, it was used directly in the final step without further purification. The final step of the reaction scheme (3.24) shows the deprotection of Fmoc group to produce **P4** by reacting with weak base (Piperidine) for 30 minutes. The yield was slightly low due to the use of column chromatography for purification.

Ligands **P1-P4** were unambiguously characterised by ^{1}H and ^{13}C-NMR, electrospray mass spectroscopy (MS), elemental analysis (EA), infrared spectroscopy (IR), and UV-vis for **P4**.

Scheme 3.24 Synthesis of 4-{[4-(1H-pyrrol-1 yl)phenyl]ethynyl}aniline **P4**. *Reagents and conditions* (**i**) H$_2$O, heat at 60 °C, 2h (**ii**) CuI, Pd(PPh$_3$)$_2$Cl$_2$, TEA, heat at 40 °C, 4h (**iii**) AcOH, reflux at 105 °C, 1h (**iv**) 15 ml of 30% Piperidine in DMF.

3.3.2. Synthesis of P5

The production of 4-(1H-pyrrol-1-yl)aniline **P5** was achieved by the copper-catalyzed Clauson–Kass reaction of 2,5-dimethoxytetrahydrofuran with amines in aqueous media proposed by Chen and co-workers (scheme 3.25).[208] The reaction proceeds smoothly, causing an observable colour change from the clear reaction mixture to yellow. The completion of the reaction was monitored by thin layer chromatography,

and final product **P5** was obtained after the purification of the crude product with column chromatography. Once again, the yield (47 %) was low due to the use of this purification. Identification and characterization of **P5** was confirmed by ^{1}H and ^{13}C-NMR, MS, EA, IR, and UV-vis spectroscopy.
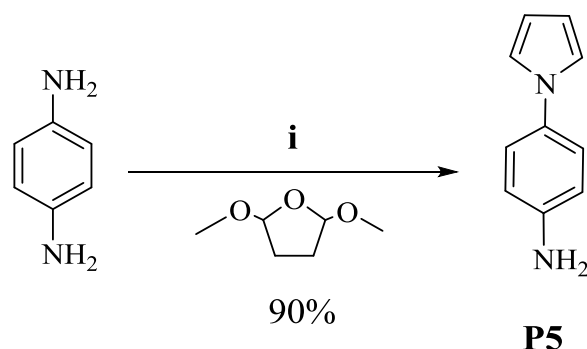

Scheme 3.25 Synthesis of 4-(1H-pyrrol-1-yl)aniline **P5.** *Reagents and conditions* (**i**) H_2O, $CuCl_2$, reflux, 2 hrs.

3.3.3. Synthesis of P6-7

The synthesis of 4-{[4-(9H-carbazol-9-yl)phenyl] ethynyl}aniline (**P7**) is outlined in scheme (3.26). Starting from carbazole, it has been possible to synthesize 9-(4-iodophenyl)-9H-carbazole **P6** by reacting with diiodobenzene in presence of Cu powder and potassium carbonate in 1,2-dichlorobenzene, refluxed at 180 ℃ for 48 hrs. However, multiple attempts to purify the product by column chromatography proved unsuccessful. Subsequently, we used Kugelrohr sublimation to purify this and isolate the product **P6** cleanly. The latter was used to access **P7** via Sonogashira coupling with 4-ethynylaniline followed by column chromatography for purification, in an excellent yield of 86 %. Compounds **P6-7** have been unambiguously characterised by ^{1}H and ^{13}C-NMR, MS, EA, IR, and for **P7** UV-vis spectroscopy.

9H-carbazole

41%

9-(4-iodophenyl)-9H-carbazole

P6

86%

4-{[4-(9H-carbazol-9-yl)phenyl]ethynyl}aniline

P7
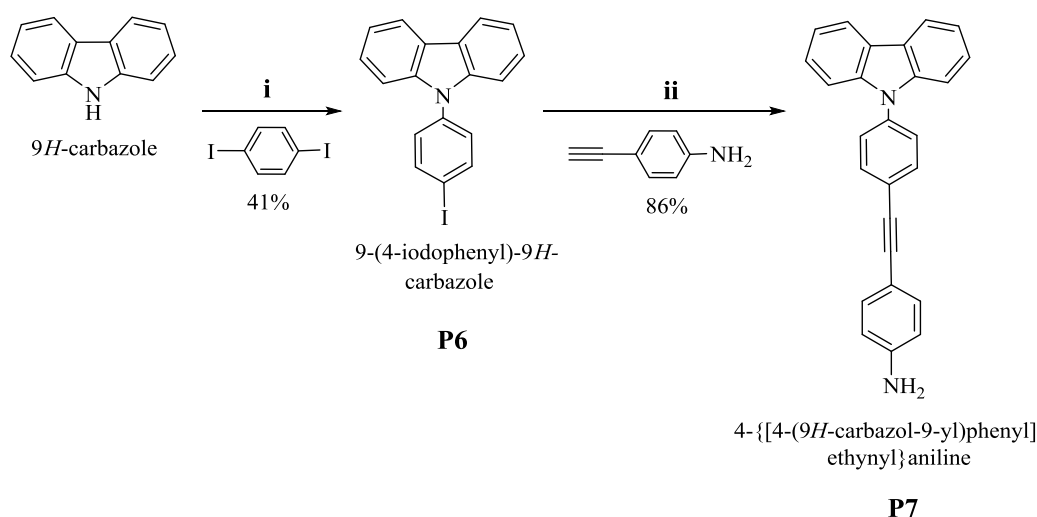
Scheme 3.26 *Reagents and conditions* (**i**) 1,4-diiodobenzene, Cu, K$_2$CO$_3$, 180 °C, 1,2-dichlorobenzene (**ii**) CuI, Pd(PPh$_3$)$_2$Cl$_2$, TEA, 47 °C, 24h.

3.3.4. Synthesis of P8

The production of 4-[(4-aminophenyl)ethynyl]-N,N-diphenylaniline **P8** was achieved once again by Sonogashira coupling between 4-bromotriphenylamine and 4-ethynylaniline in a moderate yield of 69 %, due to the use of column chromatography for purification (scheme 3.27). Identification and characterization of **P8** was confirmed by ^{1}H and ^{13}C-NMR, MS, EA, IR, and UV-vis spectroscopy.

4-bromotriphenylamine

69%

4-[(4-aminophenyl)ethynyl]-N,N-diphenylaniline

P8
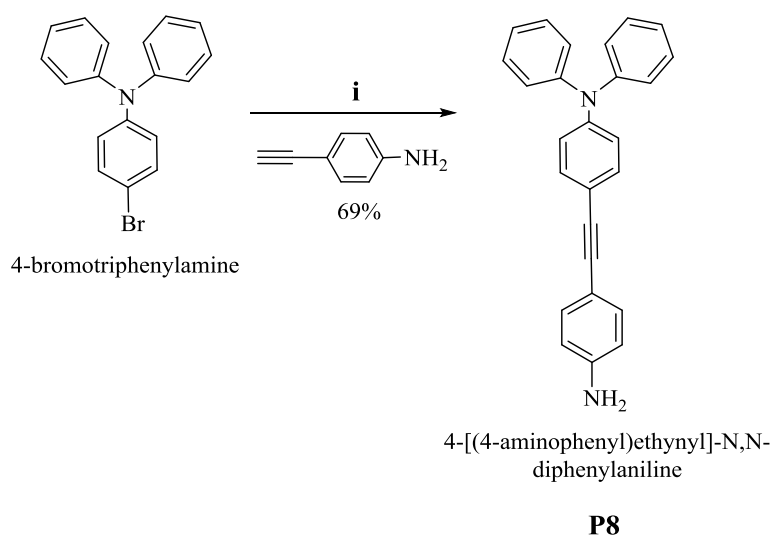
Scheme 3.27 Synthesis of 4-[(4-aminophenyl)ethynyl]-N,N-diphenylaniline **P8**. *Reagents and conditions* (**i**) CuI, Pd(PPh$_3$)$_2$Cl$_2$, PPh$_3$, TEA, reflux in THF for 96 hrs.

100

Chapter 4

Electrochemical and Optical Properties

4.1 Electrochemical Studies

4.1.1 Basic Aspects of Electrochemistry

Electrochemistry is a branch of chemistry dealing with the relationship between the electrical and chemical changes in molecules, and plays an important role in many areas of science and technology.[223,224] Electrochemical methods offer the potential to investigate chemical reactions involving electron transfer and can also be used to study the mechanisms of the electroactive species. Examples of these methods are linear sweep voltammetry, cyclic voltammetry, potential step experiments, and rotating disc electrode experiments. In a typical electrode reaction, a charge is transferred between an electrode and a studied species in solution, as illustrated in Figure (4.1).
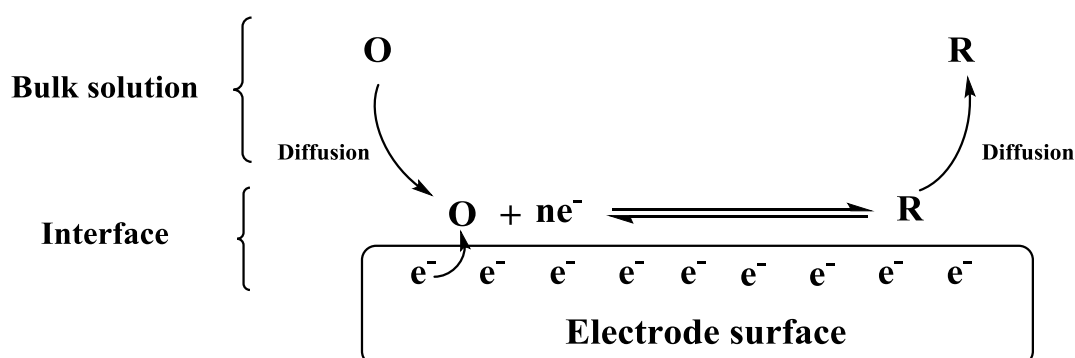
Figure 4.1 Schematic representation of an electrode reaction.

Where **O** is the oxidised form of the species, **R** is the reduced species. At a fixed potential, the system (with reversible electron transfer) will attain equilibrium defined by the Nernst equation (4.1). A current will flow for as long as the reaction continues, until the bulk concentration of **O** and **R** attain their equilibrium values, as shown in Figure (1.20).

$$E = E^{0'} + \frac{RT}{nF} \ln \frac{c_O}{c_R}$$

(4.1)

Where $E^{0'}$ is the formal potential, n is the number of electrons involved in the reaction or transferred, c_0 is the **O** concentration, c_R is the **R** concentration, R is the gas constant, F is the Faraday constant, T is the absolute temperature in Kelvin. The pre-logarithmic term becomes 0.0591 V at 298 K. In this work, two basic electrochemical techniques were used; cyclic voltammetry and chronoamperometry. These are briefly described in the following sections.

4.1.1.1 Cyclic voltammetry

Randles first reported the theoretical description for cyclic voltammetry (CV) technique in 1938.[225-227] Due to its non-destructive nature, CV has been used over several decades as one of the most effective and versatile techniques to acquire information on a wide range of both solution and surface redox processes at the thermodynamic and mechanistic levels.[228-230] In cyclic voltammetry, a three-electrode set-up is usually used with an inert working electrode, most commonly a vitreous carbon electrode, to avoid any participation by the electrode materials in the electrochemical reaction. This means that the electrode is only a heterogeneous outer sphere electron donor or acceptor. CV works by varying the potential linearly at a constant rate (the sweep rate, v) that is applied to an electroactive substance in solution and measuring the current changes as the compound is oxidised, **O**, or reduced, **R**. The potential is first set to an initial start potential, E_1, then swept at a certain scan rate to a second potential (the vertex potential, E_2) and halted. The potential is then swept backwards to the start potential, E_3, typically at the same scan rate (Figure 4.2).
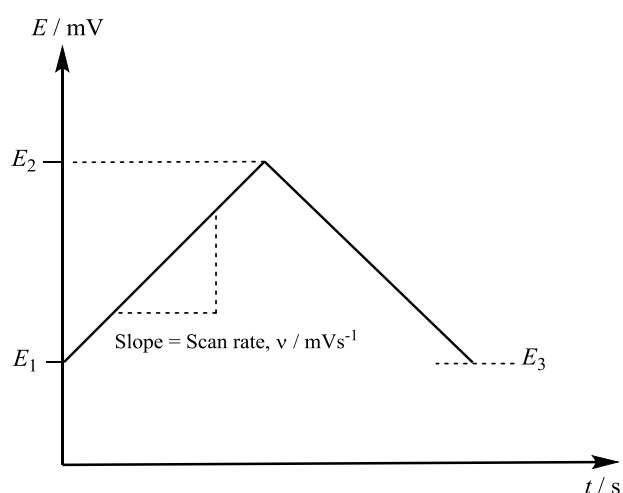
Figure 4.2 Cyclic voltammetry triangle sweep.

During the experiment, the current that results from the redox process is recorded, and then plotted as a function of the applied potential. Figure 4.3 shows the CV for a typical reversible redox species, the ferrocene (Fc) couple. In this experiment, both redox partners Fc and Fc^+ are stable on the time-scale of the experiment. Peak potentials (E_p^c and E_p^a) and the peak current (I_p^c and I_p^a) are the two sets of fundamental parameters which characterize the redox couple Fc/Fc^+.

Figure 4.3 Cyclic voltammogram of ferrocene in 0.1 M [NBu$_4$][BF$_4$] in MeCN at 100 mV s^{-1} vs Ag/AgCl.

The experimental potential can be calculated for these parameters using equation (4.2).

$$E_{1/2} = \frac{E_p^{\ a} + E_p^{\ c}}{2}$$
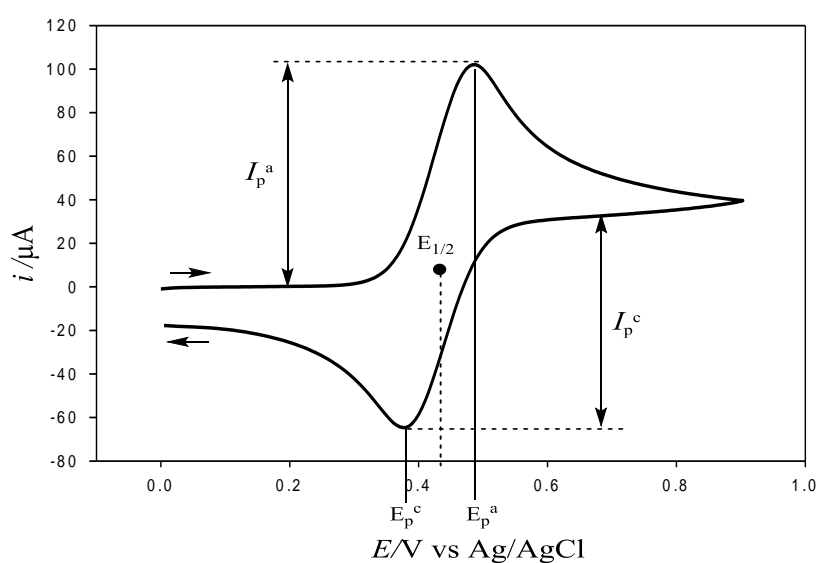
(4.2)

The magnitude of the peak potential separation $\Delta E = |E_p^a - E_p^c|$ at 100 mV s^{-1} is close to 60 mV, which is directly related to the number of electrons (n) involved in the primary electron-transfer process, as expressed in equation (4.3). For a one-electron reversible redox process, ΔE will be 59 mV. In the case of surface confined species and reversible redox process, ΔE_p is close to zero.

$$\Delta E_p = \left| E_p^{\ a} - E_p^{\ c} \right| = \frac{59}{n} \ mV$$

(4.3)

The ratio I_p^c/I_p^a can reveal some information whether the process is reversible or irreversible (in the case that the resistivity is low), for a fully reversible system, such as ferrocene this value is close to unity. Moreover, I_p increases linearly with $v^{1/2}$ for species under diffusion control, as illustrated in Figure (4.4), right. Figure (4.4), left, shows the current potential response for a range of scan rates, v, between 25–250 mV s^{-1}. If the redox couple is adsorbed on the surface, the I_p increases linearly with v instead of $v^{1/2}$ and hence the shape of the CVs will be completely different form that obtained from the solution process.
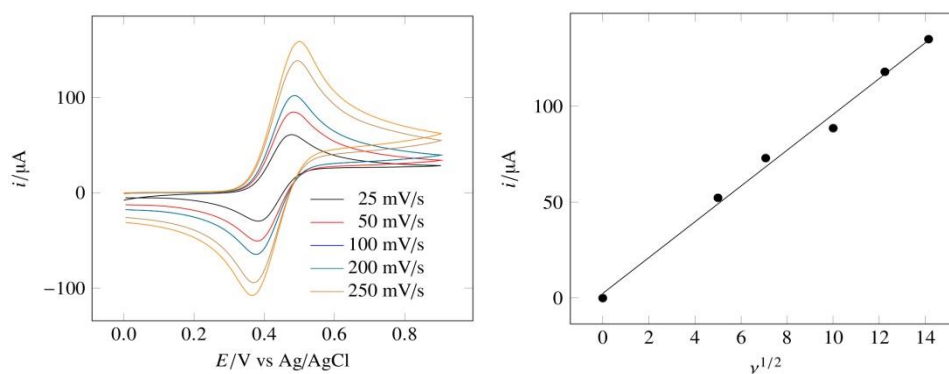

Figure 4.4 Left: CVs of ferrocene recorded at various scan rates vs Ag/AgCl in 0.1 M [Bu$_4$N][BF$_4$] in MeCN at 25 °C; Right: A plot of current peak I_p^a vs the square root of scan rate ($v^{1/2}$) for ferrocene oxidation.

4.1.1.2 Chronoamperometry

Chronoamperometry, or Potential Step Voltammetry is another useful electrochemical technique in which the potential is stepped from a value where no electro-activity is observed to a value where the current is limited by mass-transfer. The resulting current from this faradaic process is monitored as a function of time, as shown in Figure (4.5). Cottrell equation (equation 4.4) can be used to calculate the current, which is now related to the bulk reactant concentration.

$$/i/ = \frac{nFA\,|Reactant|\,\sqrt{D}}{\sqrt{\pi}\,\sqrt{t}}$$

(4.4)

The current rises instantaneously after the change in voltage and then begins to decrease as the active species, O in case of reduction or R in case of oxidation, is consumed as a function of time until reaching a plateau at a value close or equal to zero when the conversion is completed.

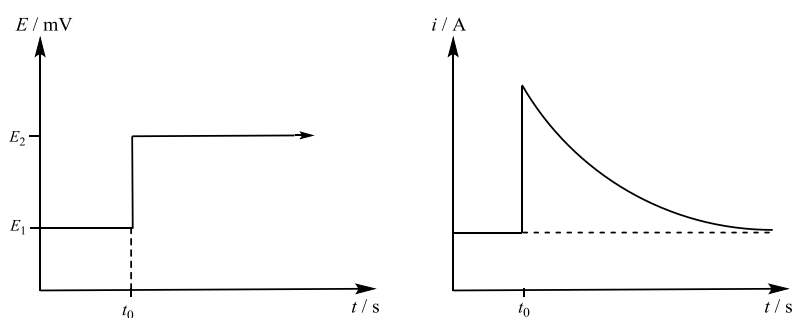**Figure 4.5** A step in the applied potential results in decay of the current.

4.1.2 Results and Discussion

4.1.2.1 Electrochemistry of imido-Lindqvist derivatives

Electrochemical measurements were performed in 0.1 [NBu$_4$][BF$_4$]-anhydrous acetonitrile at room temperature under an atmosphere of argon versus Ag/AgCl, with ferrocene as an internal reference ($E_{1/2}$ = 0.46 V vs Ag/AgCl). These measurements

were carried out in order to determine the redox potentials for the new synthesized series of organoimido Lindqvist derivatives (**2-14**), and to investigate the effect of different donor substituents on the electrochemical properties of the parent hexamolybdate cluster, **1**. Table 4.1 shows the results of these measurements, along with data for the known compound (**1**, hexamolybdate) for comparison purpose.

Table 4.1 Summary of reduction potentials ($E_{1/2}$) of compounds **1** to **14**.

Compound	$E_{1/2}$ /V[a]	ΔE / mV
1	-0.315	69
2	-0.476	63
3	-0.500	63
4	-0.496	61
5	-0.476	63
6	-0.499	61
7	-0.434	71
8	-0.486	64
9	-0.498	61
10	-0.575	71
11	-0.503	64
12	-0.503	64
13	-0.615[b]	71
14	-0.553[b]	74

[a] Using 10^{-3}- 10^{-5} M of analyte in 0.1 [NBu$_4$][BF$_4$]-anhydrous acetonitrile; scan rate of 100 mV/s ; using a glassy carbon working electrode; ferrocene as an internal reference ($E_{1/2}$ = 0.46 V vs Ag/AgCl). [b] Presence of unreacted **1** (hexamolybdate), probably due to hydrolysis.

As expected for POM species,[231] each compound shows a fully reversible electron transfer process on the CV time scale (Figure 4.6), as shown by peak separations near to the 60 mV ideal (note that the separation for Fc/Fc$^+$ under these conditions is in the range of 60 to 65 mV). This suggests that these materials have the potential to be used as molecular switches in which reduction of the {Mo$_6$} unit would turn off the charge transfer transition, decreasing the value of β.
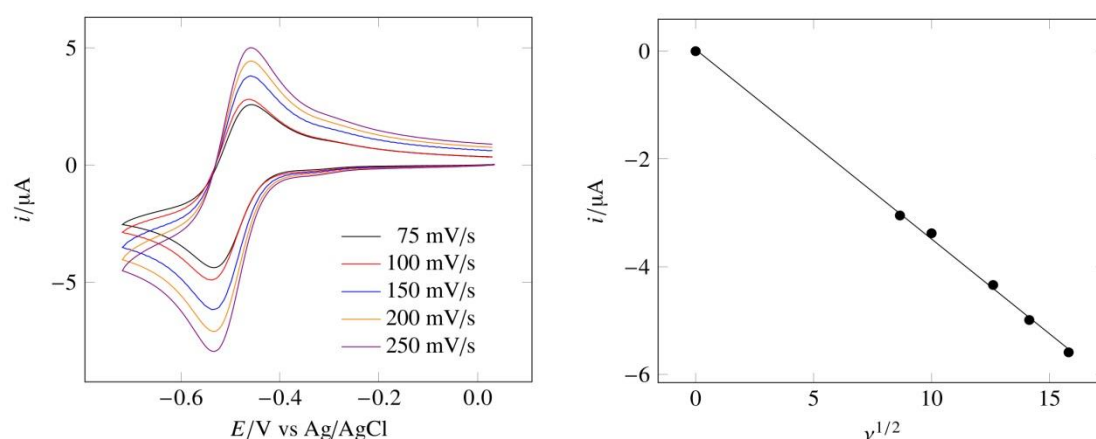
Figure 4.6 Left: CVs of **3** recorded at various scan rates vs Ag/AgCl in 0.1 M [Bu$_4$N][BF$_4$] in MeCN at 25 °C; Right: A plot of current peak I_p^c vs the square root of scan rate ($v^{1/2}$) for reduction of **3**.

Upon derivatization, there is a *ca.* 180 mV cathodic shift in the $E_{1/2}$ for reduction from **1** to most of the derivatives as seen in Figure 4.7 for **1** and **3**. This confirms that the derivative species are more electron rich, and that there is strong communication between hexamolybdate and the imido-aryl substituents which gives rise to the increased electron density on the POM.

Figure 4.7 Cyclic voltammograms of **1** (black) and **3** (blue) recorded at 100 mV/s in 0.1 M [NBu$_4$][BF$_4$]-acetonitrile versus Ag/AgCl.
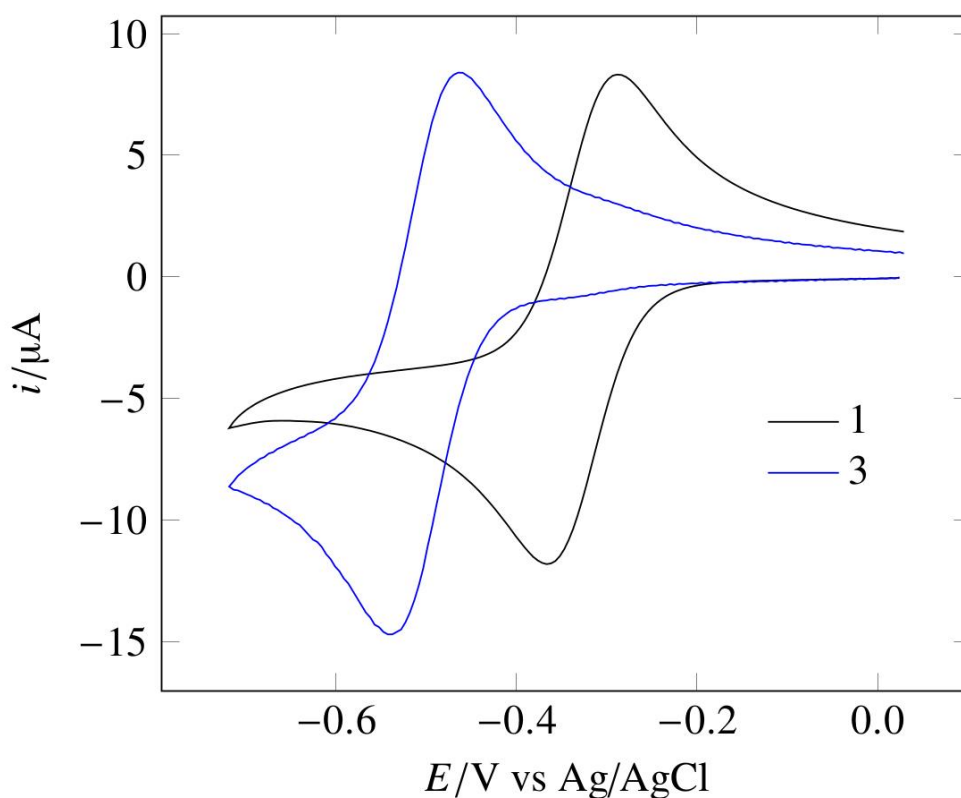
In compound **10**, containing a strong electron donor group (NMe$_2$) and the shorter phenyl bridge, there is a *ca.* 141 mV cathodic shift in reduction potential compared to its nitro analogue **7** (NO$_2$), and *ca.* 250 mV from **1**. This consistent with replacement of a strong electron acceptor group, with a strong electron donor group, which is in agreement with typical purely organic donor acceptor (A/D) systems, where increasing the strength of a donor is reflected in cathodically shifted reductions of the acceptor.[232] Compound **10** also shows a *ca.* 65 mV negative shift in reduction potentials compared to phenyl-bridged compounds **3** (D = Py) and **6** (D = alkyne), and a similar trend is seen when moving from weak electron acceptor iodo (**2**), and from **7** (NO$_2$) to moderate electron donor Py (**3**). In other words, compounds based on the

short phenyl bridge show a clear relationship between donor/acceptor strength and the reductions of the $\{Mo_6\}$ unit, consistent with strong donor/acceptor communication.

However, derivatives **4** (Py), **5** (NH_2), **8** (NO_2), **9** (NMe_2)**, 11** (NPh_2), and **12** (Cbz), where an additional ethynyl phenyl spacer is introduced, show a minimal difference in reduction potential (±15 mV) between one another (Table 4.1). This indicates that there is a degree of electronic isolation between the donor (organic groups) and POM acceptor, consistent with the NMR and X-ray data. This can be clearly seen in the comparison between **8** and **9** where the difference in reduction potential (12 mV) when the strong electron donor NMe_2 is replaced with the strong electron acceptor group NO_2 is far smaller than in the shorter systems. This suggests that in the longer derivatives the POM acceptor level is quite isolated from the donor, in contrast to many classical D/A organic systems where increasing the electron donor strength would result in cathodic shift of the reduction potential of the acceptor unit.[232,233]

Compound **14** shows an additional wave at less negative potentials than the derivative itself; this can be ascribed to (*ca.* 5 %) **1** (due to hydrolysis).   Its CV is presented in Figure 4.8, shows two reduction waves; the first one at -0.553 V attributed for **14;** more negatively shifted compared to all aryl-imido derivatives except **10**, and *bis-* derivative **13.** This can be explained as the aliphatic imido bond is more electron rich, which is consistent with the literature.[234,235] The second wave at -0.315 V is ascribed to **1**. The elemental analysis results were consistent with the product being pure, so it seems likely that a small amount of hydrolysis is occurring rapidly upon dissolution.
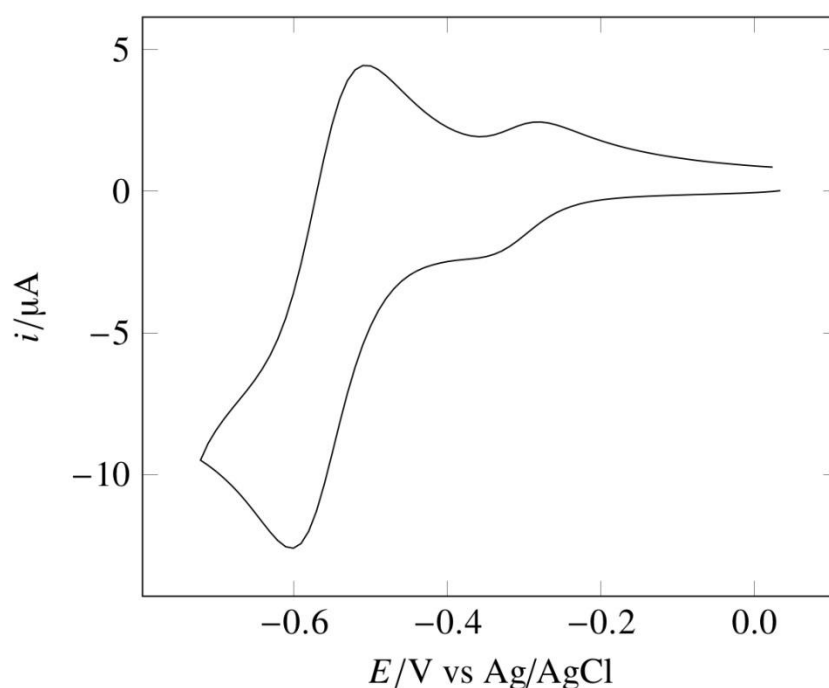
Figure 4.9 Cyclic voltammograms of **14** recorded at 100 mV/s in 0.1 M [NBu$_4$][BF$_4$]-acetonitrile versus Ag/AgCl.

Compound **13**, the *bis*-imido aryl-4-iodo hexamolybdate derivative, shows the most cathodic shift among other derivatives at -0.615 V due to the increased electron density accompanying incorporation of the ligand (NArI) compared to **2** *(mono-derivative)*. This finding is consistent with findings of past studies by Maatta that reported the synthesis and the electrochemical studies of multi-substituted organoimido Lindqvist derivatives.[234,236] Similar to compound **14**, the CV of **13** shows a second wave attributed to **1**; however, the EA results were consistent with the product being pure. Again, it seems likely that a degree of hydrolysis occurs rapidly upon dissolution.

4.2 Electronic Absorption Spectroscopy

The electronic spectra for compounds **1** to **15** have been measured in acetonitrile at ambient temperature and the results can be seen in Table 4.2. All derivatives, except **1**, showed one intense visible/near-UV absorption band caused by a ligand-to-POM

charge-transfer process (LPCT). They also show UV absorption bands, caused by the overlapping of O-to-Mo charge transfer (CT) in the $\{Mo_6\}$ acceptor unit and intra-ligand ($\pi \rightarrow \pi^*$) processes in the appended organic group, which is in line with earlier literature.[140]

Table 4.2 UV-vis absorption data for compounds **1-15** in acetonitrile at 25 ºC.

Compound	λ_{max} / nm[a] (ε, 10^3 M^{-1} cm^{-1})	E_{max} (eV)	assignment
1	223.0 (24.9)	5.56	O$\rightarrow$Mo
	261.0 (13.4)	4.75	O$\rightarrow$Mo
	323.0 (7.1)	3.84	O$\rightarrow$Mo
2	242.0 (37.0)	5.12	O$\rightarrow$Mo and $\pi\rightarrow\pi^*$
	270.0 (32.1)	4.59	O$\rightarrow$Mo and $\pi\rightarrow\pi^*$
	355.0 (27.0)	3.49	LPCT
3	223.0 (39.6)	5.56	O$\rightarrow$Mo and $\pi\rightarrow\pi^*$
	281.0 (28.2)	4.41	O$\rightarrow$Mo and $\pi\rightarrow\pi^*$
	371.0 (32.3)	3.34	LPCT
4	290.0 (40.1)	4.28	O$\rightarrow$Mo and $\pi\rightarrow\pi^*$
	386.0 (43.8)	3.21	LPCT
5	281.0 (39.2)	4.41	O$\rightarrow$Mo and $\pi\rightarrow\pi^*$
	406.0 (35.8)	3.05	LPCT
6	264.0 (36.2)	4.69	O$\rightarrow$Mo and $\pi\rightarrow\pi^*$
	358.0 (27.0)	3.46	LPCT
7	216.0 (38.3)	5.74	O$\rightarrow$Mo and $\pi\rightarrow\pi^*$
	254.0 (26.3)	4.88	O$\rightarrow$Mo and $\pi\rightarrow\pi^*$
	287.0 (20.3)	4.32	O$\rightarrow$Mo and $\pi\rightarrow\pi^*$

	370.5 (30.2)	3.35	LPCT and L→NO$_2$
8	241.0 (36.0)	5.14	O→Mo and π→π*
	269.0 (29.9)	4.60	O→Mo and π→π*
	389.0 (49.6)	3.18	LPCT and L→NO$_2$
9	247.5 (36.2)	5.02	O→Mo and π→π*
	292.0 (44.5)	4.24	O→Mo and π→π*
	421.0 (41.2)	2.94	LPCT
10	221.0 (37.5)	5.61	O→Mo and π→π*
	258.0 (30.6)	4.80	O→Mo and π→π*
	424.0 (32.0)	2.92	LPCT
11	292.0 (41.2)	4.28	O→Mo and π→π*
	326.5 (36.2)	3.74	O→Mo and π→π*
	414.0 (45.3)	2.98	LPCT
12	226.5 (70.4)	5.28	O→Mo and π→π*
	291.5 (48.4)	4.25	O→Mo and π→π*
	326.5 (31.3)	3.78	O→Mo and π→π*
	341.0 (33.7)	3.63	O→Mo and π→π*
	384.5 (43.4)	3.20	LPCT
13	228.0 (39.1)	5.43	O→Mo and π→π*
	260.5 (38.0)	4.76	O→Mo and π→π*
	354.0 (26.6)	3.50	LPCT
14	214.5 (40.0)	5.78	O→Mo and π→π*
	337.0 (7.0)	3.67	LPCT
15	262.5 (64.0)	4.72	O→W, π→π*, and LPCT

Generally, the energy of the LPCT band decreases as the donor strength increases, which depends upon the donor-based HOMO and the acceptor-based LUMO energies. Within these derivatives, the energy of the HOMO is expected to increase as the electron donor strength increases, while (based on the electrochemical results) the LUMO energy is expected to remain approximately constant in the majority of these chromophores, illustrated in Figure 4.10.
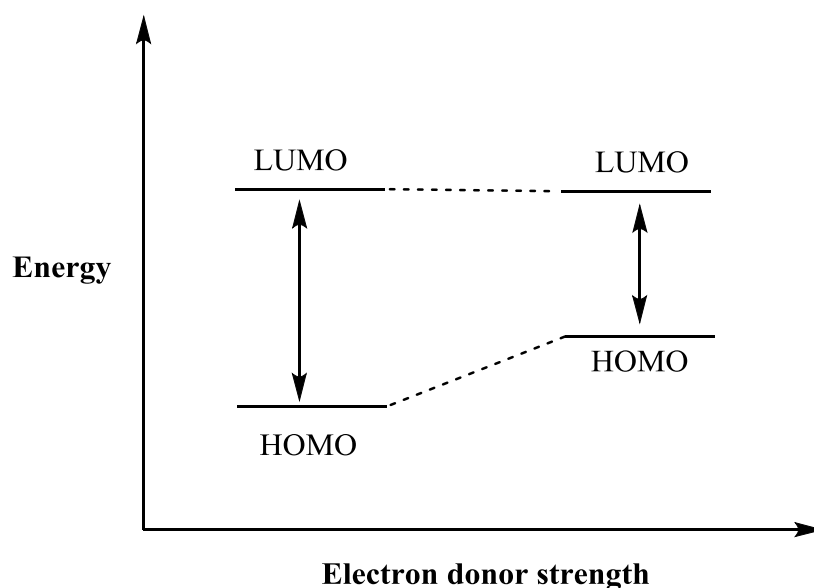

Figure 4.10 Schematic representation showing the changes in HOMO and LUMO energies caused by varying the electron donor strength.

4.2.1 Effects of the introduction of imido bond

The spectrum of **1** (black trace, Figure 4.11) shows two high energy peaks, at 223 and 261 nm associated with O-to-Mo CT, and a weaker lower energy shoulder at 323 nm. On the other hand, compound **2** (red trace, Figure 4.11), where the 4-iodophenylimido segment is introduced, also shows these high energy features; which will result from overlapping O-to-Mo and intra-ligand ($\pi \rightarrow \pi^*$) processes. It also shows a new intense band at lower energy of λ_{max} 355 nm, compared to **1**. By comparison to parent 4-iodoaniline (blue trace, Figure 4.11), the latter band is not present in the parent amine, and is ascribed to LPCT process. Notably, the molar extinction coefficient (ε) of this

band is high (27.0×10^3 M^{-1} cm^{-1}), suggesting strong coupling between the POM and the organic group, just like the NMR data. The explanation of this bathochromic shift after the introduction of the N-imido bond in these systems is the electron-withdrawing nature of the (Mo≡N) bond that also adding the {Mo$_6$} unit provides a new lower energy LUMO to the system leading to this effect. A similar trend is seen in all of the imido derivatives, upon the formation of the imido-bond.
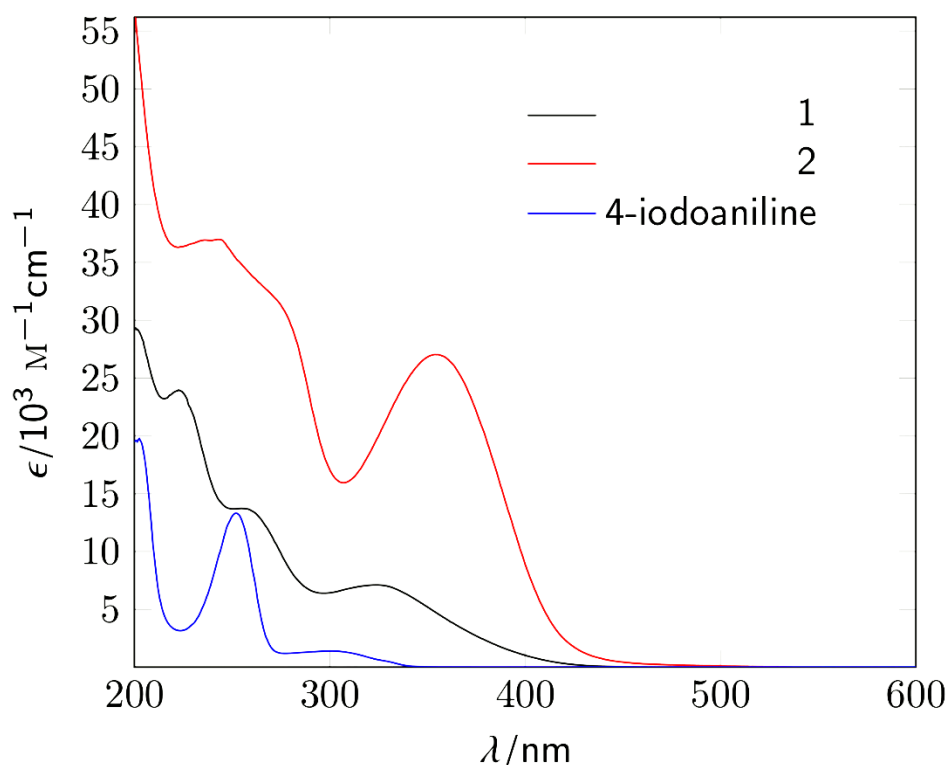

Figure 4.11 UV-visible spectra of [NBu$_4$]$_2$[Mo$_6$O$_{19}$] (**1**, black), and compound **2** (red), and 4-iodoaniline (blue) in acetonitrile at room temperature.

4.2.2 Effects of the donor and acceptor strength on the LPCT transitions

4.2.2.1 Effects of acceptor

Inductive (2) acceptor versus alkyne (6), and resonance acceptor (NO$_2$) functionalities (7)

When comparing compound **2** with **6** (Figure 4.12), where an inductive electron-withdrawing group (Iodo-) is replaced with ethynyl functionality (triple bond-conjugated group), it is clear that the energy of the LPCT band decreases, more red shift. This is due to the bigger π-system and resulting from introduction of the ethynyl group into such systems. Moreover, the electrochemical results suggest that the ethynyl group is less electron withdrawing than iodo, making the phenyl ring a better donor and helping red-shift the transition.
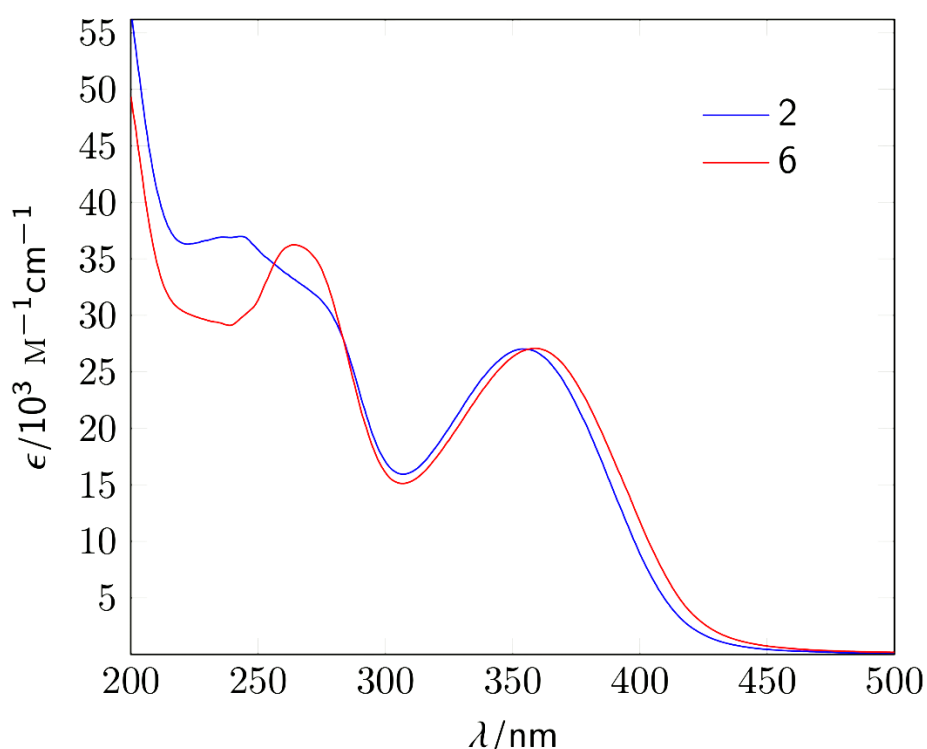

Figure 4.12 UV-visible spectra of compound **2** (blue), and **6** (red) in acetonitrile at room temperature.

The replacement of an electron donor group with an acceptor group in an A-π-D system might be expected lead to diminish the ICT bands, establishing an A-π-A configuration. Surprisingly, however, compound **7** shows similar features to other A-π-D organoimido systems, although it contains on both ends electron-accepting groups (POM and NO_2). This effect is illustrated in Figure 4.16. A reasonable explanation is that there is a charge-transfer transition from the overlapping L→NO_2

and LPCT processes resulting in such an intense, and slightly red shifted band. In addition, in this system the LUMO level of the POM is lowered in energy by communication with NO_2, which could red-shift transitions from the phenyl provided these donor levels are not lowered so much by NO_2. It also shows the high-energy bands resulting from the overlapping of O-to-Mo and intra-ligand ($\pi \rightarrow \pi^*$) processes.
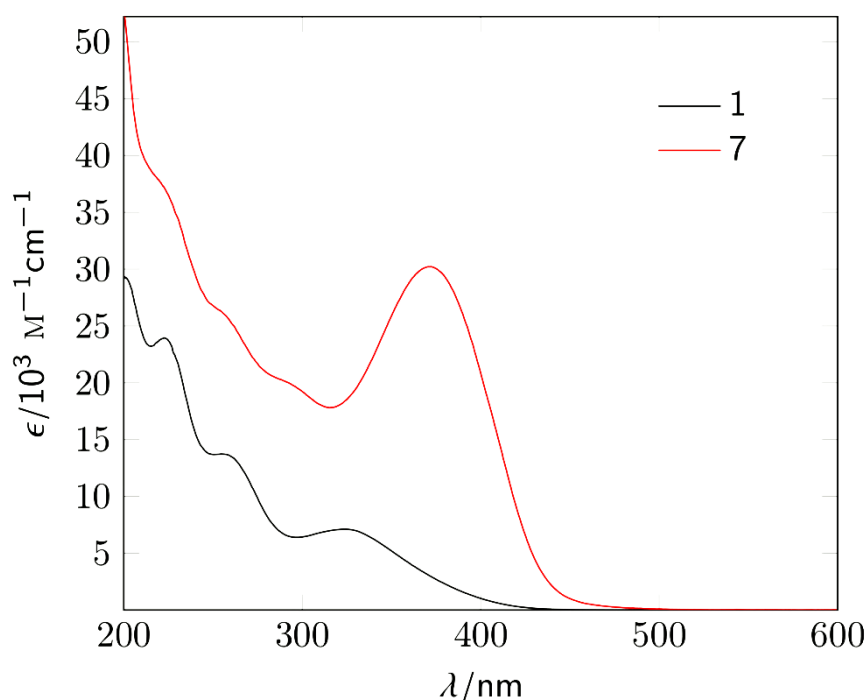

Figure 4.16 UV-visible spectra of compound **1** (black), and **7** (red) in acetonitrile at room temperature.

4.2.2.2 Effects of donor strength

In order to obtain higher β values, the strength of the electron donor is investigated, by introducing strong electron donor groups such as amino (NH_2), dimethylamino (NMe_2), diphenylamino (NPh_2), and moderate electron donor groups such as pyrrole (Py) and carbzole (Cbz) functionalities into these organoimido chromophores.

4.2.2.2.1 Short A-π-D systems

Replacement of Iodo with Py

The replacement of a weak electron withdrawing (Iodo-) with a weak electron donor (Py) results in a decrease in the energy of the LPCT (bathochromic shift behaviour) from 3.49 eV (355 nm) to 3.34 eV (371 nm), similar to the classic behaviour expected for charge transfer chromophores,[237,238] shown in Figure 4.13. It is clearly seen from Figure 4.13 that the intensity of this band is also increased (by *ca.* 20%), due to the π-conjugation effect of the pyrrole unit.
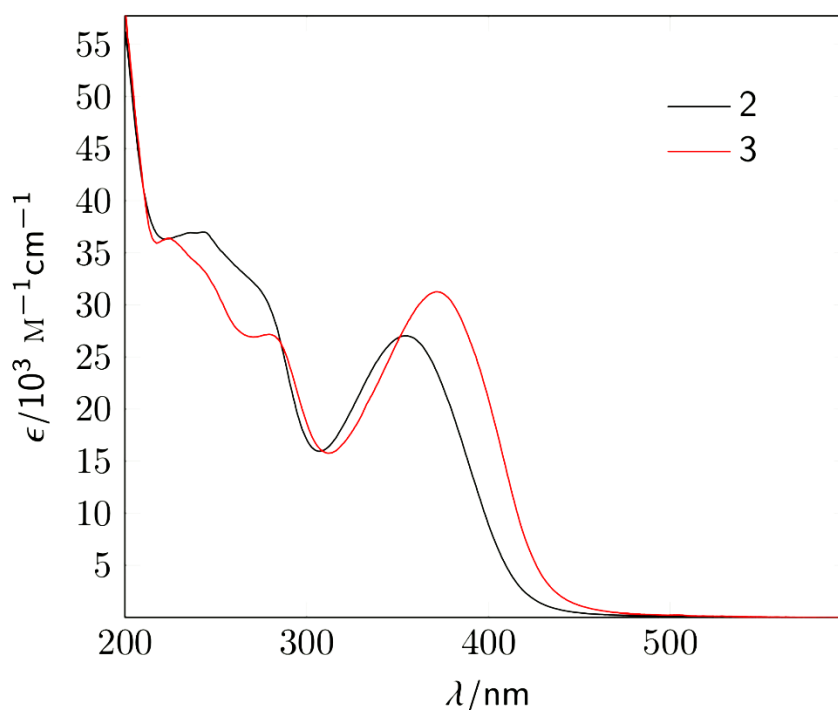

Figure 4.13 UV-visible spectra of compound **2** (black), and **3** (red) in acetonitrile at room temperature.

Replacement of Py with NMe$_2$

Moving from Py, weak electron donor (black trace, Figure 4.14), to more strongly NMe$_2$ electron donor group (red trace, Figure 4.14), causes *ca.* 53 nm (0.42 eV) red shifting of the LPCT, from 371 to 424 nm, consistent with the classical donor-

acceptor behaviour.[239,240] This confirms that the NMe_2 group is a better electron donor than Py and can therefore be expected to increase the first hyperpolarizability β.
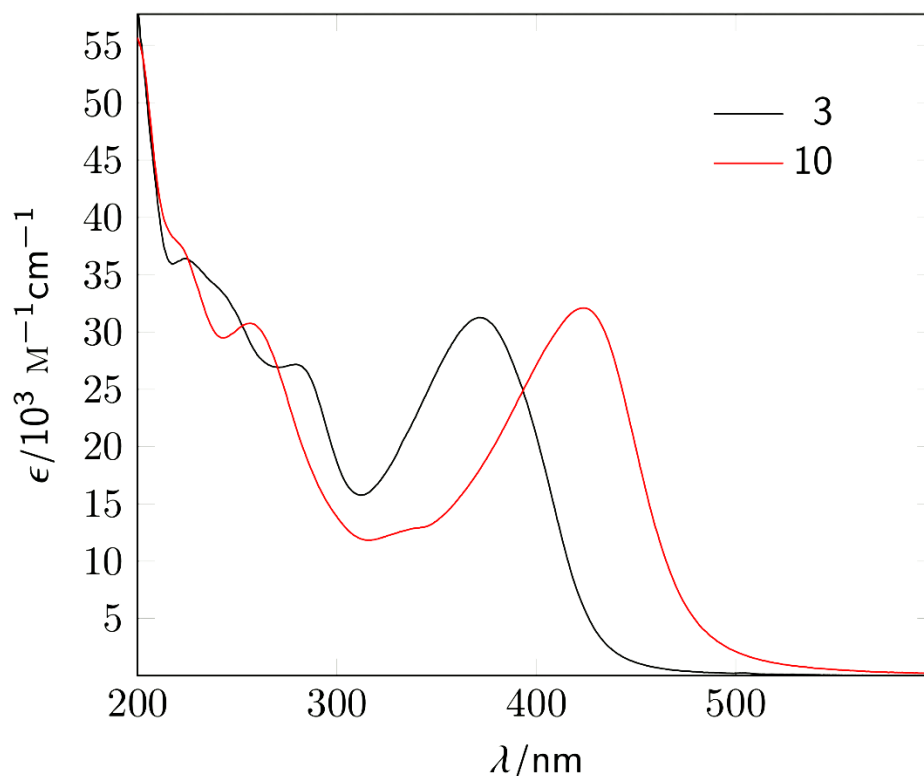

Figure 4.14 UV-visible spectra of compound **3** (black), and **10** (red) in acetonitrile at room temperature.

Introduction of aliphatic-linker pyrrole

When comparing compounds **3**, and **14** (Figure 4.15), it is clear that when the aryl spacer is replaced by aliphatic chain the energy of the LPCT band increases, and shows very similar features to underivatized hexamolybdate (**1**). This demonstrates that direct charge-transfer from the imido-N bond is not mainly responsible for the LPCT band; there must be a contribution from the strong d-π interactions between the hexamolybdate framework and the π-conjugated aryl group.
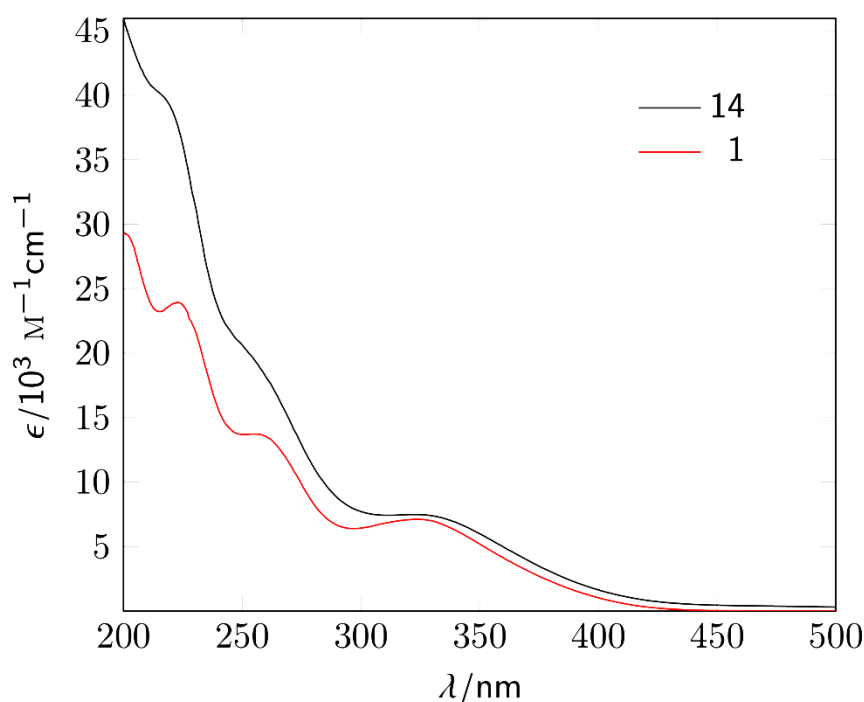
Figure 4.15 UV-visible spectra of compound **14** (black), and **1** (red) in acetonitrile at room temperature.

4.2.2.2.2 Long A-π-D systems

Replacement of Py with NMe$_2$, NH$_2$, NPh$_2$, and Cbz

By comparison with short systems of compounds **3**, and **10**, a similar trend is seen in the analogous extended systems of **4**, and **9** by replacing Py with NMe$_2$ group. A red shift of the LCPT band from 386 nm to 421 nm can be seen in Figure 4.16. However, in compound **4** the π-conjugation of Py group intensifies this band, consistent with classical donor-acceptor behaviour.
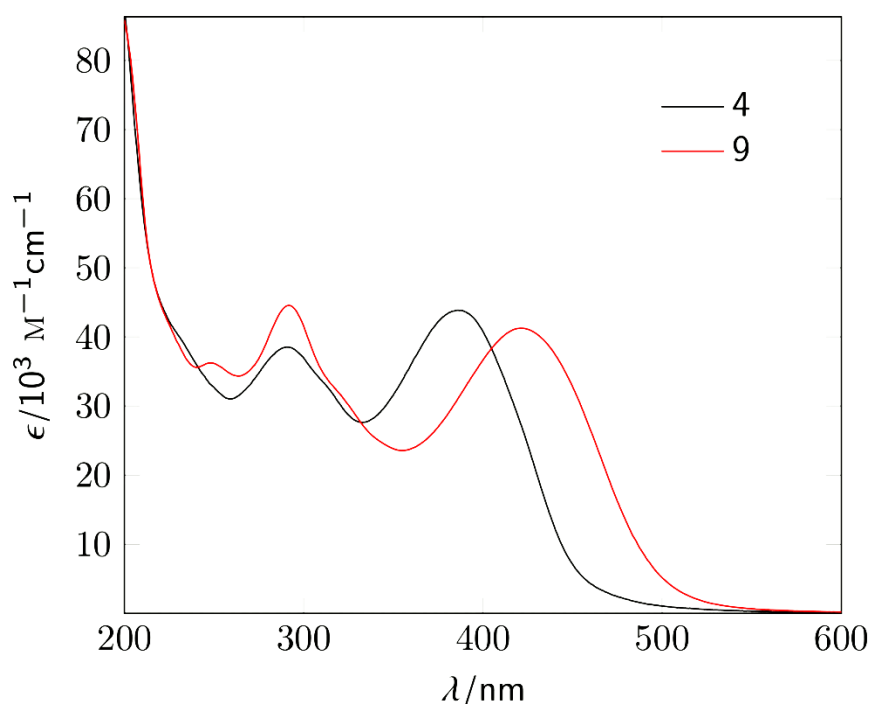
Figure 4.16 UV-visible spectra of compound **4** (black), and **9** (red) in acetonitrile at room temperature.

When comparing compounds **5**, **9**, **11**, and **12**, which have NH_2, NMe_2, NPh_2, and Cbz donor functionalities respectively, it is noticed that the energy of the LPCT decreases as follows: **9 (NMe_2)** < **11 (NPh_2)** < **5 (NH_2)** < **12 (Cbz)**. This effect is illustrated in Figure 4.17 for these chromophores. Compound **9** has the lowest LPCT energy, λ_{max} of 421 nm (2.94 eV) with molar extinction coefficient (41.2×10^3 M^{-1} cm^{-1}), but **11** shows more intense and higher energy band than **9** of λ_{max} of 414 nm (2.99 eV) with molar excitation coefficient (45.3×10^3 M^{-1} cm^{-1}) due to its large π-character, shown in Figure 4.18. This behaviour of the LPCT in **9** is the expected result, and suggests that **9** should show the highest second order NLO response.

12 (Cbz-functionalized derivative) shows 4 high energy bands ascribed to intra-ligand ($\pi \rightarrow \pi^*$) processes of the π-conjugated bridge and carbazole group and also shows the highest LPCT band energy of λ_{max} of 384 nm among the other three derivatives.

Despite its large π-character, **12** seems to be a less efficient donor. The reason for this is that the nitrogen lone pair is less available and is conjugated (involved) with the carbazole π-system.
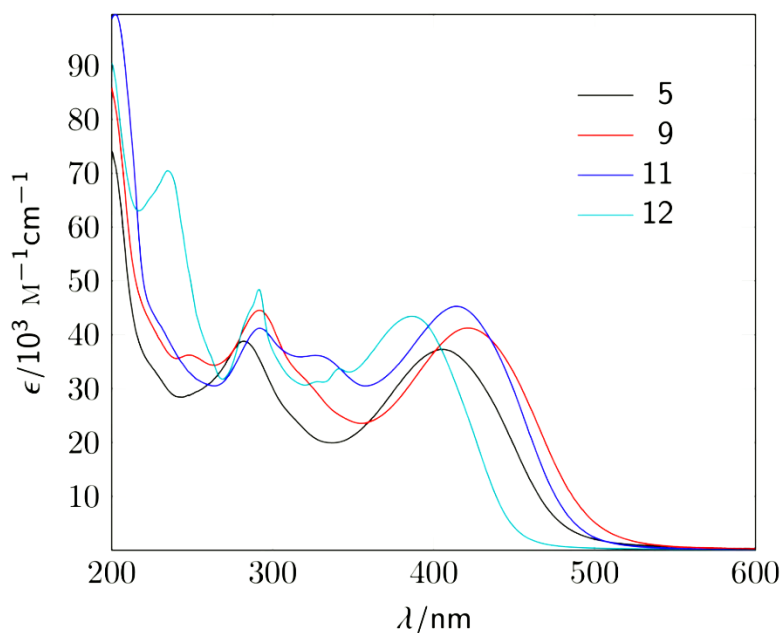

Figure 4.17 UV-visible spectra of compound **5** (black), **9** (red), **11** (blue), and **12** (green) in acetonitrile at room temperature.
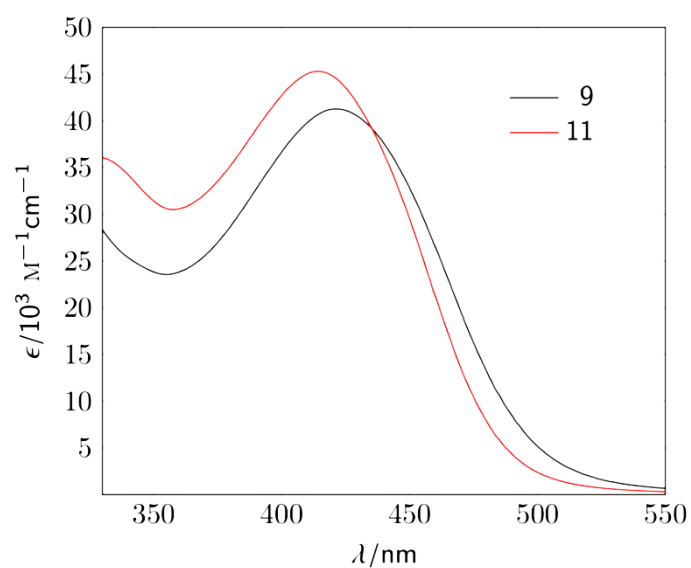

Figure 4.18 UV-visible spectra of compound **9** (black), and **11** (red) in acetonitrile at room temperature

4.2.3 Effects of Extending Conjugation

The objective of designing and analysing π-extended systems is to investigate the effect of the extension of π-bridges (elongation) on the linear and non-linear optical properties of these derivatives. When comparing derivatives **3**, and **7** with **4**, and **8**, it is clearly seen that increasing the π-conjugation length results in a shift of the LPCT band to lower energy with an increase in the intensity of this band. For instance, within the series containing Py functionality, **4** (λ_{max} = 386.0) shows bathochromic shifts of 15 nm compared to **3** (λ_{max} = 371.0), shown in Figure 4.19. However, when comparing **10** (short-NMe$_2$) with **9** (long-NMe$_2$), the trend seems to be anomalous, the short system (**10**) is unusually more red shifted (λ_{max} = 424 nm) compared to the long system (**9**) of λ_{max} = 421 nm, just like the electrochemistry results (the most negatively shifted redox potential among all *mono*-phenylimido derivatives is for **10**). As this electrochemical measurement suggests the LUMO of **10** is significantly raised compared to that of the other systems, it suggests the HOMO of this compound must also be high in energy.
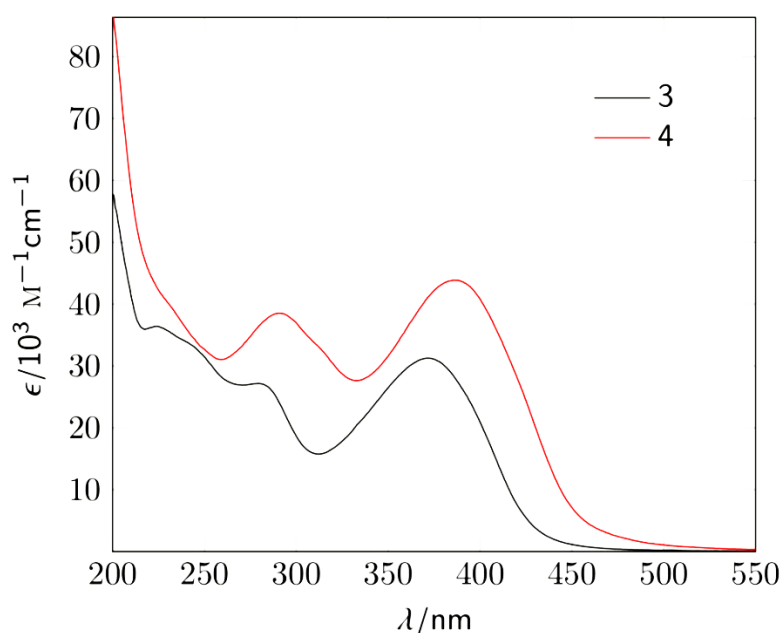

Figure 4.19 UV-visible spectra of compound **3** (black), and **4** (red) in acetonitrile at room temperature.

4.2.1 Effects of the type of POM

Compound **15**, as a model of organosilyl Keggin systems, shows only one intense UV absorption band, in a similar position to those of the parent aniline (4-(trimethoxysilyl)aniline) and POM, Figure 4.20. Therefore, it is likely that this band is simply caused by an overlap of the POM-based O➔W and ligand based $\pi \rightarrow \pi^*$ transitions, implying a weak interaction between the POM and the organic segment (aryl-amine). Thus, **15** is expected to be inactive as NLO chromophore.
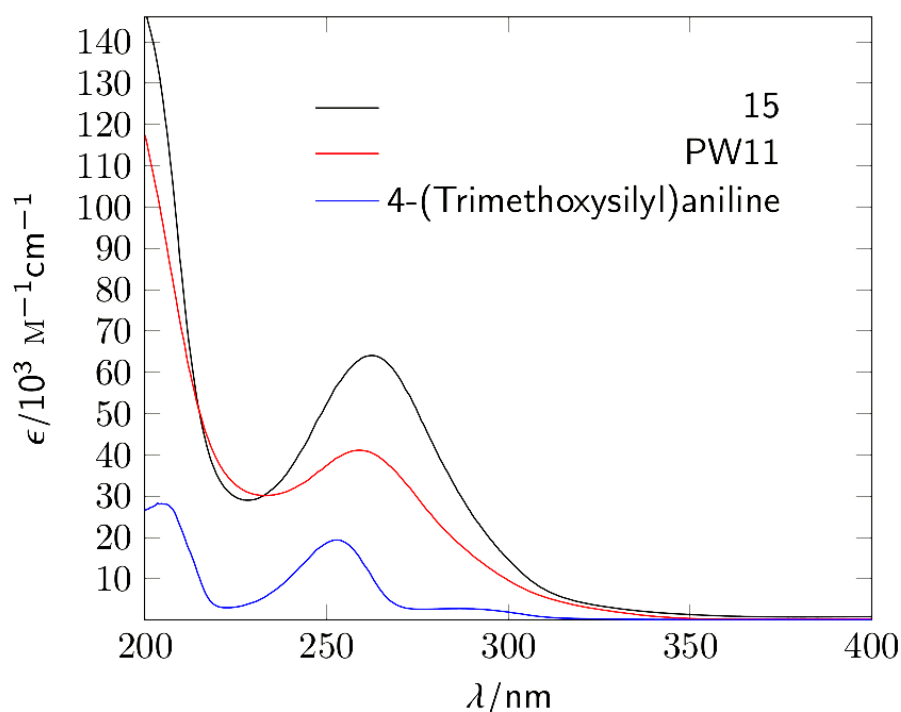
Figure 4.20 UV-visible spectra of compound **15** (black), **PW11** ($(Bu_4N)_4[H_3PW_{11}O_{39}]$) (red), and **4-(trimethoxysilyl)aniline** (blue) in acetonitrile at room temperature.

4.3 Spectroelectrochemistry, bulk electrolysis and stability studies

4.3.1 Spectroelectrochemical studies

In chapter 1, a brief description of a redox switching strategy for NLO responses in A-π-D molecules was provided with a schematic representation demonstrating this

method. In order to investigate such properties, a spectroelectrochemical cell (Honeycomb Spectroelectrochemical (AKSTCKIT3), Pine Research Instrumentation) was used for switching processes on linear optical responses between two states; oxidized "O", "On"; and reduced "R", "Off". Compounds (*c.a.* 10^{-3} - 10^{-5}) of interest were dissolved in 0.1 M [NBu$_4$][BF$_4$]-anhydrous MeCN. A silver wire was used as reference electrode, gold as counter and mesh gold as working electrode. The design of the cells allows to perform oxidation and reduction electrochemically (connected to a potentiostat) while the linear optical absorption is recorded using UV-vis spectrophotometer, is shown in Figure 4.21.[205]
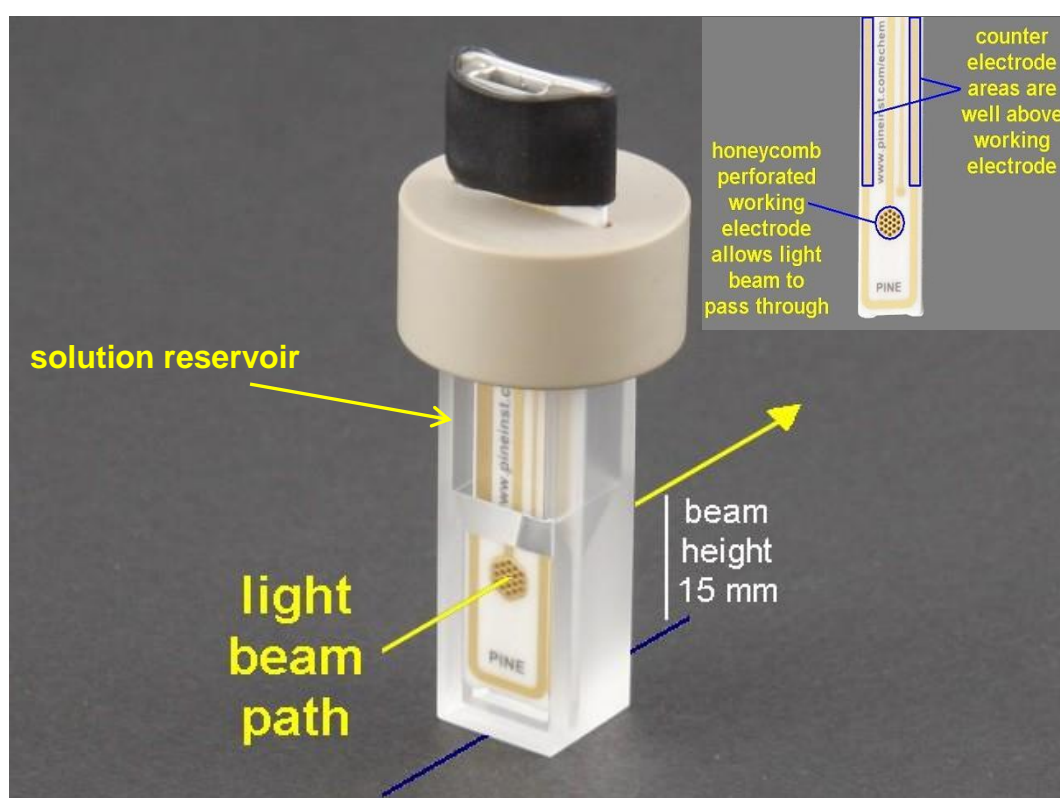

Figure 4.21 Schematic representation of the Honeycomb Spectroelectrochemical used for SE studies. Figure was adapted and reproduced from reference 205.[205]

Initial results suggested that redox-switching of the imido-POM optical properties may be possible. When applying a negative potential of –0.75 V (chronoamperometerically) to reduce compound **3**), the LPCT band intensity started to decrease until near complete extinction of their LPCT band, with isobestic points observed at *ca.* 265 and 215 nm. The completion of the reduction is determined if no significant current is measured during the chronoamperometry experiment, also no further change in the absorption responses.

The LPCT transition was (apparently) completely regenerated by re-oxidation at an applied potential of 0 V vs silver wire (Figure 4.22). These redox processes were repeated in a cycle up to 3 times for **3**, with no significant loss of absorbance in the LPCT band, and it is noteworthy that these measurements were carried out in the ambient atmosphere.
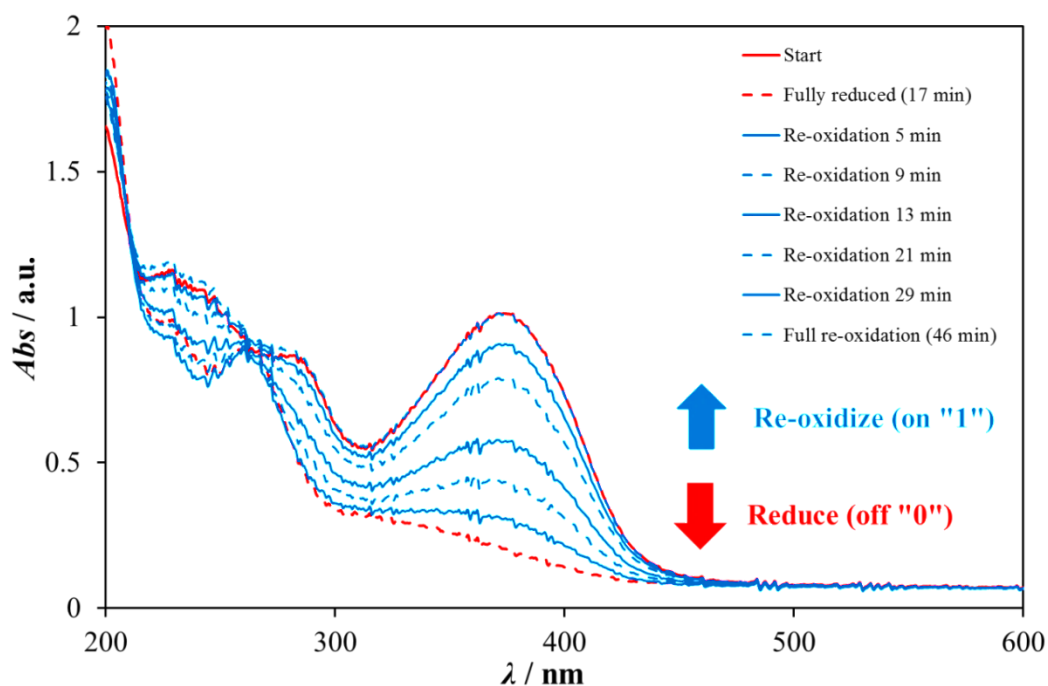

Figure 4.22 UV-visible spectro-electrochemistry on compound **3**. After several minutes at an applied potential of – 0.75 V vs silver wire, the LPCT band is completely extinguished (dashed red trace). The LPCT band is then competely regenerated after several minutes at an applied potential of 0 V vs silver wire (blue traces).

The resulting spectrum of these processes (Figure 4.20) looks similar to the combination of the ligand (**P5**), and reduced {Mo$_6$} **1** (Figure 4.23). This suggested (erroneously, *vide infra*) that reduction switches off the LPCT process, producing species where a reduced {Mo$_6$} cluster is connected to a ligand with little electronic communication between the two. Although $[Mo_6O_{19}]^{3-}$ also has transitions in the visible and NIR (490 nm and 862 nm),[241] their weak extinction coefficients (< 350 M$^-$^{1} cm^{-1}) compared to the LPCT mean that they are not observed at the concentrations used in this experiment. Similar observations were obtained for number of these compounds, and the apparent ability to reduce and re-oxidize and turning "on" and "off" the LPCT transitions suggested it was worth investigating these derivatives further for switching of HRS responses.
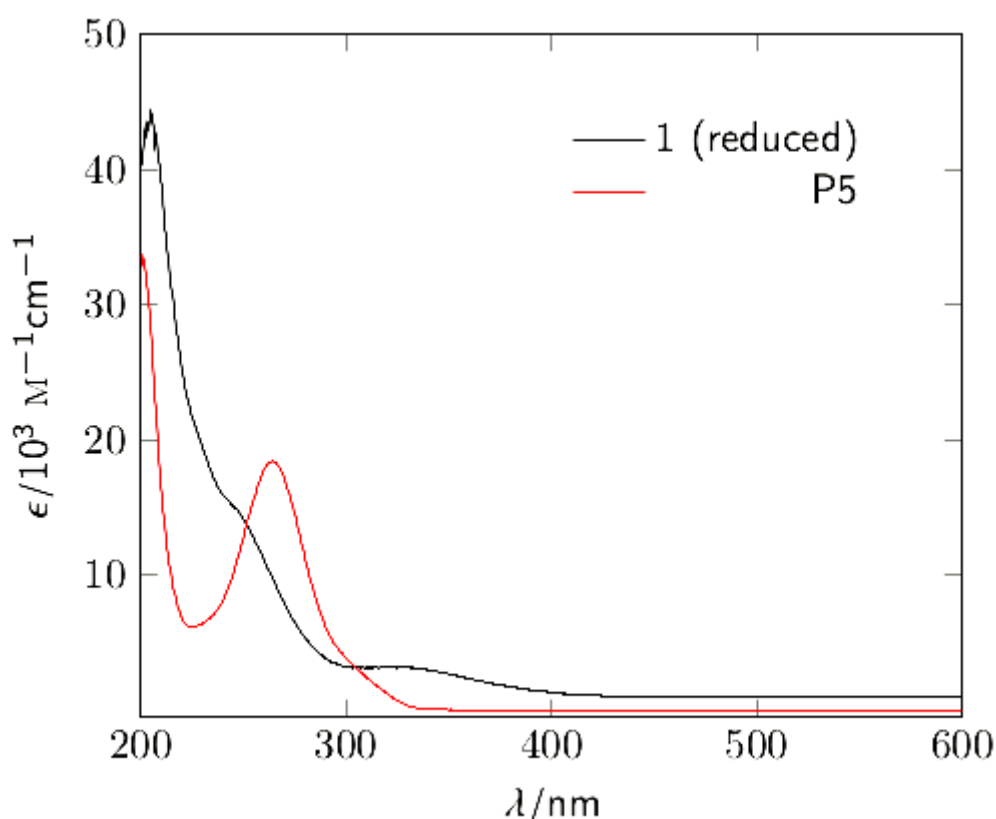

Figure 4.23 UV-vis spectra of reduced form of compound **1,** and **P5** in MeCN.

4.3.2 Bulk electrolysis

The apparently promising spectroelectrochemical results were followed up by bulk electrochemistry, to see if electro-reduced species could be produced for HRS measurements. In order to perform the switching NLO measurements, controlled potential electrolysis was attempted for some compounds, with the objective of producing bulk samples of the reduced anions. This was investigated on gold, platinum and carbon cloth working electrodes, under dry Ar with an Ag wire pseudo-reference electrode separated in another compartment from the working and Pt counter electrode, using 0.1 M [NBu$_4$][PF$_6$] or [NBu$_4$][BF$_4$] in CaH$_2$-dried acetonitrile as an electrolyte. Surprisingly, in all cases, the result was hydrolysis of the derivatized anion (in this case **3**), with disappearance of the derivative peak and appearance of a peak at a more positive potential, consistent with production of hexamolybdate (**1**), Figure 4.24.
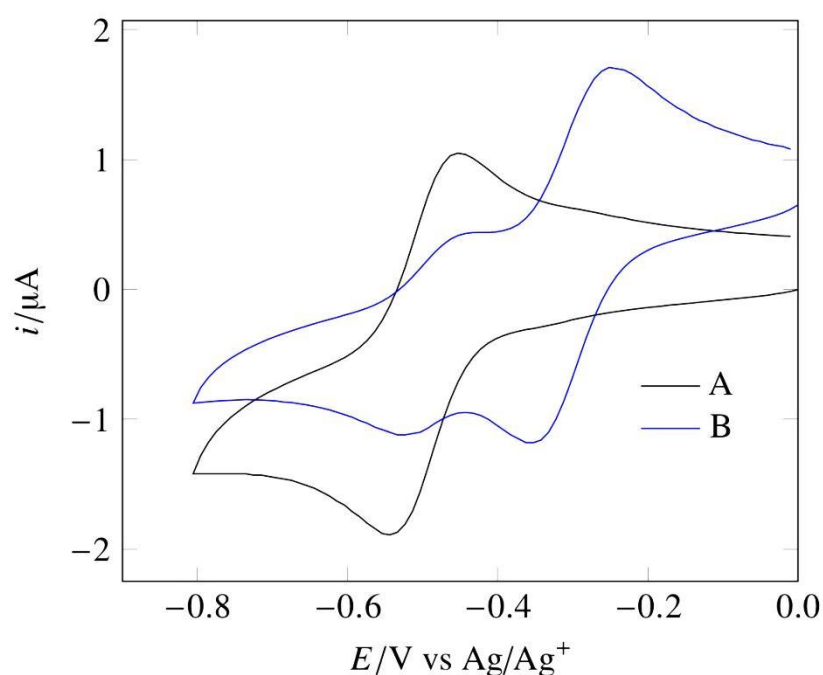

Figure 4.24 Cyclic voltammograms of a 0.13 mM solution of **3** , (**A**) before and (**B**) after controlled potential electrolysis for 1500 s at - 0.7 V (vs Ag wire), in 0.1 M [NBu$_4$][PF$_6$]. The **3**$^{2-/3-}$ peak disappears while a peak consistent with **1**$^{2-/3-}$ grows in at more positive potential.

The only explanation of the observations from bulk electrolysis is that the results obtained from the spectro-electrochemical measurements were deceptive. The reason this occurred is likely related to the design of the spectroelectrochemical cell, which holds a reservoir solution of the oxidized material at the top and an analyzing compartment in the bottom (see Figure 4.21). In the absence of an applied voltage, diffusion between the two compartments is extremely slow – no change in the absorption profile is observed over one hour after reduction if no voltage is applied. However, once a voltage is applied, the change in the charge on the anode and the cathode enhances the migration of ions in the cell and thus enhances the movement (diffusion) of the oxidized material (high concentration) from the top reservoir to the bottom of the cell (low concentration of the oxidized material) compensating the hydrolyzed material. This causes the LPCT band to re-appear as a fresh oxidized material is supplied to the analyzing compartment of the cell. It is interesting to know that the re-oxidation process were taking 45 minutes and the reduction process were taking 17 minutes, which implies that these processes were diffrerent precesses.

The conclusion is that the reduced states of these compounds are too sensitive for study by HRS, which requires concentrations $\leq 10^{-5}$ M, takes at least 30 minutes per measurement, and cannot be performed in a glove box. Mechanistic study of the hydrolysis of these compounds is an interesting subject to find out the optimum conditions minimizing the effect of such behaviour and could be explored in the future.

4.3.3 Stability of the resting states

In their resting states, most compounds, except **11** to **14**, are stable in MeCN (at 10^{-5} M concentration or higher) for several weeks or more, as seen in Figure 4.25.
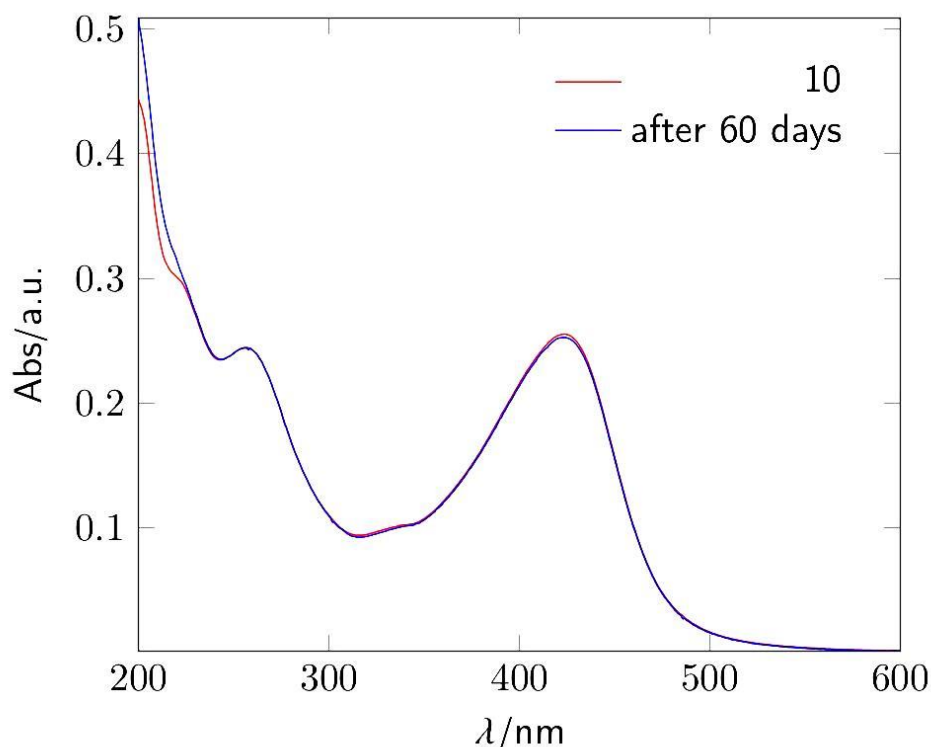
Figure 4.25 UV-visible of compound **10** (red) after storing at ambient conditions for 60 days (blue), showing no significant changes in the absorption spectrum.

Compound **11** to **14** (NPh$_2$ and Cbz donors, aliphatic derivative, and *bis*-derivative) show hydrolysis, for example **11** shows significant hydrolysis after exposure for 15 minutes to ambient conditions, can be seen from the UV-vis spectra at different time intervals (see Figure 4.26). This was supported by NMR results: new peaks consistent with the parent aniline ligand appear while the derivative peaks decrease over time.

From these results and the bulk electrolysis results, it can be concluded that the relationship between structure features and stability of these derivatives is complicated and it might be driven by the relationship between imido bond and the electron density. The observed results seem to suggest that protonation of N in the imido bond is important in the decomposition process of these species.
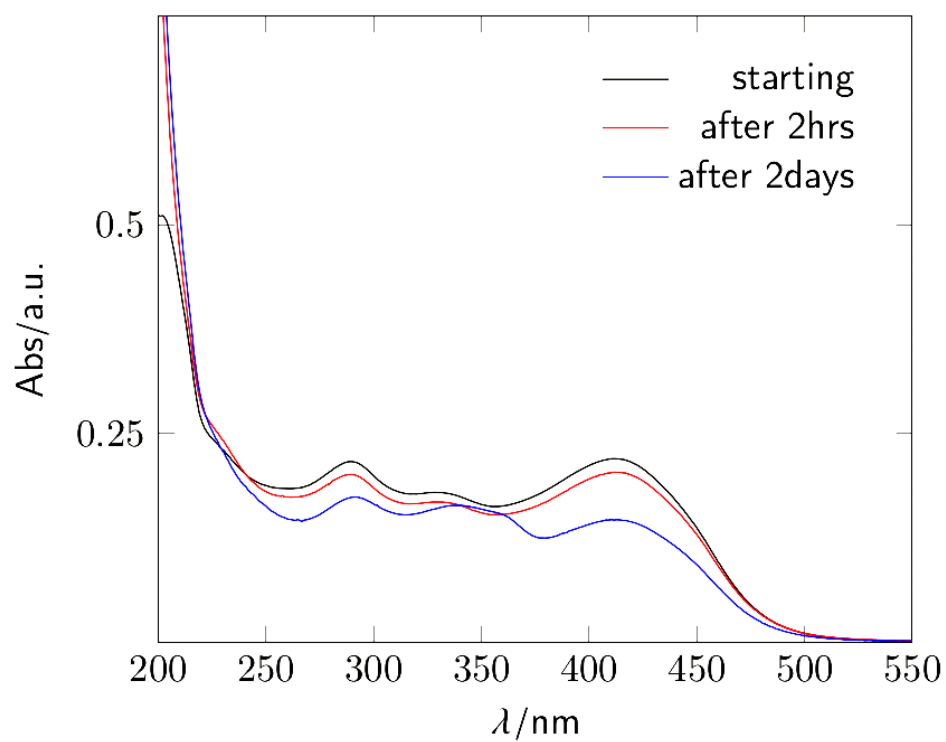
Figure 4.26 UV-visible of compound **11** (black) after exposure for 15 minutes to ambient conditions then monitoring the absorption after 2 hours (red), and 2 days (blue).

Chapter 5

Non-Linear Optical Properties

5.1 **Hyper-Rayleigh Scattering (HRS) experimental set-up**

In chapter 1, the basics of the HRS technique were briefly discussed. In this chapter, details of the experimental set-up, and the measurements of the second hyperpolarizability, β, will be presented. These were obtained with two different set-ups, at two different wavelengths: 800 and 1064 nm.

Figure 5.1 shows the schematic view of the 800 nm-HRS set-up. A high powered, narrow focus pulsed laser, in conjunction with sensitive detectors is used to optimise the signal to noise (S/N) ratio. This set-up also applies in the 1064 nm system, but the photomultiplier (PMT) detector is replaced by a spectrograph coupled to an intensified charge-coupled device enabling wavelength-dependent HRS measurements with excellent S/N ratio and with reliable calibration against the pure solvent over a very broad wavelength range. This sensitivity and high S/N ratio is needed in order to measure the off-resonant β values of molecules, as the second harmonic scattered light signal is normally low in non-resonant conditions.
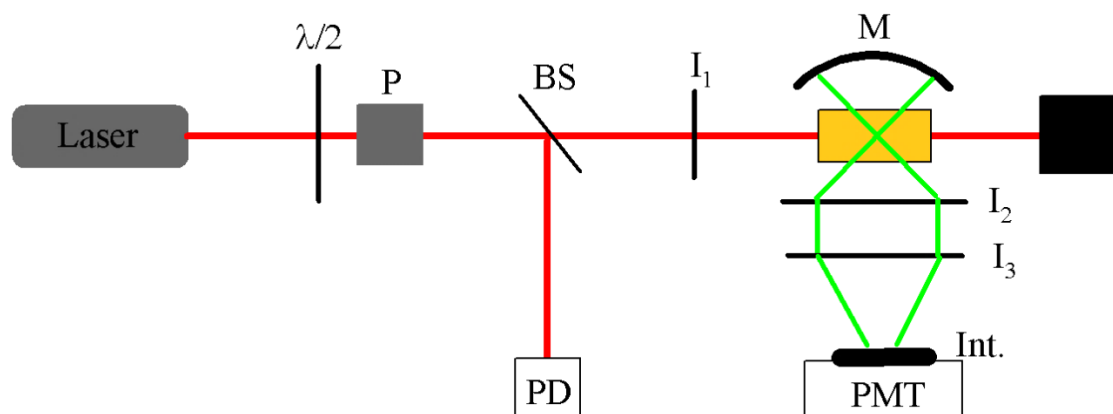

Figure 5.1 Scheme of the set-up for femtosecond hyper-Rayleigh scattering in solution at 800 nm; P = polarizer, $\lambda/2$ = half-wave plate, BS = beam splitter, I_1 = focusing lens, M = concave mirror, I_2 = aspheric lens, I_3 = plano-convex lens, int. = interference filter (400 nm), PD = photodiode, PMT = photomultiplier.

The fundamental input light intensity can be controlled by rotation of the half-wave plate in the front of the polarizer and can be monitored by the photodiode after splitting off a part of it by the beam splitter. An efficient collection system consisting of two lenses; an aspheric lens and a plano-convex lens, and a mirror was used to collect the frequency-doubled scattered light. The latter is detected by a photomultiplier equipped with an interference filter ensuring only $\lambda/2$ light is detected. The external reference method is used to analyse the data of the HRS measurements, using crystal violet in the 800 nm measurements, and acetonitrile in the 1064 nm measurements.[30,242-244] The hyper-Rayleigh scattered light $I_{2\omega}$ is quadratically dependent on the fundamental input intensity I_{ω} (equation 5.1) for a solution, where both solvent and solute are noncentrosymmetric and contribute to the HRS signal:

$$I_{2\omega} = QC\ I_{\omega}^2$$

(5.1)

QC is the quadratic coefficient and expressed in equation (5.2)

$$QC = G\left[N_s \left\langle \beta_{HRS,s}^2 \right\rangle + N_x \left\langle \beta_{HRS,X}^2 \right\rangle \right]$$

(5.2)

Where N_s is the concentration of the solvent, $\beta_{HRS,s}$ is hyperpolarizability of the solvent, N_X the concentration of the scattering molecule, $\beta_{HRS,X}$ is the hyperpolarizability of this molecule, and G is an experimental factor and depends upon the scattering geometry and the local field corrections at optical frequencies. The quadratic curves of the second-order scattered light intensities are obtained by plotting the scattered light intensities versus the fundamental light intensities for different concentrations; for both the reference and molecule of interest (Figure 5.2). As the concentration increases, the quadratic coefficients increase and thus a linear line is obtained between the plotted quadratic coefficients and the concentrations. The linear relation is lost in the case of self-absorption at the second harmonic wavelength, which happens at high concentrations. This problem can be practically eliminated by working at low concentrations ($\sim 10^{-4}$-10^{-6} M).
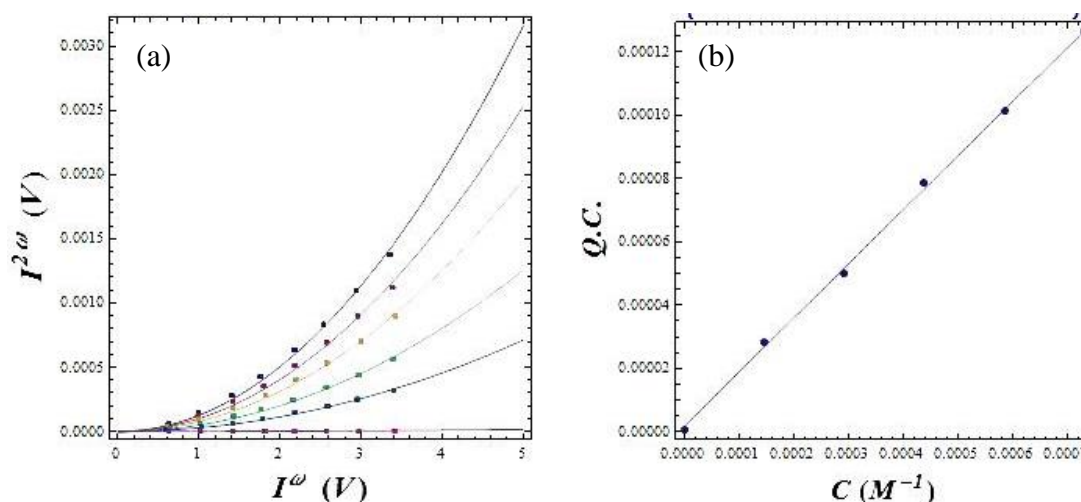
Figure 5.2 (a) HRS signal ($I_{2\omega}$) versus the input intensity (I_ω) for crystal violet in methanol at different concentrations. The solid lines are curves, fitted to equation (1.1), (b) Quadratic coefficients (QC) obtained from the curves in (a) versus the corresponding concentration of crystal violet in methanol. The solid line is a fit to equation (5.2).

Finally, the first hyperpolarizability β_{HRS} of the sample is calculated from the ratio of the slopes determined for both the reference and the sample using equation (5.3):

$$\frac{\text{slope}_{ref}}{\text{slope}_{sample}} = \frac{\left\langle \beta^2_{HRS} \right\rangle_{ref}}{\left\langle \beta^2_{HRS} \right\rangle_{sample}}$$

(5.3)

As HRS is an incoherent scattering process, it must be distinguished from any other sources of incoherent light such as multi-photon fluorescence (MPF). A systematic overestimation of β can result if no attention is paid to this potential contribution. This overestimating error can be avoided by making a distinction in the frequency domain[243] or in the time domain[245] between the immediate HRS and time-delayed fluorescence. The frequency domain approach is experimentally simpler, and faster than the time domain approach. In this approach, the discrimination is characterized by the fluorescence life-time (τ) in the frequency domain where the fluorescence is

demodulated and then acquires a phase shift with respect to the HRS scattering. The fluorescence wave (M_F) can be brought out-of-phase with the HRS signal by increasing the amplitude modulation frequency of the excitation wave (M_R) which results in elimination of fluorescence contribution from the HRS signal at a particular amplitude modulation frequency, as shown in Figure (5.3). The experimental β values are plotted versus modulation frequency and if there is any fluorescence contribution, a decrease in β values should be noted, as shown in Figure (5.4).
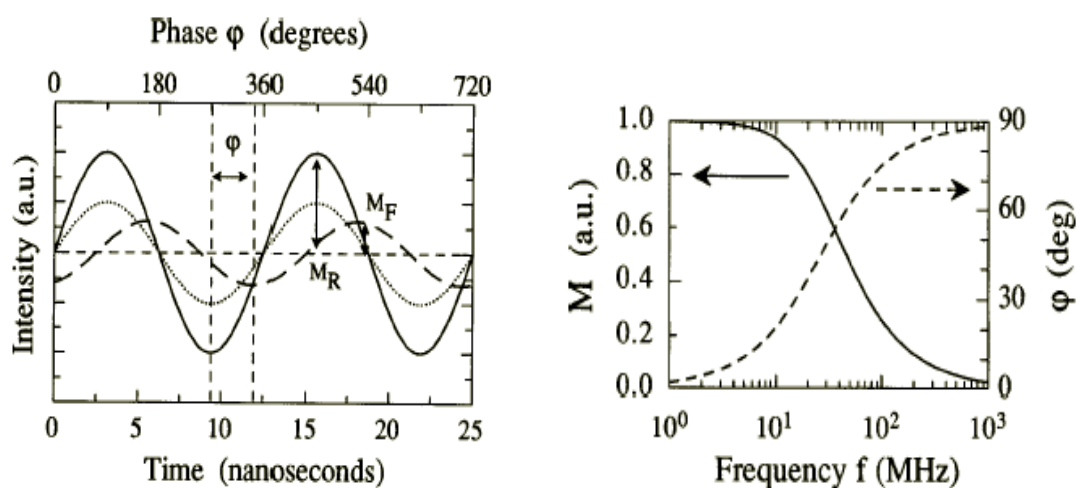
Figure 5.3 (a) Schematic representation of the fluorescence (dashed line) demodulation from the HRS (dotted line) response on a high-frequency amplitude modulation of 80 MHz (solid line) which leads to a phase shift φ of 72° between the excitation wave and the fluorescence wave, corresponding to a fluorescence lifetime of 6 ns. (b) Phase shift φ in degrees and demodulation (M) vs the excitation frequency f.[246] Reproduced with permission from reference 241.
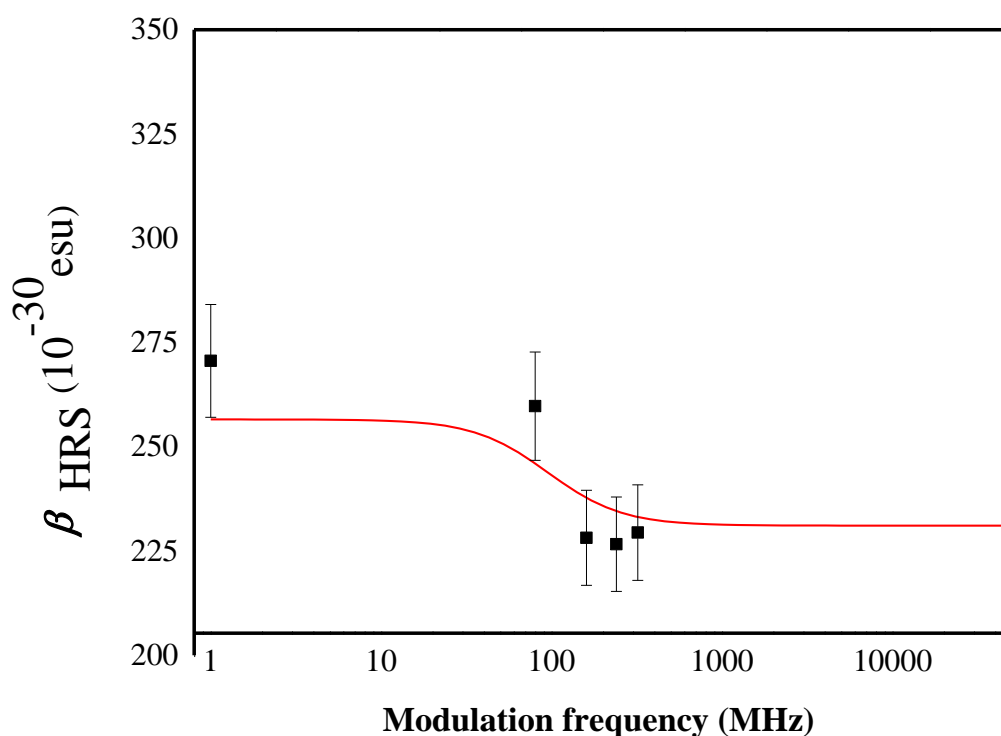
Figure 5.4 Dependence of β on the modulation frequency of compound **4**.

Instead of using demodulation (time consuming), the 1064 nm system uses spectral distinction to discriminate or distinguish the MPF from the HRS signal. Typically, MPF is much broader than the spectrally narrow HRS line. The HRS signal, which is essentially mirroring the spectral width of the fundamental laser beam, is determined by taking a10 nm interval of the total peak area of the signal, centred around the second-harmonic wavelength 532 nm (dotted line in Figure 5.5). Thus, it can be corrected by subtracting the broad Stokes shifted fluorescence contribution; usually by means of a linear fit, from the HRS response, as shown in Figure (5.5).
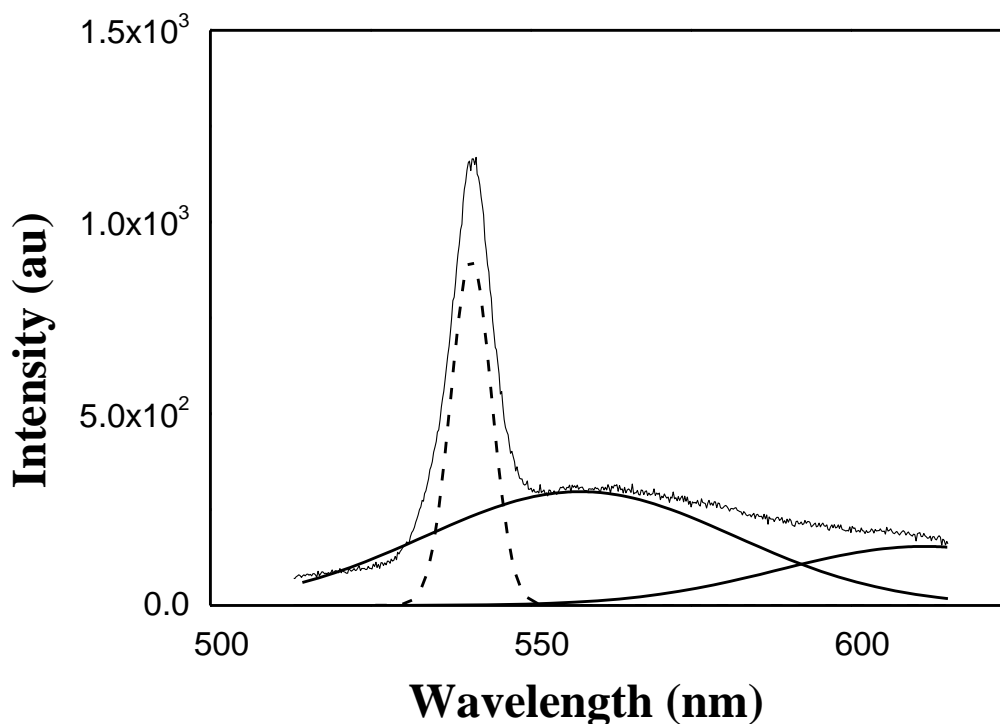
Figure 5.5 Multiphoton fluorescence spectrum of complexes **10** and the HRS peak (dashed) is superimposed on the broad MPF band (solid).

5.2 Stark spectroscopy

Stark measurements are performed on a frozen glass sample and the absorption spectrum is recorded in the presence and absence of an applied electrical field. The Stark spectrum is obtained by calculating the difference between these two results. The spectrum is described by equation 5.1:[20]

$$\Delta\varepsilon\ (v)\ /\ v = \left[A_x\varepsilon\ (v)\ /\ v + \frac{B_x}{15h} \ \text{x}\ \frac{\partial(\varepsilon\ (v)/v)}{\partial\ v} \ + \ \frac{C_x}{30h^2} \ \text{x}\ \frac{\partial^2\ (\varepsilon\ (v)/v)}{\partial\ v^2} \right] F^2_{int}$$

$$(5.1)$$

$\Delta\varepsilon(v)$ = overall Stark response, v = frequency of the light (Hz), within the brackets are the zeroth, first and second derivatives of the electronic absorption spectrum $\varepsilon(v)$.

The dipole moment change, $\Delta\mu_{12}$ and transition dipole moment μ_{12} can be calculated by using Equation 5.2 from the oscillator strength f_{os}:

$$|\mu_{12}| = \left[f_{os} /(1.08 \times 10^{-5} (E_{max})) \right]^{1/2}$$

(5.2)

Where E_{max} is recorded in wavenumbers (cm^{-1}).

The diabatic dipole moment change $\Delta\mu_{ab}$ can be calculated using the two state analysis of the CT transition, is shown in equation 5.3:

$$\Delta\mu^2_{ab} = \Delta\mu^2_{12} + 4\mu^2_{12}$$

(5.3)

Equation 5.4 gives the degree of delocalization C_b^2 and the electronic coupling matrix element H_{ab} for the diabatic states:

$$C_b^2 = \frac{1}{2}\left[1 - \left(\frac{\Delta\mu^2_{12}}{\Delta\mu^2_{12} + 4\mu^2_{12}} \right)^{1/2} \right]$$

$$|H_{ab}| = \left| \frac{E_{max}(\mu_{12})}{\Delta\mu_{ab}} \right|$$

(5.4)

β_0 is then calculated from the derived values of E_{max}, $\Delta\mu_{12}$, and μ_{12} using the two state model equation (chapter1, equation 1.6).

5.3 Nonlinear Optical Measurements

5.3.1 HRS studies

HRS studies have been used to directly determine the first hyperpolarizability β values for compounds **2** to **12** and **15** in acetonitrile solution using both 800 nm and 1064 nm laser fundamentals. Firstly, we used 800 nm laser fundamental to determine the dynamic rather than the static β values. These measurements are useful to show whether the compounds are active or not before any further investigations, taking the advantages of this set-up that has a very high signal-to-noise HRS signal. However, these measurements will be affected by the resonance enhancement effects as all compounds have λ_{max} close to the 400 nm second harmonic. This leads to overestimated dynamic β values but underestimated static β (β_0) due to overestimated resonance correction factors.

For 1D dipolar molecules, β_{800} and β_{1064} are the orientationally averaged hyperpolarizability values at 800 and 1064 nm respectively. The β_{zzz} values (calculated at each wavelength) are the dominant tensor components along the charge-transfer Z axis, which can be used to compare with β_{EFISH} values of other literature 1D chromophores. While, β_0 is the static value of the first hyperpolarizability and in this work it could only be calculated from the 1064 nm laser fundamental measurements as it needs to be measured under non-resonant conditions. Hence, it provides more accurate and comparable values for different chromophores at different wavelengths.
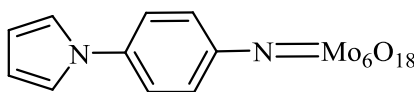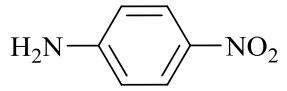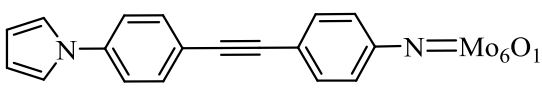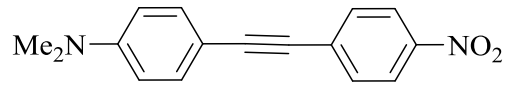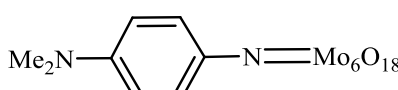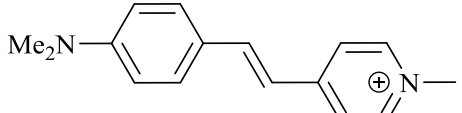
Table 5.1 presents the results of these measurements and table 5.2 shows the structures and data for some previously reported compounds along with some of the synthesized POM-based chromophores for the purpose of comparison.

Table 5.1 ICT and HRS data for compounds **2**-**12**, and **15**.

	λ_{max} / nm	E_{max} /eV	β_{800}[a] /10^{-30}esu	$\beta_{zzz,800}$[b] /10^{-30}esu	$\beta_{0,800}$[c] /10^{-30}esu	β_{1064}[d] /10^{-30}esu	$\beta_{zzz,1064}$[e] /10^{-30}esu	$\beta_{0,1064}$[f] /10^{-30}esu
2	355.0	3.49	<25	-	-	<25	-	-
3	371.0	3.34	121(±14)	292 (7)	32[g]	51(±4)	123 (±10)	56 (±5)
4	386.0	3.21	231(±23)	557 (±10)	29[g]	59(±4)	142 (±10)	59 (±5)
5	406.0	3.05	297(±26)	717 (±13)	17[g]	154(±9)	371 (±22)	133 (±12)
6	358.0	3.46	<25	-	-	<25	-	-
7	370.5	3.35	<25	-	-	<25	-	-
8	389.0	3.18	<25	-	-	<25	-	-
9	421.0	2.94	337 (±60)	813 (±20)	63[g]	182 (±23)	439 (±60)	139 (±20)
10	424.0	2.92	125(±24)	301 (±12)	27[g]	117 (±3)	282 (±9)	87 ((±5)
11	414.0	2.98	217(±45)	524 (±16)	27[g]	95 (±3)	229 (±9)	77 (±5)
12	384.5	3.20	177(±35)	427 (±17)	25[g]	62 (±15)	149 (±45)	62 (±15)
15	262.5	4.72	<25	-	-	<25	-	-

[a] Experimental first hyperpolarizability measured using an 800 nm laser. [b] First hyperpolarizability calculated from β_{800} assuming a single dominant tensor component along the z molecular dipole axis; can be calculated by dividi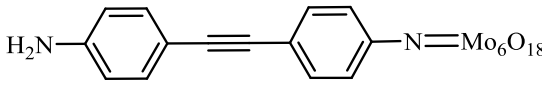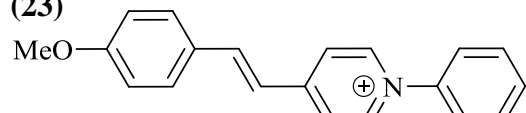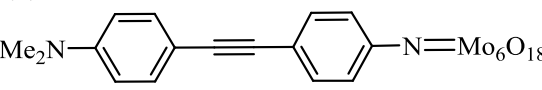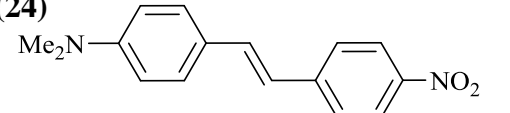ng β_{800} by a factor of 0.414. [c] Static first hyperpolarizability estimated from $\beta_{zzz,800}$ via the two-state model. [d] Experimental first hyperpolarizability measured using a 1064 nm laser. [e] First hyperpolarizability calculated from β_{1064} assuming a single dominant tensor component along the z molecular dipole axis; can be calculated by dividing β_{1064} by a factor of 0.414. [f] Static first hyperpolarizability estimated from $\beta_{zzz,1064}$ via the two-state model. The esu units can be converted to SI units (C^3 m^3 r^2) by dividing by a factor of 2.693 x 10^{-20}. [g] Underestimated due to proximity of LPCT maximum to the SH wavelength at 400 nm.

Table 5.2 Organic chromophores with comparable donors, π-systems and/or absorption profiles to the synthesized POM-based chromophores, and β_0 values obtained under non-resonant conditions.[247-249]

(3) λ_{max} = 371 nm; β_0 = 56	(20) λ_{max} = 371 nm; β_0 = 17
(10) λ_{max} = 386 nm; β_0 = 59	(21) λ_{max} = 415 nm; β_0 = 46
(4) λ_{max} = 424 nm; β_0 = 87	(22) λ_{max} = 470 nm; β_0 = 25
(5) λ_{max} = 406 nm; β_0 = 133	(23) λ_{max} = 426 nm; β_0 = 46
(9) λ_{max} = 421 nm; β_0 = 139	(24) λ_{max} = 437 nm; β_0 = 53

800 nm measurements

The reported β values are the averages taken from measurements at different amplitude modulation frequencies, with the fluorescence of **4** corrected for by demodulation fitting to provide a fluorescence free value of β. Significant dynamic 2nd order non-linearities (β_{zzz}) of up to 813×10^{-30}esu (for compound **9**) were obtained with substantial increases in activity as the electron donor strength, or the π-conjugation length increases. These results show that modifications used to enhance β in purely organic chromophores also apply to organoimido-POMs. For instance, replacing the weak electron donor pyrrole in compound **4** with the stronger electron

donor NH$_2$ in compound **5**, almost increases the activity by 30%. The activity is increased further by introducing the NMe$_2$ electron donor in compound **9**.

Extending the π-conjugated bridge nearly doubles the response in most cases, this is seen from **3** to **4**, and also from **10** to **9**. It is somewhat surprising that the activity of compound **11** as well as **12** was lower than expected, where diphenylamine and carbazole electron donor functionalities are introduced, respectively. These results are likely to be related to the stability of these compounds, which have been proved more vulnerable to hydrolysis than the other compounds. Hydrolysis of samples during measurement to inactive $[Mo_6O_{19}]^{2-}$ and the parent aniline may dilute the concentration of active material and hence lower the response. All molecules that did not have a resonance donor such as compounds **2** (Iodo), **6** (ethynyl), **7** (short-π NO$_2$ system), and **8** (long-π NO$_2$ system), and also compound **15** (PW$_{11}$ Keggin system) show no measureable activity compared to the solvent.

However, the β_0 values do not show any logical trend. This is due to the underestimation of β_0 caused by the λ_{max} values being close to the second harmonic wavelength of 400 nm. This is most severe for compound **5**, whose λ_{max} is only 6 nm away from the second harmonic.

1064 nm measurements

To enable measurement of static β values, we instead used the 1064 nm source. In all cases, this means the 532 nm SH wavelength is > 100 nm from the absorption maximum, and residual absorptions are low. However, at 1064 nm, β_{zzz} values are lower for all derivatives, most likely because resonance enhancement is effectively eliminated (non-resonant conditions), which were needed to provide a fair comparison of the activity (the static first hyperpolarizability, β_0) of these derivatives with other literature materials.

The β_0 values generally increase as the electron donor strength or the length of π-conjugation increases, in accord with the observed trend in the LPCT band energies, and consistent with the two state model.[17] In all cases, compounds bearing weak (I, ethynyl) or strong (NO_2) acceptor functionalities showed no measureable activity compared to the solvent. When these are replaced with electron donor groups such as Py, Cbz, NPh_2, NH_2, and NMe_2, the compounds become active, confirming that the POM is an acceptor in these systems. This is in contrast with calculations in the literature where the POM was proposed as an electron donor in systems functionalized with acceptors, such as NO_2 on the other end.[196,250] Our experimental results are far more consistent with the known properties of POMs: it is difficult to envisage how the POM can be anything but the acceptor in these systems – the POM consists of 6 Mo^{VI} centres (i.e. d^0) and oxo groups which also hold onto electrons tightly. It also has reductions at easily accessible potentials (unlike the organic group) indicating it must be the LUMO.

Differences in β_0 between the donor functionalized derivatives are generally consistent with the decreases in the LPCT band energies, as can be seen in table 5.1. The highest value is attributed to compound **9** (π-extended -system NMe_2), of 139×10^{-30} esu. Increases in $\beta_{0, 1064}$ occur when moving from **10** (short-system NMe_2) to **9** (π-extended -system NMe_2), which is logical, in view of the extended π-system of **9**. Similar trends were seen when moving from **3** (short-system Py) to **4** (π-extended -system Py). Similar observations to the 800 nm measurements for compounds **11** and **12**, that is lower activities than expected, were made at 1064 nm.

Compared to compound **22** in table 5.2, the DAS$^+$ cation (technologically exploited in terahertz generation), the β_0 values obtained comfortably higher under non-resonant conditions, and also compare well to those of many other, more active stilbazolium chromophores with stronger donors and much lower energy transitions, which means red-shifted absorption and hence poorer

transparency.[251,252] When comparing *p*-nitroaniline (table 5.2, compound **20**) with these compounds, **20** shows better transparency, but for a large sacrifice in β. For example, compound **3** has a similar absorption profile to **20** but its β_0 is three times higher. A similar trend was seen for compound **9** (its β is three times higher) that has similar π-bridge length and absorption profile to compound **21** in table 5.2.

Far higher β-values have been obtained with other organic acceptors,[253] but with a lower transparency (transparency-efficiency trade-off). For instance, tricyanopyrroline (TCP)-based chromophores show a very large molecular *dynamic* first hyperpolarizability (β) of 8700 ($\pm$702) 10^{-30} esu, but with large red-shift (λ_{max} = 700 nm) and hence poor transparency.[253] In fact, when comparing to reasonable structural and spectral analogues, POMs have higher β_0 in all cases (Table 5.2). Furthermore, to our knowledge **9** shows the highest non-resonant β_0 compared to dipolar organic compounds with similar transparency and a comparable donor and bridge size.

In order to evaluate the performance of these POM-based chromophores compared to other dipolar organic chromophores, an analysis between the electron number adjusted β ($\beta_0/N^{3/2}$ where N = π-conjugated electrons in bridge) and λ_{max} was used.[254] This analysis suggests an apparent limit for most dipolar organic materials, as shown in Figure 5.6. Compound **10** comfortably exceeds this apparent limit of $\beta_0/N^{3/2}$ = 2.7 when λ_{max} = 424 (for **10**, $\beta_0/N^{3/2}$ = 5.9 when λ_{max} = 424), and compound **3** does so too of when λ_{max} = 370 (for **3**, $\beta_0/N^{3/2}$ = 3.8, the apparent limit at λ_{max} = 371 is $\beta_0/N^{3/2}$ = 1.5). Compound **9** and **4** are just above this limit, as seen in Figure 5.6.[23]

However, there are a few purely organic examples in the literature exceeding this apparent limit such as TICT chromophores[255] and a pyridinium tetrazolate.[256] They break these limits more notably than our POM-based chromophores, due to their

unusual electronic structure. This raises the question of how our POM-based materials show such high performance and what are the reasons that make the POM behave as an unusually efficient acceptor. One factor may be the relativistic effects, which exist in heavy elements where the electron speed is close to the speed of light. These effects can strongly influence the chemical and physical properties such as linear and non-linear optical properties.[257] They can cause an increase in the spatial separation (increases charge separation; $\Delta\mu_{12}$) by increasing the localisation and concentrating the LUMO around the heavy atom and hence lead to increase β value based on the two state model.[258] $\Delta\mu_{12}$ is present in the two state model equation and β is proportional to $\Delta\mu_{12}$.

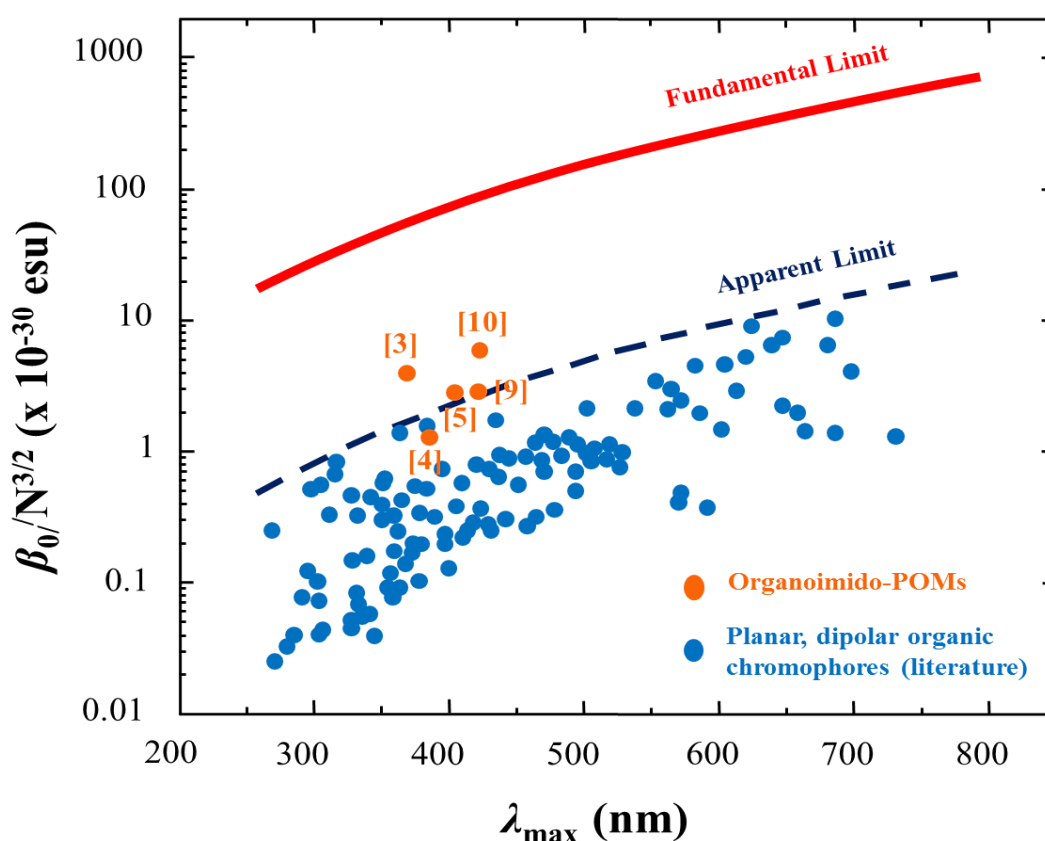**Figure 5.6** Data showing electron number adjusted β values ($\beta_0/N^{3/2}$ where N = π-conjugated electrons in bridge) plotted against the wavelength of maximum absorption, λ_{max} for organoimido-POM chromophores, and planar, dipolar organic chromophores from the literature. **10**, **9**, **3**, and **5** both exceed expected performance limits for comparable organic systems.[23]

5.3.2 Raman and Stark spectroscopy

To help explain why these POM-based chromophores break empirical organic performance limits, further investigations were performed using Raman and Stark spectroscopies. Taken together, the HRS measurements, electronic spectroscopy and the cyclic voltammetry results (Chapter 4) would appear to indicate an unusual electronic structure for these derivatives. They all appear to have same transitions, but only some have the NLO activity and all showed more or less the same redox potential shifts from their parent $[Mo_6O_{19}]^{2-}$ except compound **8** (short-π NO_2 system) and **10** (short-π NMe_2 system). Therefore, while we use the shorthand LPCT, we are uncertain of the extent of involvement of the POM framework in the observed charge transfer transitions: without further measurements, it is impossible to exclude the possibility that the imido-N in fact acts as the acceptor in most cases. Below are outlined results suggesting the POM is indeed the acceptor.

Raman spectroscopic studies

Raman spectroscopy is a light-scattering spectroscopic technique that can be used to provide information about molecular symmetric and non-symmetric vibration modes. It provides a useful means to investigate the nature of new electronic transitions.[259] If the excitation wavelength coincides with the electronic transition, Raman modes that are associated with parts of the molecule or supramolecular assembly are enhanced in intensity, compared to excitation with a source that does not coincide with the electronic transition. Raman spectroscopic studies have been carried out on compounds **1** ($[Mo_6O_{19}]^{2-}$), **2** (short-π iodo system), and **9** (long-π NMe_2 system) in acetonitrile solution at 785 nm, and 532 nm. UV-vis spectroscopic results showed that 785 nm is well beyond the absorption of any of these molecules, while at 532 nm a small but significant absorption remains in the case of **9** but there is apparently no absorption from the other two (**1**, and **2**). Figure 5.7 shows the Raman spectra of **1** at 532 nm and 785 nm with acetonitrile as a reference. The signals of **1** are entirely swamped by solvent.
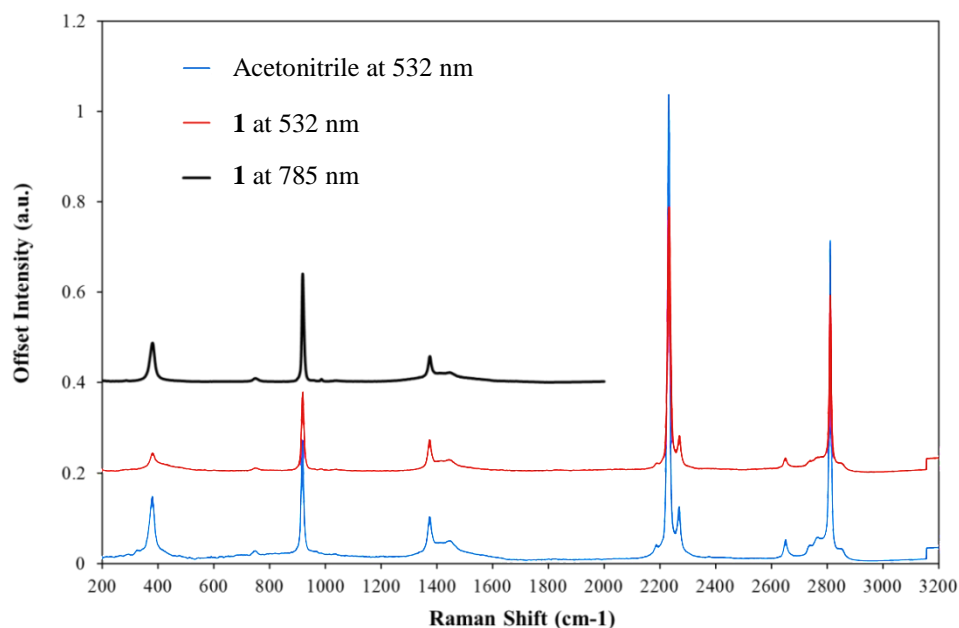
Figure 5.7 Raman spectrum of **1** in acetonitrile showing no difference to acetonitrile at 532 and 785 nm.

Compound **2** showed a slight enhancement of the POM bands around 990 cm^{-1}, i.e. the Mo=O and Mo=N, and significant enhancement of other bands from the organic system compared to the acetonitrile background (Figure 5.8). These results indicate that there must still be very small absorbance from this compound at 532 nm and that the POM is involved in the transition. This can be clearly seen in compound **9**, which absorbs significantly at 532 nm (ε_{532} = 1195 M^{-1} cm^{-1}) and shows a very significant enhancement of the POM Raman bands when excited at this wavelength (the POM bands become more intense than acetonitrile peak). The organic bands are also greatly enhanced, as shown in Figure 5.9. These results confirm that the POM is definitely vibrationally excited by the electronic transition responsible for the NLO effects. However, it cannot be argued for definite that POM is the initial electron acceptor rather than imido-N, because electron transfer to imido-N, bonded to POM might put the POM into a vibrationally excited state. It is also possible that initial electron transfer to imido-N occurs, followed by subsequent transfer to POM. However, it is clear that the POM is involved and therefore can influence the excited state.
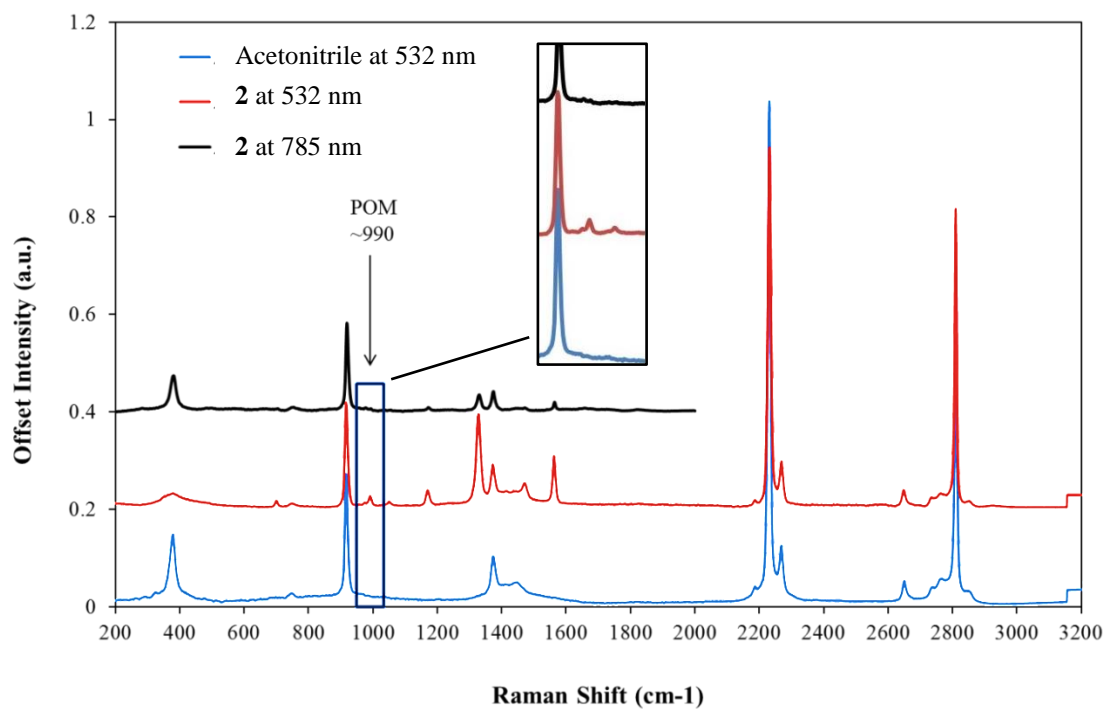
Figure 5.8 Raman spectra of **2** in acetonitrile showing enhancement of the POM bands at 990 cm^{-1}. Inset shows enlarged POM bands.
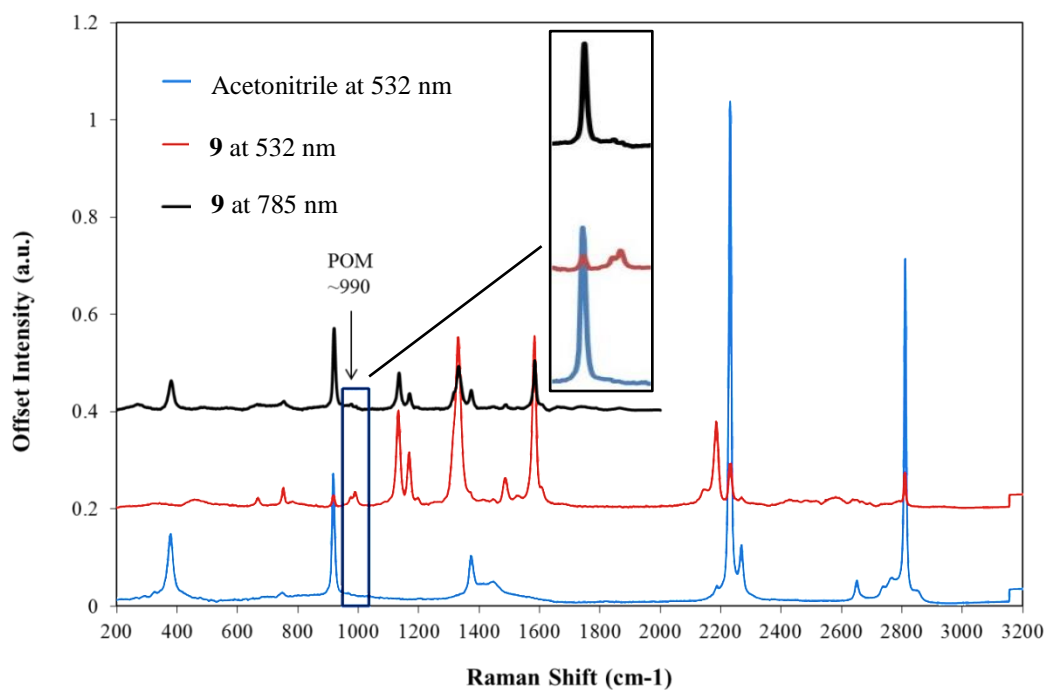

Figure 5.9 Raman spectra of **9** in acetonitrile showing the very significant enhancement in the POM band at 990 cm^{-1} and the organic bands. Inset shows enlarged POM bands.

Stark spectroscopic studies

In order to investigate the molecular electronic properties of this series of organoimido Lindqvist derivatives and to understand their β responses better, Stark spectroscopic studies have been carried out on compounds **6** to **10**. Measurements were performed in butyronitrile glasses at 77 K to afford dipole moment changes $\Delta\mu_{12}$ for the LPCT bands. Table 5.3 shows selected data for compounds **6** (short-π alkyne system), **7** (short-π NO_2 system), **8** (long-π NO_2 system), **9** (long-π NMe_2 system), and **10** (short-π NMe_2 system). This provides a series from strong acceptor group, through very weak acceptor to strong donor, as well as three compounds inactive by HRS (**6**, **7**, and **8**), and two of the most active (**9** and **10**). Figure 5.10 presents the representative electronic absorption and Stark spectra of these compounds. Compound **9** and **10** showed significant red shift ca. 20 nm upon forming acetonitrile glasses, but **6**, **7** and **8** did not show such shifts. This is the first observation that suggests the nature of the transitions may be different between the two sets of compounds, despite similar appearance and position.

Table 5.3 Stark spectroscopic data for compounds **6**, **7**, **8**, **9**, and **10**.

	μ_{12} [a] (D)	$\Delta\mu_{12}$ [b] (D)	r_{12} [c] (Å)	f_{os}	$\Delta\mu_{ab}$ [d] (D)	R_{ab} (Å)	H_{ab} [e] (eV)	C_b^2 [f]	β_0 [g] (10^{-30} esu)
6	7.52	1.69	0.355	0.739	15.14	3.14	1.17	0.445	9
7	8.73	5.79	1.20	0.966	18.40	3.835	1.585	0.345	46
8	11.90	5.97	1.24	1.68	24.56	5.11	1.51	0.38	99
9	9.43	21.62	4.49	0.92	28.71	5.98	0.89	0.12	296
10	8.39	10.14	2.11	0.75	19.62	4.08	1.21	0.24	103

[a] Transition dipole moment derived using equation 5.2. [b] Dipole moment difference between diabatic states derived from $f_{int}\Delta\mu_{12}$ using $f_{int} = 1.33$. [c] Delocalised electron-transfer distance derived from $\Delta\mu_{12}/e$. [d] Diabatic dipole moment change derived from equation 5.3. [f] Degree of delocalisation derived from equation 5.4. [g] Static first hyperpolarizability derived from equation 1.6 in chapter 1.

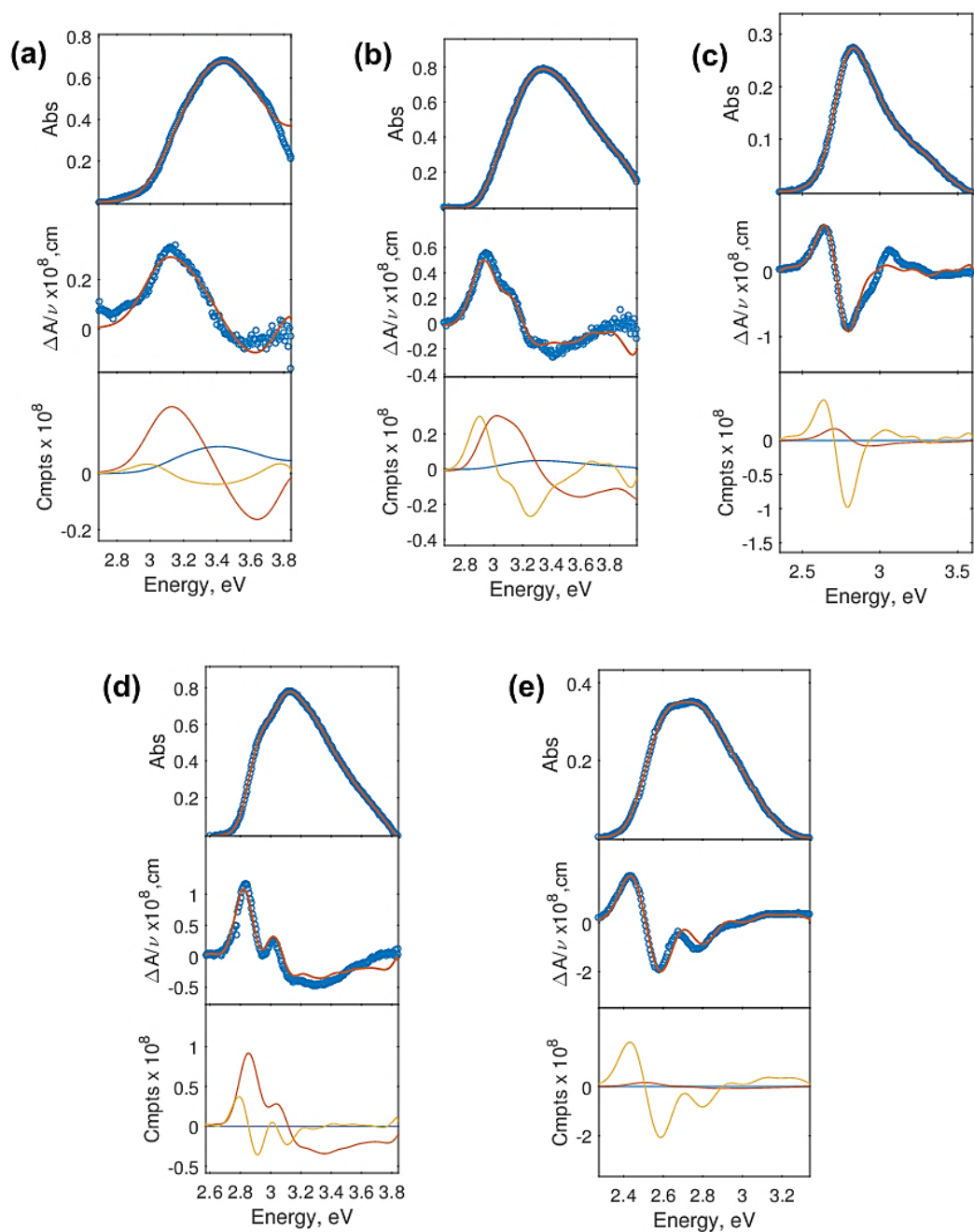**Figure 5.10** Electroabsorption spectra and calculated fits for (a) **6**, (b)**7**, (c) **10**, (d) **8**, and (e) **9** in external fields. Top panel: absorption spectrum; middle panel: electroabsorption spectrum, experimental (blue) and fits (red) according to the Liptay equation; bottom panel: contribution of the 0th (blue), 1st (orange) and the 2nd (yellow) derivatives of the absorption spectrum to calculated fits.

The experimental fits shown in Figure 5.10 are obtained via linear combination of the zero, first and second derivative to fit the actual observed Stark spectrum. Use of a Gaussian fitting approach would allow a closer fit to the actual data, but in some cases, such an approach risks invoking transitions that do not really exist. In addition, the majority of Stark data in the literature to which we compare were fitted using the experimental approach.

The visual inspection of the spectra and their fits can qualitatively give some information about these derivatives. In the case of Compound **6**, using very high concentrations and high electric fields was necessary to obtain measurable signal (with noisy background), and the fit was relatively poor, even of the simple absorption spectrum. These observations, and the weak contribution of the 2nd derivative to the fit indicate that the transition actually only has a very weak charge transfer character. This is reflected in the calculated values where high delocalization C_b^2, and a small dipole moment change were obtained. However, due to this weak charge transfer character, these results will not be very accurate. A possible explanation for the weak charge transfer character might be that the CT process is occurring between two large delocalized systems. For this reason, the dipolar character may be very diffuse and weak with no β response observed in HRS.

Compound **7**, and **8** (NO_2 systems) showed stronger signals than compound **6**, with stronger charge transfer character. However, the contribution of 1st derivative is still strong. Noticeably, the calculated dipole moment changes and charge transfer distances are essentially the same in both compounds (long and short-π systems). This suggests that the measured spectrum may result from the combination of aryl-to-POM and aryl-to-NO_2 charge transfers. As these two charge transfers directions are opposite to each other (shown in Figure 5.11); therefore, the Stark derived β_0 is not valid and hence explains the inactivity that was observed by HRS.
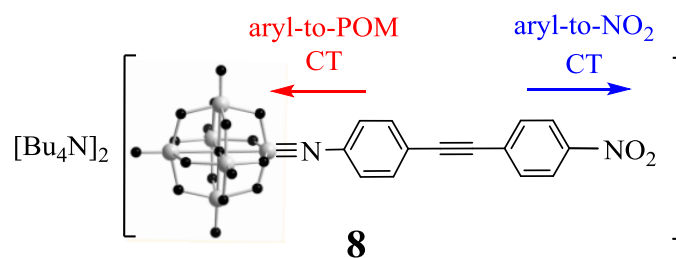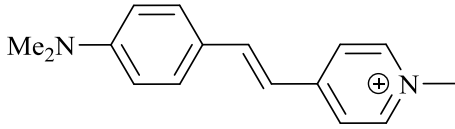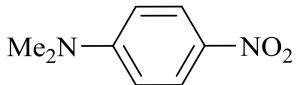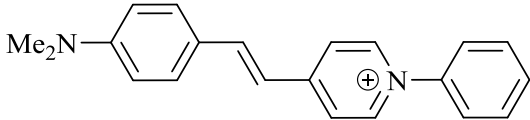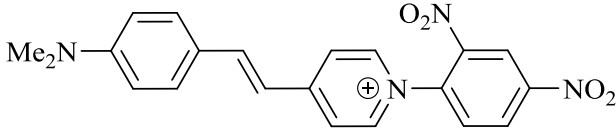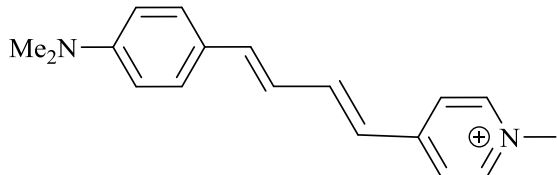
Figure 5.11 Schematic representation of compound **8** showing the two CT directions are opposite to each other, and hence cancelling each other out.

Compound **10** gave a spectrum that can be compared to room temperature electroabsorption data obtained on *N,N'*-dimethylnitroaniline.[260] Inspection of the fit indicates strong charge transfer character due to the dominant contribution of the second derivative. The calculated charge transfer distance of 2.1 Å is significantly longer than that in the literature for the nitro analogue of 1.3 Å, compound **25** in table 5.4. This suggests that the increased charge separation is due to the participation of POM, lengthening the charge transfer distance. In compound **9**, the fit is even more dominated by the second derivative indicating strong charge transfer character. The dipole moment change and charge transfer distance are longer than compound **10** due to the longer-π system. When comparing to stilbazolium chromophores with a single bridging alkene (compound **22** and **26** in table 5.4) which have r_{12} of 3.4 Å and corresponding $\Delta\mu_{12}$ of 16.2 D, the charge transfer distance in **9** is longer at around 4.5 Å, and the corresponding $\Delta\mu_{12}$ is 21.62 D. This distance is longer than would be expected if the charge transfer were extended one bond onto imido N. In fact, the distance is even longer than typically seen (around 4.2 angstroms) in extended stilbazoliums containing two double bonds in the bridge (compound **28**),[251,252] as seen in Table 5.4, and is also longer than in stilbazoliums with nitro functionalities as secondary acceptors (compound **27**). These results are in agreement with Raman results and strongly imply that initial electron transfer (ET) involves the POM framework, as Stark will only provide information on initial ET events, not subsequent processes.

Table 5.4 Literature organic chromophores with their r_{12}, and $\Delta\mu_{12}$ values for comparison with organoimido-POMs

	Structure	r_{12} / Å	$\Delta\mu_{12}$
22	Me$_2$N—(structure: stilbazolium with N-methyl pyridinium)	3.4	9.1
25	Me$_2$N—NO$_2$	1.3	6.2
26	Me$_2$N—(structure: stilbazolium with N-phenyl pyridinium)	3.4	9.4
27	Me$_2$N—(structure with O$_2$N and NO$_2$ substituted phenyl on pyridinium)	3.8	9.5
28	Me$_2$N—(structure: extended diene with N-methyl pyridinium)	4.2	10

Therefore, it seems that the long charge transfer distance due to the involvement of the POM gives an unusual high $\Delta\mu_{12}$ (dipole moment change) for the length of organic system employed. However, μ_{12} remains comparable to typical organics (e.g. stilbazoliums). Interestingly, this high $\Delta\mu_{12}$ is achieved without the large red shift that would occur if $\Delta\mu_{12}$ were to be increased by typical organic means (e.g. extending π-conjugation). Therefore, this unusual high charge separation seems to be the reason that causes such strong NLO performance of these derivatives, which is similar to that in the TICTOID systems.[56,261] In short chromophores, the electron number adjusted β values are further above "the apparent limit", as the effect of POM will be stronger

when organic system becomes smaller. These results are also consistent with those of Su *et.al.*[190,193,262,263] who showed in their calculations that LUMO are located on POM, and HOMO on organic system (although for organic systems with no strong donor group) with relatively little spatial overlap leading to strong charge separation.

Chapter 6

*POM-based polymeric films and surface characterisation*

Electropolymerisation permits the direct deposition of a thin, well-adhered, and highly conductive polymer films onto electrode surfaces. In this work, we have chosen pyrrole and carbazole as units for construction of new electropolymers, covalently functionalized with certain POM clusters as redox active units. This chapter describes the production of three *N*-substituted pyrrole-functionalized POM films, based on compounds **3**, **4**, and **14** (for comparison purpose) and one carbazole-functionalized POM film, compound **12**, these are shown in Scheme 6.1. It also presents the study of the conditions required for electrochemical polymerization of the monomers described in chapter 2. Surface functionality is identified by the use of reflectance fourier transform infrared spectroscopy (RFT-IR), X-ray photoelectron spectroscopy (XPS), and EDX. Surface morphology features are investigated by scanning electron microscopy (SEM) images. SEM-FIB (Focused Ion Beam)[264,265] and transmission electron microscopy (TEM) techniques are used to determine and explore the cross section-area and features respectively. To the best of our knowledge, this is the first work on electropolymerized-conjugated polymers covalently functionalized with Lindqvist clusters.
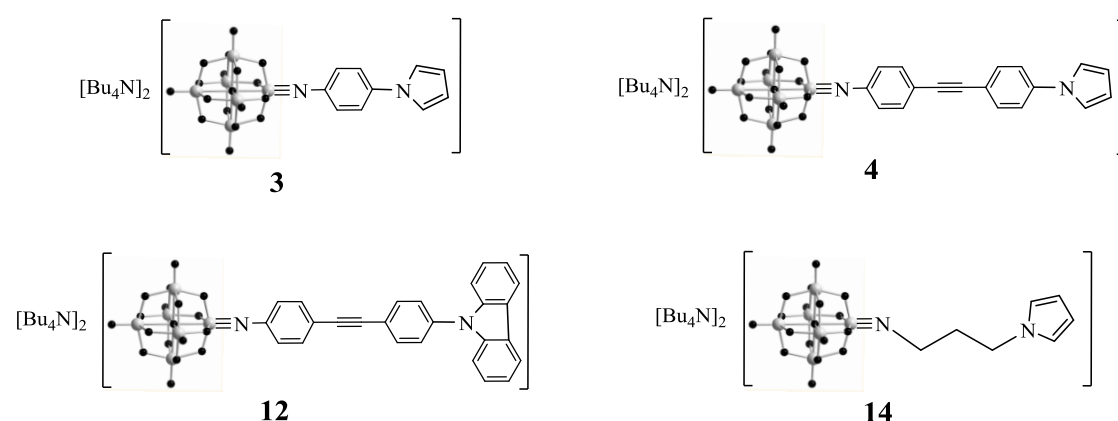
Scheme 6.1 Structures of POM-based derivatives **3, 4, 12**, and **14**.

6.1. Polypyrroles and polycarbazoles

Conjugated polymers are of interest as NLO materials due to their large second-order and also third-order nonlinearities, fast response, and their ease of fabrication for targeted applications. One of the most important characteristics of these conducting polymers is their reversible redox properties. They can be considered as semiconductors, with a partially filled valence band and an empty conduction band separated by an energy gap. For example, polypyrrole polymers are insulators in the reduced form, while in the oxidized form are conducting polymers where the polypyrrole is partially charged via electrochemical process (applying a positive potential), as shown in Scheme 6.2. The conducting polymers are attractive candidates for applications in optoelectronics as they can combine interesting optical and electrical properties, such as photoluminescence (PL), and electroluminescence (EL).[266,267] These include polypyrroles, polythiophenes, polycarbazoles, and polyanilines; however, they are relatively little studied in NLO.
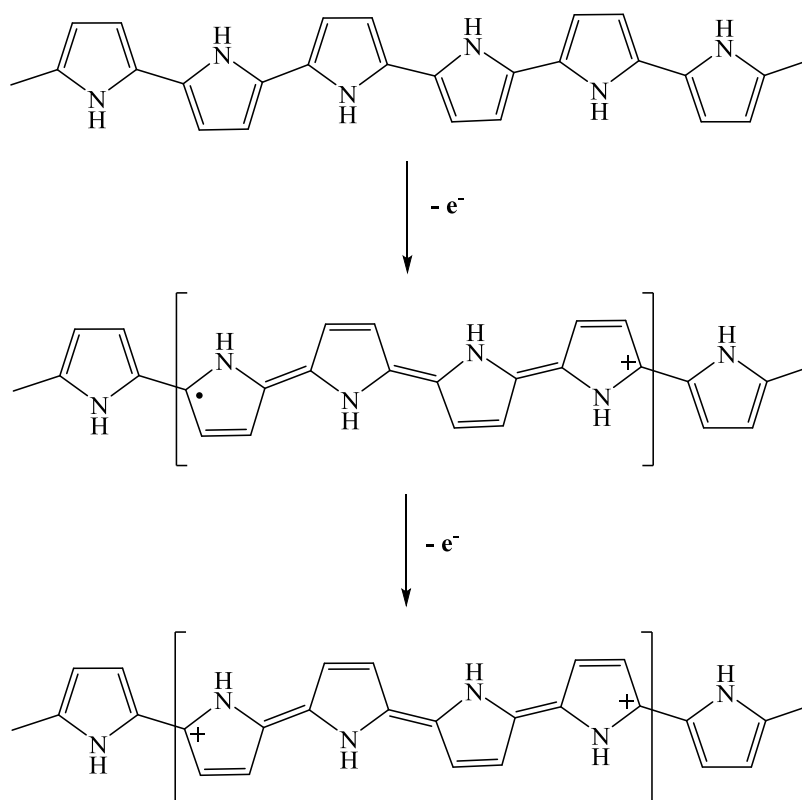
Scheme 6.2 Electronic steps showing the formation polaron and bipolaron resulting in partially charged polypyrrole.

Conducting polymers can be produced by either chemical or electrochemical methods. The first synthesis of conducting polymers was reported by Letherby and co-workers in 1862 with the formation of polyaniline in dilute sulphuric acid.[268] Later, Shirakawa *et al.* studied the effects of anionic doping on the conductivity of the these polymers.[269] The conducting nature of these polymers comes from their conjugated backbone, consisting of alternating carbon-carbon single and double bonds. Many of conducting polymers are electron donors upon photo-excitation especially in their neutral (semiconducting) state such as pyrrole and carbazole. Several studies investigating the properties of these polymers such as electrical conductivity, and redox properties have been carried out.[270-272] It has conclusively been shown that these intrinsic properties are highly dependent on the polymerisation conditions such as pH, temperature, solvent, electrolyte, and monomer substitutions.[271,273-275]

In the last two decades, research has been focused on pyrrole-based polymers due to their structural versatility, stability, high conductivity, electrochemical properties, ease of modification via either structural derivations or copolymerization, and finally ease of generation chemically or electrochemically.[170,276] The electrochemical polymerisation method has been applied to produce polymeric films on the electrode surface allowing the possibility of controlling the size, thickness, and shape of films. Based on these properties, polypyrroles offer many advantages in the fabrication of many electronic and optical devices such as thin films transistors, Schottky diodes, hybrid solar cells, switches, and light-emitting diodes (LED).[277-280] In the field of NLO materials, Janamurugan and co-workers reported the first study on the NLO properties of polypyrrole polymers in 2010.[281] They noticed the occurrence of the SHG in polypyrrole powders synthesized by a chemical oxidative polymerization method at room temperature.

The mechanism proposed by Diaz *et al.* for pyrrole polymerisation is the most commonly referred to throughout the literature, and is thought to stand even for

substituted pyrroles.[282,283] In this mechanism, the initiation step involves electron transfer followed by a series of chemical reactions, as illustrated in Figure (6.3), resulting in well-adhered film on the electrode surface However, it is shown that *N*-substituted pyrroles exhibit three times lower conductivity than the parent pyrroles and in some cases the *N*-functionality can inhibit the polymerisation process by either steric hinderance or nucleophilic attack on the polymerizable unit..

Monomer Oxidation

Dimer formation

Chain propagation
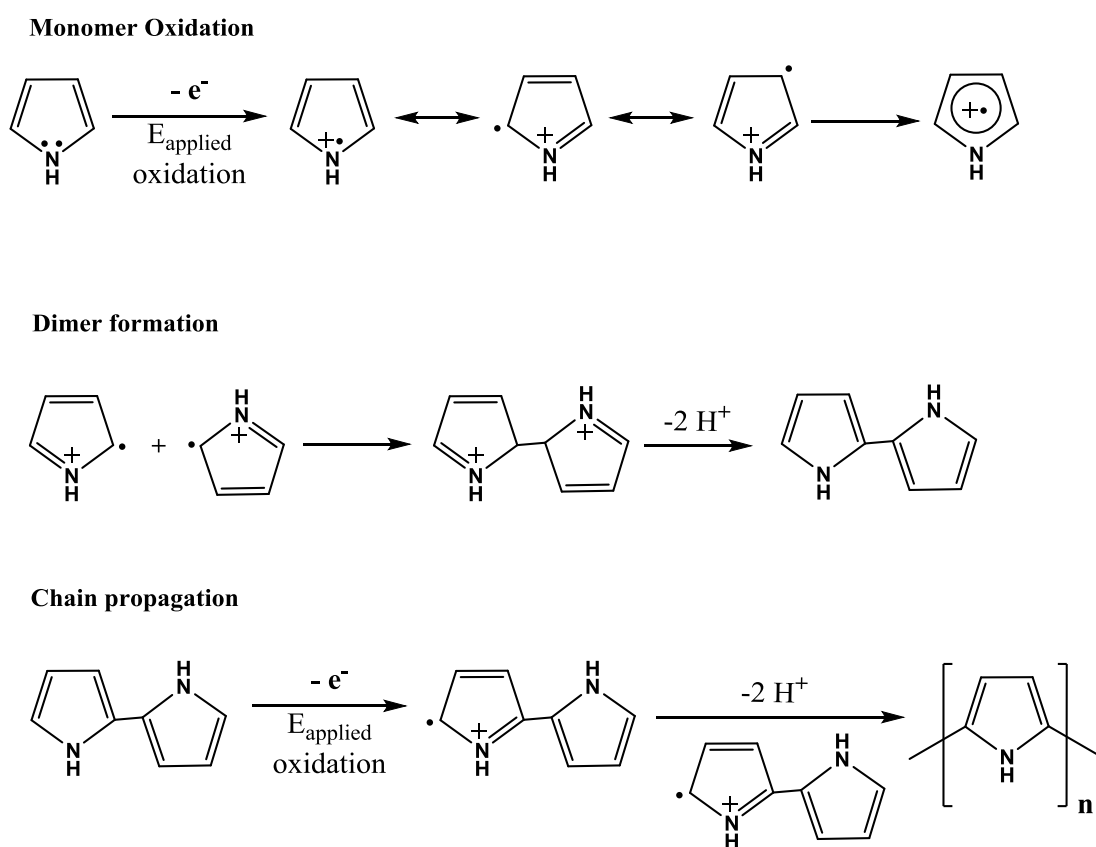
Figure 6.3 The classical mechanism for the electropolymerisation of pyrrole.

Carbazole is an analogue of fluorene, consisting of a nitrogen-bridged biphenyl. However, the chemistry of carbazole is very different from fluorene due to the electron donating effect of the nitrogen atom. Carbazole is very stable to environmental and chemical degradations, and it can be easily derivatised via its nitrogen group and also via the 3, and 6-positions.[284] Therefore, carbazoles have also been widely investigated and used as building blocks in the field of conducting

polymers for many electronic and photonic applications.[285-289] Polycarbazole is one of the most important conducting polymers due to its photoconductive and electron donating properties. For instance, it has been used as a blue light emitter in LED devices.[287] Only poly (3,6-carbazole) can be made via oxidative polymerisation. Polycarbazole can also be made by the anodic electropolymerisation of the precursor monomer, where the carbazole is oxidised to form a cationic radical.[290-292] These radicals couple to form oligomers, dimers, and also another cationic carbazole molecule and after many cycles of this process, a film of the polymer is formed on the electrode surface, as shown in Figure (6.4).
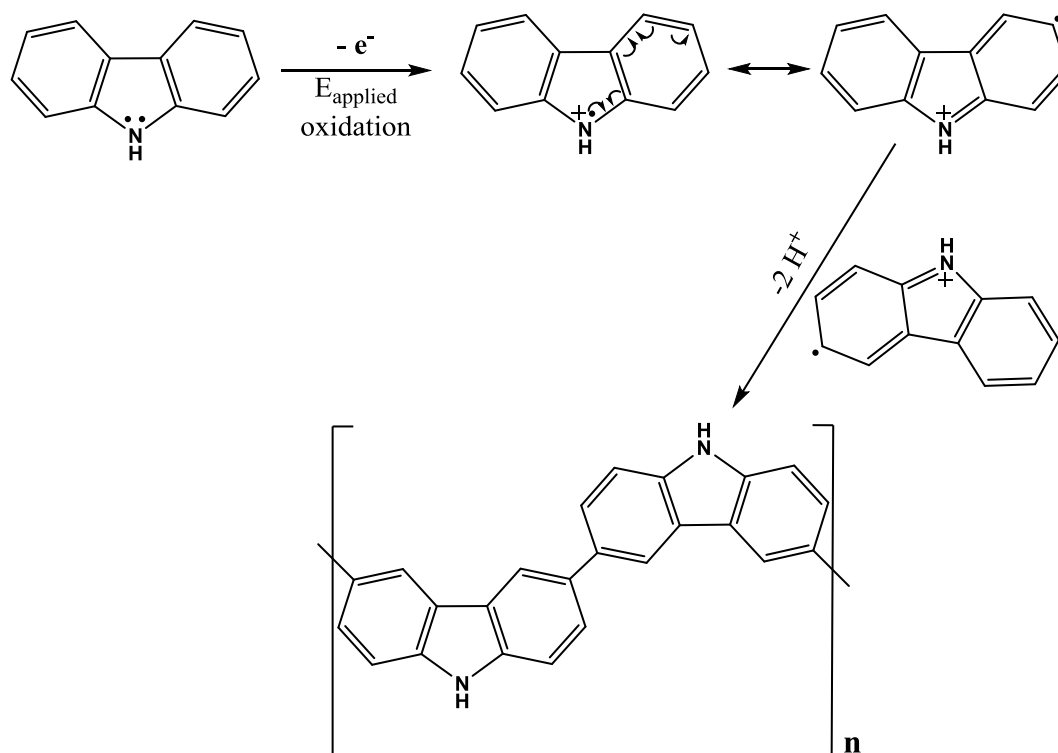

Figure 6.4 Proposed mechanistic scheme for the electropolymerization of carbazole.

6.2. Film formation by electropolymerisation

Various electrochemical techniques such as potentiostatic (controlled-potential), galvanostatic (constant-current), and potentiodynamic (scanned-potential) can be used to achieve electropolymerisation resulting in deposition of a film on the electrode

surface. Cyclic voltammetry, a potentiodynamic (scanned-potential) technique, can be used as a method of producing and monitoring the growth of the conducting polymer film on the surface. A current-potential diagram resulting from CV studies can be used to investigate the reversibility of electron transfer. The ability of monomers to electropolymerise (produce polymeric films) can be assessed by performing CV studies.

For instance, the CV studies of pyrrole polymerization show monomer oxidation (formation of the cation radical oxidized pyrrole) and the oxidation and reduction of the polymer film subsequently formed on the electrode surface. Figure 6.5 shows the current-potential diagram for pyrrole electropolymerisation on a platinum electrode in 0.1 [NBu$_4$][BF$_4$]-MeCN solution with the potential referenced to an aqueous Ag/AgCl electrode. The CV was scanned from -0.5V to 1V at a scan rate of 100 mV/s for 10 cycles.
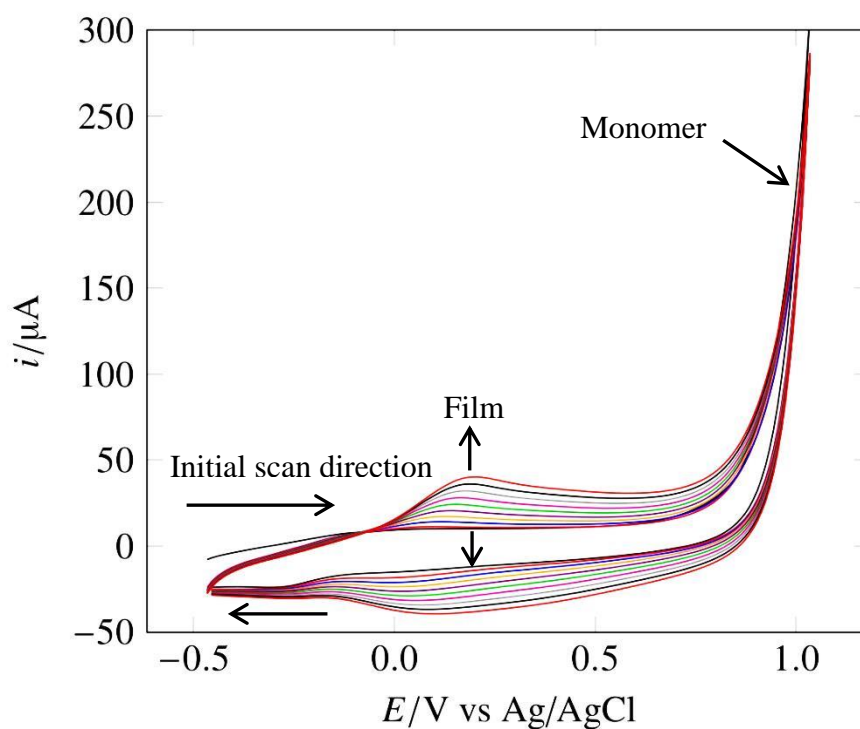

Figure 6.5 CVs of poly(pyrrole) formation on Pt surface in 0.1 [NBu$_4$][BF$_4$]-MeCN solution with aqueous Ag/AgCl reference electrode, at a scan rate of 100 mV/s.

6.2.1 Polypyrroles-based materials

Electropolymerisation of Monomers

CV studies were carried out to investigate the ability of monomers **3**, **4**, **12**, and **14** to polymerise and produce polymer films. The experiments were carried out in a standard 0.1 [NBu$_4$][BF$_4$]-MeCN solution with 2×10^{-3} M of each monomer in a three compartment electrochemical cell. During these experiments, all conditions such as temperature, solvent, electrolyte, and monomer concentrations were kept the same. None of pyrrole-functionalized compounds (**3**, **4**, and **14**) showed any sign of polymerisation, even when the applied potential is increased significantly (up to +1.8 V). Peak monomer oxidation potentials were noticed at 1.4 V for these derivatives (shown in Figure 6.6); however, subsequent oxidations resulted in poor and broad peak currents with no film deposited onto the electrode surface. This is not surprising, as *N*-substituted pyrroles often show a lack of polymerization, due to steric hindrance (presence of the sterically demanding phenyl ring and [Mo$_6$O$_{18}$]$^{2-}$ cluster), and possibly nucleophilic attack from the negatively charged [Mo$_6$O$_{18}$]$^{-2}$ cluster.[293-296]
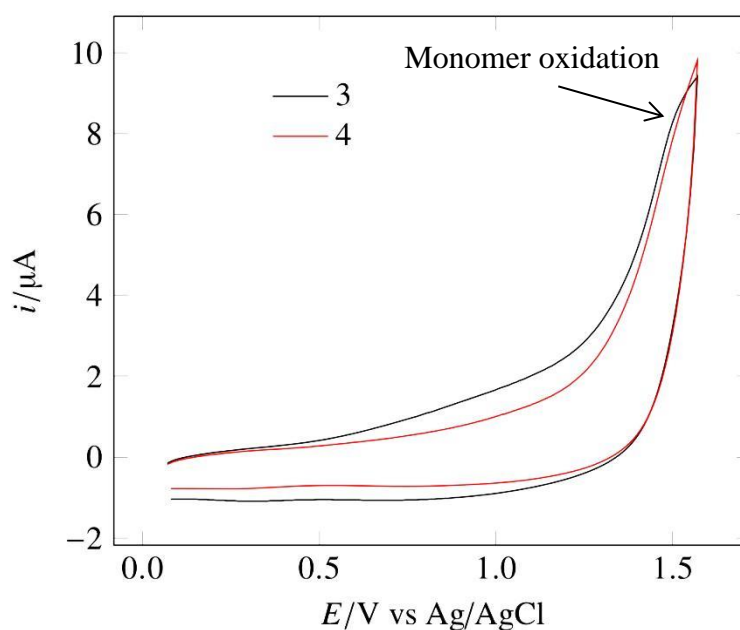

Figure 6.6 CVs showing the peak oxidation at 1.4 V of monomer **3** (blue trace) and **4** (red trace) using glassy carbon (GC) at scan rate of 100 mV/s.

Co-polymerisation has been shown to be one solution for such problems, where a polymerizable monomer is mixed with the desired monomer.[274,295] Thus, we found that the derivative monomers would co-electropolymerize with underivatized pyrrole at up to 70 mol. % of **3**, and **4**, and up to 90 mol. % of **14** on Pt, graphite and fluorine tin oxide coated glass (FTO).

Figure 6.7 shows the CV studies of the co-electropolymerisation of **3** : Py (pyrrole) at 70 : 30 % ratio. These have characteristic features showing oxidation of the co-monomers to form radical cations, and the subsequent oxidation and reduction of the co-polymer film. The experiment was carried out with a FTO working electrode with standard conditions mentioned for earlier experiments for 10 cycles and this resulted in a matt black colour (reduced state) deposited film onto the FTO surface (Figure 6.8a). Importantly, the peak oxidation potential is positively shifted (by *ca.* 0.4 V) compared to underivatized pyrrole. This can be attributed to the presence of compound **3**, and is consistent with the literature, where functionalization of pyrrole, especially N-substituted, may introduce electronic effects that shift the oxidation potential of the monomer.[296] This change in potential implies the involvement of monomer **3** derivative in polymerisation reactions and hence suggests the formation of polymer chains possessing a distribution of the derivativatised and underivatized pyrrole units.

Compound **4** was co-polymerized with pyrrole in the same conditions used for **3** (mentioned above), and the film was gold / yellow in the reduced state (neutral). It is shown in Figure 6.8b. Compound **14** was co-polymerized with pyrrole at similar fashion to compounds **3**, and **4**, at 90 mol. % of **14** to form a matt black film in the reduced state (Figure 6.8c). It is not clear why different film colours have been obtained for these materials, but it may be related to steric and derivatisation effects.
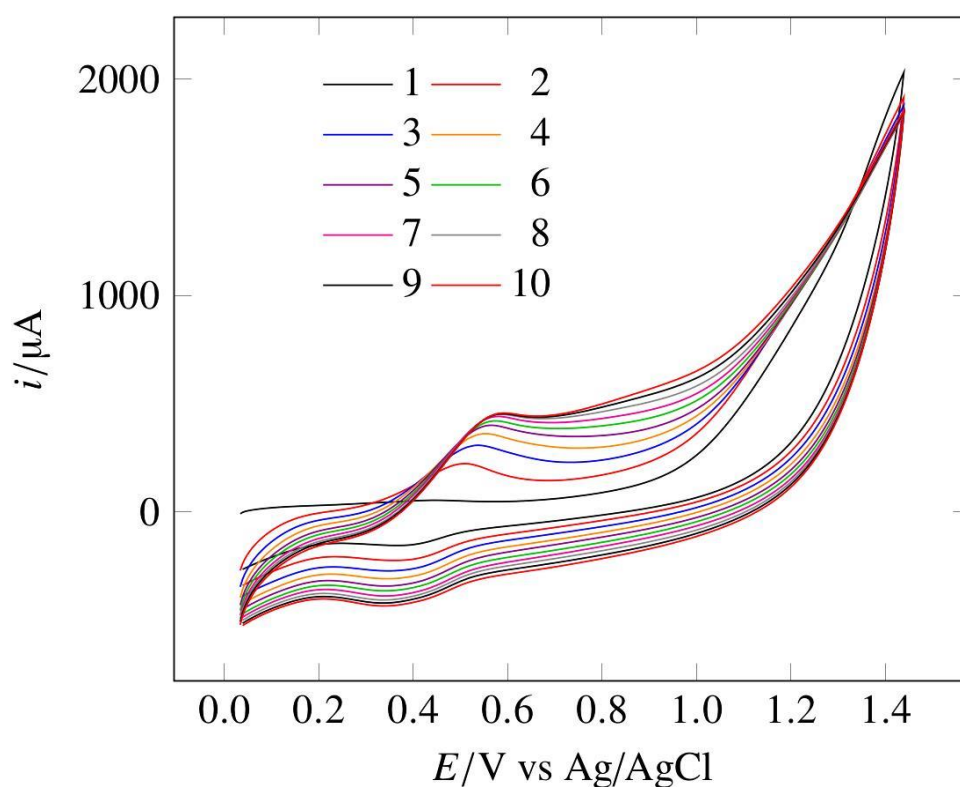
Figure 6.7 CVs showing co-electropolymerization of **3** and pyrrole (70:30 ratio) on FTO, were run from 0V to 1.4V at scan rate of 100 mV/s for 10 cycles. Note the higher potential required for electropolymerization *vs* underivatized pyrrole, strongly implying involvement of the derivative monomer in the polymerization process.

Figure 6.8 FTO electrodes coated with: a) co-polymer of **3** : Py at 70:30 % ratio, b) co-polymer of **4** : Py at 70:30 % ratio, and c) co-polymer of **14** : Py at 90:10 % ratio. The colours are obtained for the reduced states of these polymeric films.

Electrochemical properties of the polymers

The electrodes coated with polymeric films were washed with freshly distilled acetonitrile and dried before investigating the reduction of the {Mo_6} units. The electrochemical experiment was carried out in 0.1 M [NBu_4][BF_4]-MeCN, at different sc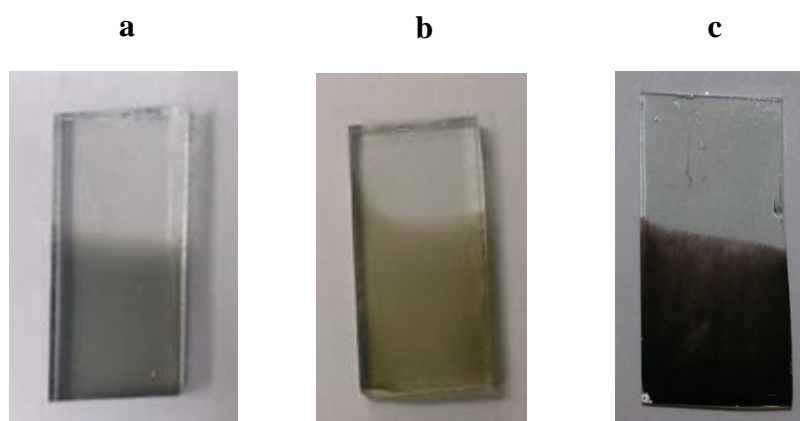an rates using one compartment electrochemical cell under an atmosphere of inert gas such as Ar or N_2. Figure 6.9 shows the CV response from 10 cycles of **3**-Py co-polymer film. The film shows a well-defined reversible electrochemical behaviour at a slightly more negatively shifted redox potentials to the monomer at -0.55 V and fast redox process on the CV time scale. The smaller peak potential separation of 40 mV of the film compared to monomer **3**, confirms the presence of a surface confined POM species.
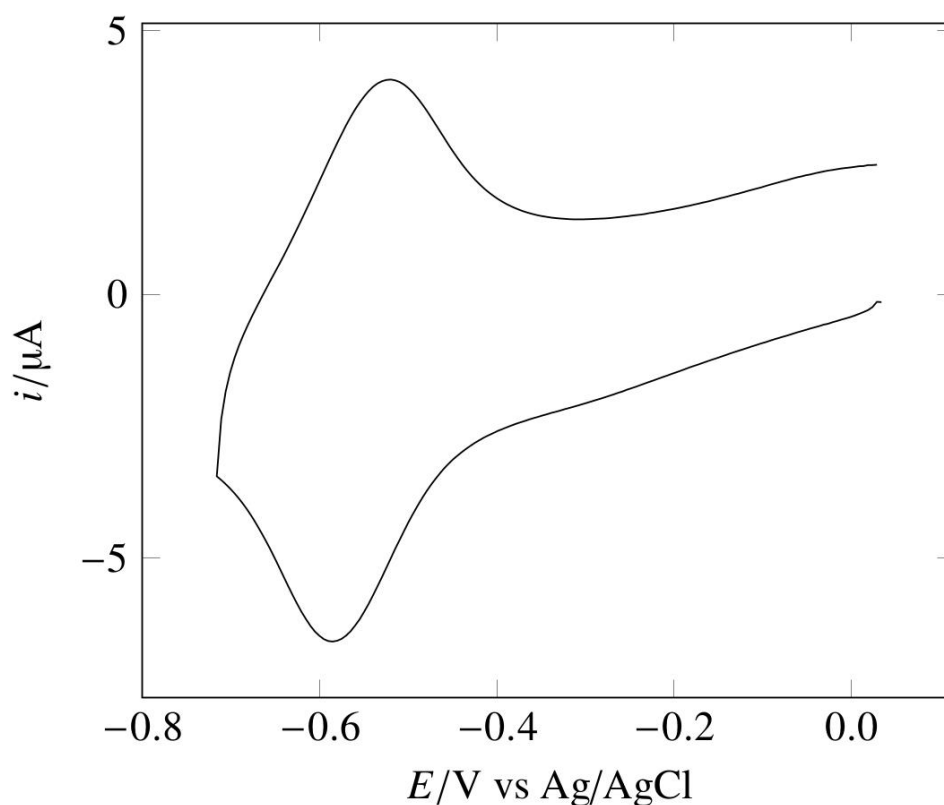

Figure 6.9 CV showing {Mo_6} redox wave in the Py-**3** co-polymer, 0.1 M [NBu_4][BF_4] in MeCN, scan rate 100 mV/s, working electrode glassy carbon of 7 mm^2 surface area.

In order to investigate the film stability, consecutive cyclic voltammograms were carried out from 0V to -0.75V at 100 mV/s scan rate in 0.1 M [NBu$_4$][BF$_4$]-MeCN for 60 cycles, on the film 10 deposition cycles. On the CV timescale the resulting film of the polypyrrole-**3** co-polymer can undergo around 15 redox cycles (Figure 6.10) with only minimal changes, indicating the high stability of this films, due to the covalent linkage between the derivative and pyrrole units. This is clearly noticed when comparing polypyrrole-**3** with an analogue made by the inclusion of [Mo$_6$O$_{19}$]$^{2-}$ in polypyrroles, the latter showed a large decrease in the current intensity with shifting to less negative potential when moving from the redox cycle 1 to 20 (Figure 6.11). This has not been seen in the case of polypyrrole-**3** co-polymer

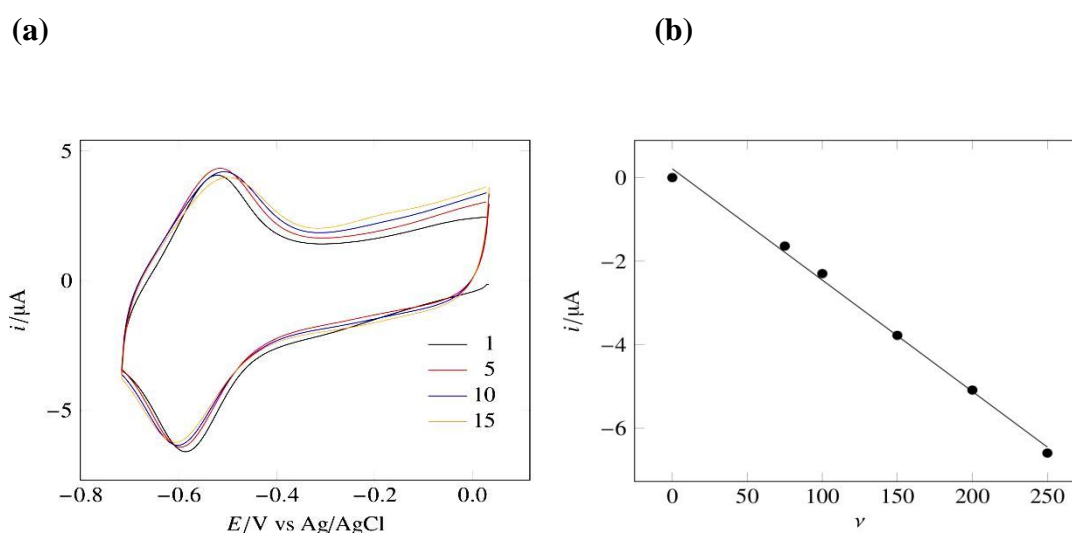**(a)**   **(b)**

Figure 6.10 (a) Consecutive cyclic voltammograms of a polypyrrole-**3** film showing minimal changes from redox cycle 1 to 15. Electrolyte is 0.1 M [NBu$_4$][BF$_4$] in MeCN, scan rate 100 mV/s, working electrode glassy carbon. **(b)** A plot of current peak I_p^c vs the scan rates (v) for reduction of polypyrrole-**3** co-polymer film**.**
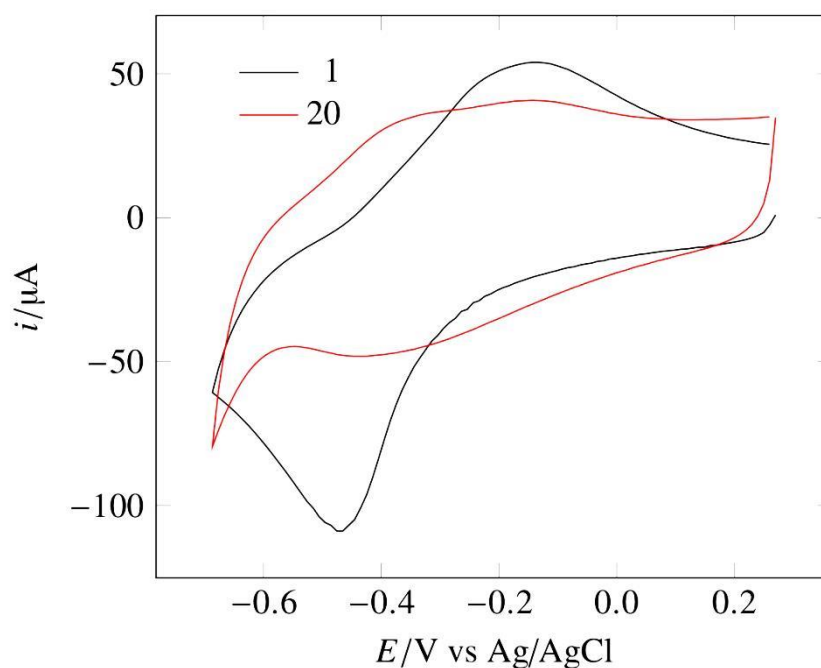
Figure 6.11 CVs of $[Mo_6O_{19}]^{2-}$ -polypyrrole inclusion film showing the leaching out of anion after the first redox cycle. Electrolyte is 0.1 M $[NBu_4][BF_4]$ in MeCN, scan rate 100 mV/s, working electrode glassy carbon.

To this end, we wondered whether the increased bulk of the organoimido POM and the ability of organic fragment to form π-π interaction with pyrrole units causes this stability in the derivative-pyrrole co-polymer. Inclusion films of derivative **2** (iodo functionality) in polypyrrole film which has relatively similar size, and π-character to derivative **3** were prepared and studied to investigate such possible effects. Figure 6.12 presents the CV of **2**-inclusion polypyrrole film of 10 depositions cycles thickness, which shows a very large intensity wave in the first cycle, but a much smaller and shows weaker waves in the second cycle. This indicates the loss of a large amount of the anion as it is reduced due to the charge balance (the anion is expelled after reduction units and is replaced by $[BF_4]^-$ when the pyrrole is oxidized). From cycle 2 to 20, this decrease was smaller, but still occurred as shown in Figure 6.12.
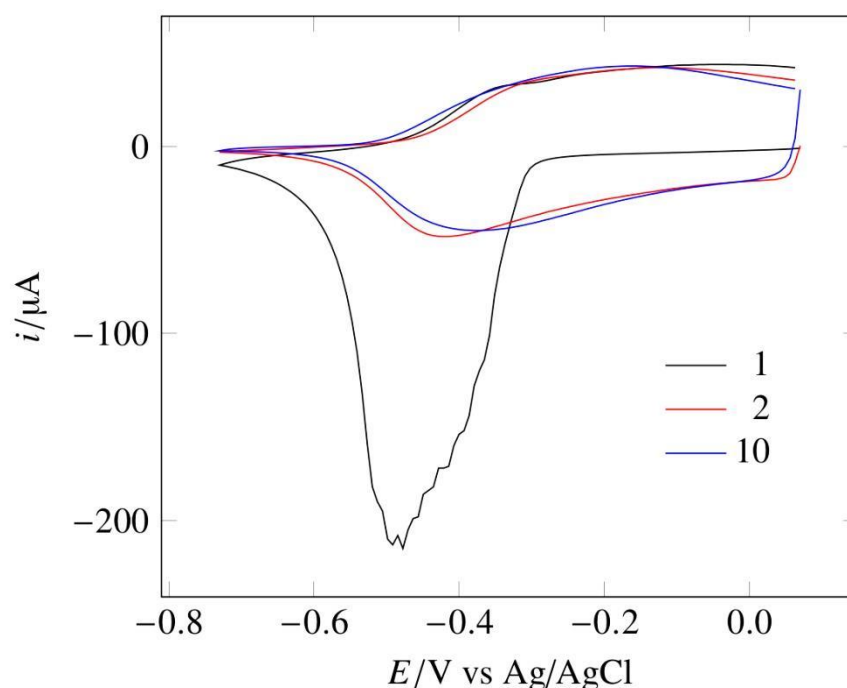
Figure 6.12 CVs of **2**-polypyrrole inclusion film showing the leaching out of large amount of anion after the first redox cycle. The electrolyte is 0.1 M [NBu$_4$][BF$_4$] in MeCN, scan rate 100 mV/s, working electrode glassy carbon.

.

CVs of the **3**-Py co-polymer film from 15 to 60 cycles show the loss of the {Mo$_6$}-imido peak, along with growth of a new peak at less negative potential (shown in Figure 6.13). This is similar to the results from the bulk electro-reduction of the parent monomer described in chapter 4, and the new peak most likely results from [Mo$_6$O$_{19}$]$^{2-}$ produced by hydrolysis, and trapped in the film. The new [Mo$_6$O$_{19}$]$^{2-}$ peak is similar to that obtained from inclusion of [Mo$_6$O$_{19}$]$^{2-}$ in polypyrrole film (shown in Figure 6.14). Similar observations are noted even in CaH$_2$-dried MeCN, working under argon, and using dried-DCM. Similar observations were obtained for the Py-**4** co-polymer films.
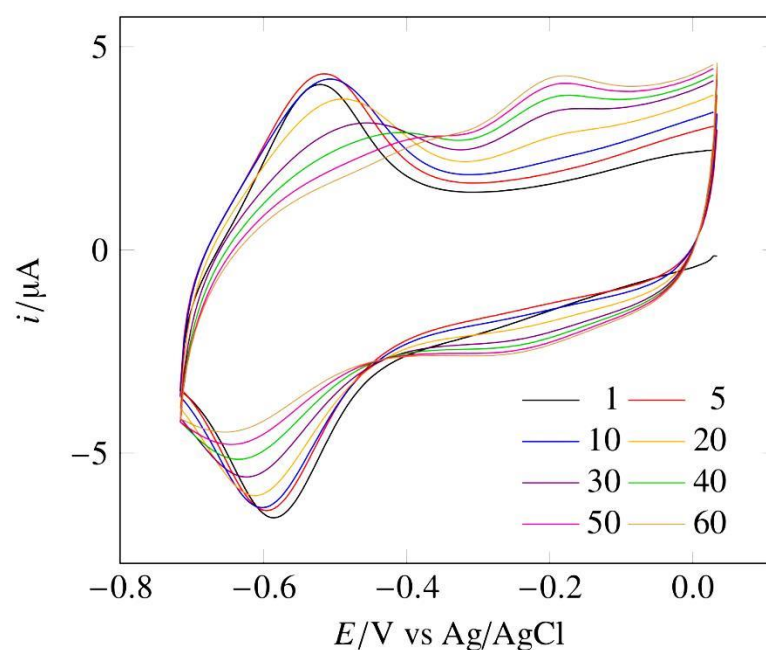
Figure 6.13 Consecutive cyclic voltammograms of a polypyrrole-**3** film showing loss of the imido-Lindqvist peak, and growth of a new peak ascribed to $[Mo_6O_{19}]^{2-}$, over 50 cycles. Electrolyte is 0.1 M $[NBu_4][BF_4]$ in MeCN, scan rate 100 mV/s, working electrode glassy carbon.
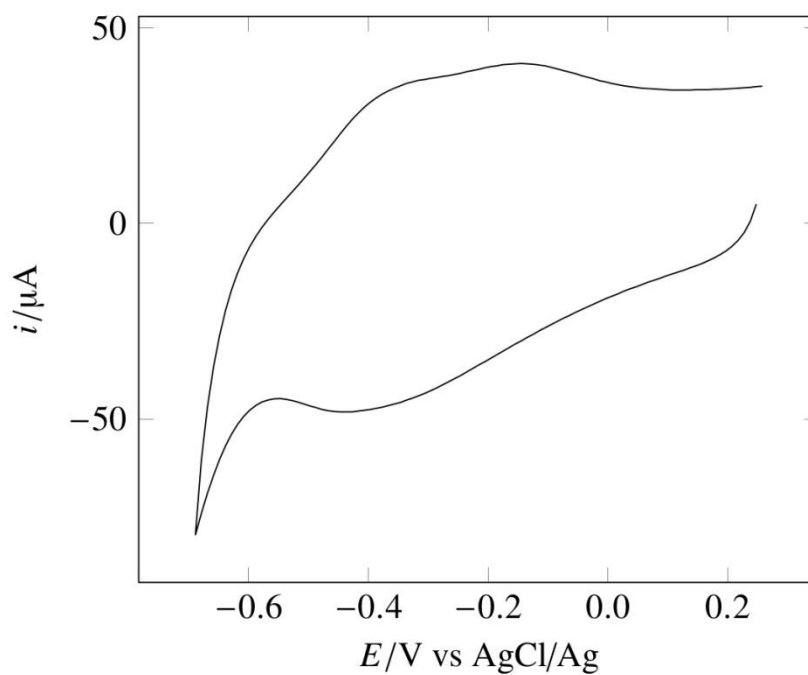
Figure 6.14 Consecutive cyclic voltammograms of a polypyrrole-inclusion $[Mo_6O_{19}]^{2-}$ of 15 deposition cycles film thickness. Electrolyte is 0.1 M $[NBu_4][BF_4]$ in MeCN, scan rate 100 mV/s, working electrode glassy carbon.

The electrogenerated polypyrrole-**14** films were studied by CV in 0.1 M [NBu$_4$][BF$_4$] in MeCN. Figure 6.15 shows the CVs of freshly prepared films of polypyrrole-**14** co-polymers in the ratio of 70 (**14**):30 (Py), and 90 (**14**):10 (Py) at different scan rates. These films indicate that charge transport slows at high loadings of {Mo$_6$}. Peak separations for the {Mo$_6$} reduction are much larger (ca. 360 mV, vs < 50 mV) for films synthesized with a 90 (**14**) : 10 (Py) ratio (Figure 6.14a) than with 70 (**14**) : 30 (Py) (Figure 6.15b). The effect is most noticeable in thick films.

The increased "resistive" behaviour with an increased fraction of {Mo$_6$} derivative is surprising, as higher concentrations of {Mo$_6$} should increase the probability of a charge-hopping mechanism. The effect may be related to diffusion of tetrabutylammonium cations through the film (as seen in Scheme 6.16), which becomes slower as the number of {Mo$_6$} groups increases steric demand and the need for charge compensation due to increased negative charge. Similar behaviour has been reported by other studies.[297-299]

(a)

(b)
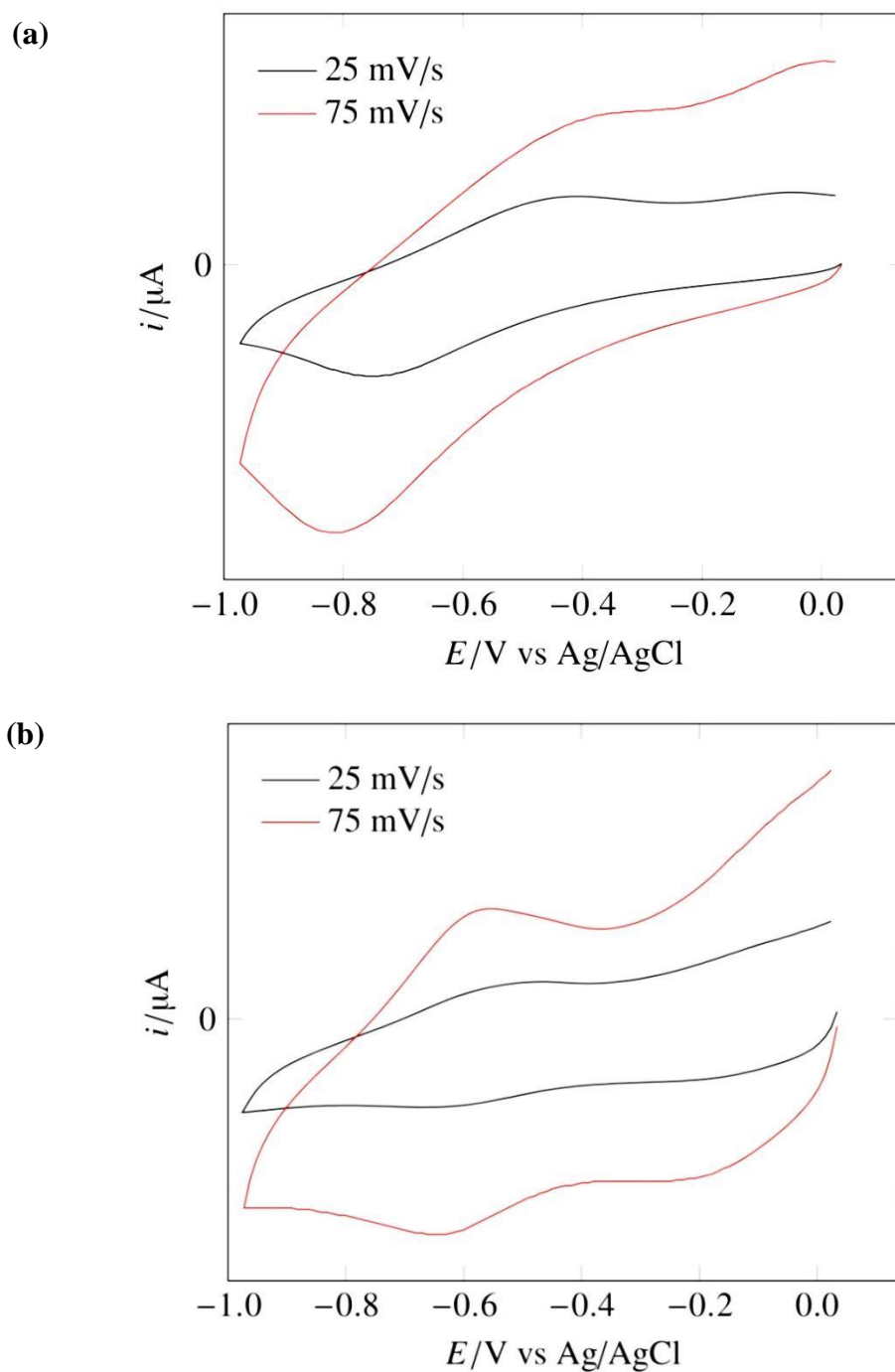
Figure 6.15 CVs showing {Mo$_6$} redox wave in the: **(a)** 90(**14**) : 10(Py) ratio, and **(b)** 70(**14**) : 30(Py) ratio co-polymer, in 0.1 M [NBu$_4$][BF$_4$] in MeCN, at scan rates 25 (black traces) and 75 (red traces) mV/s.
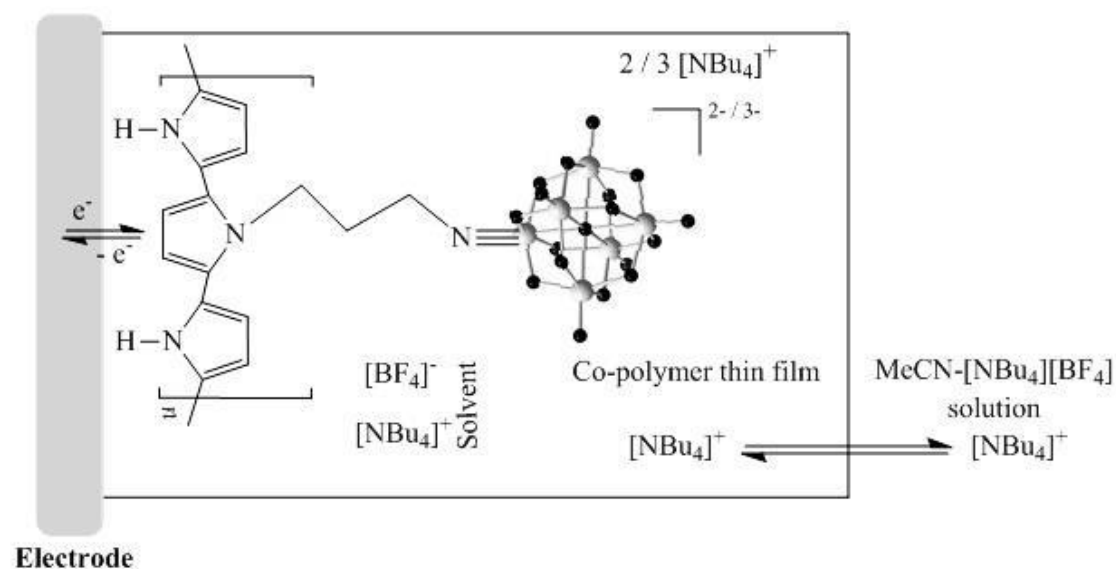
Scheme 6.16 Schematic representation of diffusion of tetrabutylammonium cations at a thin film of polypyrrole-**14** co-polymer.

6.2.2 Spectroscopic characterization and morphology of the polymer films

Reflectance Fourier-transform (FT) IR characterization

The polypyrrole-**3** co-polymer was studied by reflectance FT-IR spectroscopy to identify the surface functionalities. Fresh films of the co-polymer were deposited on platinum (Pt) working electrode, then washed with fresh MeCN and allowed to air dry with no marking of cracking or peeling. Spectra were measured against the uncoated polished Pt electrode, and the spectra were compared with those for monomer and polypyrrole only films. The FT-IR spectrum of monomer **3** (Figure 6.17) showed the characteristic Mo=O stretch at 940 and an imido stretch Mo=N at 947 cm^{-1}.
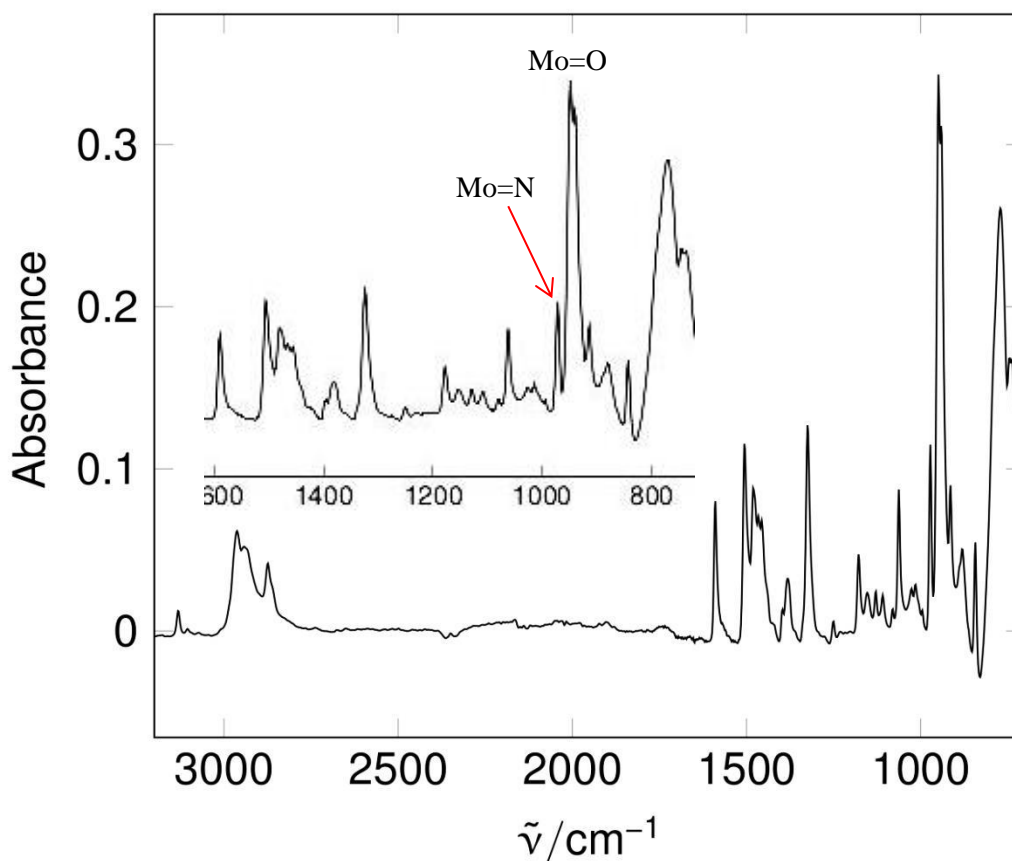
Figure 6.17 FTIR spectrum of monomer **3** using ATR technique showing the characteristic Mo=O stretch at 940 and an imido stretch Mo=N at 947 cm^{-1}.

When comparing **3** with its corresponding co-polymer (Figure 6.18, red trace), the latter showed a shift in the position and a combination of these functional groups (Mo=O and Mo=N) between 950-916 cm^{-1}. Figure 6.17 presents the reflectance FT-IR spectra of polypyrrole-**3** co-polymer (black trace) and polypyrrole only (red trace), showing a clear difference to undervitized polypyrrole with the presence of $[BF_4]^-$ peak at 1070 cm^{-1} in both films, which is consistent with the literature.[300]

Studying the other materials (**4**, and **14**-polypyrrole co-polymer) by reflectance FT-IR spectroscopy has been attempted, but we could not obtain adequate quality spectra.
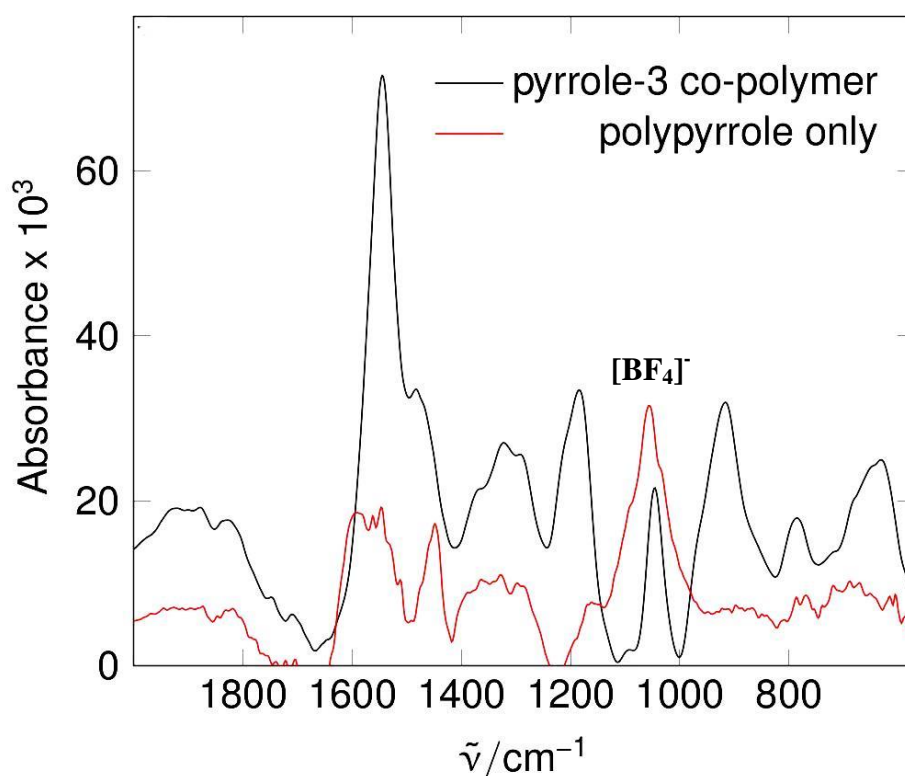
Figure 6.18 Reflectance FTIR spectrum of a Pt disc electrode coated with polypyrrole only (red trace) and the polypyrrole-**3** co-polymer (red trace).

UV-vis spectroscopy

The polypyrrole-**3**, and polypyrrole-**4** co-polymer films deposited on FTO glass were studied by UV-vis spectroscopy before (at potential of 0 V) and after full reduction (at potential of − 0.75 V) of {Mo$_6$} units in the films. The results are shown in Figure 6.19. In the case of the polypyrrole-**3** co-polymer, the UV-vis of the reduced film shows some sort of structural changes that led to an increase in the background absorption of the spectrum, but there is a more clearly resolved peak in the region where monomer **3** shows an absorption band between 350-380 nm.
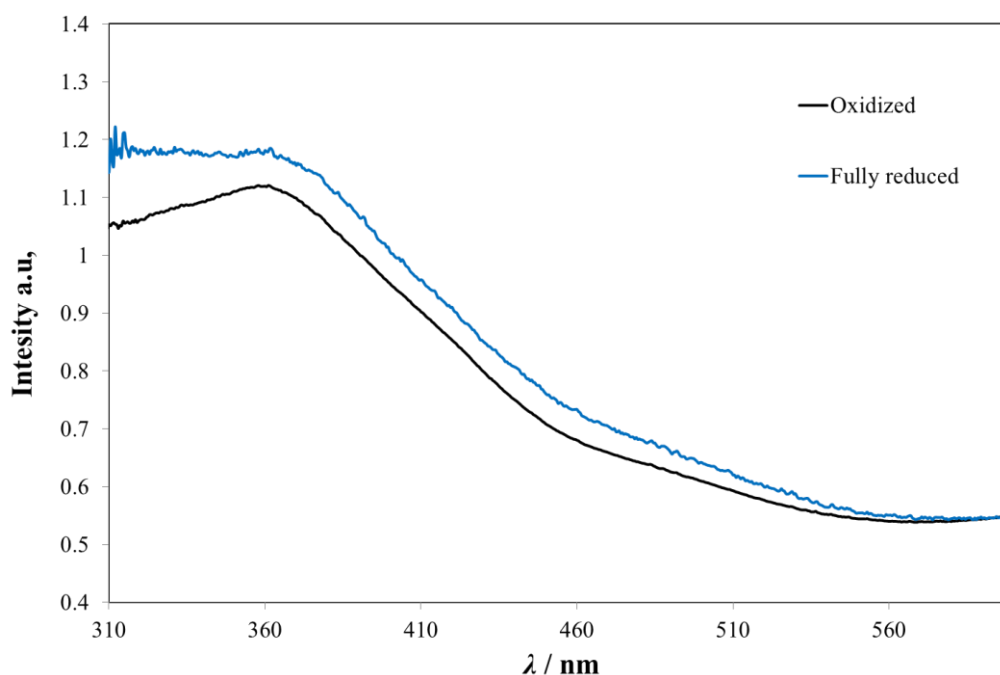
Figure 6.19 UV-vis spectra of polypyrrole-**3** co-polymer film, 20 deposition cycles thickness on FTO glass, showing the difference between the oxidized (black trace), and in the fully reduced state (blue trace) absorption.

The UV-vis results of the polypyrrole-**4** co-polymer film showed more clear changes (decrease) in the absorption band upon reduction (Figure 6.20), which is in agreement with the hypothesis of hydrolysis of the derivatives leading to such decrease in the absorption, just like the spectroelectrochemistry results for the corresponding monomer in Chapter 4. The SEM-EDX of the prepared film showed a large change in the % ratio between carbon (C) and molybdenum (Mo) upon reduction, in the oxidized form the ratio is 10 : 1 (C : Mo) and is 15 : 1 (C : Mo) upon reduction. This increase in the C % ratio is consistent with hydrolysis of $\{Mo_6\}$ derivative, and its leaching out into the solution.
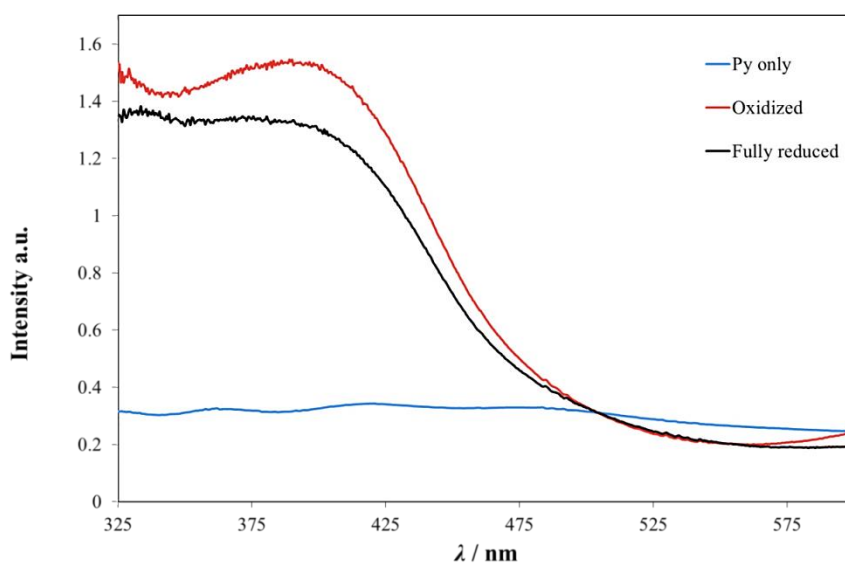
Figure 6.20 UV-vis spectra of polypyrrole-**4** co-polymer film with polypyrrole only (blue trace) film as a reference, 20 deposition cycles thickness on FTO glass, showing a clear change in the absorption between the oxidized (red trace), and the fully reduced state (black trace).

XPS characterization

Polypyrrole-**3** co-polymer was the only polymer that could be assessed by reflectance FT-IR spectroscopy. Therefore, XPS was used to identify elements and their chemical states present in the surface of the samples by irradiating the FTO electrode coated with polymer films with an X-ray and measuring the kinetic energy of surface electrons.[301] Figure 6.21 shows an XPS spectrum representative of the Mo3d core level for the polypyrrole-**4**, polypyrrole-**3**, polypyrrole-1**4** co-polymers.

The principal doublets obtained are Mo(VI), as labelled in Figure 6.21, corresponding to the Mo^{6+} state. Similar features were seen for different film thicknesses. The XPS was able to provide elemental compositions of the surfaces in atomic % (Table 6.1), with a ratio between the POM-derivatised monomer and the underivatised pyrroles in these films to be 1 to 2 for most cases. It has been shown in the literature that polypyrrole has a charge of + 0.33 per monomer in its reduced state.[302] If there was a

charge inclusion of the POM derivatives, one would therefore expect 6 underivatized pyrrole units for each POM unit. These results are therefore consistent with covalent connection.
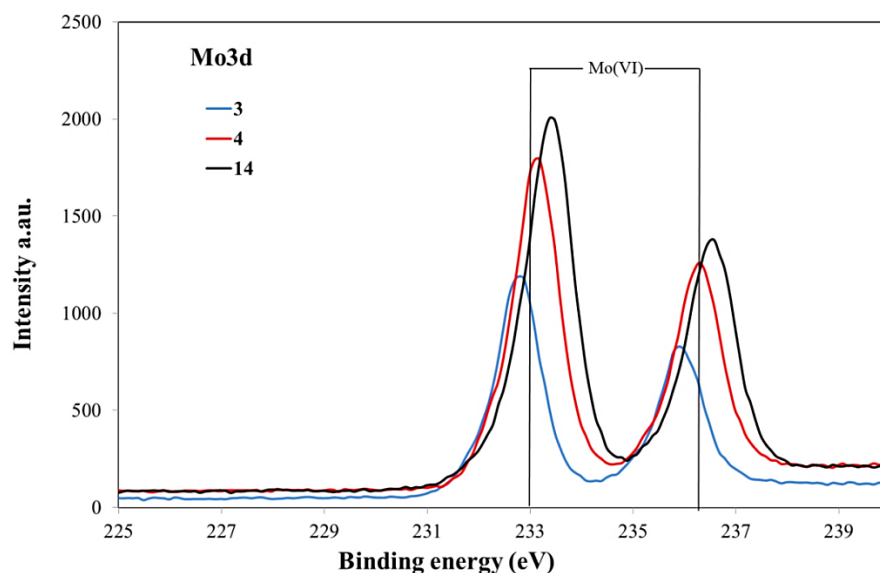
Figure 6.21 XPS spectrum of the Mo3d core levels for polypyrrole-**4** (red trace), polypyrrole-**3** (blue trace), and polypyrrole-**14** (black trace) co-polymers of 20 deposition cycles film thickness.

Table 6.1 XPS surface elemental analysis of different film thicknesses of polypyrrole-**3** co-polymer, polypyrrole-**4** co-polymer, and polypyrrole-**14** co-polymer

Co-polymer / % ratio / film thickness cycles	Elemental Abundance (Atomic %)						
	C 1s %	F 1s %	Mo 3d %	N 1s %	Na 1s %	O 1s %	S 2p %
polypyrrole-**3** / 30-70 / 20	69.16		6.96	5.23	0.34	17.25	1.05
polypyrrole-**4** / 30-70 / 10	75.76		4.70	4.63	0.00	14.00	0.92
polypyrrole-**4** / 30-70 / 20	75.49		5.00	5.16	0.01	14.17	0.17
polypyrrole-**4** / 30-70 / 30	72.34		5.90	4.19	0.00	17.27	0.31
polypyrrole-**14** / 30-70 / 20	67.14		8.29	3.92	0.00	19.93	0.72
polypyrrole-**14** / 10-90 / 20	65.11		7.72	4.56	0.44	20.84	1.33
Polypyrrole / 100 / 20	73.36	0.38	0.22	8.93	0.25	14.44	2.43

Morphological studies

The morphology of polypyrroles has been shown to uneven; however *N*-substituted pyrroles have been found to show more even morphology.[303] An SEM study was carried out to investigate the morphology of the polymers on FTO glass electrodes, at different film thickness. Uniform raspberry-like nucleation growth films have been obtained with no remarkable features (Figure 6.22), within the resolution limits of the microscope. EDX of the deposited film on FTO shows the presence of C, Mo, Sn, Si, O, F (Figure 6.23). These results are consistent with ratio between the POM-derivatised monomer and the underivatised pyrroles of 1 to 2, just like the XPS results.
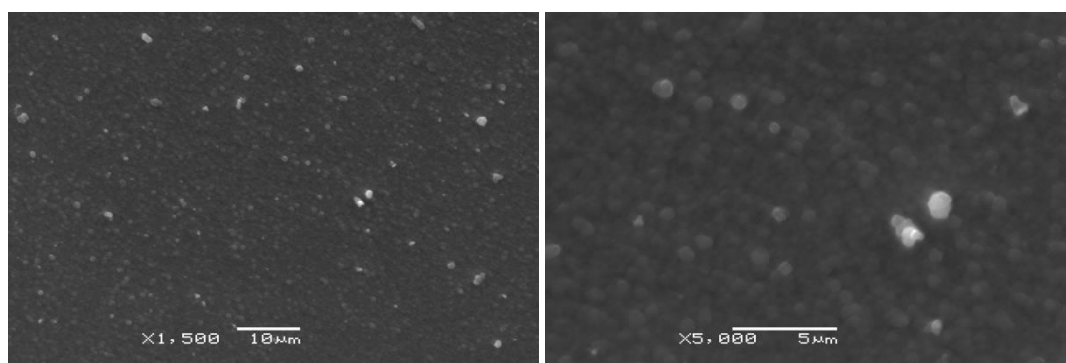
Figure 6.22 SEM images of polypyrrole-14 co-polymer at 10:90 % ratio, 10 cycles film thickness on FTO electrode showing raspberry-like nucleation growth [304] film with no remarkable features.
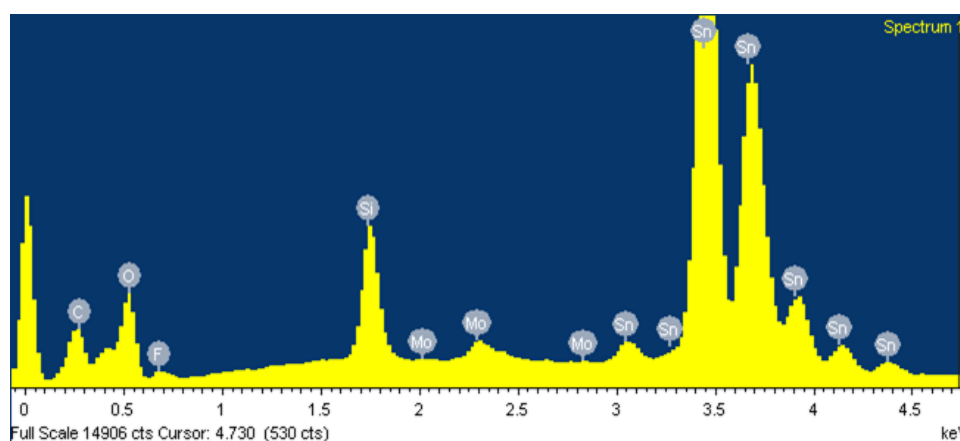
Figure 6.23 EDX of the surface of polypyrrole-**14** co-polymer at 10:90 % ratio, 10 cycles film thickness on FTO electrode.

Further study of the morphology of these films was performed using high-resolution TEM at the Leeds EPSRC National Nanoscience Facility (LENNF). Sample preparation involved the use of the FIB-SEM technique for cross-section TEM (for both film thickness determination and bulk morphological studies). By taking advantage of the combination of FIB with an SEM, it was possible to have high-resolution images for the surface of the polymer films. Figure 6.24 shows the SEM images of polypyrrole-**4** (30:70 % ratio) of 10 cycles film thickness, which exhibits an smooth surface. In the high-magnification image, the amorphous nature can be clearly observed, with no phase separated domains. TEM images show clearly that the topography of the films is relatively similar to that of the FTO substrate (Figure 6.25). Films thicknesses were between 60 to 120 nm depending on the number of deposition cycles.
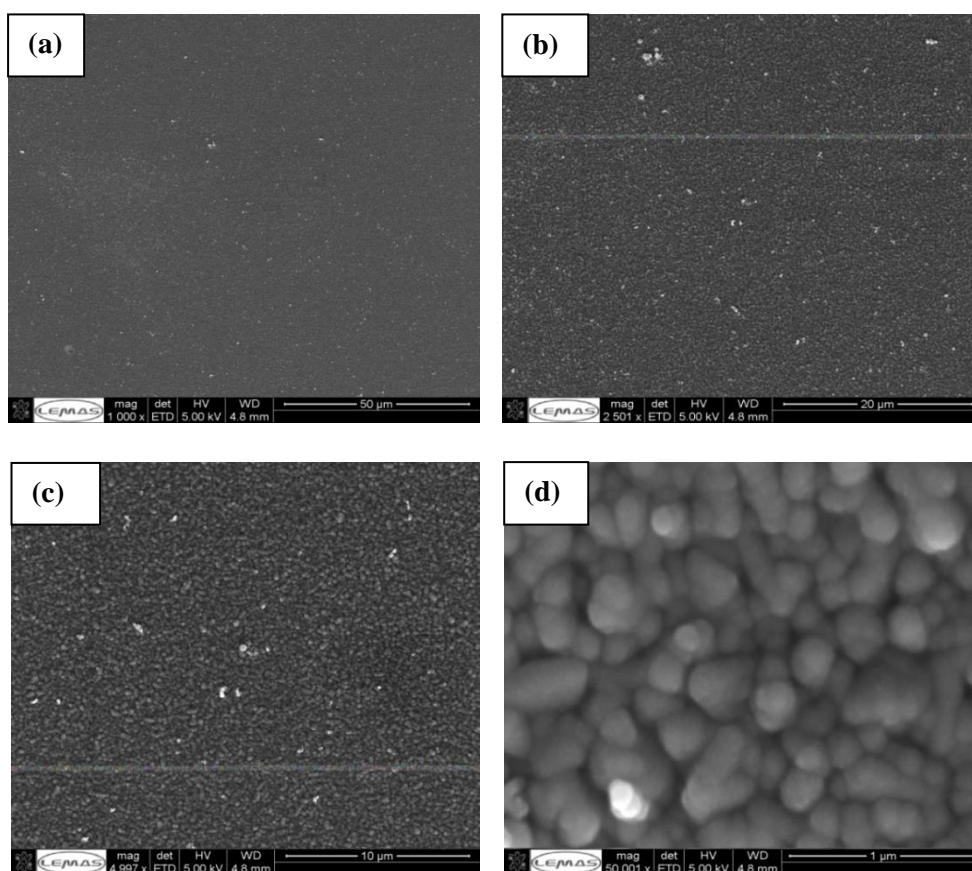
Figure 6.24 SEM images of the polypyrrole-**4** co-polymer at 30:70 % ratio, 10 cycles film thickness on FTO electrode showing no domains of phase separation.
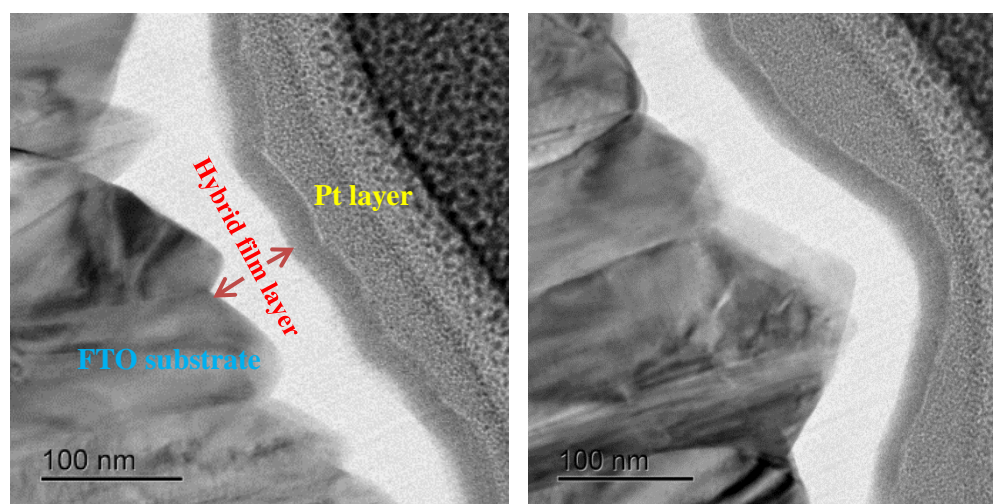
Figure 6.25 TEM cross-sectional view images of polypyrrole-**4** co-polymer at 30:70 % ratio, 10 cycles film thickness (60 nm) on FTO electrode.

The cross-sectional TEM images (the bulk) of the film is shown in Figure 6.26, with similar features observed to the surface SEM images. EDX was carried out along the cross-section at different locations of each sample. Figure 6.27 shows the EDX of the cross-sectional area of polypyrrole-**4** co-polymer at 30:70 % ratio, 10 cycles film thickness on an FTO electrode. Just like the XPS and the EDX-SEM results, the results in Figure 6.27 confirm the presence of C, Mo, O, Cu (from sample holder) elements with a ratio of 1 to 2 between the POM-derivatised monomer and the underivatised pyrroles.
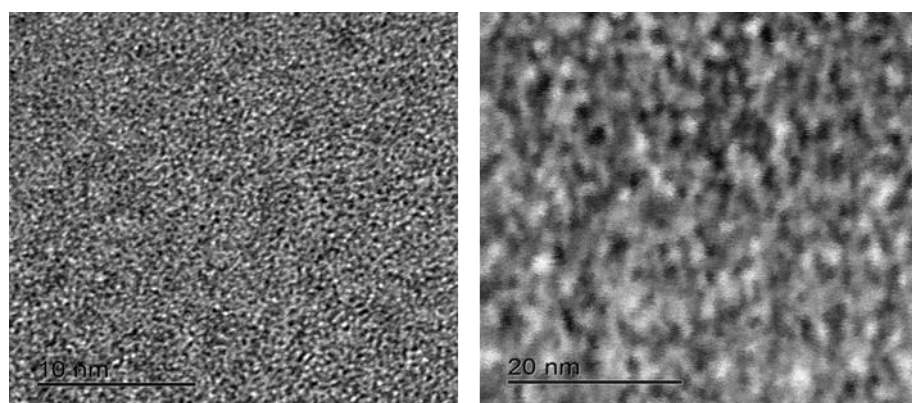
Figure 6.26 Cross-sectional TEM images of polypyrrole-**4** co-polymer at 30:70 % ratio, 10 cycles film thickness (60 nm).
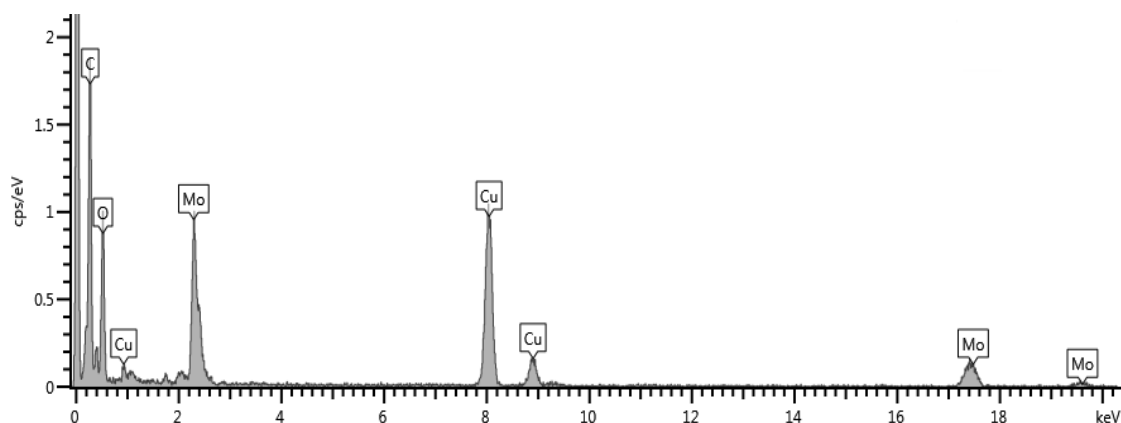
Figure 6.27 EDX of the cross section of polypyrrole-**4** co-polymer at 30:70 % ratio, 10 cycles film thickness (60 nm).

6.2.3 Polycarbazole-based materials

Electropolymerisation of Monomers

It is important to mention that monomer **12** was obtained later in the course of this project and we are awaiting for its films to be fully characterized at LENNF. The carbazole **12** (2mM) is readily electropolymerized in 0.1 [NBu$_4$][BF$_4$]-MeCN at FTOelectrode in a three compartment electrochemical cell to form a yellowish film (shown in Figure 6.28). This is in agreement with literature, where *N*-derivatized carbazoles electropolymerise in a similar fashion to pyrroles and are less sensitive to derivatisation.[305] The electropolymerisation experiment was also carried out with a FTO working electrode in 0.1 [NBu$_4$][BF$_4$]-MeCN solution with aqueous Ag/AgCl reference electrode, from 0 V to 1.5 V at scan rate of 100 mV/s for 10 cycles, and is presented in Figure 6.29.

Figure 6.28 FTO electrode coated with poly-**12** film.
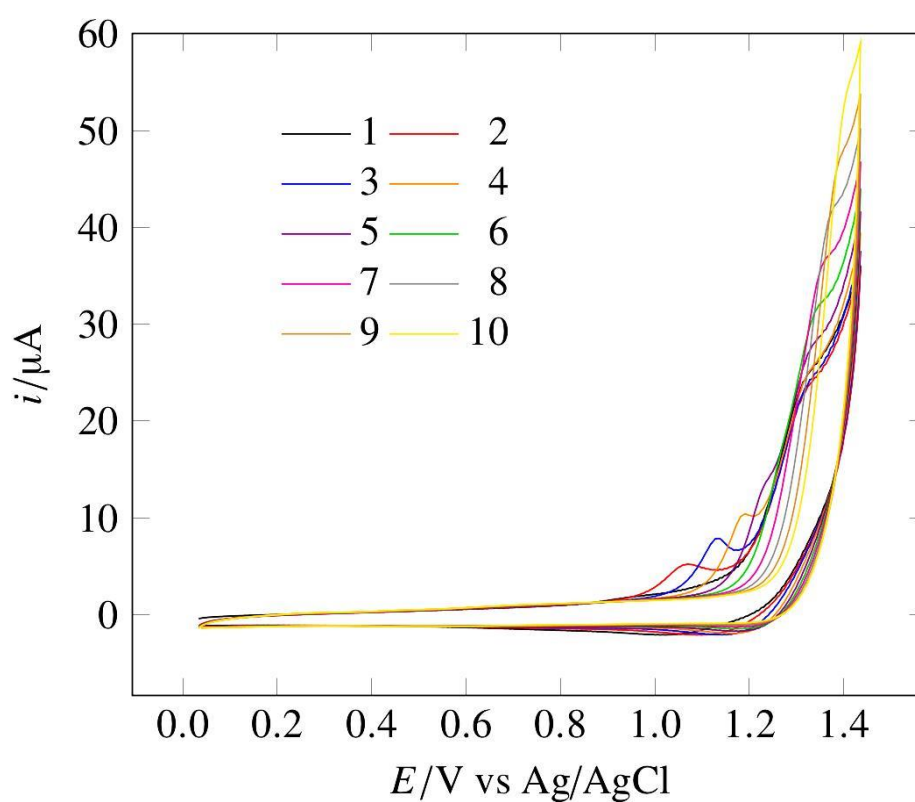
Figure 6.29 CVs showing electropolymerization of **12** on FTO, were run from 0V to 1.5V at scan rate of 100 mV/s for 10 cycles.

Electrochemical properties of the polymers

The electrochemical behaviour of a freshly prepared **12** polymer film is illustrated in Figure 6.30. The CV clearly shows an $\{Mo_6\}$-imido peak in the first cycle (Figure 6.30, black trace) at a scan rate of 100 mV/s. However, this peak is clearly lost in the

second cycle, along with growth of a new peak at less negative potential (Figure 6.30, red trace), is likely ascribed to $[Mo_6O_{19}]^{2-}$ produced by hydrolysis. This result indicates that poly-**12** is more vulnerable to hydrolysis than other polymer derivatives.

.
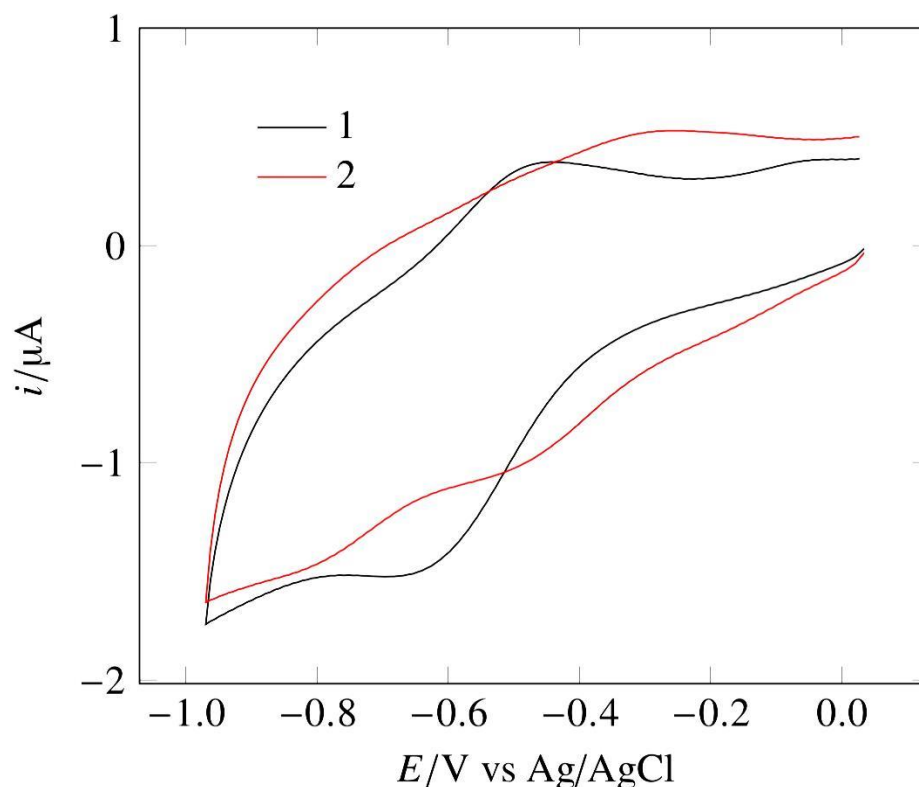
Figure 6.30 Consecutive cyclic voltammograms of a **12** polymer film showing loss of the imido-Lindqvist peak (which is present in the first cycle, black trace), and growth of a new peak ascribed to $[Mo_6O_{19}]^{2-}$, in the second cycle (red trace). Electrolyte is 0.1 M [NBu$_4$][BF$_4$] in MeCN, scan rate 100 mV/s.

Morphological studies

The morphologies of the poly-**12** films have been investigated by SEM only. Figure 6.31 shows the SEM surface images of poly-**12** with 10 deposition cycles film thickness on an FTO electrode surface, showing the smooth nature. EDX results show the presence of Mo, N, O, C, Sn, Si traces, shown in Figure 6.32. Interestingly, the

SEM of the 20 deposition cycles film thickness on FTO electrode surface (Figure 6.33) shows uneven morphology, with surface nodulation. A possible interpretation could be that these nodules are crystals of [NBu$_4$][BF$_4$] electrolyte; however, the films were very well washed and the EDX results on those spots were similar to the rest of the film. However, this is an interesting result, which would be further explored in the future with high resolution SEM and cross-sectional TEM studies.
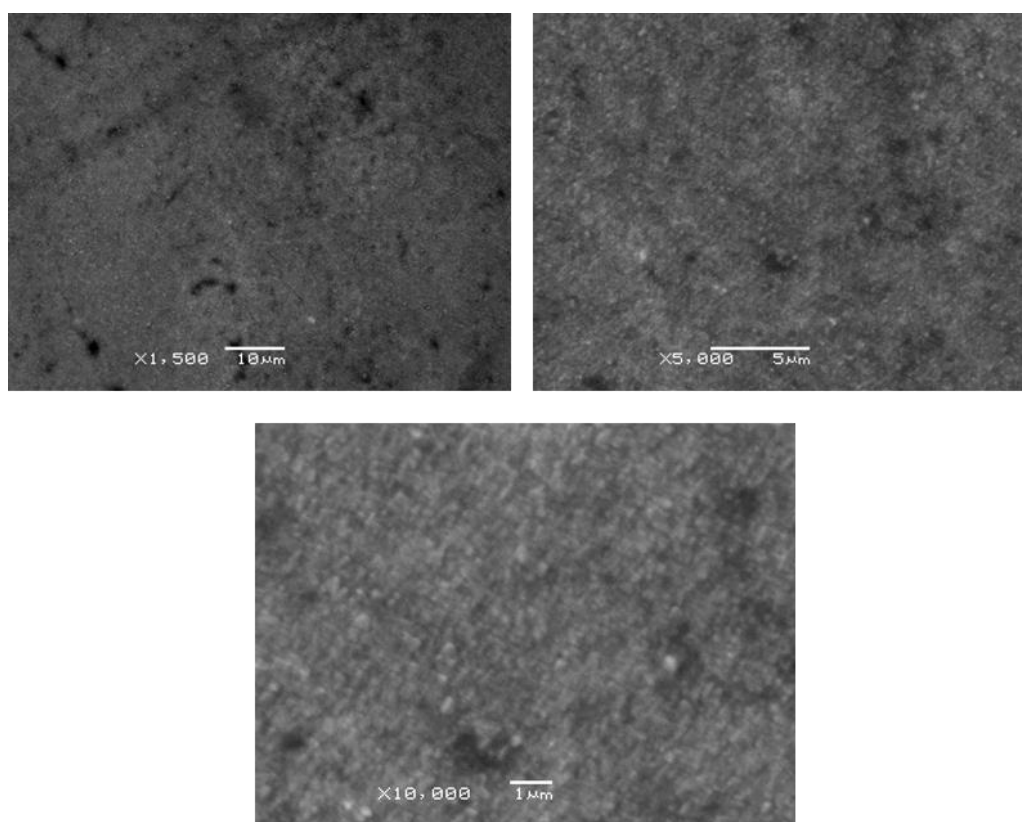
Figure 6.31 SEM images of 12 polymer 10 deposition cycles film on FTO electrode surface with different magnifications.
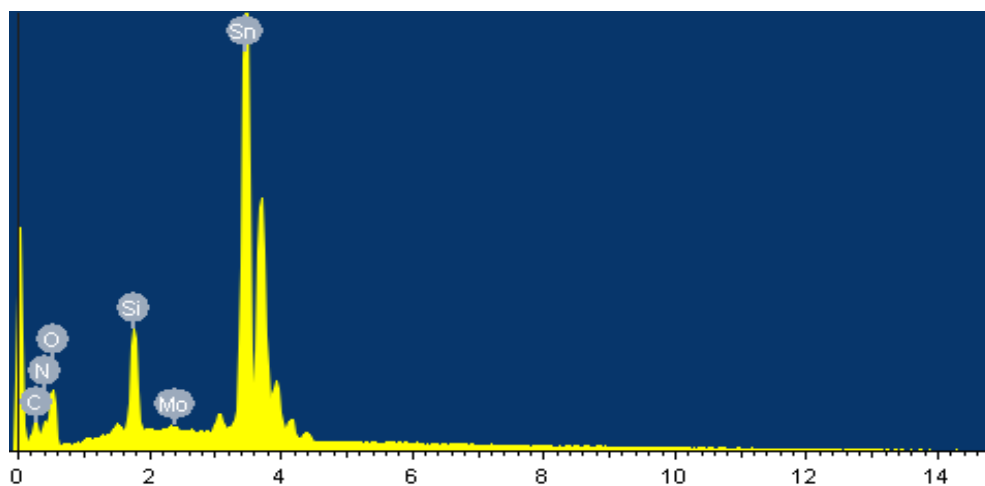
Figure 6.32 EDX of the surface of **12** polymer of 10 cycles film thickness on FTO electrode.
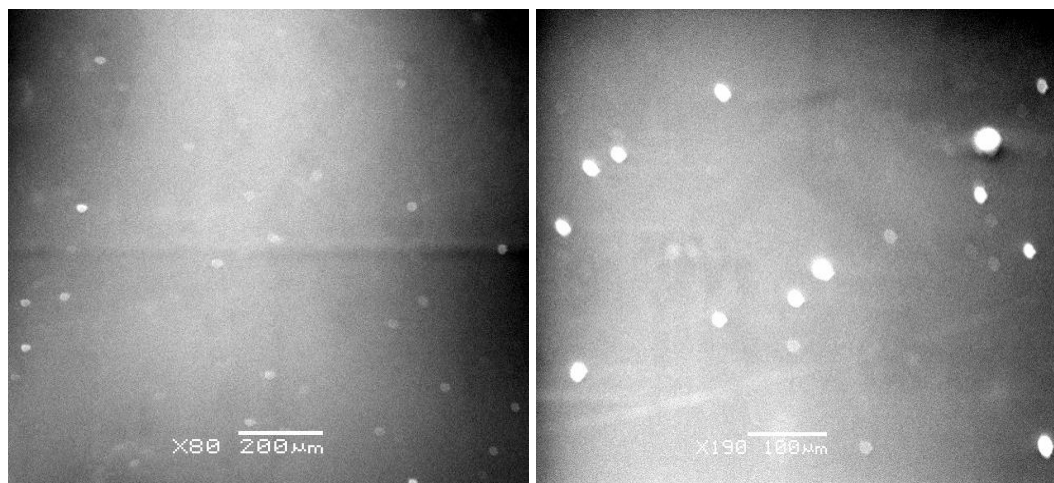
Figure 6.33 SEM images of **12** polymer of 20 deposition cycles film on FTO electrode surface showing surface nodulation.

Chapter 7

Conclusions and Future Work

A new series of organo-imido Lindqvist derivatives has been synthesized using a DCC coupling protocol. This series features donor and acceptor groups from strong acceptor (NO_2), through very weak acceptors (iodo and ethynyl) and weak donors (pyrrole, carbazole) to strong donors (diphenylamino, NH_2, NMe_2), with different π-conjugated bridge lengths (phenyl and diphenylacetylene spacers). In order to access these new compounds several new precursor amines were also produced.

All the new compounds have been fully characterised using 2D, ^{13}C, and ^1H-NMR, mass spectrometry, elemental analysis, and infra-red spectroscopy. X-ray crystal structures have been solved for nine of these derivatives including one photo-inactive derivative, and eight photo-active derivatives. UV-vis studies show that as the electron donor strength or π-conjugated bridge increases the LPCT band red-shifts. Cyclic voltammetry studies show cathodic shift in the {Mo_6} potential upon derivatisation confirming that electron density is donated from the organic groups to the {Mo_6} unit, but that in most cases the redox potential varies little between the different organic derivatives. Attempts to study the redox-switched optical properties of these materials by spectroelectrochemistry and bulk electrolysis studies show the occurrence of rapid hydrolysis in the reduced state of these derivatives. Four of the derivatives have been functionalised with polymerizable groups (pyrrole, carbazole) that enable electrochemical processing into redox-active thin films. The electropolymerisation of pyrrole derivatives was only successful in the presence of underivatized pyrrole, but the carbazole derivative can be electropolymerized alone. However, the latter showed less stability (probably due to hydrolysis) in the ambient conditions.

Hyper-Rayleigh scattering studies on the new derivatives show significant β-values in systems featuring pyrrole, NH_2, carbazole, diphenylamino, and NMe_2 donors. The static β_0 responses (obtained at 1064 nm) can be enhanced by tailoring the organic group, and reach up to 139×10^{-30} esu (for the derivative featuring the

diphenylacetylene space and NMe$_2$ donor). These are higher than those of the vast majority of purely organic materials of similar donor strength, π-system size and absorption profile. Consequently, the electron number adjusted β values of several organoimido-POMs exceed the apparent limits (vs absorption maximum) for most dipolar organic materials. Stark and Raman spectroscopic studies confirm the involvement of POM framework in the LPCT transition, which gives an unusually high dipole moment change, and hence displays strong NLO performance.

Future work

❖ Investigating the hydrolysis (mechanism) and finding the conditions that would reduce the tendency to hydrolyse are required. For example, adding base or using super dry solvent as it is thought that protonation may play an important role in this process.

❖ In this thesis, because of the cost and commercial availability of suitable aniline precursors, we worked with simple 1,4-substituted anilines. Moreover, at the time there was nothing in the literature addressing hydrolysis problems and we were focused on measuring the NLO properties of these materials. However, tailoring the organic component of these derivatives to increase the steric hindrance of the ortho-substituents around the Mo=N imido bond could decrease the tendency to hydrolysis. Finally, using metal mixed systems (Mo and W) where the imido bond is on the W atom instead of Mo may be another option that could be explored to increase the stability of these derivatives while only minimally changing their electrochemical and photophysical properties.

❖ Ways towards bulk active NLO materials are needed, and it would be interesting to explore ways to produce oriented films, or non-centrosymmetric crystalline materials. This might be cation metatheses with salts followed by further crystallizations, which may afford crystals with polar packing

arrangements. For redox-switched NLO, crystalline materials are not suitable. Therefore, poling alignment of polymers is another option that could be explored.

❖ DFT calculations are in progress in order to theoretically predict and evaluate the NLO performance and the associated electronic properties of these derivatives.

❖ It would be interesting also to explore the activity of these materials as third order NLO materials, e.g. for two photon absorption.

Appendix

A. Full Crystallographic Data : Attached CD

B. Publications from this work

1- Invited review: Ahmed Al-Yasari, and John Fielden, *Polyoxometalates in Visible-Light Photocatalysis and Solar Energy Conversion*, Rev. Adv. Sci. Eng. 2014, 4, 1–16.

2- Primary research paper: Ahmed Al-Yasari, Nick Van Steerteghem, Hani El Moll, Koen Clays and John Fielden, *Donor–acceptor organo-imido polyoxometalates: high transparency, high activity redox-active NLO chromophores*, Dalton Transactions 2016, DOI: 10.1039/C6DT00115G.

References

(1)   Sanchez, C.; Ribot, F.; Lebeau, B. *J. Mater. Chem.* **1999**, *9*, 35.

(2)   Lebeau, B.; Innocenzi, P. *Chem. Soc. Rev.* **2011**, *40*, 886.

(3)   Darder, M.; Colilla, M.; Lara, N.; Ruiz-Hitzky, E. *J. Mater. Chem.* **2002**, *12*, 3660.

(4)   Ritchie, J. E. In *Hybrid Materials: Synthesis, Characterization, and Applications*; Wiley-VCH Verlag GmbH & Co. KGaA: **2007**, p 401.

(5)   De Souza, F.; Leite, E. *ChemInform* **2011**, *42*.

(6)   Etienne, M.; Guillemin, Y.; Grosso, D.; Walcarius, A. *Anal. Bioanal. Chem.* **2013**, *405*, 1497.

(7)   Karakhanov, E.; Maximov, A.; Kardashev, S.; Kardasheva, Y.; Zolotukhina, A.; Rosenberg, E.; Allen, J. In *Macromolecular Symposia*; Wiley Online Library: **2011**, *304*, p 55.

(8)   Dias Carlos, L. A.; Sá Ferreira, R. A.; de Zea Bermudez, V. In *Hybrid Materials*; Wiley-VCH Verlag GmbH & Co. KGaA, **2007**, p 337.

(9)   Xiong, L.; Chen, Z.; Tian, Q.; Cao, T.; Xu, C.; Li, F. *Anal. Chem.* **2009**, *81*, 8687.

(10) Chen, J.; Zhao, J. X. *Sens.* **2012**, *12*, 2414.

(11) Notake, T.; Nawata, K.; Kawamata, H.; Matsukawa, T.; Qi, F.; Minamide, H. *Opt. Expr.* **2012**, *20*, 25850.

(12) Flytzanis, C. In *Nonlinear Optical Materials and Devices for Applications in Information Technology*; Miller, A., Welford, K. R., Daino, B., Eds.; Springer Netherlands: Dordrecht, **1995**, p 1.

(13) Franken, P. A.; Hill, A. E.; Peters, C. W.; Weinreich, G. *Phys. Rev. Lett.* **1961**, *7*, 118.

(14) Boyd, R. W. In *Nonlinear Optics (Second Edition)*; Academic Press: San Diego, **2003**, p 1.

(15) Bass, M.; Mahajan, V. N.; Optical Society of America. *Handbook of optics*; 3rd ed.; McGraw-Hill: New York, **2010**.

(16) Shen, Y. R. *The principles of nonlinear optics*; Wiley classics library ed.; Wiley-Interscience: Hoboken, N.J., **2003**.

(17) Oudar, J. L.; Chemla, D. S. *Opt. Commun.* **1975**, *13*, 164.

(18) Oudar, J. L. *J. Chem. Phys.* **1977**, *67*, 446.

(19) Bosshard, C.; Knöpfle, G.; Prêtre, P.; Günter, P. *J. Appl. Phys.* **1992**, *71*, 1594.

(20) Karki, L.; Vance, F. W.; Hupp, J. T.; LeCours, S. M.; Therien, M. J. *J. Am. Chem. Soc.* **1998**, *120*, 2606.

(21) Coe, B. J.; Foxon, S. P.; Pilkington, R. A.; Sánchez, S.; Whittaker, D.; Clays, K.; Depotter, G.; Brunschwig, B. S. *Organometallics* **2015**, *34*, 1701.

(22) Coe, B. J.; Harris, J. A.; Brunschwig, B. S. *J. Phys. Chem. A* **2002**, *106*, 897.

(23) Tripathy, K.; Moreno, J. P.; Kuzyk, M. G.; Coe, B. J.; Clays, K.; Kelley, A. M. *J. Chem. Phys.* **2004**, *121*, 7932.

(24) Terhune, R. W.; Maker, P. D.; Savage, C. M. *Phys. Rev. Lett.* **1965**, *14*, 681.

(25) Hollis, D. B. *Am. Mineral* **1988**, *73*, 701.

(26) Zyss, J.; Ledoux, I. *Chem. Rev.* **1994**, *94*, 77.

(27) Wu, Y.; Mao, G.; Li, H.; Petschek, R. G.; Singer, K. D. *J. Opt. Soc. Am. B: Opt. Phys.* **2008**, *25*, 495.

(28) Levine, B. F.; Bethea, C. G. *J. Chem. Phys.* **1975**, *63*, 2666.

(29) Green, K. A.; Cifuentes, M. P.; Corkery, T. C.; Samoc, M.; Humphrey, M. G. *Angew. Chem. Int. Ed.* **2009**, *48*, 7867.

(30) Clays, K.; Persoons, A. *Phys. Rev. Lett.* **1991**, *66*, 2980.

(31) Verbiest, T.; Clays, K.; Rodriguez, V. *Second-order nonlinear optical characterization techniques : an introduction*; CRC ; London : Taylor & Francis [distributor]: Boca Raton, Fla., **2009**.

(32) Steerteghem, N. V., MSc dissertation, KU Leuven, **2013**.

(33) Hsu, C.-C.; Liu, S.; Wang, C. C.; Wang, C. H. *J. Chem. Phys.* **2001**, *114*, 7103.

(34) Wang, C. H.; Lin, Y. C.; Tai, O. Y.; Jen, A. K.-Y. *J. Chem. Phys.* **2003**, *119*, 6237.

(35) Hung, S. T.; Wang, C. H.; Kelley, A. M. *J. Chem. Phys.* **2005**, *123*, 144503.

(36) Wang, C. H.; Woodford, J. N.; Jen, A. K. Y. *Chem. Phys.* **2000**, *262*, 475.

(37) Shoute, L. C. T.; Bartholomew, G. P.; Bazan, G. C.; Kelley, A. M. *J. Chem. Phys.* **2005**, *122*, 184508.

(38) Shoute, L. C. T.; Blanchard-Desce, M.; Kelley, A. M. *J. Phys. Chem. A* **2005**, *109*, 10503.

(39) Shoute, L. C. T.; Helburn, R.; Kelley, A. M. *J. Phys. Chem. A* **2007**, *111*, 1251.

(40) Shoute, L. C. T.; Woo, H. Y.; Vak, D.; Bazan, G. C.; Myers Kelley, A. *J. Chem. Phys.* **2006**, *125*, 054506.

(41) Long, N. J. *Angew. Chem. Int. Ed.* **1995**, *34*, 21.

(42) Chen, C.-t.; Liu, G.-z. *Annu. Rev. Mater. Sci.* **1986**, *16*, 203.

(43) Fan, Y. X.; Eckardt, R. C.; Byer, R. L.; Route, R. K.; Feigelson, R. S. *Appl. Phys. Lett.* **1984**, *45*, 313.

(44) Dehu, C.; Meyers, F.; Bredas, J. L. *J. Am. Chem. Soc.* **1993**, *115*, 6198.

(45) Huggard, P. G.; Blau, W.; Schweitzer, D. *Appl. Phys. Lett.* **1987**, *51*, 2183.

(46) Cheng, L. T.; Tam, W.; Marder, S. R.; Stiegman, A. E.; Rikken, G.; Spangler, C. W. *J. Phys. Chem.* **1991**, *95*, 10643.

(47) Marder, S. R.; Gorman, C. B.; Tiemann, B. G.; Cheng, L. T. *J. Am. Chem. Soc.* **1993**, *115*, 3006.

(48) Marder, S. R.; Perry, J. W. *Adv. Mater.* **1993**, *5*, 804.

(49) Bourhill, G.; Bredas, J.-L.; Cheng, L.-T.; Marder, S. R.; Meyers, F.; Perry, J. W.; Tiemann, B. G. *J. Am. Chem. Soc.* **1994**, *116*, 2619.

(50) Duan, X.-M.; Okada, S.; Oikawa, H.; Matsuda, H.; Nakanishi, H. *Jpn. J. Appl. Phys.* **1994**, *33*, L1559.

(51) Notake, T.; Nawata, K.; Kawamata, H.; Matsukawa, T.; Qi, F.; Minamide, H. *Opt. Expr.* **2012**, *20*, 25850.

(52) Dhenaut, C.; Ledoux, I.; Samuel, I. D. W.; Zyss, J.; Bourgault, M.; Bozec, H. L. *Nature* **1995**, *374*, 339.

(53) McDonagh, A. M.; Humphrey, M. G.; Samoc, M.; Luther-Davies, B.; Houbrechts, S.; Wada, T.; Sasabe, H.; Persoons, A. *J. Am. Chem. Soc.* **1999**, *121*, 1405.

(54) Coe, B. J.; Foxon, S. P.; Helliwell, M.; Rusanova, D.; Brunschwig, B. S.; Clays, K.; Depotter, G.; Nyk, M.; Samoc, M.; Wawrzynczyk, D.; Garín, J.; Orduna, J. *Chem. Eur. J.* **2013**, *19*, 6613.

(55) Kang, H.; Zhu, P.; Yang, Y.; Facchetti, A.; Marks, T. J. *J. Am. Chem. Soc.* **2004**, *126*, 15974.

(56) Shi, Y.; Lou, A. J. T.; He, G. S.; Baev, A.; Swihart, M. T.; Prasad, P. N.; Marks, T. J. *J. Am. Chem. Soc.* **2015**, *137*, 4622.

(57) Beverina, L.; Sanguineti, A.; Battagliarin, G.; Ruffo, R.; Roberto, D.; Righetto, S.; Soave, R.; Lo Presti, L.; Ugo, R.; Pagani, G. A. *Chem. Commun.* **2011**, *47*, 292.

(58) Kang, H.; Facchetti, A.; Stern, C. L.; Rheingold, A. L.; Kassel, W. S.; Marks, T. J. *Org. Lett.* **2005**, *7*, 3721.

(59) Frazier, C. C.; Harvey, M. A.; Cockerham, M. P.; Hand, H. M.; Chauchard, E. A.; Lee, C. H. *J. Phys. Chem.* **1986**, *90*, 5703.

(60) Calabrese, J. C.; Cheng, L. T.; Green, J. C.; Marder, S. R.; Tam, W. *J. Am. Chem. Soc.* **1991**, *113*, 7227.

(61) Green, M. L. H.; Marder, S. R.; Thompson, M. E.; Bandy, J. A.; Bloor, D.; Kolinsky, P. V.; Jones, R. J. *Nature* **1987**, *330*, 360.

(62) Bandy, J. A.; Bunting, H. E.; Garcia, M.-H.; Green, M. L. H.; Marder, S. R.; Thompson, M. E.; Bloor, D.; Kolinsky, P. V.; Jones, R. J.; Perry, J. W. *Polyhedron* **1992**, *11*, 1429.

(63) Marder, S. R.; Perry, J. W.; Tiemann, B. G.; Schaefer, W. P. *Organometallics* **1991**, *10*, 1896.

(64) Kroener, R.; Heeg, M. J.; Deutsch, E. *Inorg. Chem.* **1988**, *27*, 558.

(65) Verbiest, T.; Houbrechts, S.; Kauranen, M.; Clays, K.; Persoons, A. *J. Mater. Chem.* **1997**, *7*, 2175.

(66) Bruce, D. W.; O'Hare, D.; Walton, R. I. *Molecular materials*; Wiley: Chichester, **2010**.

(67) Priyadarshy, S.; Therien, M. J.; Beratan, D. N. *J. Am. Chem. Soc.* **1996**, *118*, 1504.

(68) Sen, A.; Ray, P. C.; Das, P. K.; Krishnan, V. *J. Phys. Chem.* **1996**, *100*, 19611.

(69) Bruce, D. W.; Thornton, A. *Mol. Cryst. Liq. Cryst. Sci. Technol., Sect A* **1993**, *231*, 253.

(70) Kanis, D. R.; Lacroix, P. G.; Ratner, M. A.; Marks, T. J. *J. Am. Chem. Soc.* **1994**, *116*, 10089.

(71) Mata, J.; Uriel, S.; Peris, E.; Llusar, R.; Houbrechts, S.; Persoons, A. *J. Organomet. Chem.* **1998**, *562*, 197.

(72) Caruso, U.; De Maria, A.; Panunzi, B.; Roviello, A. *J. Polym. Sci., Part A: Polym. Chem.* **2002**, *40*, 2987.

(73) Bourgault, M.; Baum, K.; Le Bozec, H.; Pucetti, G.; Ledoux, I.; Zyss, J. *New J. Chem.* **1998**, *22*, 517.

(74) Cariati, E.; Pizzotti, M.; Roberto, D.; Tessore, F.; Ugo, R. *Coord. Chem. Rev.* **2006**, *250*, 1210.

(75) Wise, D. L. *Electrical and optical polymer systems*; M. Dekker: New York, **1998**.

(76) Dakin, J.; Brown, R. G. W. *Handbook of optoelectronics*; Taylor & Francis: New York ; London, **2006**.

(77) Green, K. A.; Cifuentes, M. P.; Samoc, M.; Humphrey, M. G. *Coord. Chem. Rev.* **2011**, *255*, 2530.

(78) Asselberghs, I.; Zhao, Y.; Clays, K.; Persoons, A.; Comito, A.; Rubin, Y. *Chem. Phys. Lett* **2002**, *364*, 279.

(79) Asselberghs, I.; Clays, K.; Persoons, A.; Ward, M. D.; McCleverty, J. *J. Mater. Chem.* **2004**, *14*, 2831.

(80) Coe, B. J. *Chem. Eur. J.* **1999**, *5*, 2464.

(81) Whittall, I. R.; Humphrey, M. G.; Samoc, M.; Swiatkiewicz, J.; Luther-Davies, B. *Organometallics* **1995**, *14*, 5493.

(82) Fernández-Acebes, A.; Lehn, J.-M. *Chem. Eur. J.* **1999**, *5*, 3285.

(83) Loucif-Saibi, R.; Nakatani, K.; Delaire, J. A.; Dumont, M.; Sekkat, Z. *Chem. of Mater.* **1993**, *5*, 229.

(84) Coe, B. J.; Houbrechts, S.; Asselberghs, I.; Persoons, A. *Angew. Chem. Int. Ed.* **1999**, *38*, 366.

(85) Boubekeur-Lecaque, L.; Coe, B. J.; Clays, K.; Foerier, S.; Verbiest, T.; Asselberghs, I. *J. Am. Chem. Soc.* **2008**, *130*, 3286.

(86) Malaun, M.; Reeves, Z. R.; Paul, R. L.; Jeffery, J. C.; McCleverty, J. A.; Ward, M. D.; Asselberghs, I.; Clays, K.; Persoons, A. *Chem. Commun.* **2001**, 49.

(87) Malaun, M.; Kowallick, R.; McDonagh, A. M.; Marcaccio, M.; Paul, R. L.; Asselberghs, I.; Clays, K.; Persoons, A.; Bildstein, B.; Fiorini, C.; Nunzi, J.-M.; Ward, M. D.; McCleverty, J. A. *J. Chem. Soc., Dalton Trans..* **2001**, 3025.

(88) Powell, C. E.; Humphrey, M. G.; Cifuentes, M. P.; Morrall, J. P.; Samoc, M.; Luther-Davies, B. *J. Phys. Chem. A* **2003**, *107*, 11264.

(89) Powell, C. E.; Cifuentes, M. P.; Morrall, J. P.; Stranger, R.; Humphrey, M. G.; Samoc, M.; Luther-Davies, B.; Heath, G. A. *J. Am. Chem. Soc.* **2003**, *125*, 602.

(90) Weyland, T.; Ledoux, I.; Brasselet, S.; Zyss, J.; Lapinte, C. *Organometallics* **2000**, *19*, 5235.

(91) Cifuentes, M. P.; Powell, C. E.; Morrall, J. P.; McDonagh, A. M.; Lucas, N. T.; Humphrey, M. G.; Samoc, M.; Houbrechts, S.; Asselberghs, I.; Clays, K.; Persoons, A.; Isoshima, T. *J. Am. Chem. Soc.* **2006**, *128*, 10819.

(92) Kajzar, F.; Swalen, J. D. *Organic thin films for waveguiding nonlinear optics*; Gordon and Breach: Australia ; United Kingdom, **1996**.

(93) O. A. Aktsipetrov, N. N. A., E. D. Mishina, V. R. Novak *JETP Lett.* **1983**, *37*, 207.

(94) Karl, W. B.; Keith, A. H.; Michael, M.; Ajay, N.; Chengjiu, W.; James, T. Y. In *Mater. for Nonlinear Opt., Am. Chem. Soc.* **1991**, *455*, p 303.

(95) Kajzar, F.; Okada-Shudo, Y.; Meritt, C.; Kafafi, Z. *Synth. Metals* **2001**, *117*, 189.

(96) Bosshard, C.; Flörsheimer, M.; Küpfer, M.; Günter, P. *Opt. Commun.* **1991**, *85*, 247.

(97) Dalton, L. R.; Benight, S. J.; Johnson, L. E.; Knorr, D. B.; Kosilkin, I.; Eichinger, B. E.; Robinson, B. H.; Jen, A. K. Y.; Overney, R. M. *Chem. of Mater.* **2011**, *23*, 430.

(98) Kajzar, F.; Lee, K.-S.; Jen, A. Y. In *Polymers for Photonics Applications II*; Lee, K.-S., Ed.; Springer Berlin Heidelberg: **2003**; *161*, p 1.

(99) Cabanetos, C.; Bentoumi, W.; Silvestre, V.; Blart, E.; Pellegrin, Y.; Montembault, V.; Barsella, A.; Dorkenoo, K.; Bretonnière, Y.; Andraud, C.; Mager, L.; Fontaine, L.; Odobel, F. *Chem. of Mater.* **2012**, *24*, 1143.

(100) E. E. Havinga, P. V. P. In *Electrochromism of Organic Dyes in Polymer Matrices, in Electro-Optics and Dielectrics of Macromolecules and Colloids*; Springer Verlag: New York, **1979**, p 89.

(101) Khalil, M. A.; Vitrant, G.; Raimond, P.; Chollet, P. A.; Kajzar, F. *Appl. Phys. Lett.* **2000**, *77*, 3713.

(102) Getmanenko, Y. A.; Hales, J. M.; Balu, M.; Fu, J.; Zojer, E.; Kwon, O.; Mendez, J.; Thayumanavan, S.; Walker, G.; Zhang, Q.; Bunge, S. D.; Brédas, J.-L.; Hagan, D. J.; Van Stryland, E. W.; Barlow, S.; Marder, S. R. *J. Mater. Chem.* **2012**, *22*, 4371.

(103) Moylan, C. R.; Ermer, S.; Lovejoy, S. M.; McComb, I. H.; Leung, D. S.; Wortmann, R.; Krdmer, P.; Twieg, R. J. *J. Am. Chem. Soc.* **1996**, *118*, 12950.

(104) Moylan, C. R.; Ermer, S.; Lovejoy, S. M.; McComb, I. H.; Leung, D. S.; Wortmann, R.; Krdmer, P.; Twieg, R. J. *J. Am. Chem. Soc.* **1996**, *118*, 12950.

(105) Marder, S. R.; Kippelen, B.; Jen, A. K. Y.; Peyghambarian, N. *Nature* **1997**, *388*, 845.

(106) Lee, K. S.; Chung, S. J. *Polymers for photonics applications II : nonlinear optical, photorefractive and two-photon absorption polymers*; Springer: Berlin ; London , **2003**.

(107) Wu, W.; Qin, J.; Li, Z. *Polymer* **2013**, *54*, 4351.

(108) Jen, A. K. Y.; Rao, V. P.; Wong, K. Y.; Drost, K. J. *J. Chem. Soc., Chem. Commun.* **1993**, 90.

(109) Luo, J.; Haller, M.; Li, H.; Kim, T. D.; Jen, A. K. Y. *Adv. Mater.* **2003**, *15*, 1635.

(110) Zhang, C.; Wang, C.; Dalton, L. R.; Zhang, H.; Steier, W. H. *Macromolecules* **2001**, *34*, 253.

(111) Allen, N. S. *Photochemistry and photophysics of polymer materials*; Wiley: Oxford, **2010**.

(112) Samyn, C.; Verbiest, T.; Persoons, A. *Macromol. Rapid Commun.* **2000**, *21*, 1.

(113) Liu, S.; Tang, Z. *Nano Today* **2010**, *5*, 267.

(114) Long, D.-L.; Burkholder, E.; Cronin, L. *Chem. Soc. Rev.* **2007**, *36*, 105.

(115) Mitchell, S. G.; de la Fuente, J. M. *J. Mater. Chem.* **2012**, *22*, 18091.

(116) Walsh, J. J.; Bond, A. M.; Forster, R. J.; Keyes, T. E. *Coord. Chem. Rev.* **2016**, *306*, 217.

(117) Zhou, Y.; Chen, G.; Long, Z.; Wang, J. *RSC Adv.* **2014**, *4*, 42092.

(118) Berzelius, J. J. *Annalen der Physik* **1826**, *82*, 369.

(119) Keggin, J. F. *Nature* **1933**, *131*, 908.

(120) Cheng, S. A.; Otero, T. F. *Synth. Metals* **2002**, *129*, 53.

(121) Klemperer, W. G. *Inorg. Synth.* **1990**, *27*, 71.

(122) Hasenknopf, B. *Front Biosci-Landmrk* **2005**, *10*, 275.

(123) Gouzerh, P.; Che, M. *Actual Chimique* **2006**, 9.

(124) Wu, P. F.; Li, Q.; Ge, N.; Wei, Y. G.; Wang, Y.; Wang, P.; Guo, H. Y. *Eur. J. Inorg. Chem.* **2004**, 2819.

(125) Proust, A.; Matt, B.; Villanneau, R.; Guillemot, G.; Gouzerh, P.; Izzet, G. *Chem. Soc. Rev.* **2012**, *41*, 7605.

(126) Zhang, J.; Xiao, F.; Hao, J.; Wei, Y. *Dalton Trans.* **2012**, *41*, 3599.

(127) Azcarate , I.; Huo, Z.; Farha , R.; Goldmann , M.; Xu, H.; Hasenknopf, B.; Lacôte , E.; Ruhlmann, L. *Chem. Eur. J.* **2015**, *21*, 8271.

(128) Kang, H.; Zubieta, J. *J. Chem. Soc., Chem. Commun.* **1988**, 1192.

(129) *Polyoxometalates: from Platonic Solids to Anti-Retroviral Activity*,; W. Clegg, R. J. E., K. A. Fraser, C. Lax and D. G. Richards, Ed.; ed.M. T. Pope and A. Muller, Kluwer, Dordrecht, **1994**.

(130) Wei, Y.; Xu, B.; Barnes, C. L.; Peng, Z. *J. Am. Chem. Soc.* **2001**, *123*, 4083.

(131) Wu, P.; Li, Q.; Ge, N.; Wei, Y.; Wang, Y.; Wang, P.; Guo, H. *Eur. J. Inorg. Chem.* **2004**, *2004*, 2819.

(132) Zhu, Y.; Wang, L.; Hao, J.; Yin, P.; Zhang, J.; Li, Q.; Zhu, L.; Wei, Y. *Chem. Eur. J.* **2009**, *15*, 3076.

(133) Kang, J.; Xu, B.; Peng, Z.; Zhu, X.; Wei, Y.; Powell, D. R. *Angew. Chem. Int. Ed.* **2005**, *44*, 6902.

(134) He, T.; He, J.; Lu, M.; Chen, B.; Pang, H.; Reus, W. F.; Nolte, W. M.; Nackashi, D. P.; Franzon, P. D.; Tour, J. M. *J. Am. Chem. Soc.* **2006**, *128*, 14537.

(135) Strong, J. B.; Ostrander, R.; Rheingold, A. L.; Maatta, E. A. *J. Am. Chem. Soc.* **1994**, *116*, 3601.

(136) Strong, J. B.; Yap, G. P. A.; Ostrander, R.; Liable-Sands, L. M.; Rheingold, A. L.; Thouvenot, R.; Gouzerh, P.; Maatta, E. A. *J. Am. Chem. Soc.* **2000**, *122*, 639.

(137) Xu, L.; Lu, M.; Xu, B. B.; Wei, Y. G.; Peng, Z. H.; Powell, D. R. *Angew. Chem. Int. Ed.* **2002**, *41*, 4129.

(138) Li, Q.; Wu, P.; Wei, Y.; Wang, Y.; Wang, P.; Guo, H. *Inorg. Chem. Commun* **2004**, *7*, 524.

(139) Lu, M.; Xie, B.; Kang, J.; Chen, F.-C.; Yang; Peng, Z. *Chem. of Mater.* **2005**, *17*, 402.

(140) Xu, B.; Wei, Y.; Barnes, C. L.; Peng, Z. *Angew. Chem. Int. Ed.* **2001**, *40*, 2290.

(141) Baker, L. C. W.; Figgis, J. S. *J. Am. Chem. Soc.* **1970**, *92*, 3794.

(142) Zheng, S.-T.; Yang, G.-Y. *Chem. Soc. Rev.* **2012**, *41*, 7623.

(143) Klemperer, R. K. C. H. a. W. G. *J. Am. Chem. Soc.* **1976**, *100*, 2.

(144) Gouzerh, P.; Proust, A. *Chem. Rev.* **1998**, *98*, 77.

(145) Knoth, W. H. *J. Am. Chem. Soc.* **1979**, *101*, 759.

(146) Judeinstein, P.; Deprun, C.; Nadjo, L. *J. Chem. Soc., Dalton Trans..* **1991**, 1991.

(147) Agustin, D.; Dallery, J.; Coelho, C.; Proust, A.; Thouvenot, R. *J. Organomet. Chem.* **2007**, *692*, 746.

(148) Artero, V.; Proust, A.; Herson, P.; Villain, F.; Cartier dit Moulin, C.; Gouzerh, P. *J. Am. Chem. Soc.* **2003**, *125*, 11156.

(149) Matt, B.; Renaudineau, S.; Chamoreau, L. M.; Afonso, C.; Izzet, G.; Proust, A. *J. Org. Chem.* **2011**, *76*, 3107.

(150) Gouzerh, P.; Proust, A. *Chem. Rev.* **1998**, *98*, 77.

(151) Matt, B.; Xiang, X.; Kaledin, A. L.; Han, N.; Moussa, J.; Amouri, H.; Alves, S.; Hill, C. L.; Lian, T.; Musaev, D. G.; Izzet, G.; Proust, A. *Chem. Sci.* **2013**, *4*, 1737.

(152) Sousa, J. L. C.; Santos, I. C. M. S.; Simoes, M. M. Q.; Cavaleiro, J. A. S.; Nogueira, H. I. S.; Cavaleiro, A. M. V. *Catal. Commun.* **2011**, *12*, 459.

(153) Fontananova, E.; Drioli, E.; Donato, L.; Bonchio, M.; Carraro, M.; Gardan, M.; Scorrano, G. *Desalination* **2006**, *200*, 705.

(154) Dolbecq, A.; Dumas, E.; Mayer, C. d. R.; Mialane, P. *Chem. Rev.* **2010**, *110*, 6009.

(155) Liu, L.; Wang, S.-M.; Li, C.; Liu, C.-G.; Ma, C.-L.; Han, Z.-B. *J. Mater. Chem. C* **2015**, *3*, 5175.

(156) Yang, G.; Gong, J.; Yang, R.; Guo, H.; Wang, Y.; Liu, B.; Dong, S. *Electrochem. Commun.* **2006**, *8*, 790.

(157) Lopez, X.; Carbo, J. J.; Bo, C.; Poblet, J. M. *Chem. Soc. Rev.* **2012**, *41*, 7537.

(158) Liu, S.; Kurth, D. G.; Möhwald, H.; Volkmer, D. *Adv. Mater.* **2002**, *14*, 225.

(159) Liz-Marza\n, L. M.; Kamat, P. V. *Nanoscale materials*; Kluwer Academic Publishers: Boston ; London, **2003**.

(160) Clemente-León, M.; Ito, T.; Yashiro, H.; Yamase, T.; Coronado, E. *Langmuir* **2007**, *23*, 4042.

(161) Joo, N.; Renaudineau, S.; Delapierre, G.; Bidan, G.; Chamoreau, L.-M.; Thouvenot, R.; Gouzerh, P.; Proust, A. *Chem. Eur. J.* **2010**, *16*, 5043.

(162) Liu, S.; Xu, L.; Li, F.; Guo, W.; Xing, Y.; Sun, Z. *Electrochim Acta* **2011**, *56*, 8156.

(163) Xu, B.; Xu, L.; Gao, G.; Jin, Y. *Appl. Surface Sci.* **2007**, *253*, 3190.

(164) Jin, L.; Fang, Y.; Hu, P.; Zhai, Y.; Wang, E.; Dong, S. *Chem. Commun.* **2012**, *48*, 2101.

(165) Xu, B.; Xu, L.; Gao, G.; Yang, Y.; Guo, W.; Liu, S.; Sun, Z. *Electrochim Acta* **2009**, *54*, 2246.

(166) Li, C.; O'Halloran, K. P.; Ma, H.; Shi, S. *J. Phys. Chem. B* **2009**, *113*, 8043.

(167) Ammam, M. *J. Mater. Chem. A* **2013**.

(168) Lapkowski, M.; Turek, W.; Barth, M.; Lefrant, S. *Synth. Metals* **1995**, *69*, 127.

(169) Hillman, A. R.; Loveday, D. C.; Bruckenstein, S. *J. Electroanal. Chem.* **1989**, *274*, 157.

(170) Lewis, T. W.; Wallace, G. G.; Smyth, M. R. *The Analyst* **1999**, *124*, 213.

(171) Gómez-Romero, P.; Chojak, M.; Cuentas-Gallegos, K.; Asensio, J. A.; Kulesza, P. J.; Casañ-Pastor, N.; Lira-Cantú, M. *Electrochem. Commun.* **2003**, *5*, 149.

(172) Cuentas-Gallegos, A. K.; Lira-Cantú, M.; Casañ-Pastor, N.; Gómez-Romero, P. *Adv. Funct. Mater.* **2005**, *15*, 1125.

(173) Kasem, K. K.; Schultz, F. A. *Can. J. Chem.* **1995**, *73*, 858.

(174) Coronado, E.; Gómez-García, C. J. *Chem. Rev.* **1998**, *98*, 273.

(175) Vaillant, J.; Lira-Cantu, M.; Cuentas-Gallegos, K.; Casan-Pastor, N.; Gomez-Romero, P. *Progress in Solid State Chem* **2006**, *34*, 147.

(176) Adamczyk, L.; Kulesza, P. J.; Miecznikowski, K.; Palys, B.; Chojak, M.; Krawczyk, D. *J. Electrochem. Soc.* **2005**, *152*, E98.

(177) Fabre, B.; Bidan, G. *Electrochim Acta* **1997**, *42*, 2587.

(178) Anwar, N.; Vagin, M.; Laffir, F.; Armstrong, G.; Dickinson, C.; McCormac, T. *The Analyst* **2012**, *137*, 624.

(179) Gomez-Romero, P.; Cuentas-Gallegos, K.; Lira-Cantu, M.; Casan-Pastor, N. *J. Mater. Sci.* **2005**, *40*, 1423.

(180) Cheng, S. A.; Otero, T. F. *Synth. Metals* **2002**, *129*, 53.

(181) Inzelt, G.; Kertesz, V.; Nyback, A. S. *J. Solid State Electrochem.* **1999**, *3*, 251.

(182) Abrantes, L. *Electrochim Acta* **2002**, *47*, 1481.

(183) Judeinstein, P. *Chem of Mater* **1992**, *4*, 4.

(184) Xu, B.; Lu, M.; Kang, J.; Wang, D.; Brown, J.; Peng, Z. *Chem. of Mater.* **2005**, *17*, 2841.

(185) Xu, L.; Lu, M.; Xu, B.; Wei, Y.; Peng, Z.; Powell, D. R. *Angew. Chem. Int. Ed.* **2002**, *41*, 4129.

(186) Errington, R. J.; Petkar, S. S.; Middleton, P. S.; McFarlane, W.; Clegg, W.; Coxall, R. A.; Harrington, R. W. *J. Am. Chem. Soc.* **2007**, *129*, 12181.

(187) Errington, R. J.; Petkar, S. S.; Middleton, P. S.; McFarlane, W.; Clegg, W.; Coxall, R. A.; Harrington, R. W. *Dalton Trans.* **2007**, 5211.

(188) Zhuang, J.; Yan, L.; Liu, C.; Su, Z. *Eur. J. Inorg. Chem.* **2009**, *2009*, 2529.

(189) Yan, L.-K.; Su, Z.-M.; Guan, W.; Zhang, M.; Chen, G.-H.; Xu, L.; Wang, E.-B. *J. Phys. Chem. B* **2004**, *108*, 17337.

(190) Yan, L.; Yang, G.; Guan, W.; Su, Z.; Wang, R. *J. Phys. Chem. B* **2005**, *109*, 22332.

(191) Yan, L.-K.; Jin, M.-S.; Zhuang, J.; Liu, C.-G.; Su, Z.-M.; Sun, C.-C. *J. Phys. Chem. A* **2008**, *112*, 9919.

(192) Yan, L.; Jin, M.; Song, P.; Su, Z. *J. Phys. Chem. B* **2010**, *114*, 3754.

(193) Wen, S.; Yang, G.; Yan, L.; Li, H.; Su, Z. *Chem. Phys. Chem* **2013**, *14*, 610.

(194) Zhuang, J.; Yan, L.; Liu, C.; Su, Z. *Eur. J. Inorg. Chem.* **2009**, *2009*, 2529.

(195) Ju, W.-W.; Zhang, H.-T.; Xu, X.; Zhang, Y.; Xu, Y. *Inorg. Chem.* **2014**, *53*, 3269.

(196) Janjua, M. R. S. A. *Inorg. Chem.* **2012**, *51*, 11306.

(197) Janjua, M. R. S. A.; Liu, C.-G.; Guan, W.; Zhuang, J.; Muhammad, S.; Yan, L.-K.; Su, Z.-M. *J. Phys. Chem. A* **2009**, *113*, 3576.

(198) Ramzan Saeed Ashraf Janjua, M.; Guan, W.; Yan, L.; Su, Z.-M. *Current Phys. Chem.* **2011**, *1*, 99.

(199) Matt, B.; Xiang, X.; Kaledin, A. L.; Han, N.; Moussa, J.; Amouri, H.; Alves, S.; Hill, C. L.; Lian, T.; Musaev, D. G.; Izzet, G.; Proust, A. *Chem. Sci.* **2013**, *4*, 1737.

(200) Matt, B.; Fize, J.; Moussa, J.; Amouri, H.; Pereira, A.; Artero, V.; Izzet, G.; Proust, A. *Energy Env. Sci.* **2013**, *6*, 1504.

(201) Song, P.; Yan, L.-K.; Guan, W.; Liu, C.-G.; Yao, C.; Su, Z.-M. *J Molecular Graphics and Modelling* **2010**, *29*, 13.

(202) Armarego, W. L. F.; Chai, C. L. L. *Purification of Laboratory Chemicals*; Butterworth-Heinemann, **2003**.

(203) Le Gall, T.; Passos, M. S.; Ibrahim, S. K.; Morlat-Therias, S.; Sudbrake, C.; Fairhurst, S. A.; Queiros, M. A.; Pickett, C. J. *J. Chem. Soc., Perkin Trans. 1* **1999**, 1657.

(204) Bar-Nahum, I.; Narasimhulu, K. V.; Weiner, L.; Neumann, R. *Inorg. Chem.* **2005**, *44*, 4900.

(205) Instrumentation, P. R.; Pine Research Instrumentation: **2015**; Vol. 2015.

(206) Gawande, M. B.; Branco, P. S. *Green Chem.* **2011**, *13*, 3355.

(207) D'Silva, C.; Walker, D. A. *J. Org. Chem.* **1998**, *63*, 6715.

(208) Deng, H.-J.; Fang, Y.-J.; Chen, G.-W.; Liu, M.-C.; Wu, H.-Y.; Chen, J.-X. *Appl. Organomet. Chem.* **2012**, *26*, 164.

(209) Elming, N. C.-K., N. *Acta Chem. Scand* **1952**, *6*, 867.

(210) Klemperer, W. G. In *Inorg. Synth.*; John Wiley & Sons, Inc.: **2007**, p 74.

(211) 1.171.36.21), C. V. *Agilent Technologies, Inc.; Santa Clara: CA, United States* **2012**.

(212) b27), C.-S. E. V. *Rigaku Corporation; Tokyo: Japan* **2013**.

(213) Sheldrick, G. M. S., Programs for Crystal Structure Analysis (Release 97-2) *University of Göttingen: Göttingen, Germany* **1997**.

(214) Farrugia, L. *J. Appl. Cryst.* **1999**, *32*, 837.

(215) Olbrechts, G.; Wostyn, K.; Clays, K.; Persoons, A. *Opt. Lett.* **1999**, *24*, 403.

(216) Campo, J.; Desmet, F.; Wenseleers, W.; Goovaerts, E. *Opt. Expr.* **2009**, *17*, 4587.

(217) Shin, Y.-g. K.; Brunschwig, B. S.; Creutz, C.; Sutin, N. *J. Phys. Chem.* **1996**, *100*, 8157.

(218) Carraro, M.; Gross, S. *Materials* **2014**, *7*, 3956.

(219) Bar-Nahum, I.; Narasimhulu, K. V.; Weiner, L.; Neumann, R. *Inorg. Chem.* **2005**, *44*, 4900.

(220) Lv, C.; Khan, R. N. N.; Zhang, J.; Hu, J.; Hao, J.; Wei, Y. *Chem. Eur. J.* **2013**, *19*, 1174.

(221) Pladzyk, A.; Ponikiewski, Ł.; Lan, Y.; Powell, A. K. *Inorg. Chem. Commun* **2012**, *20*, 66.

(222) Lu, M.; Nolte, W. M.; He, T.; Corley, D. A.; Tour, J. M. *Chem. of Mater.* **2009**, *21*, 442.

(223) Bard, A. J.; Faulkner, L. R. *Electrochemical methods : fundamentals and applications*; 2nd ed.; Wiley India Ltd.: New Delhi, **2006**.

(224) D. Pletcher (Author), R. G. C., R. Peat (Contributor),   L. M. Peter (Contributor), J. Robinson *Instrumental methods in electrochemistry*; Horwood Pub.: Chichester, **2001**.

(225) Wang, Y. a.; Compton, R. d. s. Thesis (Ph.D.), University of Oxford, **2012**.

(226) Smithe, G. M. *Electroanalytical chemistry : new research*; Nova Science ; Lancaster : Gazelle [distributor]: Hauppauge, N.Y., **2008**.

(227) Vassos, B. H.; Ewing, G. W. *Electroanalytical chemistry*; Wiley: New York ; Chichester, **1983**.

(228) Evans, L. A.; University of Hull: Hull, **2008**.

(229) Fernandez, H.; Zon, M. A. *Recent developments and applications of electroanalytical chemistry*; Research Signpost: Kerala, **2002**.

(230) Rubinstein, I. *Physical electrochemistry : principles, methods, and applications*; Dekker: New York, **1995**.

(231) Sadakane, M.; Steckhan, E. *Chem. Rev.* **1998**, *98*, 219.

(232) Coe, B. J.; Fielden, J.; Foxon, S. P.; Harris, J. A.; Helliwell, M.; Brunschwig, B. S.; Asselberghs, I.; Clays, K.; Garín, J.; Orduna, J. s. *J. Am. Chem. Soc.* **2010**, *132*, 10498.

(233) Brabec, C. J.; Dyakonov, V.; Scherf, U. *Organic photovoltaics : materials, device physics, and manufacturing technologies*; Wiley-VCH: Weinheim, **2008**.

(234) Strong, J. B.; Yap, G. P. A.; Ostrander, R.; Liable-Sands, L. M.; Rheingold, A. L.; Thouvenot, R.; Gouzerh, P.; Maatta, E. A. *J. Am. Chem. Soc.* **2000**, *122*, 639.

(235) Li, Q.; Wang, L.; Yin, P.; Wei, Y.; Hao, J.; Zhu, Y.; Zhu, L.; Yuan, G. *Dalton Trans.* **2009**, 1172.

(236) Pope, M. T.; Yamase, T. *Polyoxometalate chemistry for nano-composite design*; Kluwer Academic/Plenum Publishers: New York, N.Y. ; London, **2002**.

(237) Marder, S. R. *Chem. Commun.* **2006**, 131.

(238) Wolff, J. J.; Wortmann, R. In *Adv. Phys. Org. Chem.*; Bethell, D., Ed.; Academic Press: **1999**, *32*, p 121.

(239) Nalwa, H. S.; Miyata, S. o. *Nonlinear optics of organic molecules and polymers*; CRC: Boca Raton, Fla. ; London, **1996**.

(240) Goodson, T. G. *Linear and nonlinear optics of organic materials IX : 2 and 4-5 August 2009, San Diego, California, United States*; SPIE: Bellingham, Wash., **2009**.

(241) Che, M.; Fournier, M.; Launay, J. P. *J. Chem. Phys.* **1979**, *71*, 1954.

(242) Verbiest, T.; Meyers, F.; Brédas, J. L.; Clays, K.; Persoons, A. *Opt. Lett.* **1993**, *18*, 525.

(243) Olbrechts, G.; Wostyn, K.; Clays, K.; Persoons, A. *Opt. Lett.* **1999**, *24*, 403.

(244) Yang, S. K.; Ahn, H. C.; Jeon, S.-J.; Asselberghs, I.; Clays, K.; Persoons, A.; Cho, B. R. *Chem. Phys. Lett* **2005**, *403*, 68.

(245) Noordman, O. F. J.; van Hulst, N. F. *Chem. Phys. Lett* **1996**, *253*, 145.

(246) Olbrechts, G.; Strobbe, R.; Clays, K.; Persoons, A. *Rev. Sci. Instru.* **1998**, *69*, 2233.

(247) Coe, B. J.; Harris, J. A.; Asselberghs, I.; Clays, K.; Olbrechts, G.; Persoons, A.; Hupp, J. T.; Johnson, R. C.; Coles, S. J.; Hursthouse, M. B.; Nakatani, K. *Adv Funct Mater* **2002**, *12*, 110.

(248) Cheng, L. T.; Tam, W.; Stevenson, S. H.; Meredith, G. R.; Rikken, G.; Marder, S. R. *J. Phys. Chem.* **1991**, *95*, 10631.

(249) Oudar, J. L.; Chemla, D. S. *J. Chem. Phys.* **1977**, *66*, 2664.

(250) Janjua, M. R. S. A.; Guan, W.; Yan, L.; Su, Z.-M.; Karim, A.; Akbar, J. *Eur. J. Inorg. Chem.* **2010**, *2010*, 3466.

(251) Coe, B. J.; Harris, J. A.; Asselberghs, I.; Clays, K.; Olbrechts, G.; Persoons, A.; Hupp, J. T.; Johnson, R. C.; Coles, S. J.; Hursthouse, M. B.; Nakatani, K. *Adv. Funct. Mater.* **2002**, *12*, 110.

(252) Coe, B. J.; Harris, J. A.; Asselberghs, I.; Wostyn, K.; Clays, K.; Persoons, A.; Brunschwig, B. S.; Coles, S. J.; Gelbrich, T.; Light, M. E.; Hursthouse, M. B.; Nakatani, K. *Adv. Funct. Mater.* **2003**, *13*, 347.

(253) Jang, S.-H.; Luo, J.; Tucker, N. M.; Leclercq, A.; Zojer, E.; Haller, M. A.; Kim, T.-D.; Kang, J.-W.; Firestone, K.; Bale, D.; Lao, D.; Benedict, J. B.; Cohen, D.; Kaminsky, W.; Kahr, B.; Brédas, J.-L.; Reid, P.; Dalton, L. R.; Jen, A. K. Y. *Chem. of Mater.* **2006**, *18*, 2982.

(254) Clays, K.; Coe, B. J. *Chem. of Mater.* **2003**, *15*, 642.

(255) Kang, H.; Facchetti, A.; Jiang, H.; Cariati, E.; Righetto, S.; Ugo, R.; Zuccaccia, C.; Macchioni, A.; Stern, C. L.; Liu, Z.; Ho, S.-T.; Brown, E. C.; Ratner, M. A.; Marks, T. J. *J. Am. Chem. Soc.* **2007**, *129*, 3267.

(256) Gaudette, A. I.; Jeon, I.-R.; Anderson, J. S.; Grandjean, F.; Long, G. J.; Harris, T. D. *J. Am. Chem. Soc.* **2015**, *137*, 12617.

(257) Azenha, E. l. G.; Serra, A. C.; Pineiro, M.; Pereira, M. M.; Seixas de Melo, J.; Arnaut, L. G.; Formosinho, S. J.; Rocha Gonsalves, A. M. d. A. *Chem. Phys.* **2002**, *280*, 177.

(258) Milne, B. F.; Nogueira, F.; Cardoso, C. *Dalton Trans.* **2013**, *42*, 3695.

(259) Keyes, T. E.; Gicquel, E.; Guerin, L.; Forster, R. J.; Hultgren, V.; Bond, A. M.; Wedd, A. G. *Inorg. Chem.* **2003**, *42*, 7897.

(260) Hemant K . Sinhaa, K. Y. A. *Can. J. Chem.* **1991**, *69*, 7.

(261) Shi, Y.; Frattarelli, D.; Watanabe, N.; Facchetti, A.; Cariati, E.; Righetto, S.; Tordin, E.; Zuccaccia, C.; Macchioni, A.; Wegener, S. L.; Stern, C. L.; Ratner, M. A.; Marks, T. J. *J. Am. Chem. Soc.* **2015**, *137*, 12521.

(262) Song, P.; Yan, L.-K.; Guan, W.; Liu, C.-G.; Yao, C.; Su, Z.-M. *J. Molecular Graphics and Modelling* **2010**, *29,* 13.

(263) Wang, J.; Cong, S.; Wen, S.; Yan, L.; Su, Z. *J. Phys. Chem. C* **2013**, *117*, 2245.

(264) Orloff, J.; Swanson, L. W.; Utlaut, M. *J. Vacuum Sci. and Tech. B* **1996**, *14*, 3759.

(265) Steve, R.; Robert, P. *J. Micromechanics and Microengineering* **2001**, *11*, 287.

(266) Carl Matthias, I.; Karsten, H.; Vitali, S.; Florent, Y.; Jörg, R. *Jpn. J. Appl. Phys.* **2008**, *47*, 554.

(267) Komaba, S.; Fujihana, K.; Osaka, T.; Aiki, S.; Nakamura, S. *J. Electrochem. Soc.* **1998**, *145*, 1126.

(268) Letheby, H. *J. Chem. Soc.* **1862**, *15*, 161.

(269) Shirakawa, H.; Louis, E. J.; MacDiarmid, A. G.; Chiang, C. K.; Heeger, A. J. *J. Chem. Soc., Chem. Commun.* **1977**, 578.

(270) Tat'yana, V. V.; Oleg, N. E. *Russ. Chem. Rev.* **1997**, *66*, 443.

(271) Sabouraud, G. S., Saïd Brodie, Nancy *Chem. Soc. Rev.* **2000**, *29*, 283.

(272) Patois, T.; Lakard, B.; Martin, N.; Fievet, P. *Synth. Metals* **2010**, *160*, 2180.

(273) Cross, M. G.; Walton, D.; Morse, N. J.; Mortimer, R. J.; Rosseinsky, D. R.; Simmonds, D. J. *J. Electroanal. Chem. and Int. Electrochem.* **1985**, *189*, 389.

(274) Heinze, J. r.; Frontana-Uribe, B. A.; Ludwigs, S. *Chem. Rev.* **2010**, *110*, 4724.

(275) Zhou, M.; Heinze, J. *J. Phys. Chem. B* **1999**, *103*, 8451.

(276) Liebscher, J.; Karsten, S.; Ameen, M.; Kalläne, S.; Nan, A.; Turcu, R. *Synthesis* **2010**, *2010*, 3021.

(277) Wang WY, T. P., Luo SH, Lin JY *Electrochim Acta* **2014**, *137*, 6.

(278) To Thi Kim, L.; Debiemme-Chouvy, C.; Gabrielli, C.; Perrot, H. *Langmuir* **2012**, *28*, 13746.

(279) Shin, K.-H.; Cho, J.; Jang, J.; Jang, H. S.; Park, E. S.; Song, K.; Kim, S. H. *Org. Electron* **2012**, *13*, 715.

(280) Gümüş, A.; Altındal, Ş. *Mater. Sci. Semicond. Process* **2014**, *28*, 66.

(281) J., J. P. P. V. D. S. M. P. C. *Optoelectron Adv. Mater. – Rapid Commun.* **2010**, *4*, 553.

(282) Waltman, R. J.; Bargon, J. *Tetrahedron* **1984**, *40*, 3963.

(283) Genies, E. M.; Bidan, G.; Diaz, A. F. *J. Electroanal. Chem. and Int. Electrochem.* **1983**, *149*, 101.

(284) Conn, M. M.; Deslongchamps, G.; de Mendoza, J.; Rebek, J. *J. Am. Chem. Soc.* **1993**, *115*, 3548.

(285) Shao, H.; Chen, X.; Wang, Z.; Lu, P. *J. Luminescence* **2007**, *127*, 349.

(286) Tan, L.-L.; Xie, L.-J.; Shen, Y.; Liu, J.-M.; Xiao, L.-M.; Kuang, D.-B.; Su, C.-Y. *Dyes Pigm.* **2014**, *100*, 269.

(287) Vicente, J.; Gil-Rubio, J.; Zhou, G.; Bolink, H. J.; Arias-Pardilla, J. *J. Polym. Sci., Part A: Polym. Chem.* **2010**, *48*, 3744.

(288) Hayashi, M.; Sakamoto, R.; Nishihara, H. *Chem. Eur. J.* **2012**, *18*, 8610.

(289) Kakuta, T.; Shirota, Y.; Mikawa, H. *J. Chem. Soc., Chem. Commun.* **1985**, 553.

(290) Mengoli, G.; Musiani, M. M.; Schreck, B.; Zecchin, S. *J. Electroanal. Chem. and Int. Electrochem.* **1988**, *246*, 73.

(291) Cattarin, S.; Mengoli, G.; Musiani, M. M.; Schreck, B. *J. Electroanal. Chem. and Int. Electrochem.* **1988**, *246*, 87.

(292) Ambrose, J. F.; Nelson, R. F. *J. Electrochem. Soc.* **1968**, *115*, 1159.

(293) Sadki, S.; Schottland, P.; Brodie, N.; Sabouraud, G. *Chem. Soc. Rev.* **2000**, *29*, 283.

(294) Thompson, B. C.; Abboud, K. A.; Reynolds, J. R.; Nakatani, K.; Audebert, P. *New J. Chem.* **2005**, *29*, 1128.

(295) Reynolds, J. R.; Poropatic, P. A.; Toyooka, R. L. *Macromolecules* **1987**, *20*, 958.

(296) Wallace, G. G. *Conductive electroactive polymers : intelligent materials systems*; 2nd ed. ed.; CRC: Boca Raton, Fla. ; London, **2002**.

(297) Chu, S. Y.; Kilmartin, P. A.; Jing, S.; Bowmaker, G. A.; Cooney, R. P.; Travas-Sejdic, J. *Synth. Metals* **2008**, *158*, 38.

(298) L., A. A. A. A. C. T. R. *J Chilean Chem Soc* **2009**, *54*, 14.

(299) Pickett, C. J.; Ryder, K. S.; Moutet, J.-c. *J. Chem. Soc., D Trans* **1993**, 3695.

(300) Le Gall, T.; S. Passos, M.; K. Ibrahim, S.; Morlat-Therias, S.; Sudbrake, C.; A. Fairhurst, S.; Arlete Queiros, M.; J. Pickett, C. *J. Chem. Soc., Perkin Trans. 1* **1999**, 1657.

(301) Oura, K.; Katayama, M.; Zotov, A. V.; Lifshits, V. G.; Saranin, A. A. **2003**.

(302) Kang, E. T.; Neoh, K. G.; Ong, Y. K.; Tan, K. L.; Tan, B. T. G. *Macromolecules* **1991**, *24*, 2822.

(303) Abaci, U.; Guney, H. Y.; Kadiroglu, U. *Electrochim Acta* **2013**, *96*, 214.

(304) Yao, T.; Wang, C.; Wu, J.; Lin, Q.; Lv, H.; Zhang, K.; Yu, K.; Yang, B. *J. Colloid and Interface Sci.* **2009**, *338*, 573.

(305) Li, J.; Grimsdale, A. C. *Chem. Soc. Rev.* **2010**, *39*, 2399.